Steam Reforming Kinetics of Olefins and Aromatics over Spinel Oxide Catalysts

---

A

Dissertation

Presented to
the faculty of the School of Engineering and Applied Science
University of Virginia

---

in partial fulfillment
of the requirements for the degree

Doctor of Philosophy

by

Lu Yang

May 2021

APPROVAL SHEET

This
Dissertation
is submitted in partial fulfillment of the requirements
for the degree of
Doctor of Philosophy

Author: Lu Yang

This Dissertation has been read and approved by the examing committee:

Advisor: Robert Davis

Advisor:

Committee Member: William Epling

Committee Member: Christopher Paolucci

Committee Member: Gaurav Giri

Committee Member: Joshua Choi

Committee Member: Sen Zhang

Committee Member:

Accepted for the School of Engineering and Applied Science:

Craig H. Benson, School of Engineering and Applied Science

May 2021

ABSTRACT

Ethane steam cracking is the predominant method for industrial production of ethylene in the United States. However, the economy of this process is significantly impeded by the periodic shutdown due to coke deposition. Although catalytic coking facilitated by the metallic alloy surface can be effectively suppressed by the barrier oxide layers formed upon oxidative pretreatment, radical coking still occurs at the high temperatures applied for steam cracking. To develop catalytic barrier oxide layers that further relieve radical coke accumulation through *in situ* steam gasification of coke under steam cracking environments, the activity and stability of various spinel oxide components from the barrier oxide layers in steam reforming of olefins and aromatics, which are model reactions for steam gasification of coke, were investigated.

Powder samples of Mn-Cr-O spinel oxides ($Mn_xCr_{3-x}O_4$) as well as single oxides of Cr and Mn that are representative of the conventional $MnCr_2O_4/Cr_2O_3$ protective oxide layers were synthesized and characterized. Results from X-ray diffraction (XRD), X-ray absorption spectroscopy (XAS) and X-ray photoelectron spectroscopy (XPS) indicated that excess Mn in $Mn_{1.5}Cr_{1.5}O_4$ exists as Mn^{3+} that partially substitutes the Cr^{3+} in the octahedral sites of the spinel lattice, whereas Cr separates into Cr_2O_3 when in excess. A single oxide of Mn (Mn_3O_4) showed the highest steam reforming rate for both ethylene and toluene at 873 K, but deactivated due to reduction to MnO. The Mn-Cr-O spinel catalysts and Cr_2O_3 were structurally stable under these reforming conditions. While Cr_2O_3 was initially more active for olefin reforming than the spinel catalysts, it deactivated rapidly due to coke deposition. The Mn-rich $Mn_{1.5}Cr_{1.5}O_4$ spinel catalyst exhibited both the highest reforming rate and stability during steam reforming of aromatics, potentially attributed to the excess Mn^{3+} sites stabilized by the spinel lattice.

The steam reforming rate of olefins and aromatics was nearly first order in the individual hydrocarbon and slightly inhibited by H_2O. The reforming kinetics are explained by a Mars-van Krevelen type mechanism, in which the inhibition by H_2O is attributed to the competitive adsorption between hydrocarbon and H_2O. While excess H_2 did not affect the reforming rate of olefins and benzene, the rate of toluene reforming was strongly inhibited by excess H_2 resulting in negative first order kinetics. Results from diffuse reflectance infrared Fourier transform spectroscopy (DRIFTS) of toluene adsorption on the spinel surface suggest H_2 likely inhibits the oxidation of the highly reactive side methyl group of toluene. Consistent with the observed

negative first order in H_2, toluene steam reforming showed the highest apparent activation energy compared to olefins and benzene.

Powder catalysts of Ni-based spinel oxides (NiM_2O_4) that are present in the Al_2O_3 protective oxide layers of the Al-enhanced cracker alloy were also synthesized and characterized. Results from temperature-programmed reduction in H_2 (H_2-TPR) indicate the reduction of Fe^{3+} in $NiFe_2O_4$ accelerated the reduction of Ni into Ni-Fe alloy particles for that sample, whereas $NiAl_2O_4$ and $NiCr_2O_4$ reduced to Ni metal at much higher temperatures. Consistent with this observation, the spinel structure of $NiFe_2O_4$ degraded to Ni-Fe alloy particles that severely coked during ethylene steam reforming at 873 K. While both $NiAl_2O_4$ and $NiCr_2O_4$ remained structurally stable, the ethylene reforming rate and the amount of coke deposited increased substantially for both catalysts after re-oxidation. These findings suggest a detrimental role of Ni-based spinel oxides for the barrier oxide layers, since the oxidative pretreatment for coke removal likely also facilitates the agglomeration of small Ni metal particles into NiO aggregates, which are more prone to reduction and catalyze coke deposition when exposed to a reducing environment like steam cracking.

Finally, two Co-Cr-O spinel oxides ($Co_xCr_{3-x}O_4$) were synthesized and characterized to explore the ethylene steam reforming activity of Co spinel oxides. The XRD and XPS results suggest the excess Co in $Co_{1.5}Cr_{1.5}O_4$ exists as Co^{3+} that likely resides in the octahedral sites to replace Cr^{3+} by analogy to $Mn_{1.5}Cr_{1.5}O_4$. The Co^{2+} sites in stoichiometric $CoCr_2O_4$ were reduced to Co metal at high temperatures. The reduction of $Co_{1.5}Cr_{1.5}O_4$ with excess Co likely occurred in a stepwise manner with the reduction of Co^{3+} to Co^{2+} occurring at lower temperatures prior to reduction of Co^{2+}. Both $CoCr_2O_4$ and $Co_{1.5}Cr_{1.5}O_4$ were structurally stable during ethylene steam reforming at 873 K. The reforming rate over $Co_{1.5}Cr_{1.5}O_4$ was one order-of magnitude higher than that over $CoCr_2O_4$ and was proposed to be attributed to the excess Co^{3+} sites. The steady-state ethylene reforming rate remained unchanged after re-oxidation for both $CoCr_2O_4$ and $Co_{1.5}Cr_{1.5}O_4$, suggesting a better stability of Co-Cr-O spinel oxides against reduction to metal particles compared to the Ni-based spinel oxides under identical reforming conditions.

Acknowledgements

First of all, I would like to thank the patient guidance and continuous support from my thesis advisor, Prof. Robert Davis. Your creative while meticulous attitude in catalysis research has deeply influenced me and set me a great paradigm as a scientist and engineer. In retrospect, although I have learned countless pieces of knowledge and experience from you in the past four years, I never felt even getting a bit closer to the wisdom you have. In addition to research, you have also introduced many aspects of American culture and life to me, which is of great help for an international student like myself to adapt to the new environment.

Secondly, I want to acknowledge the Dow Chemical Company for funding my graduate study. I am also grateful to our collaborators on the project, including Maxim Bukhovko and Prof. Christopher Jones from the Georgia Institute of Technology, Prof. Pradeep Agrawal from the Michigan Technological University, and Dr. Liwei Li and Dr. Andrzej Malek from the Dow Hydrocarbons R&D, who have constantly provided insightful feedback on my research and shared a great amount of advice for my career development.

Furthermore, I appreciate the fruitful discussions with Prof. William Epling and Prof. Christopher Paolucci. The both collaborative and competitive environment established by the three groups was critical for the success of all PhD students in our catalysis community and has expanded my knowledge to a great extent. In addition, I am grateful to all the indispensable support from my previous and current colleagues that underlies my success, including but not limited to: Dr. Jiahan Xie, Dr. Nicholas Kaylor, Dr. James Kammert, Dr. Gordon Brezicki, Tyler Prillaman, Dr. Yuntao Gu, Naomi Miyake, Ryan Zelinsky, Yu-Ren Chen, Silvia Marino, Colby Whitcomb and Konstantin Mamedov.

In the end, I want to thank the understanding and support from my parents, who provide me the courage to embrace and face the difficulties I encountered during my PhD study. Empathetic support and encouragement from many previous colleagues at Peking University, who are currently PhD candidates in the United States, are also acknowledged.

Table of contents

List of Figures and Schemes

(Captions may be partially omitted for brevity.)

List of Tables

Chapter 1 Introduction

1.1 Ethylene production from steam cracking of ethane

Ethylene ($H_2C=CH_2$) is one of the most essential raw materials in the chemical and polymer industry. During the World War II, the production of ethylene rapidly increased to fulfill the demands on styrene-derived synthetic rubbers, where ethylene reacted with benzene to form ethylbenzene [1], a primary precursor for the production of styrene through dehydrogenation [2] (**Scheme 1.1**). Although polyethylene was first commercialized early in 1939, the importance of ethylene in the polymer industry was not fully recognized until the 1950s when the high-density polyethylene (HDPE) entered the market as stiff and heat-resistant plastics thanks to the discovery of Cr-based (Hogan and Banks [3]) and Ti-based (Ziegler [4]) catalysts [5]. In addition to ethylbenzene and polyethylene, ethylene is also responsible for the production of ethylene oxide, vinyl acetate and 1,2-dichloroethane, which are the precursors for various types of chemicals (*e.g.*, ethoxylates, ethylene glycol and glycol esters) and polymers (*e.g.*, polyesters and polyvinyl chloride) in the modern petrochemical industry (**Scheme 1.1**) [6,7].

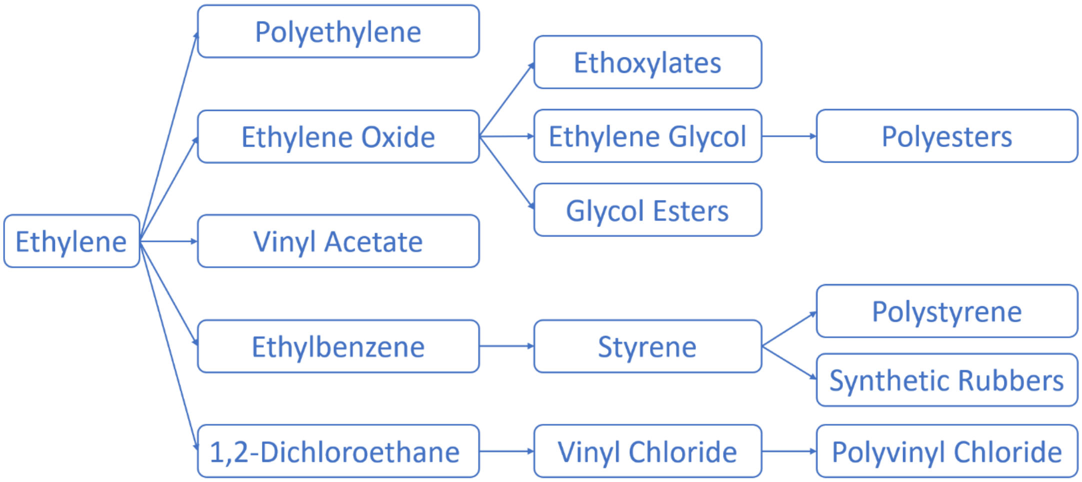

Scheme 1.1 Common routes for chemical production derived from ethylene. This scheme is adapted from ref. [7].

The United States (US) is both a major producer and consumer of ethylene in the world [8,9]. Production of ethylene in the US has steadily increased over the recent years and surpassed 30 million metric tons per year in 2018 (**Figure 1.1**), which makes ethylene one of the most produced industrial chemicals [10]. Ethylene production in the US is predominated by the steam cracking of heavier hydrocarbon feedstocks. Liquid feedstocks like naphtha are generally preferred globally because of their convenience in transportation [11]. However, as a result of the rapid shale gas developments, the feedstock for steam crackers in the US has gradually shifted from naphtha to ethane for a better economy [11,12]. Compared to naphtha, steam cracking of ethane is highly selective toward ethylene but produces less heavier byproducts including propylene, butadiene and aromatics [13].

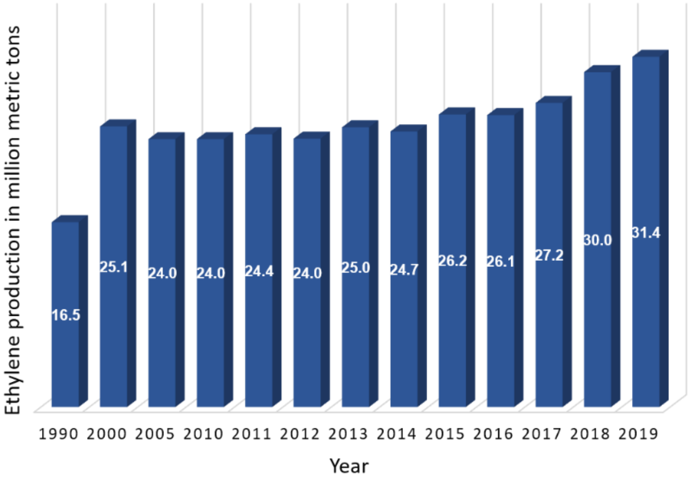

Figure 1.1 Ethylene production in the United States. Source: American Chemistry Council, 2020.

A simplified procedure of ethane steam cracking is shown in **Figure 1.2**. During ethane steam cracking, ethane is diluted with steam and co-fed into a tubular reactor maintained at elevated temperatures (1023-1273 K) to initiate the radical process [14,15]. The desired reaction during this step is dehydrogenation of ethane to ethylene:

$$C_2H_6 \rightarrow C_2H_4 + H_2 \quad \Delta H_r^o = 136.5\ kJ{\cdot}mol^{-1} \tag{1.1}$$

The cracking is then immediately quenched by cooling the effluent gas with water through a transfer line heat exchanger (TLE) to prevent further condensation of the olefins into undesired heavier side products [16,17]. Finally, the quenched effluent gas is directed sequentially through multiple separation columns to collect valuable cracking products and recover the unreacted ethane.

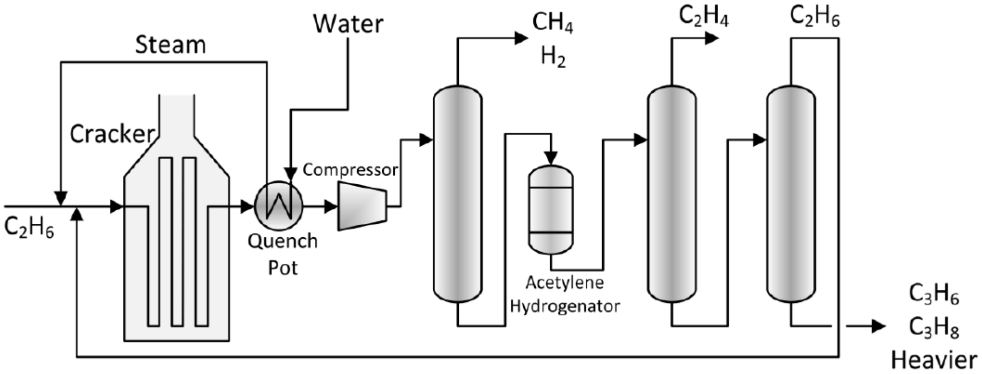

Figure 1.2 A simplified schematic for ethane steam cracking process. This schematic is adapted from ref. [7].

1.2 Coke deposition during steam cracking

One important side reaction during steam cracking is the formation of carbonaceous deposits, commonly known as coke, on the internal surfaces of the tubular cracking reactor (**Figure 1.3a**). Although dilution with steam has been shown to suppress coke deposition by reducing the gas phase partial pressure of the feedstock hydrocarbon [18,19], accumulation of coke is generally inevitable upon continuous operation under the extreme conditions for steam cracking. Coke deposition reduces the cross-sectional area (**Figure 1.3a**) and increases the pressure drop across the tubular reactor, shifting the product selectivity towards undesired heavier products [20,21]. The deposited carbon also carburizes the alloy surfaces, leading to degradation of the anti-coking protective oxide layers (**Figure 1.3b**) [22]. Moreover, extra heat input is required to compensate for the increase in heat transfer resistance from coke layers [20,21]. When metallurgic limits of the reactor alloy are reached, operation of the steam cracker has to be ceased for coke removal through combustion in an oxygen-containing gas flow (commonly air-steam mixtures) [23,24]. Such periodic shutdown can vary from 20 to 60 days depending on the cracking reaction conditions [24,25], which significantly impedes the profitability of the steam cracking process.

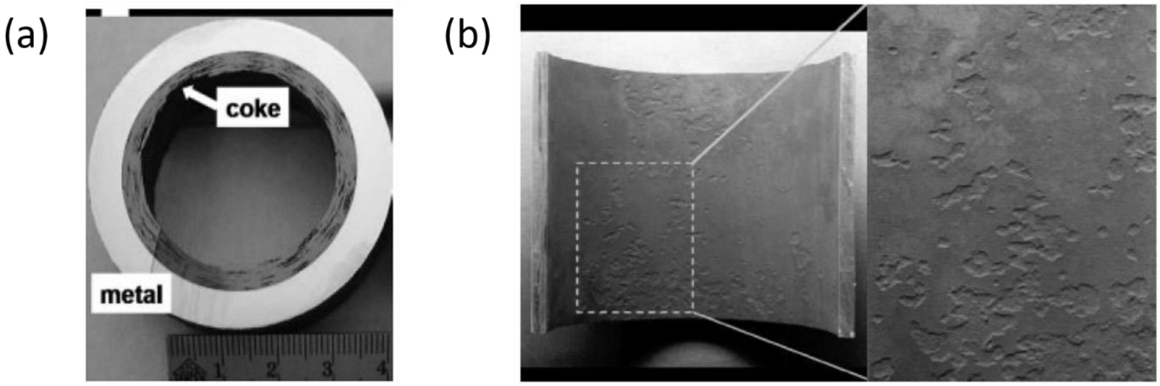

Figure 1.3 (a) Coke layers deposited on the internal surfaces of a tubular cracking reactor; (b) Failure of the protective oxide layers due to carburization. These figures are adapted from ref. [22].

Coke deposition during steam cracking can be classified into three types of mechanisms, namely catalytic coking, radical coking and droplet condensation coking [26]. Catalytic coking and radical coking contribute mainly to coke deposition in the cracking reactor, whereas droplet condensation coking mostly occurs downstream the cracking reactor in the TLE at lower temperatures [26,27].

Catalytic coking occurs over various types of metal particle sites present on the surfaces of the cracking reactor, which is commonly fabricated from superalloys of Fe, Ni and Cr [26,28]. These sites catalyze coke deposition at temperatures as low as 773 K, resulting in a much higher coking rate over these metallic surfaces compared to inert oxide materials [26,28]. As shown in **Figure 1.4**, hydrocarbon precursor is converted to coke upon chemisorption on the metal active sites [27]. The formed coke can diffuse through the metal particles [27]. Subsequent accumulation of carbon causes a pressure buildup and disrupts the grain boundary, eventually raising the metal particles from the surface by continuous growth of carbon filaments from gas phase precipitation [27]. Since catalytic coking is highly dependent on the reactive metal particle sites, this type of coking mechanism is particularly important upon decoking when the clean metallic surfaces are exposed [26,29].

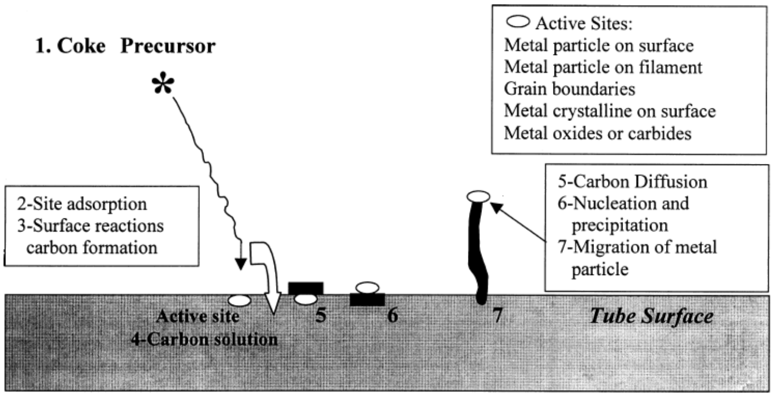

Figure 1.4 Schematic of catalytic coking mechanism over metallic surfaces. This figure is adapted from ref. [27].

Radical coking takes place through a series of reactions among gas phase radicals and is therefore almost independent on the nature of the reactor surface [29,30]. Since the initiation of gas phase free radicals is highly endothermic, radical coking only prevails at high temperatures [26]. The mechanism of radical coking is generally complicated. **Figure 1.5** shows a sequence of steps proposed for coke growth during ethane steam cracking. Reactive radicals are generated by hydrogen abstraction, allowing the insertion of gas phase olefins [31]. Subsequently, aromatic rings are formed through cyclization and dehydrogenation, which increase the molecular size of the coke [31]. Consistent with this mechanism, industrial pyrolytic coke formed through radical coking is highly graphitic with very low hydrogen content and requires higher temperature to oxidize [27,28]. The rate of radical coking correlates with the ability of the hydrocarbon precursor to produce active radicals, which generally follows the trend: acetylenes > olefins > aromatics > paraffins [26,27].

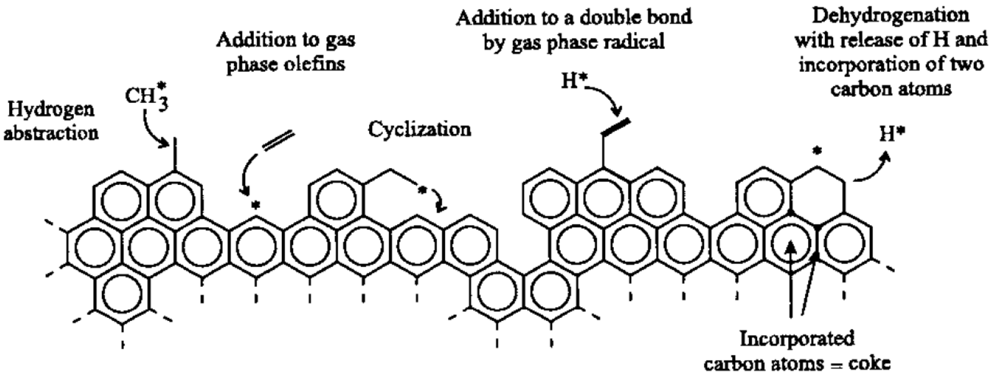

Figure 1.5 Schematic of radical coking mechanism. This figure is adapted from ref. [31].

Droplet condensation coking involves the formation of polyaromatics condensed from simple aromatic intermediates at lower temperatures commonly in the TLE [26,27]. When the condensed droplets and soot particles collide with the reactor surface, these condensates likely adhere to the surface and further incorporated into the existing coke layers through dehydrogenation [27,29]. Since this coking mechanism arises from condensation of aromatics from the gas phase, the coking rate is not affected by the chemical features of the reactor surface while being significantly higher for aromatics and acetylenes (likely due to trimerization into aromatics) [26,32].

1.3 Development of anti-coking barrier layers

Numerous research efforts have been dedicated to suppressing catalytic coke deposition during the steam cracking process. The major approach is to create a barrier layer on the internal surfaces of the tubular cracking reactor, known as the anti-coking barrier layer [26]. As shown in **Figure 1.6a**, catalytic coking (green, filamentous coke) and radical coking (black, granular coke) occur simultaneously during steam cracking when bare metallic surfaces of the reactor tube are exposed [33]. Upon pretreatment or coating, a barrier layer can form on top of the reactor tube surfaces, which separate the metallic sites (*i.e.*, Ni and Fe) from being in contact with the gas phase hydrocarbon precursors (**Figure 1.6b**) [28,33]. Barrier layer materials are commonly inert like Al_2O_3 [34,35], TiC and SiC [36]. While the presence of a barrier layer effectively inhibits catalytic coking, radical coking can still occur through gas phase radical reactions, which is independent of the active sites on the surface [26,33]. To further relieve the accumulation of radical coke, the concept of "catalytic coating" has been developed, which incorporates active components (*e.g.*, perovskites [37] and Ce-Zr mixed oxides [16]) into the barrier layer for catalyzing *in situ* steam gasification of radical coke into carbon oxides and dihydrogen (**Figure 1.6c**) [33,37] .

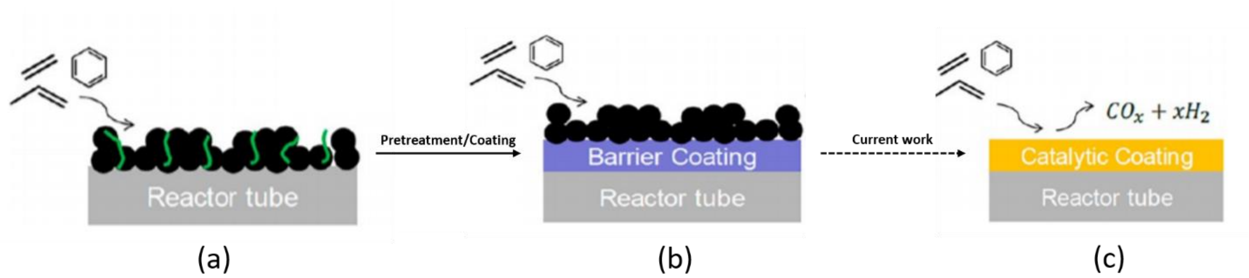

Figure 1.6 Schematic illustration of coking behavior over (a) bare tube, (b) barrier coating and (c) catalytic coating. These figures are adapted from ref. [33].

One of the state-of-the-art barrier layers for steam crackers is the $MnCr_2O_4$-Cr_2O_3 spinel oxide layer that forms upon oxidative pretreatment of the Mn-containing Fe-Ni-Cr alloy surfaces [38]. Since MnO and Cr_2O_3 exhibit a lower equilibrium partial pressure of oxygen than FeO and NiO, it is possible to form a spinel oxide layer of Mn and Cr (enriched with $MnCr_2O_4$) under controlled pretreatment conditions that separates the metallic Fe and Ni in the base alloy from the gas phase [39]. Indeed, such $MnCr_2O_4$ spinel barrier layers have been shown to significantly suppress coke deposition during steam cracking of light naphtha [40,41]. As shown in **Figure 1.7a**, the coking rate over the $MnCr_2O_4$-coated alloy decreased to less than a half compared to that over the uncoated alloy [41]. The filamentous coke deposited on the uncoated alloy (**Figure 1.7b**) as a result of catalytic coking over metal particle sites was not observed when coated with the $MnCr_2O_4$ spinel (**Figure 1.7c**) [41]. In addition, the stoichiometric $MnCr_2O_4$ spinel has been reported to be more resistant to carburization (to form metal carbides) than Cr_2O_3 especially in the presence of steam, suggesting good stability of the $MnCr_2O_4$ spinel barrier layer under steam cracking conditions [42,43]. Non-stoichiometric Mn-Cr-O spinel oxides with excess Mn (*i.e.*, $Mn^{2+}(Mn_xCr_{1-x})_2{}^{3+}O_4$ [44]) have also been identified on the Fe-Ni-Cr alloy surfaces after the exposure to carburizing environments (2 % CH_4 in H_2) at high temperatures [45]. It was found that the stability of these Mn-Cr-O spinel oxides against carburization varied with both stoichiometry between Mn and Cr and oxygen partial pressure [46].

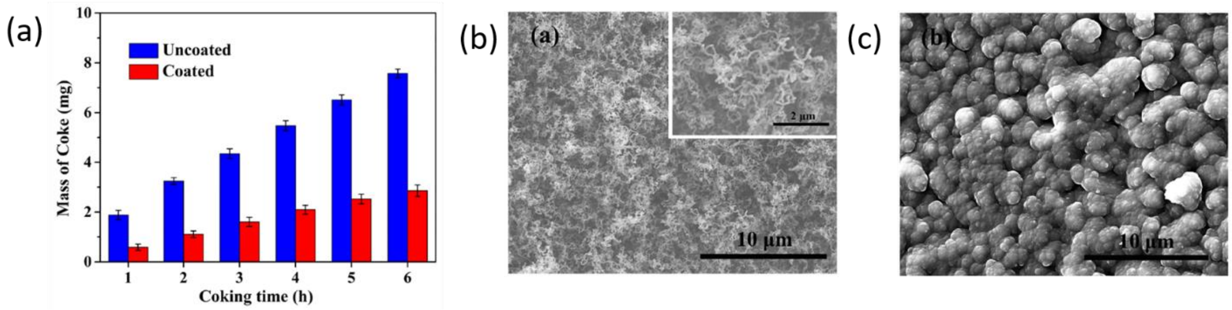

Figure 1.7 (a) Cumulative amount of coke deposited on uncoated and coated alloy sample and morphology of coke deposited on (b) uncoated and (c) coated alloy sample during steam cracking of light naphtha at 1123 K. These figures are adapted from ref. [41].

The innovative Al-containing Fe-Ni-Cr alloy has gained more attention recently due to their enhanced anti-coking performance and resistance to carburization during steam cracking [34,35]. These improvements are associated with the Al_2O_3 protective barrier layer formed upon oxidative pretreatment of the Al-containing alloy surfaces [24], which surpasses the stability of Cr_2O_3 under carburizing environments above 1200 K [47]. Compared to the aforementioned $MnCr_2O_4$-Cr_2O_3 barrier layer, the alloy surfaces protected by the Al_2O_3 barrier exhibited a lower coking rate and deteriorated less over time during ethane steam cracking [38]. While Al_2O_3 (mostly α phase in this case) is inert, the $NiAl_2O_4$ spinel can form on the alloy surfaces after oxidative pretreatment due to its high thermodynamic stability, which was both suggested by thermodynamic calculations [20,38] (See **Table 1.1** for instance) and observed experimentally [48]. Formation of other Ni-based spinel oxides including $NiCr_2O_4$ and $NiFe_2O_4$ was predicted as well [20,38]. Although the Ni-based spinel oxides ($NiAl_2O_4$ in particular) might possibly be active for steam gasification of coke since they have been reported to catalyze steam reforming of various hydrocarbons even without reductive pretreatment [49–51], these spinels are unlikely to be effective components for catalytic coatings due to potential catalytic coking facilitated by Ni metal particles formed via *in situ* reduction of Ni^{2+} under steam cracking conditions.

Table 1.1 Mole fraction of different components under preoxidation and cracking atmospheres calculated for an Al-enhanced alloy from thermodynamics

Phase	Al_2SiO_5	Cr_2O_3	Fe	$MnCr_2O_4$	Ni	$NiAl_2O_4$	$NiCr_2O_4$	$NiFe_2O_4$	SiO_2
Preoxidation	-	0.483	-	-	-	0.257	0.145	0.108	0.008
Cracking	0.008	0.351	0.136	0.393	0.092	-	-	-	0.020

These data are adapted from ref [38].

1.4 Objective of the present dissertation

Herein, in an effort to mitigate radical coke accumulation, we have systematically investigated the activity and stability of representative spinel oxides in the barrier oxide layers to provide insights for improving the design of catalytic coatings. These spinel oxides were synthesized in powder form and evaluated in steam reforming of a series of unsaturated hydrocarbons, including olefins and aromatics, which are important side reactions during steam cracking and simplified model reactions for steam gasification of coke. Steam reforming converts a hydrocarbon into carbon oxides and dihydrogen when co-fed with steam at elevated temperatures.

Particularly in the present thesis, we have studied steam reforming of ethylene, propylene, benzene and toluene:

Ethylene Steam Reforming:

$$C_2H_4 + 2H_2O \rightarrow 2CO + 4H_2 \qquad \Delta H_r^o = 210.1\ kJ \cdot mol^{-1} \tag{1.2}$$

Propylene Steam Reforming:

$$C_3H_6 + 3H_2O \rightarrow 3CO + 6H_2 \qquad \Delta H_r^o = 373.9\ kJ \cdot mol^{-1} \tag{1.3}$$

Benzene Steam Reforming:

$$C_6H_6 + 6H_2O \rightarrow 6CO + 9H_2 \qquad \Delta H_r^o = 705.2\ kJ \cdot mol^{-1} \tag{1.4}$$

Toluene Steam Reforming:

$$C_7H_8 + 7H_2O \rightarrow 7CO + 11H_2 \qquad \Delta H_r^o = 868.7\ kJ \cdot mol^{-1} \tag{1.5}$$

Other side reactions concurrent with steam reforming include:

Water-gas Shift:

$$CO + H_2O \rightarrow CO_2 + H_2 \quad \Delta H_r^o = -41.2\ kJ \cdot mol^{-1} \tag{1.6}$$

Methanation:

$$CO + 3H_2 \rightarrow CH_4 + H_2O \quad \Delta H_r^o = -205.9\ kJ \cdot mol^{-1} \tag{1.7}$$

Steam reforming of hydrocarbons has been widely studied over metal particle catalysts (*e.g.*, Ni [52–54], Pd [55,56] and Rh [56,57]) while less explored over metal oxide catalysts. It is worth emphasizing that the current dissertation does not aim to develop steam reforming catalysts with higher efficiency for H_2 production. Instead, the rate and kinetics of olefins and aromatics steam reforming over the spinel oxides were examined as surrogate reactions that might be correlated with their performance in steam gasification of coke [19,58,59], as well as limiting the degradation of olefin products from steam reforming when a catalytic coating is applied.

In Chapter 2, Mn-Cr-O spinel oxides with different stoichiometry were thoroughly characterized using diffraction and spectroscopy to understand the structure and speciation of excess Mn and Cr. The spinel catalysts were evaluated in ethylene steam reforming and compared to single oxides of Mn and Cr. Subsequently, reforming kinetics of propylene, benzene and toluene over the same group of Mn-Cr-O spinel oxides were investigated and compared to those of ethylene reforming in Chapter 3. The strong inhibition of H_2 observed for toluene steam reforming was further probed using infrared spectroscopy on aromatic adsorption over the spinel surface. The stability of Ni-based spinel oxides was compared in temperature-programmed reduction and ethylene steam reforming in Chapter 4. The rate and amount of coke deposited during ethylene steam reforming after catalyst re-oxidation were studied to address potential reduction of Ni spinel oxides into small Ni metal particles under steam reforming conditions. Finally, the speciation of excess Co and its influence on ethylene reforming rate were explored over two Co-Cr-O spinel oxides in Chapter 5. The ethylene reforming rate over the MCr_2O_4 spinel catalysts with respect to different tetrahedral M^{2+} cations was also compared.

1.5 References for Chapter 1

[1] T.F. Degnan, C.M. Smith, C.R. Venkat, Alkylation of aromatics with ethylene and propylene: Recent developments in commercial processes, Appl. Catal. A Gen. 221 (2001) 283-294.

[2] I. Kainthla, J.T. Bhanushali, R.S. Keri, B.M. Nagaraja, Activity studies of vanadium, iron, carbon and mixed oxides based catalysts for the oxidative dehydrogenation of ethylbenzene to styrene: A review, Catal. Sci. Technol. 5 (2015) 5062-5076.

[3] J.P. Hogan, R.L. Banks, Polymers and production thereof, US Patent 2 825 721 (1958), to

Philips Petroleum Company.

[4] L. Cerruti, Historical and philosophical remarks on Ziegler-Natta catalysts a discourse on industrial catalysis, Hyle. 5 (1999) 3-41.

[5] C. Boswell, 1950s: The petrochemical boom, 2014. https://chemweek.com/CW/Document/63790/1950s-The-petrochemical-boom

[6] Siemens Industry, Petrochemical Industry - Ethylene Plant Application Note, 2018. https://cache.industry.siemens.com/dl/files/563/109770563/att_995347/v1/PIAAP-00002-0118-Ethylene.pdf

[7] A. Muñoz Gandarillas, Influence of the Reactor Coil Material on Coke Formation during Steam Cracking of Hydrocarbons (Doctoral dissertation), 2014.

[8] IHS Markit, Ethylene - Chemical Economics Handbook, 2020. https://ihsmarkit.com/products/ethylene-chemical-economics-handbook.html

[9] Statista, Largest global producers of ethylene based on production capacity in 2013, 2019. https://www.statista.com/statistics/267498/largest-producers-of-ethylene-worldwide/

[10] J.T. Moore, C. Hren, P.J. Mikulecky, The Top 10 Industrial Chemicals. https://www.dummies.com/education/science/chemistry/the-top-10-industrial-chemicals/

[11] I. Amghizar, L.A. Vandewalle, K.M. Van Geem, G.B. Marin, New Trends in Olefin Production, Engineering. 3 (2017) 171-178.

[12] Q. Wang, X. Chen, A.N. Jha, H. Rogers, Natural gas from shale formation - The evolution , evidences and challenges of shale gas revolution in United States, Renew. Sustain. Energy Rev. 30 (2014) 1-28.

[13] P.C.A. Bruijnincx, B.M. Weckhuysen, Shale Gas Revolution: An Opportunity for the Production of Biobased Chemicals?, Angew. Chem. Int. Ed. 52 (2013) 11980-11987.

[14] L. Yang, M.P. Bukhovko, G. Brezicki, A. Malek, L. Li, C.W. Jones, P.K. Agrawal, R.J. Davis, Steam reforming of ethylene over manganese-chromium spinel oxides, J. Catal. 380 (2019) 224-235.

[15] S.M. Sadrameli, Thermal/catalytic cracking of hydrocarbons for the production of olefins: A state-of-the-art review I: Thermal cracking review, Fuel. 140 (2015) 102-115.

[16] K. Yin, S. Mahamulkar, J. Xie, H. Shibata, A. Malek, L. Li, C.W. Jones, P. Agrawal, R.J. Davis, Catalytic reactions of coke with dioxygen and steam over alkaline-earth-metal-doped cerium-zirconium mixed oxides, Appl. Catal. A Gen. 535 (2017) 17-23.

[17] K.M. Van Geem, I. Dhuyvetter, S. Prokopiev, M.F. Reyniers, D. Viennet, G.B. Marin, Coke formation in the transfer line exchanger during steam cracking of hydrocarbons, Ind. Eng. Chem. Res. 48 (2009) 10343-10358.

[18] K.G. Mittal, Cracking paraffinic hydrocarbons to make alpha olefins-a review, J. Chem. Technol. Biotechnol. 36 (1986) 291-299.

[19] M.P. Bukhovko, L. Yang, L. Li, A. Malek, R.J. Davis, P.K. Agrawal, C.W. Jones, Gasification of Radical Coke with Steam and Steam-Hydrogen Mixtures over Manganese-Chromium Oxides, Ind. Eng. Chem. Res. 59 (2020) 10813-10822.

[20] S.A. Sarris, N. Olahova, K. Verbeken, M.F. Reyniers, G.B. Marin, K.M. Van Geem, Optimization of the in Situ Pretreatment of High Temperature Ni-Cr Alloys for Ethane Steam Cracking, Ind. Eng. Chem. Res. 56 (2017) 1424-1438.

[21] A.E. Muñoz Gandarillas, K.M. Van Geem, M.F. Reyniers, G.B. Marin, Coking resistance of specialized coil materials during steam cracking of sulfur-free naphtha, Ind. Eng. Chem. Res. 53 (2014) 13644-13655.

[22] D. Jakobi, R. Gommans, Typical failures in pyrolysis coils for ethylene cracking, Mater. Corros. 54 (2003) 881-886.

[23] S. Mahamulkar, K. Yin, T. Sulmonetti, H.T. Kwon, R.J. Davis, L. Li, H. Shibata, A. Malek, C.W. Jones, P.K. Agrawal, α-Alumina supported doped ceria catalysts for steam gasification and oxidation of radical coke, Chem. Eng. Res. Des. 151 (2019) 1-9.

[24] S. Mahamulkar, K. Yin, M.T. Claure, R.J. Davis, L. Li, H. Shibata, A. Malek, C.W. Jones, P.K. Agrawal, Thermally stable α-alumina supported ceria for coking resistance and oxidation of radical coke generated in-situ, Fuel. 218 (2018) 357-365.

[25] K.M. Sundaram, P.S. Van Damme, G.F. Froment, Coke Deposition in the Thermal Cracking of Ethane, AlChE J. 27 (1981) 946-951.

[26] S. Mahamulkar, K. Yin, P.K. Agrawal, R.J. Davis, C.W. Jones, A. Malek, H. Shibata, Formation and Oxidation/Gasification of Carbonaceous Deposits: A Review, Ind. Eng. Chem. Res. 55 (2016) 9760-9818.

[27] J. Towfighi, M. Sadrameli, A. Niaei, Coke formation mechanisms and coke inhibiting methods in pyrolysis furnaces, J. Chem. Eng. Japan. 35 (2002) 923-937.

[28] S. Mahamulkar, K. Yin, R.J. Davis, H. Shibata, A. Malek, C.W. Jones, P.K. Agrawal, In Situ Generation of Radical Coke and the Role of Coke-Catalyst Contact on Coke Oxidation, Ind. Eng. Chem. Res. 55 (2016) 5271-5278.

[29] L.F. Albright, J.C. Marek, Mechanistic model for formation of coke in pyrolysis units producing ethylene, Ind. Eng. Chem. Res. 27 (1988) 755-759.

[30] H. Cai, A. Krzywicki, M.C. Oballa, Coke formation in steam crackers for ethylene production, Chem. Eng. Process. 41 (2002) 199-214.

[31] V. Van Speybroeck, D. Van Neck, M. Waroquier, S. Wauters, M. Saeys, G.B. Marin, Ab initio study on elementary radical reactions in coke formation, Int. J. Quantum Chem. 91 (2003) 384-388.

[32] F.D. Kopinke, G. Zimmermann, S. Nowak, On the mechanism of coke formation in steam cracking-conclusions from results obtained by tracer experiments, Carbon. 26 (1988) 117-124.

[33] S.H. Symoens, N. Olahova, A.E. Muñoz Gandarillas, H. Karimi, M.R. Djokic, M.F. Reyniers, G.B. Marin, K.M. Van Geem, State-of-the-art of Coke Formation during Steam Cracking: Anti-Coking Surface Technologies, Ind. Eng. Chem. Res. 57 (2018) 16117-16136.

[34] A. Niaei, D. Salari, N. Daneshvar, A. Chamandeh, R. Nabavi, Effect of Tube Materials and Special Coating on Coke Deposition in the Steam Cracking of Hydrocarbons, World Acad. Sci. Eng. Technol. 1 (2007) 41-43.

[35] A. Niaei, D. Salari, J. Towfighi, A. Chamandeh, R. NabaviI, Aluminized Steel and Zinc Coating for Reduction of Coke Formation in Thermal Cracking of Naphtha, Int. J. Chem. React. Eng. 6 (2008) Note S3.

[36] P. Broutin, F. Ropital, M.F. Reyniers, G.F. Froment, Anticoking coatings for high temperature petrochemical reactors, Oil Gas Sci. Technol. 54 (1999) 375-385.

[37] C.M. Schietekat, S.A. Sarris, P.A. Reyniers, L.B. Kool, W. Peng, P. Lucas, K.M. Van

Geem, G.B. Marin, Catalytic Coating for Reduced Coke Formation in Steam Cracking Reactors, Ind. Eng. Chem. Res. 54 (2015) 9525-9535.

[38] A.E. Muñoz Gandarillas, K.M. Van Geem, M.F. Reyniers, G.B. Marin, Influence of the reactor material composition on coke formation during ethane steam cracking, Ind. Eng. Chem. Res. 53 (2014) 6358-6371.

[39] B. Bao, Z. Wang, H. Xu, J. Liu, Anti-coking Effect of $MnCr_2O_4$ Spinel Coating during Light Naphtha Thermal Cracking, Energy Procedia. 105 (2017) 4808-4813.

[40] B. Bao, J. Liu, H. Xu, B. Liu, W. Zhang, Inhibitory effect of $MnCr_2O_4$ spinel coating on coke formation during light naphtha thermal cracking, RSC Adv. 6 (2016) 68934-68941.

[41] B. Bao, J. Liu, H. Xu, Z. Wang, K. Zhang, Fabrication of spinel coating on HP40 alloy and its inhibition effect on catalytic coking during thermal cracking of light naphtha, Brazilian J. Chem. Eng. 35 (2018) 721-730.

[42] H. Li, Y. Zheng, L.W. Benum, M. Oballa, W. Chen, Carburization behaviour of Mn-Cr-O spinel in high temperature hydrocarbon cracking environment, Corros. Sci. 51 (2009) 2336-2341.

[43] H. Li, W. Chen, Stability of $MnCr_2O_4$ spinel and Cr_2O_3 in high temperature carbonaceous environments with varied oxygen partial pressures, Corros. Sci. 52 (2010) 2481-2488.

[44] A. Naoumidis, H.A. Schulze, W. Jungen, P. Lersch, Phase studies in the chromium-manganese-titanium oxide system at different oxygen partial pressures, J. Eur. Ceram. Soc. 7 (1991) 55-63.

[45] R. Yin, Carburization of 310 stainless steel exposed at 800-1100 °C in 2%CH_4/H_2 gas mixture, Corros. Sci. 47 (2005) 1896-1910.

[46] H. Li, W. Chen, High temperature carburization behaviour of Mn-Cr-O spinel oxides with varied concentrations of manganese, Corros. Sci. 53 (2011) 2097-2105.

[47] J. Yan, Y. Gao, F. Yang, Y. Bai, Y. Liu, C. Yao, S. Hou, G. Liu, Cyclic carburizing behaviour of Al modified high Si-containing HP40 alloy, Corros. Sci. 67 (2013) 161-168.

[48] A. Shaaban, Influence of $NiAl_2O_4$ spinel formation on the oxidation behavior of the Ni50Al alloy at 1273 K in air, Surf. Coat. Technol. 379 (2019) 125023.

[49] C. Fauteux-Lefebvre, N. Abatzoglou, N. Braidy, I.E. Achouri, Diesel steam reforming with a nickel-alumina spinel catalyst for solid oxide fuel cell application, J. Power Sources. 196 (2011) 7673-7680.

[50] I.E. Achouri, N. Abatzoglou, N. Braidy, S. Bastien, New insights on the role of YSZ in a $NiAl_2O_4/Al_2O_3$-YSZ catalyst, Appl. Catal. A Gen. 497 (2015) 42-50.

[51] C. Fauteux-Lefebvre, N. Abatzoglou, J. Blanchard, F. Gitzhofer, Steam reforming of liquid hydrocarbons over a nickel-alumina spinel catalyst, J. Power Sources. 195 (2010) 3275-3283.

[52] R. Coll, J. Salvadó, X. Farriol, D. Montané, Steam reforming model compounds of biomass gasification tars: conversion at different operating conditions and tendency towards coke formation, Fuel Process. Technol. 74 (2001) 19-31.

[53] J. Pu, T. Toyoda, E.W. Qian, Evaluation of Reactivities of Various Compounds in Steam Reforming over $RuNi/BaOAl_2O_3$ Catalyst, Energy Fuels 32 (2018) 1804-1811.

[54] F.M. Josuinkas, C.P.B. Quitete, N.F.P. Ribeiro, M.M.V.M. Souza, Steam reforming of model gasification tar compounds over nickel catalysts prepared from hydrotalcite precursors, Fuel Process. Technol. 121 (2014) 76-82.

[55] X. Wang, R.J. Gorte, A study of steam reforming of hydrocarbon fuels on Pd/ceria, Appl. Catal. A Gen. 224 (2002) 209-218.

[56] P.O. Graf, B.L. Mojet, J.G. van Ommen, L. Lefferts, Comparative study of steam reforming of methane, ethane and ethylene on Pt, Rh and Pd supported on yttrium-stabilized zirconia, Appl. Catal. A Gen. 332 (2007) 310-317.

[57] J.S. Lopez, V.L. Dagle, C.A. Deshmane, L. Kovarik, R.S. Wegeng, R.A. Dagle, Methane and ethane steam reforming over $MgAl_2O_4$-supported Rh and Ir catalysts: Catalytic implications for natural gas reforming application, Catalysts. 9 (2019) 801.

[58] M.P. Bukhovko, L. Yang, I. Nezam, L. Li, A. Malek, R.J. Davis, P.K. Agrawal, C.W. Jones, Enhanced Coke Gasification Activity of $Mn_{1.5}Cr_{1.5}O_4$ Spinel Catalyst during Coking in Ethylene-Steam Mixture, submitted.

[59] K. Yin, R.J. Davis, S. Mahamulkar, C.W. Jones, P. Agrawal, H. Shibata, A. Malek, Catalytic Oxidation of Solid Carbon and Carbon Monoxide over Cerium-Zirconium Mixed Oxides, AIChE J. 63 (2017) 725-738.

Chapter 2 Steam reforming of ethylene over manganese-chromium spinel oxides

Work presented in this chapter was published as:

L. Yang, M.P. Bukhovko, G. Brezicki, A. Malek, L. Li, C.W. Jones, P.K. Agrawal, R.J. Davis, Steam reforming of ethylene over manganese-chromium spinel oxides, J. Catal. 380 (2019) 224-235.

Abstract

A series of Mn-Cr-O spinel catalysts of different stoichiometry was synthesized using a sol-gel method and characterized using X-ray diffraction, X-ray photoelectron spectroscopy, X-ray absorption spectroscopy, N_2 and H_2O adsorption, and H_2-temperature programed reduction. The introduction of extra Mn to stoichiometric $MnCr_2O_4$ led to Mn^{3+} substitution in the spinel lattice of $Mn_{1.5}Cr_{1.5}O_4$ whereas excess Cr in $Mn_{0.5}Cr_{2.5}O_4$ formed Cr_2O_3. Ethylene steam reforming at atmospheric total pressure and 873 K over the Mn-Cr-O spinel catalysts was nearly first order in ethylene, negative order in water and zero order in excess dihydrogen. The reaction kinetics were consistent with a Mars-van Krevelen type mechanism. While being initially more active than the spinel catalysts, Cr_2O_3 and Mn_3O_4 (which reduced to MnO) both deactivated during ethylene steam reforming. The spinel catalysts were therefore more active and structurally stable for ethylene steam reforming than either of the pure metal oxides.

2.1 Introduction

Ethylene is one of the most essential building blocks for the chemical and polymer industries. The dominant method for the industrial scale production of ethylene and other light olefins is the steam cracking process, in which feedstock hydrocarbons are diluted in steam and heated to extremely high temperatures (1023-1273 K) to initiate the free radical process [1,2]. The desired reaction in the steam cracking of ethane is dehydrogenation to produce ethylene as shown below:

$$C_2H_6 \rightarrow C_2H_4 + H_2 \quad \Delta H_r^o = 136.5\ \text{kJ}\cdot\text{mol}^{-1} \tag{2.1}$$

To minimize the production of undesired side products like heavier aromatics, the downstream gas from the cracker is rapidly cooled in a transfer line heat exchanger. Valuable products including olefins are then separated and recovered through distillation and adsorption processes [2]. One major side reaction that limits the economy and energy efficiency of the steam cracking process is the formation of carbonaceous deposits known as coke on the inner wall of the tubular reactors [3]. The accumulation of carbon results in a higher pressure drop through the reactor, carburization of the steel surface and higher input from the furnace to compensate for the extra heat resistance [4], which consequently require the process to be halted periodically for coke removal [3,5]. The coke deposited on the reactor surface is removed by combustion and reforming in an air and steam flow at high temperatures over about 48 h, which considerably impacts process economics [1,3,5,6].

There are three well-known mechanisms for coke formation during steam cracking: catalytic coking, radical coking and droplet condensation [2]. Since catalytic coking can occur at low temperatures (773 K) [7] and depends on the chemical composition of the reactor surface, researchers have investigated various routes to suppress catalytic coking [2]. The main approach is to add barrier materials, or anti-coking layers, between the metallic sites on the steel alloy reactor surface and the hydrocarbons in the gas. One such barrier is a $MnCr_2O_4$-Cr_2O_3 protective oxide layer, which can be formed during the oxidative pretreatment of conventional Fe-Ni-Cr alloy surfaces at high temperatures [8,9]. The protective oxide layer typically contains both $MnCr_2O_4$ spinel and Cr_2O_3, separated from the underlying alloy by a SiO_2 transition layer [3,9]. This type of coated alloy surface significantly suppressed catalytic coking compared to an uncoated alloy surface in a hydrocarbon cracking environment [8,9]. Previous studies found $MnCr_2O_4$ to be more resistant to carburization compared to Cr_2O_3 [10] and the carburization resistance of $MnCr_2O_4$ increased with higher steam partial pressure [11]. Non-stoichiometric Mn-Cr-O spinel oxides (*i.e.*, $Mn_{1.5}Cr_{1.5}O_4$) have also been discovered on the alloy surface after pretreatment in a CH_4/H_2 carburizing gas mixture [12]. The carburization behavior of the Mn-Cr-O spinel oxides was reported to be affected by both the metal oxide stoichiometry and the steam partial pressure [13].

Although the catalytic coking resistance of Mn-Cr-O spinel protective layers has been reported, the catalytic performance of the Mn-Cr-O spinel oxides for important side reactions is relatively unexplored. When hydrocarbons are co-fed with steam at high temperatures, a potential side reaction is steam reforming, which generates dihydrogen and carbon oxides. In the steam reforming of ethylene, several reactions occur simultaneously:

Steam Reforming:

$$C_2H_4 + 2H_2O \rightarrow 2CO + 4H_2 \quad \Delta H_r^o = 210.1\ kJ\cdot mol^{-1} \tag{2.2}$$

Water Gas Shift:

$$CO + H_2O \rightarrow CO_2 + H_2 \quad \Delta H_r^o = -41.2\ kJ\cdot mol^{-1} \tag{2.3}$$

Methanation:

$$CO + 3H_2 \rightarrow CH_4 + H_2O \quad \Delta H_r^o = -205.9\ kJ\cdot mol^{-1} \tag{2.4}$$

Herein, we have synthesized powder catalysts of the Mn-Cr-O spinel oxides with various compositions to compare with single oxides of Mn and Cr. The catalysts were evaluated in the steam reforming of ethylene and thoroughly characterized. In particular, the influences of temperature and H_2, C_2H_4, H_2O partial pressure on the steam reforming activity were assessed over the series of spinel materials. In addition, the stability of the catalysts in the steam reforming was examined.

2.2 Experimental methods

2.2.1 Catalyst preparation

The Mn-Cr-O spinel oxides were prepared using a sol-gel method. Typically, $Mn(NO_3)_2{\cdot}4H_2O$ (97.0%, Sigma-Aldrich) and $Cr(NO_3)_3{\cdot}9H_2O$ (99.0%, Sigma-Aldrich) of the desired molar ratio were dissolved in 100 cm^3 distilled deionized water with a total metal cation concentration of 0.4 M. The metal solution was then mixed with 50 cm^3 of 1.6 M citric acid solution. The mixed solution was kept stirring at 368 K until a viscous gel formed. The gel precursor was dried in air at 393 K overnight and thermally treated at 1273 K in air for 4 h. The resulting powder was denoted as $Mn_xCr_{3-x}O_4$ ($x = 0.5, 1.0, 1.5$) depending on the starting Cr/Mn ratio in the synthesis gel. The Mn oxide (Mn_3O_4) and Cr oxide (Cr_2O_3) samples were also prepared for comparison using the same method.

2.2.2 Catalyst characterization

Powder X-ray diffraction (XRD) patterns of the catalysts were collected on a PANalytical Empyrean X-ray Diffractometer using Cu Kα radiation. Each sample was scanned at a rate of $5°{\cdot}min^{-1}$ within a range of 2θ from 15° to 80°. Rietveld Refinement of the diffraction patterns was performed using the Material Analysis Using Diffraction (MAUD) software package [14]. The reference phases include $MnCr_2O_4$ (PDF 00-054-0876), Cr_2O_3 (PDF 00-006-0504) and $Mn_{1.5}Cr_{1.5}O_4$ (PDF 00-054-0876).

Specific surface areas of the catalysts were evaluated from N_2 physisorption at 77 K on a Micromeritics ASAP 2020 analyzer using the Brunauer-Emmett-Teller (BET) method of analysis. Typically, a sample of 2 g catalyst was used for the experiment. The sample was outgassed at 473 K for 4 h before N_2 physisorption.

Scanning Electron Microscopy (SEM) images were acquired on a FEI Quanta 650 FEG-SEM with a working distance of 10 mm under the secondary electron imaging mode. Elemental analysis was further conducted using an Oxford X-Max^N Energy Dispersive X-ray Spectroscopy (EDS) detector installed on the microscope. The sample was prepared by adhering the catalyst powders to a conductive carbon tape on the sample stage. The Cr and Mn contents were analyzed based on their Kα radiation using EDS.

The elemental compositions of the catalysts were analyzed by Galbraith Laboratories (Knoxville, TN) using inductively coupled plasma optical emission spectroscopy (ICP-OES) for the Cr and Mn content.

The measurements of H_2-temperature programmed reduction (H_2-TPR) and oxygen storage capacity (OSC) were performed on a Micromeritics AutoChem II 2920 Analyzer equipped with a thermal conductivity detector (TCD) using a sample of 200 mg catalyst. For the H_2-TPR, the sample was heated to 1273 K in 5 vol % H_2 in flowing Ar at a ramp rate of 10 $K\cdot min^{-1}$. For the OSC measurement, the sample was first heated to 873 K in 10 vol % O_2 in flowing He at a ramp rate of 10 $K\cdot min^{-1}$ and held at 873 K for 30 min, followed by a He purge at 873 K for 10 min. The gas was then switched to 5 vol % H_2 in flowing Ar and the sample was reduced at 873 K for 30 min, followed by a He purge at 873 K for 30 min. The sample was then pulsed with 10 vol % O_2 in He at 873 K until saturation.

X-ray photoelectron spectroscopy (XPS) was performed using a Phi VersaProbe III spectrometer equipped with a monochromatic Al Kα radiation source (1486.7 eV) and a hemispherical analyzer. The sample was scanned using an X-ray beam size of 100 μm and the energy analyzer was operated with a passing energy of 26 eV and 50 ms dwell per step for high resolution. A dual charge compensation was utilized with a low-energy electron flood gun and a low-energy Ar ion beam during each scan. During the depth profiling scan, the sample was sputtered using a high-energy Ar ion beam with a bias of 3-5 kV in between the collection of the spectra.

X-ray absorption spectroscopy (XAS) at the Cr K edge and the Mn K edge was conducted on beamline 7-BM through the Mail-in QAS Program managed by the Synchrotron Catalysis Consortium (SCC) at the National Synchrotron Light Source II at Brookhaven National Laboratory. Spectra were processed and analyzed using the Demeter software package [15].

The amount of coke deposited on the samples was determined by thermogravimetric analysis of 30 mg sample in synthetic air at a constant ramp rate of 10 $K \cdot min^{-1}$ using a TA Instruments SDTQ600 thermogravimetric analyzer.

The H_2O adsorption isotherms of the catalysts were measured using a volumetric adsorption system described previously [16]. The sample was thermally treated at 773 K for 16 h under vacuum and cooled to 383 K for 1 h. The sample was exposed to 40 doses of H_2O through a volumetric dosing system, each of which was allowed to equilibrate with the sample over 15 min. Prior to these adsorption experiments, dissolved gas in the H_2O (HPLC Grade, Fischer Scientific) was removed by three freeze-pump-thaw cycles.

2.2.3 Steam reforming of ethylene

Catalytic steam reforming of ethylene was carried out in a fixed-bed quartz reactor (10.5 mm I.D.×12.75 mm O.D.) in a temperature range from 853 K to 893 K at atmospheric pressure over 1 g catalyst (sieved to 250~425 μm). A typical feed condition was a total flow of 100 $cm^3 \cdot min^{-1}$ (corresponding to a residence time of approximately 0.052 s at 873 K) consisting of 25 vol % C_2H_4, 50 vol % H_2O, 5 vol % N_2 and 20 vol % Ar. Using a syringe pump, H_2O was introduced into a stainless steel evaporator maintained at 413 K to ensure vaporization and uniform mixing with other gases. The reactor effluent gas was first passed through a condenser to remove unreacted H_2O, then introduced to an infrared gas analyzer (Fuji Electric ZPA) for the analysis of CO_2 and finally to an online gas chromatograph (Agilent 7890A) equipped with a CarboPlot P7 column and a TCD detector for the analysis of C_2H_4, CO, CH_4 and H_2. The production rates over the catalysts were all evaluated at an ethylene conversion below 10 %. Characteristic steam reforming activity is reported on carbon basis (production rate of C_1), defined as the sum of the production rates of CO, CO_2 and CH_4 normalized by the dinitrogen BET surface area of the catalyst:

$$r_{C_1} = \frac{F(CO)+F(CO_2)+F(CH_4)}{S_{BET}} \tag{2.5}$$

The ethylene conversion is evaluated based on the produced CO, CO_2 and CH_4:

$$C_2H_4 \text{ conversion } (\%) = \frac{F(CO)+F(CO_2)+F(CH_4)}{2F_0(C_2H_4)} \times 100\ \% \tag{2.6}$$

The selectivity was defined as the mole fraction of a certain product (H_2, CO, CO_2 and CH_4) relative to all the products:

$$\text{Selectivity of X } (\%) = \frac{F(X)}{F(H_2)+F(CO)+F(CO_2)+F(CH_4)} \times 100\ \% \tag{2.7}$$

where F(X) denotes the molar flowrate of component X measured downstream of the reactor, $F_0(C_2H_4)$ denotes the molar flowrate of C_2H_4 fed to the reactor, S_{BET} denotes the dinitrogen BET surface area of the catalyst. The material balance is discussed in Appendix A1.

2.3 Results and discussion

2.3.1 Characterizations of Mn oxide, Cr oxide and Mn-Cr-O spinel catalysts

The physical properties of the catalysts assessed using N_2 physisorption are summarized in **Table 2.1**. The cumulative pore volume of each catalyst calculated using the Barrett-Joyner-Halenda (BJH) adsorption method was very low (< 0.05 $cm^3 \cdot g^{-1}$), indicating all the catalysts are essentially non-porous. The average particle diameter estimated for $MnCr_2O_4$ from the BET surface area assuming spherical morphology is 230 nm, which is in good agreement with the surface-weighted average diameter of 240 nm measured from the SEM image (**Figure 2.1a**). This comparison suggests the average pore diameter measured from N_2 physisorption is likely due to the voids between the particle aggregates instead of intracrystalline pores [1,17]. As the catalysts are essentially non-porous, the BET surface area is attributed exclusively to external surface area.

Table 2.1 Physical properties of the fresh Mn oxide, Cr oxide and Mn-Cr-O spinel catalysts

Catalyst	BET surface area ($m^2 \cdot g^{-1}$)	Pore volume ($cm^3 \cdot g^{-1}$)[a]	Average pore diameter (Å)[b]
Mn_3O_4	1.6	0.004	100
Cr_2O_3	4.1	0.016	160
$MnCr_2O_4$	5.3	0.020	150
$Mn_{1.5}Cr_{1.5}O_4$	2.6	0.007	100
$Mn_{0.5}Cr_{2.5}O_4$	4.5	0.016	140

[a] BJH cumulative pore volume

[b] Estimated from cylindrical pore geometry ($d = \frac{4V}{A}$)

The elemental compositions of the Mn-Cr-O spinel catalysts measured from different techniques are listed in **Table 2.2**. The bulk Cr/Mn ratios measured from ICP are close to the desired starting ratios, indicating negligible loss of Mn during thermal treatment resulting from the volatility of $Mn(OH)_2$ [13]. The EDS analysis (**Figure 2.1b**) of the Mn-Cr-O spinel particles further confirms the existence of Cr and Mn mixed oxides. As the estimated penetration depth of the electron beam is sufficiently larger than the average particle size, the assessed Cr/Mn ratios from EDS are consistent with the bulk values measured from ICP. The elemental compositions near the surface region are identified by XPS (30~60 Å estimated from the mean free path of the photoelectrons). The Cr/Mn ratios of $MnCr_2O_4$ and $Mn_{1.5}Cr_{1.5}O_4$ evaluated from XPS are consistent with the values from ICP and EDS. The Cr/Mn ratio determined by XPS for $Mn_{0.5}Cr_{2.5}O_4$ was 2.9, which is significantly lower than that measured from ICP or EDS, indicating a nonuniform distribution of metals, with an enrichment of Mn close to the surface for that sample.

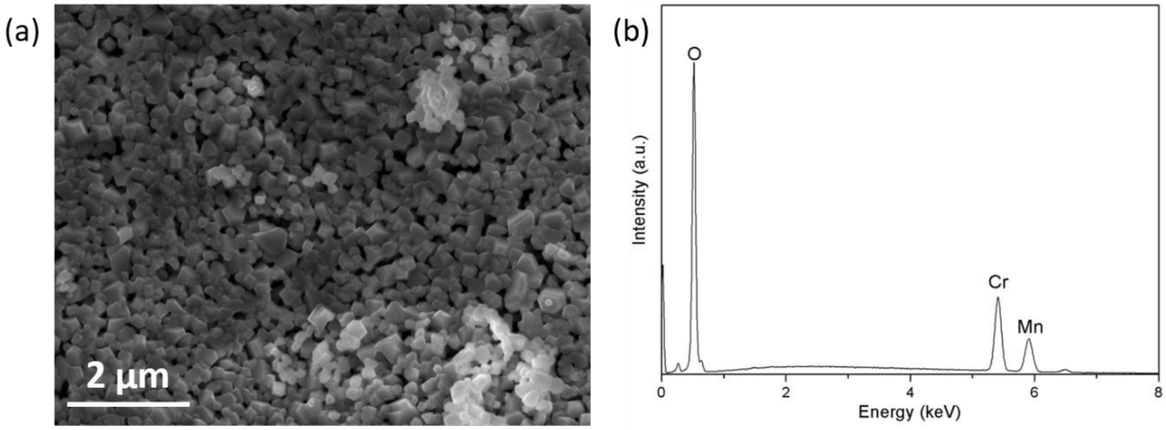

Figure 2.1 (a) SEM image and (b) EDS analysis of the fresh $MnCr_2O_4$ catalyst.

Table 2.2 Elemental composition of the Mn-Cr-O spinel catalysts measured by different techniques

Catalyst	ICP Cr/Mn	EDS Cr/Mn	XPS Cr/Mn
$MnCr_2O_4$	1.7	1.9	2.0
$Mn_{1.5}Cr_{1.5}O_4$	0.85	1.0	0.84
$Mn_{0.5}Cr_{2.5}O_4$	5.0	4.2	2.9

The phase compositions of the Mn-Cr-O spinel catalysts of different stoichiometry were characterized by XRD and compared to Mn oxide and Cr oxide. As shown in **Figure 2.2**, Cr oxide exhibits the diffraction of Cr_2O_3 as expected, whereas Mn oxide exists as Mn_3O_4, which is an oxide containing both Mn^{2+} and Mn^{3+}. The formation of Mn_3O_4 is likely due to the partial oxidation of Mn^{2+} from the nitrate precursor to Mn^{3+} and Mn^{4+} containing oxides, followed by sequential decomposition at higher temperatures [18,19]. Thus, the diffraction peak of low intensity at $2\theta = 32.9°$ is assigned to a small amount of Mn_2O_3 from incomplete decomposition. In the diffraction patterns of the Mn-Cr-O spinel catalysts, the spinel features are present in all three catalysts. A trace amount of Cr_2O_3 is present in the stoichiometric $MnCr_2O_4$. For the sample with an excess of Cr ($Mn_{0.5}Cr_{2.5}O_4$), a significant amount of Cr_2O_3 is clearly observed. For the sample with an excess of Mn ($Mn_{1.5}Cr_{1.5}O_4$), no separate Mn oxide phase was detected. These observations are all consistent with the previous reports [10,11,13,20,21]. The existence of a Mn-rich spinel phase has been discussed in earlier studies, in which Mn^{3+} was considered to substitute part of the Cr^{3+} in the octahedral sites of the spinel $MnCr_2O_4$ [11,22,23]. This substitution of Mn^{3+} for Cr^{3+} results in a slight distortion of the crystal structure, enabling us to distinguish the observed spinel features in terms of the lattice constants. The lattice constants of the spinel catalysts are evaluated using Rietveld Refinement of their diffraction patterns as shown in **Figure 2.3**. By fixing a Cr/Mn ratio

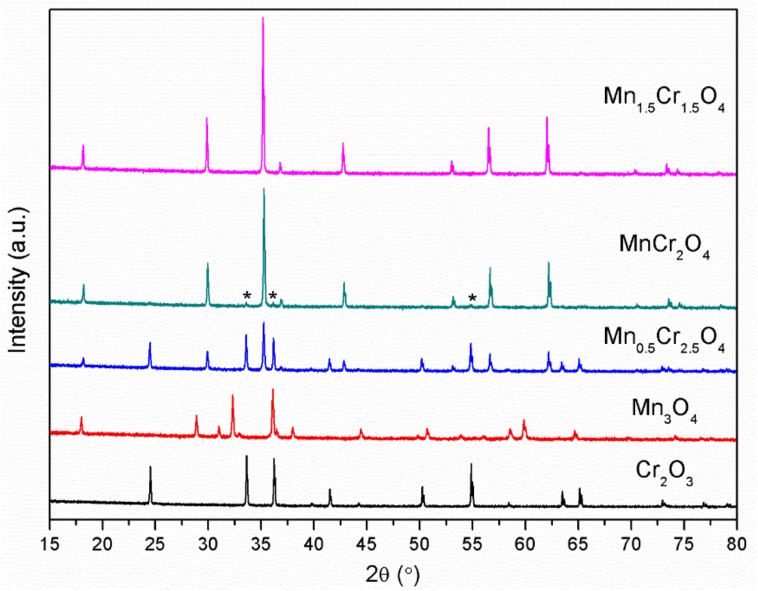

Figure 2.2 X-ray diffraction patterns of the fresh Mn oxide, Cr oxide and Mn-Cr-O spinel catalysts. The asterisks on the pattern of $MnCr_2O_4$ indicate a trace amount of Cr_2O_3.

of 1, the refined pattern of $Mn_{1.5}Cr_{1.5}O_4$ is in good agreement with the experimental diffraction data. The refined lattice constant of the $Mn_{1.5}Cr_{1.5}O_4$ sample is 8.460 Å, which is in accordance with the reported value of 8.455-8.458 Å for the $Mn_{1.5}Cr_{1.5}O_4$ phase [20,23]. The diffraction patterns of $MnCr_2O_4$ and $Mn_{0.5}Cr_{2.5}O_4$ are refined using both the $MnCr_2O_4$ spinel phase and Cr_2O_3 phase as the reference. The lattice constant refined for the $MnCr_2O_4$ spinel phase in $MnCr_2O_4$ and $Mn_{0.5}Cr_{2.5}O_4$ are 8.438 and 8.437 Å, respectively. The spinel features observed in these two catalysts are therefore assigned to the stoichiometric $MnCr_2O_4$, as the reported value of the lattice constant is 8.437-8.439 Å [24,25]. The relative amount of the $MnCr_2O_4$ spinel phase and Cr_2O_3 phase from the refinement corresponds to a Cr/Mn ratio of 2.1 for the $MnCr_2O_4$ sample and 6.0 for the $Mn_{0.5}Cr_{2.5}O_4$ sample, which are consistent with the ICP results.

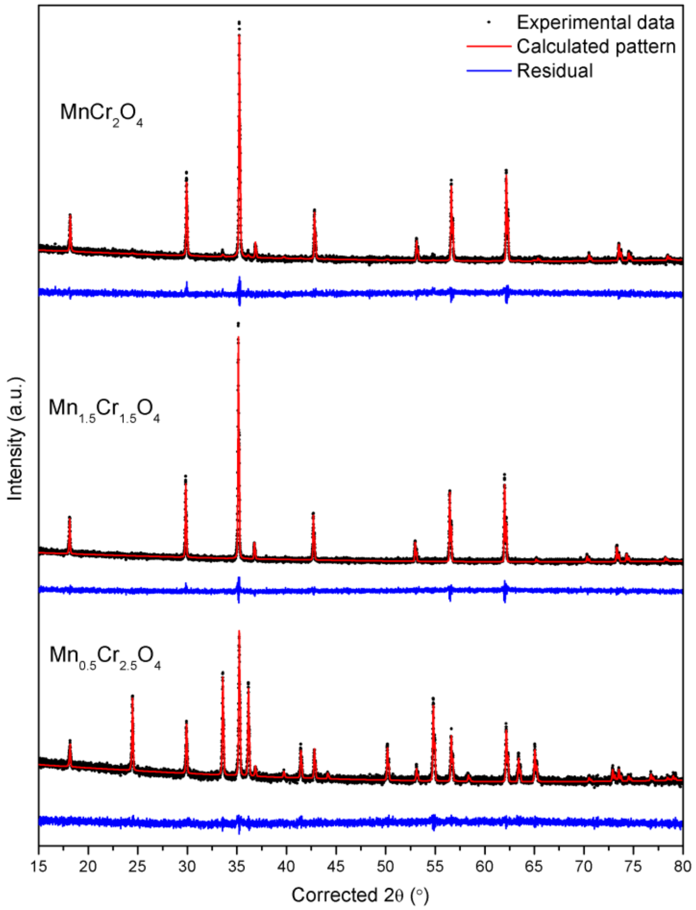

Figure 2.3 Rietveld Refinement for the XRD patterns of the fresh Mn-Cr-O spinel catalysts.

The oxidation state and coordination environment of Cr and Mn in the spinel catalysts were studied using X-ray absorption spectroscopy. As shown in **Figure A1**, the Cr K-edge spectra and Mn K-edge spectra of the samples were collected simultaneously by a continuous scan of the X-ray photon energy. Consistent with the stoichiometry of the spinel catalysts, the magnitude of the absorption at Mn K edge increases with higher Mn content when normalized by the absorption at Cr K edge. The Cr K-edge X-ray absorption near edge structure (XANES) of the Mn-Cr-O spinel catalysts are shown in **Figure 2.4a** and compared to that of Cr_2O_3. The doublet pre-edge features at around 5990 eV and 5993 eV for Cr_2O_3 are assigned to the quadrupolar 1s to 3d transition and dipolar 1s to 4p transition, respectively [26,27]. These features in Cr_2O_3 are related to the 3d-4p mixing of Cr when the coordination of the Cr site is not centrosymmetric [28,29]. Similar pre-edge features are present in $Mn_{0.5}Cr_{2.5}O_4$, which is consistent with the presence of excess Cr_2O_3 in that sample. For $MnCr_2O_4$ and $Mn_{1.5}Cr_{1.5}O_4$, the Cr K pre-edge feature at around 5990 eV is attributed to the 1s to 3d quadrupolar transition as reported for the Cr^{3+} residing in the octahedral site of the spinel structure [30], potentially resulting from a higher symmetry of the Cr site in the spinel than in Cr_2O_3. Thus the shift in edge energy between Cr_2O_3 and the spinel catalysts might be related to the different edge shape caused by the threshold 1s to 4p dipole transition. As the absorption edges for both Cr and Mn have complex shapes we arbitrarily compare the edge energy E_0 of the samples defined at half step height. The E_0 for the Cr K edge of $MnCr_2O_4$ (5999.9 eV) was 1.6 eV higher than that for Cr_2O_3 (5998.3 eV). As the edge energies of the three spinel catalysts are similar (**Figure A1**), the formal oxidation state of Cr in the three spinel catalysts is assigned to be 3+. As shown in **Figure 2.4b,** the Mn K-edge XANES of the Mn-Cr-O spinel catalysts resemble the XANES of Mn_3O_4 since Mn_3O_4 adopts a distorted spinel structure whereas all of the Mn atoms in Mn_2O_3 are octahedrally coordinated. The pre-edge feature around 6540 eV is attributed to the dipolar 1s to 3d-4p transition that has been reported for tetrahedral Mn^{2+} in the spinel structure (*i.e.*, $MnCr_2O_4$ and $MnFe_2O_4$) [31,32]. The weak pre-edge feature in Mn_2O_3 is due to the O_h symmetry in which only the quadrupolar 1s to 3d transition is allowed [33]. Therefore, the stronger pre-edge feature observed for the Mn-Cr-O spinel catalysts indicates significant presence of Mn with T_d symmetry in the spinel structure [34]. The value of E_0 for Mn_3O_4 (6547.6 eV), in which two thirds of the Mn are nominally Mn^{3+}, is only 1.4 eV higher than $MnCr_2O_4$ (6546.2 eV). The simple oxides of Mn have an E_0 value for Mn^{3+} in Mn_2O_3 that is 4-5 eV higher than Mn^{2+} in MnO [35–37]. Evidently, using the value of E_0 to assign oxidation state of Mn can be ambiguous. Nevertheless, the value of E_0 for $Mn_{1.5}Cr_{1.5}O_4$ (6546.6 eV) is slightly higher than both $MnCr_2O_4$ (6546.2 eV) and $Mn_{0.5}Cr_{2.5}O_4$ (6546.4 eV), which is consistent with some of the excess Mn in $Mn_{1.5}Cr_{1.5}O_4$ being in the +3 oxidation state.

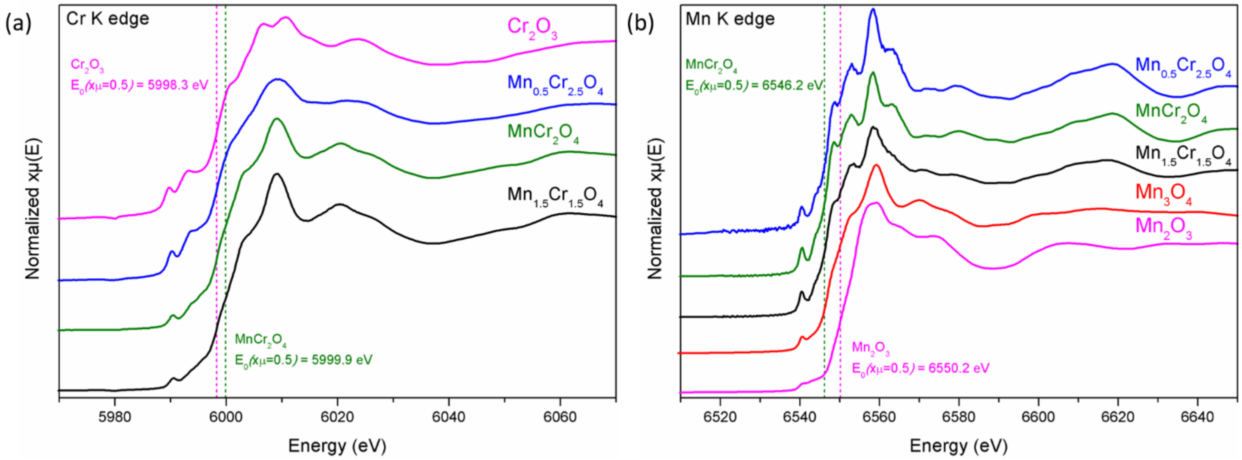

Figure 2.4 Normalized X-ray absorption near edge structure at the (a) Cr K edge and (b) Mn K edge of the fresh Mn-Cr-O spinel catalysts compared to the pure oxides. Spectra are offset for clarity.

The Fourier transformed extended X-ray absorption fine structure (EXAFS) associated with Cr and Mn in the Mn-Cr-O spinel catalysts are shown in **Figure 2.5** together with the pure oxides. As shown in **Figure 2.5a**, the distance for the Cr-O first shell is uniform across the spinel samples. The second shell of Cr in all the spinel samples is similar to that of Cr_2O_3. This second shell feature is consistent with the second nearest neighbors of octahedrally coordinated Cr. Comparatively, the first shell Mn-O distance for $MnCr_2O_4$ and $Mn_{1.5}Cr_{1.5}O_4$ (**Figure 2.5b**) is similar to their corresponding Cr-O shell distance. The second shell feature of Mn for $MnCr_2O_4$ and $Mn_{1.5}Cr_{1.5}O_4$ is significantly longer by about 0.5 Å than the Mn second shell of Mn_2O_3. The long second shell distance of Mn in the spinel catalysts is consistent with the second nearest neighbors of the tetrahedrally coordinated Mn. These observations of first and second shell features in the EXAFS are consistent with the reported EXAFS results from various spinel oxides [38–40]. Interestingly, the second shell of $Mn_{1.5}Cr_{1.5}O_4$ appears to be broad with a shoulder at a shorter distance that might arise from a fraction of the Mn residing in the octahedral site of the spinel structure, which has been claimed in the Mn-rich spinel oxides [11,20,22,23].

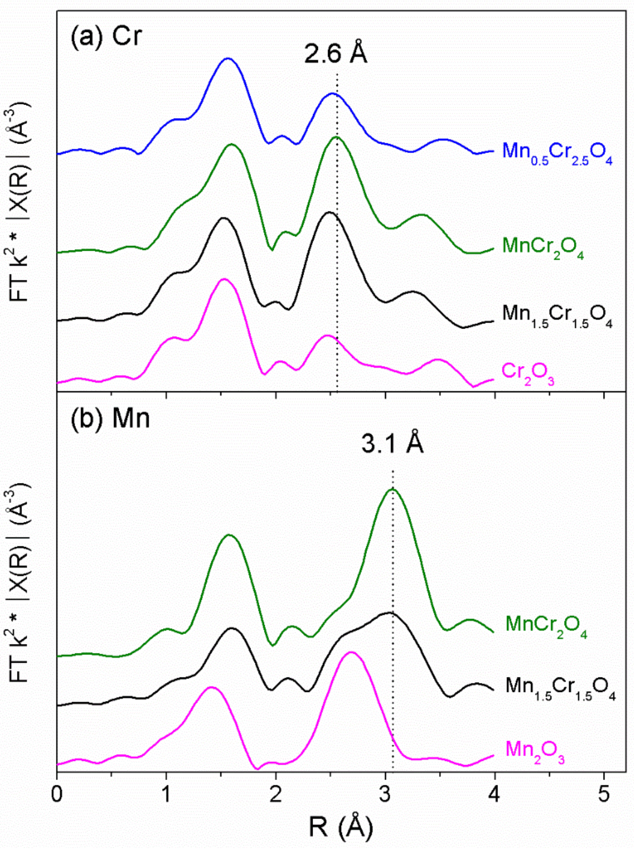

Figure 2.5 Magnitude of the Fourier-transformed EXAFS (not corrected for phase shift) from (a) Cr and (b) Mn for the fresh Mn-Cr-O spinel catalysts and the pure oxides. Spectra are offset for clarity.

The distributions of Cr and Mn in the Mn-Cr-O spinel catalysts were further investigated using EDS elemental mapping and XPS depth profiling. The EDS mappings of $MnCr_2O_4$ and $Mn_{1.5}Cr_{1.5}O_4$ (**Figure A2**) suggest uniform distributions of both Cr and Mn in the particles, which is consistent with the observation of spinel phase by XRD. Despite a significant amount of Cr_2O_3 in $Mn_{0.5}Cr_{2.5}O_4$, no discontinuity of Mn distribution was detected on the EDS mapping. **Figure 2.6** shows the changes of Cr/Mn ratios determined by XPS of the Mn-Cr-O spinel catalysts as a function of sputtering cycle. In agreement with the results in **Table 2.2**, the Cr/Mn ratios of $MnCr_2O_4$ and $Mn_{1.5}Cr_{1.5}O_4$ are almost constant regardless of sputtering cycle (or depth in the sample), indicating uniform Cr and Mn distributions from the surface to the bulk. However, the Cr/Mn ratio of $Mn_{0.5}Cr_{2.5}O_4$ gradually increases with the sputtering depth and approaches the bulk Cr/Mn ratio, which confirms the enrichment of Mn close to the surface for that sample.

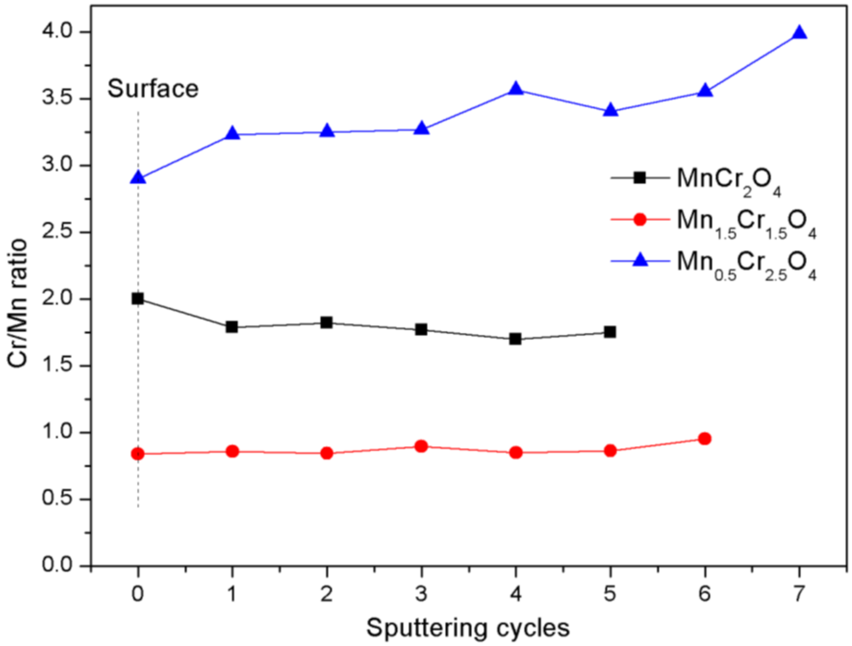

Figure 2.6 The Cr/Mn ratio of the fresh Mn-Cr-O spinel catalysts measured during XPS depth profiling. Cycle 0: surface measurement without sputtering; Cycle 1-5: presputtered with 3 kV bias for 0.5 min; Cycle 6: presputtered with 3 kV bias for 5 min; Cycle 7: presputtered with 5 kV bias for 5 min.

The speciation of Mn and Cr on the surface of the Mn-Cr-O spinel catalysts was also investigated by XPS (**Figure 2.7**). The $2p_{3/2}$ and $2p_{1/2}$ binding energies for different Mn oxides are well-known to exist over a short energy range, so direct identification of Mn^{2+} from Mn^{3+} at around 641.3 eV is difficult [41,42]. The Mn $2p_{3/2}$ peak in $MnCr_2O_4$ and $Mn_{0.5}Cr_{2.5}O_4$ both show a shake-up feature at 647.3 eV (**Figure 2.7a**), which is known to appear only when Mn^{2+} is present [43,44]. The less intense shake-up feature in $Mn_{1.5}Cr_{1.5}O_4$ may be related to the existence of Mn^{3+} on the surface. The peak in $MnCr_2O_4$ and $Mn_{0.5}Cr_{2.5}O_4$ at a binding energy of 640.0 eV is associated with the strong multiplet split of Mn^{2+} [43–46], which is consistent with the observed shake-up feature for Mn^{2+} at 647.3 eV. The Cr $2p_{3/2}$ region of all three spinel catalysts is similar.

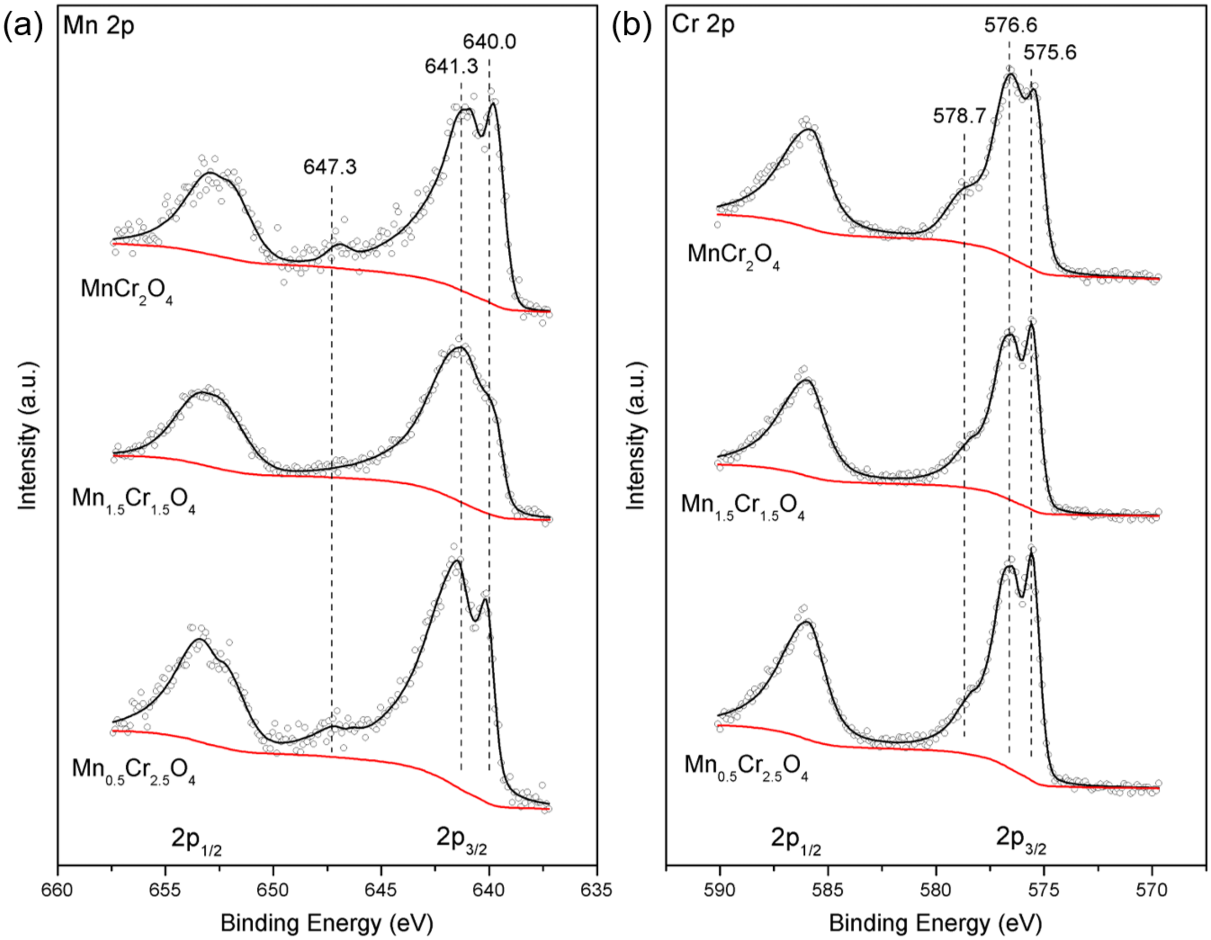

Figure 2.7 (a) Mn 2p and (b) Cr 2p X-ray photoelectron spectra on the surface of the fresh Mn-Cr-O spinel catalysts.

The two peaks at a binding energy of 576.6 eV and 575.6 eV (**Figure 2.7b**) are assigned to the multiplet split of Cr^{3+} as reported in prior studies [47,48]. The broad feature around 578.7 eV is attributed to Cr^{6+} [48] since the oxidation of Cr_2O_3 to CrO_3 at high temperature is well documented [49,50]. No obvious difference in the XPS of Mn and Cr 2p region is identified for $MnCr_2O_4$ (**Figure A3)** during the depth profiling except the disappearance of a Cr^{6+} feature, indicating a uniform speciation of Mn and Cr from the surface to the bulk. Similar observations were associated with the other spinel samples (not shown).

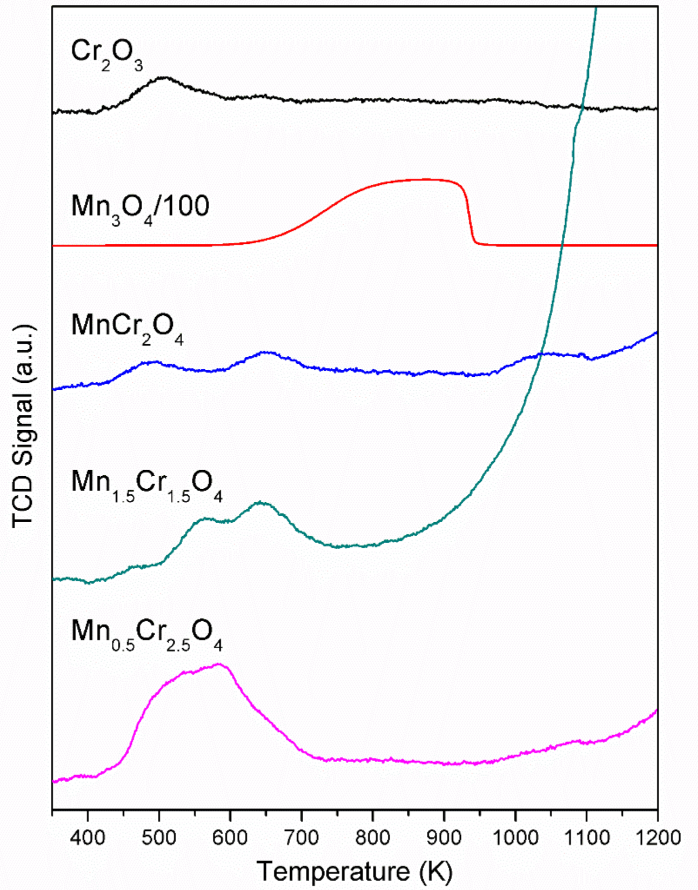

Figure 2.8 Temperature-programmed reduction in H_2 of the fresh Mn oxide, Cr oxide and Mn-Cr-O spinel catalysts.

Temperature-programmed reduction in H_2 was used to probe the redox properties of Mn oxide, Cr oxide and Mn-Cr-O spinel catalysts. As shown in **Figure 2.8**, the three spinel catalysts and Cr_2O_3 exhibit low temperature reduction features in a temperature range from 423 K to 773 K.

These features are attributed to the reduction of Cr^{6+} on the surface of $MnCr_2O_4$ or Cr_2O_3 phase [21,51,52], which is consistent with the Cr^{6+} identification in the spinel catalysts by XPS. The appearance of two features in the reduction of $MnCr_2O_4$ and $Mn_{1.5}Cr_{1.5}O_4$ may be due to the stepwise reduction of Cr^{6+} to Cr^{3+} and Cr^{3+} to Cr^{2+} as claimed in previous studies [53,54]. A very high temperature reduction above 873 K has been identified for $Mn_{1.5}Cr_{1.5}O_4$. Since MnO phase was detected by XRD after H_2-TPR of $Mn_{1.5}Cr_{1.5}O_4$ (**Figure A4a**), this peak is assigned to the reduction of surface Mn^{3+} to Mn^{2+}. For comparison, the reduction of Mn^{3+} to Mn^{2+} in Mn_3O_4 was observed starting at a much lower temperature of 573 K. The XRD pattern (**Figure A4b**) indicates Mn_3O_4 was completely reduced to MnO during the H_2-TPR experiment. Therefore, the substitution of Mn^{3+} into the spinel lattice in $Mn_{1.5}Cr_{1.5}O_4$ can effectively stabilize Mn^{3+} from being reduced to Mn^{2+}.

2.3.2 Steam reforming of ethylene over Mn oxide, Cr oxide and Mn-Cr-O spinel catalysts

Table 2.3 Steam reforming of ethylene over Mn oxide, Cr oxide and the Mn-Cr-O spinel catalysts at 873 K

Catalyst	C_2H_4 conversion[a] (%)	C_1 production rate ($\mu mol \cdot m^{-2} \cdot s^{-1}$)	Product selectivity (%)			
			CO	CO_2	CH_4	H_2
$MnCr_2O_4$	1.8	0.13	1.2	28	13	58
$Mn_{1.5}Cr_{1.5}O_4$	1.5	0.21	0.74	30	7.7	62
$Mn_{0.5}Cr_{2.5}O_4$	2.1	0.19	1.1	28	15	56
Cr_2O_3[b]	3.0	0.34	1.2	27	16	55
Mn_3O_4-i[c]	5.3	0.57	0.64	96	0.64	2.5
Mn_3O_4-f[d]	0.56	0.060	1.4	27	6.4	65

[a] Product-based conversion
[b] Initial results averaged over t < 3 h
[c] Initial results at t < 10 min
[d] Steady state results after t = 4 h

The synthesized Mn oxide, Cr oxide and Mn-Cr-O spinel catalysts were evaluated for the steam reforming of ethylene at 873 K, a temperature at which background reforming activity was

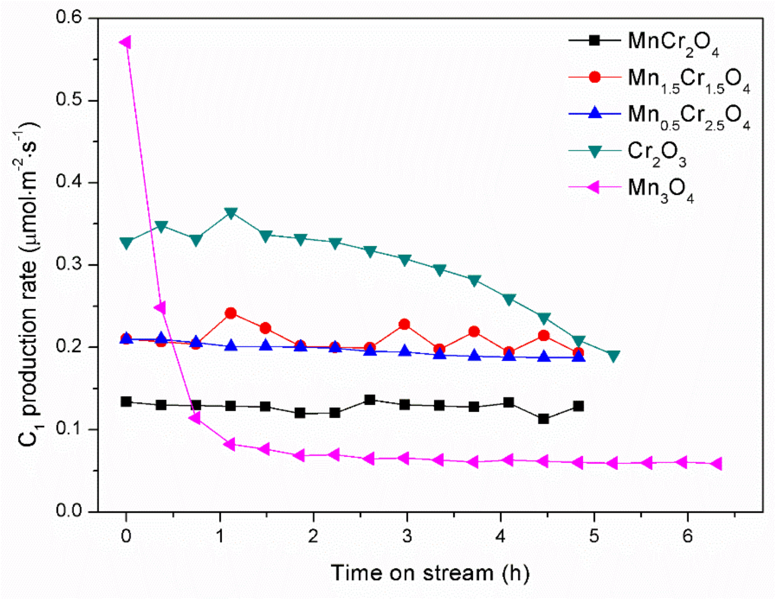

Figure 2.9 Rate of C_1 product formation during the steam reforming of ethylene over Mn oxide, Cr oxide and Mn-Cr-O spinel catalysts. Reaction conditions: 873 K, 1 g catalyst (2 g for Mn_3O_4), 100 $cm^3 \cdot min^{-1}$ total flow, 25 % C_2H_4, 50 % H_2O, 5 % N_2 and 20 % Ar.

negligible. The potential effects of heat and mass transfer limitations on the measured steam reforming rates were found to be insignificant (see Appendix A2 for a detailed analysis). As listed in **Table 2.3**, the maximum conversion among the five catalysts was 5.3 %, which was observed over Mn_3O_4 only at the beginning of reaction. The Cr_2O_3 catalyst exhibited a higher initial ethylene reforming activity than the spinel catalysts but deactivated continuously after about 3 h on stream. The Cr_2O_3 catalyst and $Mn_{1.5}Cr_{1.5}O_4$ spinel catalyst were further tested in ethylene steam reforming under similar partial pressures of H_2 for an appropriate comparison of catalyst stability. As shown in **Figure A5**, despite a higher initial reforming rate, the Cr_2O_3 catalyst rapidly deactivated after 3 h on stream and eventually became less active than the $Mn_{1.5}Cr_{1.5}O_4$ spinel catalyst, which remained stable for over 10 h on stream. Since no degradation of the Cr_2O_3 phase was detected by X-ray diffraction and the initial reforming activity of the deactivated catalyst could be fully regenerated by re-oxidation, the deactivation of the Cr_2O_3 catalyst was likely the result of coke deposition evident by the weight loss (0.22 wt %) during temperature-programmed oxidation of the spent catalyst sample. The Mn_3O_4 sample had the highest reforming rate of 0.57 $\mu mol \cdot m^{-2} \cdot s^1$ at the initial stage, but it deactivated rapidly (**Figure 2.9**). The rate after about 4 h on stream was only 10 % of the rate observed initially. The three spinel catalysts showed stable activity during steam reforming of ethylene (**Figure 2.9**). The reforming rate over $Mn_{1.5}Cr_{1.5}O_4$ (0.21 $\mu mol \cdot m^{-2} \cdot s^1$) was similar to that over $Mn_{0.5}Cr_{2.5}O_4$ (0.19 $\mu mol \cdot m^{-2} \cdot s^1$), both being slightly higher than the rate over $MnCr_2O_4$ (0.13 $\mu mol \cdot m^{-2} \cdot s^1$). The reforming product selectivity over the Mn-Cr-O spinel catalysts favored CO_2 and H_2, which is ascribed to nearly equilibrated water-gas shift reaction at 873 K in the presence of excess H_2O. Since the selectivity toward H_2 over Mn_3O_4 during the initial stage was much lower than that toward CO_2, the deactivation of Mn_3O_4 may be related to the reduction of Mn_3O_4 during the reaction. The BET surface area of Mn_3O_4 after reaction (1.4 $m^2 \cdot g^{-1}$) showed a minor decrease compared to the fresh catalyst (1.6 $m^2 \cdot g^{-1}$). In accordance with our H_2-TPR results, the XRD pattern (**Figure A6a**) of a deactivated catalyst clearly demonstrates that Mn_3O_4 was reduced to MnO during ethylene steam reforming at 873 K. Thus, the measured steady state rate of Mn_3O_4 after 4 h in **Table 2.3** actually reflects the activity of MnO, indicating MnO is much less active than Mn_3O_4 in the reaction. No obvious changes regarding the BET surface area (**Table A1**) or phase composition (**Figure A6b**) were observed for the Mn-Cr-O spinel catalysts. Thermogravimetric analysis of the Mn-Cr-O spinel catalysts (**Figure A7**) showed negligible coke deposition on the catalysts, and the weight loss below 373 K is likely the result of H_2O desorption.

2.3.3 Steam reforming kinetics of the Mn-Cr-O spinel catalysts

The kinetic behavior of ethylene steam reforming was investigated over the Mn-Cr-O spinel catalysts. **Figure 2.10** presents the influence of H_2, C_2H_4 and H_2O on the observed rate of reforming. As shown in **Figure 2.10a**, $MnCr_2O_4$ and $Mn_{0.5}Cr_{2.5}O_4$ showed almost the same C_1 production rate regardless of the H_2 partial pressure. Co-feeding H_2 changed the product selectivity

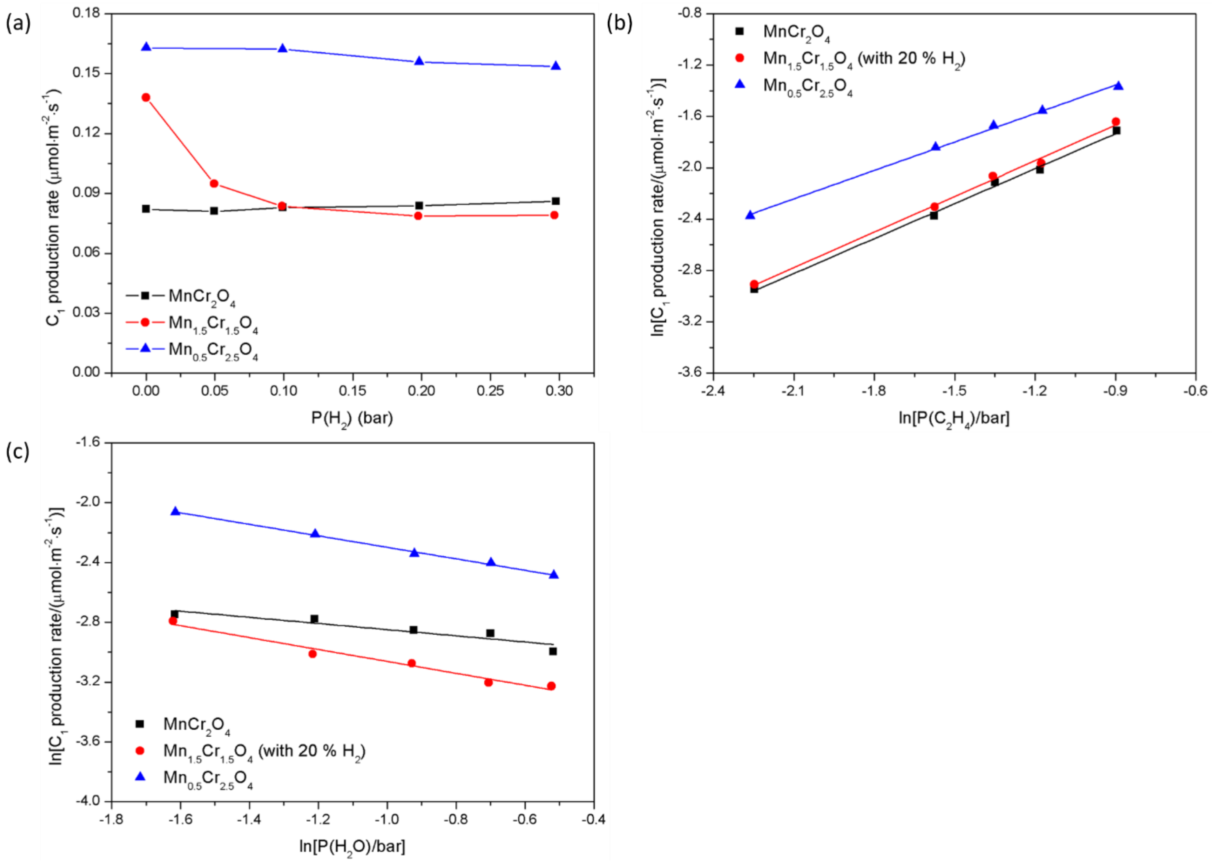

Figure 2.10 Effect of partial pressures of (a) H_2, (b) C_2H_4 and (c) H_2O on the C_1 production rate in the steam reforming of ethylene over the Mn-Cr-O spinel catalysts. Reaction conditions: 873 K, 1 g catalyst, 100 $cm^3 \cdot min^{-1}$ total flow, 20 % H_2 was co-fed for testing the effect of C_2H_4 and H_2O on $Mn_{1.5}Cr_{1.5}O_4$.

from CO_2 toward CO and CH_4, but the overall reaction order in terms of C_1 production was near zero. Interestingly, the activity of $Mn_{1.5}Cr_{1.5}O_4$ was significantly inhibited when a small amount of H_2 was co-fed, but the reaction reached zero order in H_2 at about 0.1 bar H_2. This phenomenon may be related to the regeneration of Mn^{3+} on the surface but will need to be explored further. Since the activity of $Mn_{1.5}Cr_{1.5}O_4$ is sensitive to low levels of H_2, our subsequent studies with $Mn_{1.5}Cr_{1.5}O_4$ were conducted in the presence of 20 % H_2 to assure the inhibitive effect of H_2 on the rate was similar across all measurements. As shown in **Figure 2.10b**, the steam reforming activities of all three spinel catalysts increased with increasing C_2H_4 partial pressure. Ethylene steam reforming was nearly first order in C_2H_4 over $MnCr_2O_4$ and $Mn_{1.5}Cr_{1.5}O_4$ (**Table 2.4**), while

Table 2.4 Apparent reaction orders and activation barriers for steam reforming of ethylene measured over the Mn-Cr-O spinel catalysts

Catalyst	Order in H_2	Order in C_2H_4	Order in H_2O	E_a (des.)[c] (kJ·mol^{-1})	E_a (acs.)[d] (kJ·mol^{-1})	E_a (avg.)[e] (kJ·mol^{-1})
$MnCr_2O_4$	0.03	0.91	-0.21	130	120	130
$Mn_{1.5}Cr_{1.5}O_4$	-0.05[a]	0.93[b]	-0.40[b]	150	150	150
$Mn_{0.5}Cr_{2.5}O_4$	-0.05	0.74	-0.38	200	170	190

[a] Valid when $p(H_2)$ is at least 0.1 bar

[b] Measured while co-feeding 20 % H_2

[c] Calculated from 893 K to 853 K temperature descending sequence

[d] Calculated from 853 K to 893 K temperature ascending sequence

[e] Calculated from the average rates of the descending and ascending temperature sequence

a slightly lower reaction order of 0.74 was observed for $Mn_{0.5}Cr_{2.5}O_4$. The effect of H_2O partial pressure was also investigated as shown in **Figure 2.10c**. Ethylene steam reforming over all three spinel catalysts was slightly inhibited by H_2O when the steam to carbon ratio (S/C) in the feed was greater than unity. The reaction order in H_2O under these conditions ranges from -0.21 to -0.40 over the spinel catalysts, although a more complex influence of H_2O has been identified over a wider S/C range (**Figure A8**). The inhibitive effect of H_2O suggests a higher steady state H_2O coverage compared to C_2H_4 and H_2 on the surfaces of the spinel catalysts, which can be ascribed to stronger adsorption of H_2O compared to C_2H_4 and H_2.

The apparent activation barrier of ethylene steam reforming over the Mn-Cr-O spinel catalysts was evaluated using the method described by Xie *et al* [55] to account for deactivation. The apparent activation barrier was measured in the presence of excessive H_2 for the spinel catalysts. The reactions were carried out following the temperature profile shown in **Figure 2.11c**, in which the catalyst was reacted for 20 h at 893 K to reach “steady state”, then following the descending and ascending temperature sequence in **Figure 2.11c**. As shown in **Figure 2.11a**, $MnCr_2O_4$ and $Mn_{1.5}Cr_{1.5}O_4$ both exhibited stable reforming activities with only minor deactivation observed up to 20 h. The $Mn_{0.5}Cr_{2.5}O_4$ catalyst continued to slowly deactivate, even in the presence

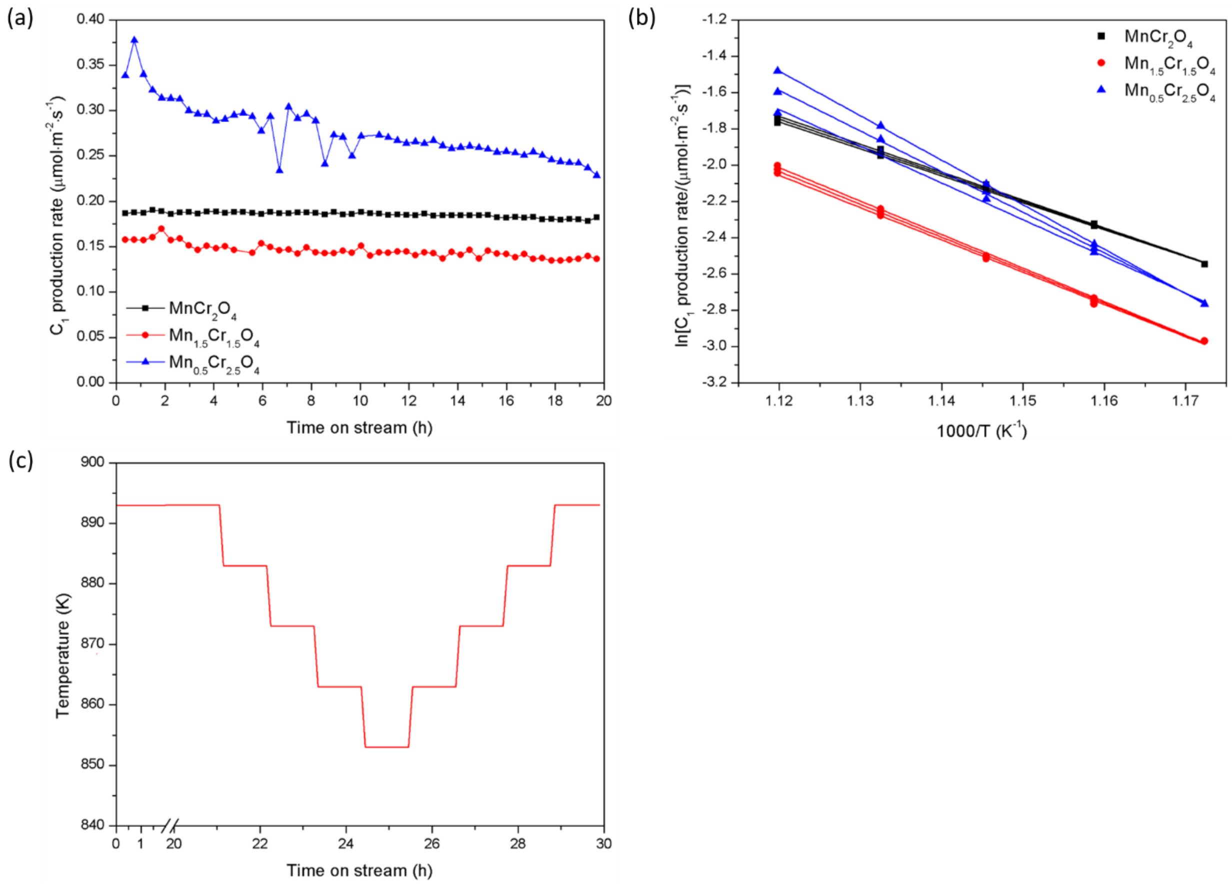

Figure 2.11 (a) Deactivation profiles at 893 K and (b) Arrhenius-type plots of the C_1 production rate within the temperature range of 853-893 K of the steam reforming of ethylene over the Mn-Cr-O spinel catalysts. Reaction conditions: 1 g catalyst, 100 $cm^3 \cdot min^{-1}$ total flow, 25 % C_2H_4, 50 % H_2O, 5 % N_2 and 20 % H_2. The temperature profile of the whole measurement is shown in (c).

of H_2. These findings suggest the excess Cr_2O_3 in $Mn_{0.5}Cr_{2.5}O_4$ may be responsible for the deactivation, potentially from surface carburization and perhaps minor coke deposition, which is in good agreement with the reported higher resistance to carburization of Mn-Cr-O spinels compared to Cr_2O_3 [10,11,13]. As shown in **Figure 2.11b**, the deactivation of $Mn_{0.5}Cr_{2.5}O_4$ caused the slope of the temperature descending sequence to deviate significantly from that of the ascending one in the Arrhenius-type plots. The apparent activation barrier measured by averaging the two sequences over $Mn_{0.5}Cr_{2.5}O_4$ was 190 $kJ \cdot mol^{-1}$ (**Table 2.4**), with an uncertainty of about 20 $kJ \cdot mol^{-1}$. As expected from the slight deactivation over $MnCr_2O_4$ and $Mn_{1.5}Cr_{1.5}O_4$, the

Arrhenius-type plots of the corresponding descending and ascending temperature sequence substantially overlapped. Both $MnCr_2O_4$ and $Mn_{1.5}Cr_{1.5}O_4$ exhibited a lower apparent activation barrier compared to $Mn_{0.5}Cr_{2.5}O_4$, the average values being 130 $kJ\cdot mol^{-1}$ and 150 $kJ\cdot mol^{-1}$, respectively.

To estimate the intrinsic turnover frequency (TOF) of the Mn-Cr-O spinel catalysts, the reported C_1 production rate would need to be further normalized by the active site density on the catalyst surface. We evaluated the surface density of redox-active oxygen sites and water adsorption sites as potential measures of active sites. As listed in **Table A2**, the oxygen storage capacity (OSC) of the Mn-Cr-O spinel catalysts was measured using O_2 pulse chemisorption and compared to the corresponding H_2 consumption during H_2-TPR up to 873 K. The measured OSC values of the spinel catalysts are in good agreement with their H_2 consumptions, indicating the redox active sites may be some surface Cr species in which Cr oxidation state is changeable. However, the highest OSC value of 28 $\mu mol\ O\cdot m^{-2}$ was observed for $Mn_{1.5}Cr_{1.5}O_4$, which significantly exceeded the possible oxygen density on a spinel oxide surface. Therefore, it is likely

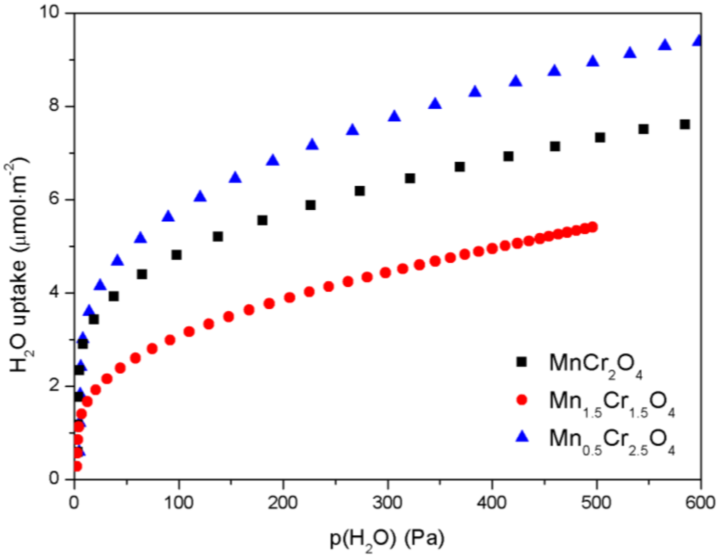

Figure 2.12 Adsorption isotherms of H_2O on the Mn-Cr-O spinel catalysts at 383 K.

Table 2.5 Estimate of turnover frequency for ethylene steam reforming base on H_2O adsorption

Catalyst	Q_m (H_2O) (μmol·m^{-2})[a]	Q_m (H_2O) (μmol·g^{-1})	Q_m (N_2) (μmol·g^{-1})[b]	C_1 production rate (μmol·m^{-2}·s^{1})[c]	TOF (s^{-1})[d]
$MnCr_2O_4$	4.8	25	54	0.13	0.027
$Mn_{1.5}Cr_{1.5}O_4$	2.9	7.5	27	0.21	0.072
$Mn_{0.5}Cr_{2.5}O_4$	5.8	26	46	0.19	0.033

[a] Extrapolated from the linear physisorption region to p(H_2O) = 0

[b] Monolayer N_2 physisorption coverage from the BET model

[c] Reaction conditions: 873 K, 1 g catalyst, 100 cm^3·min^{-1} total flow, 25 % C_2H_4, 50 % H_2O, 5 % N_2 and 20 % Ar

[d] Calculated assuming an active site density of Q_m (H_2O)

that the OSC measurement of $Mn_{1.5}Cr_{1.5}O_4$ involved subsurface oxygen atoms so the measured OSC value cannot be used as a measure of active site density. As H_2O inhibited the reforming rate on all three catalysts, we suspect that a strong interaction between H_2O and M^{n+}-O^{2-} pairs (M^{n+} = Mn^{2+}, Mn^{3+} or Cr^{3+}) leads to a higher steady state coverage of H_2O compared to C_2H_4 and H_2 on the surface of the catalysts. Therefore, the chemisorption capacity of H_2O was explored as a representative estimate of the active site density. As shown in **Figure 2.12**, the adsorption isotherms of H_2O were measured for the Mn-Cr-O spinel catalysts at 383 K. The H_2O adsorption isotherms appear to be a combination of Langmuir adsorption at low pressure followed by physisorption at higher pressures. The chemisorption capacity of H_2O was determined from a linear extrapolation of the multilayer region to p(H_2O) = 0 as described in our previous work [16]. As listed in **Table 2.5**, the H_2O chemisorption capacity per surface area of the Mn-Cr-O spinel catalysts follow the trend of $Mn_{0.5}Cr_{2.5}O_4$ > $MnCr_2O_4$ > $Mn_{1.5}Cr_{1.5}O_4$. Compared to the respective monolayer adsorption capacity of N_2 per mass from N_2 physisorption, the chemisorption capacity per mass of the catalyst is much lower. Since the effective cross-sectional area of the H_2O molecule is smaller than that of N_2 [56], we exclude the possibility that H_2O covers the surface in the same way as N_2 due to physisorption. Instead, we attribute the lower capacity of H_2O per mass to the preferential adsorption of H_2O onto specific sites of the catalyst surface. Assuming the H_2O chemisorption capacity to be the active site density, the TOF of the Mn-Cr-O spinel catalysts has been calculated and reported in **Table 2.5**. After the site density is accounted for, the TOF of $Mn_{0.5}Cr_{2.5}O_4$ (0.033 s^{-1}) is similar to that of $MnCr_2O_4$ (0.027 s^{-1}) at 873 K. A higher TOF of 0.072 s^{-1} evaluated for $Mn_{1.5}Cr_{1.5}O_4$ suggests the Mn^{3+} may be potentially more active in ethylene steam reforming compared to Mn^{2+}.

2.3.4 Ethane dehydrogenation over the $Mn_{0.5}Cr_{2.5}O_4$ catalyst

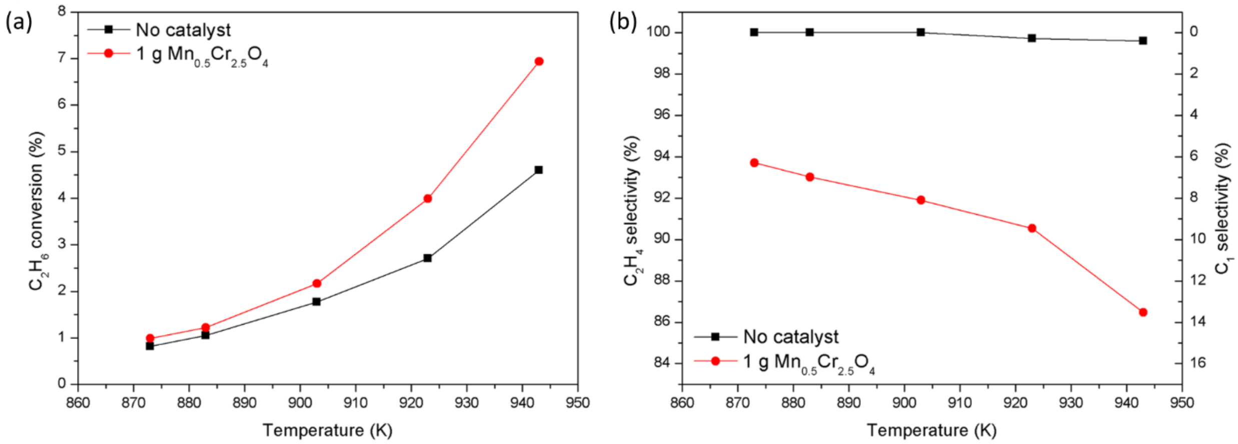

Figure 2.13 (a) Ethane conversion and (b) carbon-based product selectivity of ethane dehydrogenation without catalyst and over $Mn_{0.5}Cr_{2.5}O_4$. Reaction conditions: 873-943 K, 0 or 1 g catalyst, 100 $cm^3 \cdot min^{-1}$ total flow, 25 % C_2H_6, 50 % H_2O, 5 % N_2 and 20 % Ar.

The reactivity of ethane, which is a feed to a steam cracker, was also examined under similar steam reforming conditions using $Mn_{0.5}Cr_{2.5}O_4$ as a model catalyst. As shown in **Figure 2.13a**, the conversion of C_2H_6 at 873 K over $Mn_{0.5}Cr_{2.5}O_4$ was 1.0 %, almost identical to that without catalyst. The difference in C_2H_6 conversion between the reaction with and without catalyst increased with increasing temperature. At 943 K, the reaction with catalyst converted ethane at 6.9 %, which is higher than that without catalyst (4.6 %). The corresponding product selectivity as a function of temperature is shown in **Figure 2.13b**. In the absence of the $Mn_{0.5}Cr_{2.5}O_4$ catalyst, C_2H_6 dehydrogenated to C_2H_4 without any observed reforming reactions. The formation of CO_2 in the presence of the catalyst confirms that steam reforming of some hydrocarbon species occurred in the temperature range of 873-943 K. Detailed product selectivity for the reaction over the

$Mn_{0.5}Cr_{2.5}O_4$ catalyst is shown in **Figure A9**. As indicated from the high selectivity toward dehydrogenation (> 85 %) even in the presence of catalyst, the steam reforming of C_2H_6 was significantly less favored than the steam reforming of C_2H_4 over $Mn_{0.5}Cr_{2.5}O_4$ at these temperatures. Thus, the observed reforming products are likely derived from the steam reforming of the product C_2H_4 instead of direct reforming of C_2H_6.

2.3.5 Proposed mechanism for ethylene steam reforming over the Mn-Cr-O spinel catalysts

The steam reforming of ethylene is proposed to occur through a Mars-van Krevelen mechanism, in which C_2H_4 is oxidized by the lattice oxygen atoms O* from the catalyst surface, and the generated lattice vacancies are refilled by the dissociation of H_2O. The postulated reaction path is shown in **Scheme 2.1** for the two kinetically significant surface reactions:

$$(1) \quad C_2H_4 + O^* \xrightarrow{k_1} \text{Surface intermediates}$$

$$(2) \quad H_2O + * \xrightarrow{k_2} O^* + H_2$$

Scheme 2.1 A simplified Mars-van Krevelen mechanism proposed for ethylene steam reforming.

To simplify the mathematical derivation, we assume the oxidation rate is determined only by the initial reaction of C_2H_4 with lattice oxygen and subsequent steps are not kinetically relevant. Using the redox stoichiometry and site conservation of the lattice oxygen ($[*]_0 = [*] + [O^*]$), the reforming rate in terms of C_1 product formation r_{C_1} is obtained as:

$$\frac{[*]_0}{r_{C_1}} = \frac{1}{2k_1[C_2H_4]} + \frac{1}{k_2[H_2O]} \tag{2.8}$$

Assuming a negligible surface density of vacancies compared to the lattice oxygen ($[O^*] \gg [*]$), the first term on the right side dominates the rate expression, which agrees with the observation of the reaction being an apparent first order in C_2H_4. This simplified model gives a positive or zero order in H_2O, which cannot explain the observed inhibitive effect of H_2O on the reforming activity as seen in **Figure 2.10c**. Thus, we propose the participation of a second site S (possibly Mn^{2+}, Mn^{3+} or Cr^{3+}) on which C_2H_4 and H_2O can adsorb competitively. This modified two-site Mars-van Krevelen mechanism is described in **Scheme 2.2**:

$$\text{(1)} \quad C_2H_4 + S \overset{K_{C_2H_4}}{\rightleftarrows} C_2H_4\cdot S \quad \text{(Quasi-equilibrated)}$$

$$\text{(2)} \quad H_2O + S \overset{K_{H_2O}}{\rightleftarrows} H_2O\cdot S \quad \text{(Quasi-equilibrated)}$$

$$\text{(3)} \quad C_2H_4\cdot S + O^* \xrightarrow{k_3} \text{Surface intermediates}$$

$$\text{(4)} \quad H_2O + * \xrightarrow{k_4} O^* + H_2$$

Scheme 2.2 A modified two-site Mars-van Krevelen mechanism proposed for ethylene steam reforming.

Assuming $[O^*] \gg [*]$ as before, the reforming rate in terms of C_1 product formation r_{C_1} can be expressed as (see Appendix A3 for a detailed derivation):

$$r_{C_1} = \frac{2k_3K_{C_2H_4}[C_2H_4][S]_0[*]_0}{1 + K_{C_2H_4}[C_2H_4] + K_{H_2O}[H_2O]} \tag{2.9}$$

The inhibition by H_2O can be explained by a higher steady state coverage of H_2O than C_2H_4 on site S ($K_{C_2H_4}[C_2H_4] \ll K_{H_2O}[H_2O]$) resulting from a stronger interaction with H_2O.

2.4 Conclusions

The Mn-Cr-O spinel catalysts were found to be both active and structurally stable for ethylene steam reforming at 873 K with negligible coke deposition. The spinel catalysts outperformed the pure metal oxides since under the same reforming conditions Cr_2O_3 and Mn_3O_4 both deactivated, with Mn_3O_4 reducing to MnO *in situ*. A two-site Mars-van Krevelen type mechanism was proposed in which the slight inhibitive effect of H_2O on the steam reforming activity was ascribed to the more favorable adsorption of H_2O on the spinel surface compared to C_2H_4. The excess Cr_2O_3 in $Mn_{0.5}Cr_{2.5}O_4$ led to continuous on stream deactivation in ethylene steam reforming and a significantly higher activation barrier compared to $MnCr_2O_4$ and $Mn_{1.5}Cr_{1.5}O_4$. Under similar steam reforming conditions, ethane underwent dehydrogenation to ethylene over the $Mn_{0.5}Cr_{2.5}O_4$ catalyst without any appreciable reactivity toward steam reforming. The spinel feature in $Mn_{1.5}Cr_{1.5}O_4$ was attributed to the substitution of Cr^{3+} by Mn^{3+} given the significant expansion of the lattice constant, the additional coordination shell observed in Mn EXAFS, and the decline in intensity of the Mn^{2+} satellite feature in the Mn 2p X-ray photoelectron spectrum. The highest TOF for reforming over the spinel catalysts was observed over $Mn_{1.5}Cr_{1.5}O_4$ and may be attributed to the presence of Mn^{3+}.

2.5 References for Chapter 2

[1] K. Yin, S. Mahamulkar, J. Xie, H. Shibata, A. Malek, L. Li, C.W. Jones, P. Agrawal, R.J. Davis, Catalytic reactions of coke with dioxygen and steam over alkaline-earth-metal-doped cerium-zirconium mixed oxides, Appl. Catal. A Gen. 535 (2017) 17-23.

[2] S. Mahamulkar, K. Yin, P.K. Agrawal, R.J. Davis, C.W. Jones, A. Malek, H. Shibata, Formation and Oxidation/Gasification of Carbonaceous Deposits: A Review, Ind. Eng. Chem. Res. 55 (2016) 9760-9818.

[3] A.E. Muñoz Gandarillas, K.M. Van Geem, M.F. Reyniers, G.B. Marin, Influence of the reactor material composition on coke formation during ethane steam cracking, Ind. Eng. Chem. Res. 53 (2014) 6358-6371.

[4] S. Mahamulkar, K. Yin, R.J. Davis, H. Shibata, A. Malek, C.W. Jones, P.K. Agrawal, In Situ Generation of Radical Coke and the Role of Coke-Catalyst Contact on Coke Oxidation, Ind. Eng. Chem. Res. 55 (2016) 5271-5278.

[5] C.M. Schietekat, S.A. Sarris, P.A. Reyniers, L.B. Kool, W. Peng, P. Lucas, K.M. Van Geem, G.B. Marin, Catalytic Coating for Reduced Coke Formation in Steam Cracking Reactors, Ind. Eng. Chem. Res. 54 (2015) 9525-9535.

[6] A.E. Muñoz Gandarillas, K.M. Van Geem, M.F. Reyniers, G.B. Marin, Coking resistance of specialized coil materials during steam cracking of sulfur-free naphtha, Ind. Eng. Chem. Res. 53 (2014) 13644-13655.

[7] H. Cai, A. Krzywicki, M.C. Oballa, Coke formation in steam crackers for ethylene production, Chem. Eng. Prog. 41 (2002) 199-214.

[8] B. Bao, Z. Wang, H. Xu, J. Liu, Anti-coking Effect of $MnCr_2O_4$ Spinel Coating during Light Naphtha Thermal Cracking, Energy Procedia. 105 (2017) 4808-4813.

[9] B. Bao, J. Liu, H. Xu, B. Liu, W. Zhang, Inhibitory effect of $MnCr_2O_4$ spinel coating on coke formation during light naphtha thermal cracking, RSC Adv. 6 (2016) 68934-68941.

[10] H. Li, Y. Zheng, L.W. Benum, M. Oballa, W. Chen, Carburization behaviour of Mn-Cr-O spinel in high temperature hydrocarbon cracking environment, Corros. Sci. 51 (2009) 2336-2341.

[11] H. Li, W. Chen, Stability of $MnCr_2O_4$ spinel and Cr_2O_3 in high temperature carbonaceous environments with varied oxygen partial pressures, Corros. Sci. 52 (2010) 2481-2488.

[12] R. Yin, Carburization of 310 stainless steel exposed at 800-1100 °C in $2\%CH_4/H_2$ gas mixture, Corros. Sci. 47 (2005) 1896-1910.

[13] H. Li, W. Chen, High temperature carburization behaviour of Mn-Cr-O spinel oxides with varied concentrations of manganese, Corros. Sci. 53 (2011) 2097-2105.

[14] L. Lutterotti, M. Bortolotti, G. Ischia, I. Lonardelli, H.R. Wenk, Rietveld texture analysis from diffraction images, Z. Kristallogr. Suppl. 26 (2007) 125-130.

[15] B. Ravel, M. Newville, ATHENA, ARTEMIS, HEPHAESTUS: Data analysis for X-ray absorption spectroscopy using IFEFFIT, J. Synchrotron Radiat. 12 (2005) 537-541.

[16] Z.D. Young, S. Hanspal, R.J. Davis, Aldol Condensation of Acetaldehyde over Titania, Hydroxyapatite, and Magnesia, ACS Catal. 6 (2016) 3193-3202.

[17] K. Yin, R.J. Davis, S. Mahamulkar, C.W. Jones, P. Agrawal, H. Shibata, A. Malek, Catalytic Oxidation of Solid Carbon and Carbon Monoxide over Cerium-Zirconium Mixed Oxides, AIChE J. 63 (2017) 725-738.

[18] B. Liu, P.S. Thomas, A.S. Ray, R.P. Williams, The effect of sampling conditions on the thermal decomposition of electrolytic manganese dioxide, J. Therm. Anal. Calorim. 76 (2004) 115-122.

[19] E.R. Stobbe, B.A. De Boer, J.W. Geus, The reduction and oxidation behaviour of manganese oxides, Catal. Today 47 (1999) 161-167.

[20] E. Stefan, J.T.S. Irvine, Synthesis and characterization of chromium spinels as potential electrode support materials for intermediate temperature solid oxide fuel cells, J. Mater. Sci. 46 (2011) 7191-7197.

[21] M.A. Zamudio, N. Russo, D. Fino, Low Temperature NH_3 Selective Catalytic Reduction of NO_x over Substituted $MnCr_2O_4$ Spinel-Oxide Catalysts, Ind. Eng. Chem. Res. 50 (2011) 6668-6672.

[22] A.M. Garbers-Craig, R.J. Dippenaar, High-Temperature Phase Relations in Selected MnO-CrO_x-Containing Systems, J. Am. Ceram. Soc. 81 (1998) 933-938.

[23] B.L. Chamberland, J.A. Kafalas, J.B. Goodenough, Characterization of $MnCrO_3$ and $CrMnO_4$, Inorg. Chem. 16 (1977) 44-46.

[24] X. Liu, Z. Xiong, S.R. Shieh, Q. He, L. Deng, Y. Zhang, L. Chang, F. Wang, X. Hong, Z. Chen, Non-monotonic compositional dependence of isothermal bulk modulus of the $(Mg_{1-x}Mn_x)Cr_2O_4$ spinel solid solutions, and its origin and implication, Solid Earth Sci. 1 (2016) 89-100.

[25] F.F. Fava, I. Baraille, A. Lichanot, C. Larrieu, R. Dovesi, On the structural, electronic and magnetic properties of $MnCr_2O_4$ spinel, J. Phys. Condens. Matter 9 (1997) 10715-10724.

[26] E. Rozsályi, L. Verger, D. Cabaret, A. Juhin, DFT+U calculation of the Cr K pre-edge structures in $ZnCr_2O_4$, J. Phys. Conf. Ser. 712 (2016) 012001.

[27] S. Ould-Chikh, O. Proux, P. Afanasiev, L. Khrouz, M.N. Hedhili, D.H. Anjum, M. Harb, C. Geantet, J.M. Basset, E. Puzenat, Photocatalysis with chromium-doped TiO_2: Bulk and surface doping, ChemSusChem. 7 (2014) 1361-1371.

[28] F. De Groot, G. Vankó, P. Glatzel, The 1s x-ray absorption pre-edge structures in transition metal oxides, J. Phys. Condens. Matter 21 (2009) 104207.

[29] L. Qiao, H.Y. Xiao, S.M. Heald, M.E. Bowden, T. Varga, G.J. Exarhos, M.D. Biegalski, I.N. Ivanov, W.J. Weber, T.C. Droubay, S.A. Chambers, The impact of crystal symmetry on the electronic structure and functional properties of complex lanthanum chromium oxides, J. Mater. Chem. C 1 (2013) 4527-4535.

[30] A. Juhin, C. Brouder, M.A. Arrio, D. Cabaret, P. Sainctavit, E. Balan, A. Bordage, A.P. Seitsonen, G. Calas, S.G. Eeckhout, P. Glatzel, X-ray linear dichroism in cubic compounds: The case of Cr^{3+} in $MgAl_2O_4$, Phys. Rev. B 78 (2008) 195103.

[31] D. Carta, M.F. Casula, P. Floris, A. Falqui, G. Mountjoy, A. Boni, C. Sangregorio, A. Corrias, Synthesis and microstructure of manganese ferrite colloidal nanocrystals, Phys. Chem. Chem. Phys. 12 (2010) 5074-5083.

[32] M. Bellotto, G. Artioli, C. Cristiani, P. Forzatti, G. Groppi, On the Crystal Structure and Cation Valence of Mn in Mn-Substituted Ba-β-Al_2O_3, J. Catal. 179 (1998) 597-605.

[33] R.S. Liu, L.Y. Jang, J.M. Chen, Y.C. Tsai, Y.D. Hwang, R.G. Liu, X-ray Absorption Studies in Spinel-Type $LiMn_2O_4$, J. Solid State Chem. 128 (1997) 326-329.

[34] F. Farges, Ab initio and experimental pre-edge investigations of the Mn K-edge XANES in oxide-type materials, Phys. Rev. B 71 (2005) 155109.

[35] M.M. Najafpour, F. Ebrahimi, M. Amini, M. Rahimi, A. El-Sawy, S.L. Suib, Nano-sized Mn oxides as true catalysts for alcohol oxidation by a mononuclear manganese(II) complex, Dalt. Trans. 44 (2015) 15121-15125.

[36] Y. Gorlin, B. Lassalle-Kaiser, J.D. Benck, S. Gul, S.M. Webb, V.K. Yachandra, J. Yano, T.F. Jaramillo, In Situ X-ray Absorption Spectroscopy Investigation of a Bifunctional Manganese Oxide Catalyst with High Activity for Electrochemical Water Oxidation and Oxygen Reduction, J. Am. Chem. Soc. 135 (2013) 8525-8534.

[37] S.S. Farvid, T. Sabergharesou, L.N. Hutfluss, M. Hegde, E. Prouzet, P. V. Radovanovic, Evidence of charge-transfer ferromagnetism in transparent diluted magnetic oxide nanocrystals: Switching the mechanism of magnetic interactions, J. Am. Chem. Soc. 136 (2014) 7669-7679.

[38] C.M.B. Henderson, J.M. Charnock, D.A. Plant, Cation occupancies in Mg, Co, Ni, Zn, Al ferrite spinels: A multi-element EXAFS study, J. Phys. Condens. Matter 19 (2007) 076214.

[39] V. Krishnan, R.K. Selvan, C.O. Augustin, A. Gedanken, H. Bertagnolli, EXAFS and XANES investigations of $CuFe_2O_4$ nanoparticles and $CuFe_2O_4$-MO_2 (M = Sn, Ce) nanocomposites, J. Phys. Chem. C 111 (2007) 16724-16733.

[40] T. Tangcharoen, W. Klysubun, A. Ruangphanit, W. Pecharapa, A comparison of cation distribution and valence state in spinel crystal structure of zinc and nickel ferrites using the synchrotron X-ray absorption spectroscopy (XAS) analysis, Integr. Ferroelectr. 155 (2014) 80-90.

[41] B.J. Tan, K.J. Klabunde, P.M.A. Sherwood, XPS Studies of Solvated Metal Atom Dispersed Catalysts. Evidence for Layered Cobalt-Manganese Particles on Alumina and Silica, J. Am. Chem. Soc. 113 (1991) 855-861.

[42] J.C. Carver, G.K. Schweitzer, T.A. Carlson, Use of X-Ray Photoelectron Spectroscopy to Study Bonding in Cr, Mn, Fe, and Co Compounds, J. Chem. Phys. 57 (1972) 973-982.

[43] H.W. Nesbitt, D. Banerjee, Interpretation of XPS Mn (2p) spectra of Mn oxyhydroxides and constraints on the mechanism of MnO_2 precipitation, Am. Mineral. 83 (1998) 305-315.

[44] M.C. Biesinger, B.P. Payne, A.P. Grosvenor, L.W.M. Lau, A.R. Gerson, R.S.C. Smart, Resolving surface chemical states in XPS analysis of first row transition metals, oxides and hydroxides: Cr, Mn, Fe, Co and Ni, Appl. Surf. Sci. 257 (2011) 2717-2730.

[45] E.S. Ilton, J.E. Post, P.J. Heaney, F.T. Ling, S.N. Kerisit, XPS determination of Mn oxidation states in Mn (hydr)oxides, Appl. Surf. Sci. 366 (2016) 475-485.

[46] P.S. Bagus, E.S. Ilton, Effects of covalency on the p-shell photoemission of transition metals: MnO, Phys. Rev. B 73 (2006) 155110.

[47] E. Ünveren, E. Kemnitz, S. Hutton, A. Lippitz, W.E.S. Unger, Analysis of highly resolved x-ray photoelectron Cr 2p spectra obtained with a Cr_2O_3 powder sample prepared with adhesive tape, Surf. Interface Anal. 36 (2004) 92-95.

[48] C.J. Keturakis, M. Zhu, E.K. Gibson, M. Daturi, F. Tao, A.I. Frenkel, I.E. Wachs, Dynamics of CrO_3-Fe_2O_3 Catalysts during the High-Temperature Water-Gas Shift Reaction: Molecular Structures and Reactivity, ACS Catal. 6 (2016) 4786-4798.

[49] D. Mandrino, M. Godec, M. Torkar, M. Jenko, Study of oxide protective layers on stainless steel by AES, EDS and XPS, Surf. Interface Anal. 40 (2008) 285-289.

[50] P. Berthod, Kinetics of high temperature oxidation and chromia volatilization for a binary Ni-Cr alloy, Oxid. Met. 64 (2005) 235-252.

[51] L.F. Liotta, A.M. Venezia, G. Pantaleo, G. Deganello, M. Gruttadauria, R. Noto, Chromia on silica and zirconia oxides as recyclable oxidizing system: Structural and surface characterization of the active chromium species for oxidation reaction, Catal. Today 91-92 (2004) 231-236.

[52] B. Grzybowska, J. Słoczyński, R. Grabowski, K. Wcisło, A. Kozłowska, J. Stoch, J. Zieliński, Chromium Oxide/Alumina Catalysts in Oxidative Dehydrogenation of Isobutane, J. Catal. 178 (1998) 687-700.

[53] B.M. Weckhuysen, R.A. Schoonheydt, J.-M. Jehng, I.E. Wachs, S.J. Cho, R. Ryoo, S. Kijistra, E. Poels, Combined DRS-RS-EXAFS-XANES-TPR Study of Supported Chromium Catalysts, J. Chem. Soc. Faraday Trans. 91 (1995) 3245-3253.

[54] Y. Ramesh, P. Thirumala Bai, B. Hari Babu, N. Lingaiah, K.S. Rama Rao, P.S. Sai Prasad, Oxidative dehydrogenation of ethane to ethylene on Cr_2O_3/Al_2O_3-ZrO_2 catalysts: the influence of oxidizing agent on ethylene selectivity, Appl. Petrochem. Res. 4 (2014) 247-252.

[55] Z. Xie, B. Yan, L. Zhang, J.G. Chen, Comparison of Methodologies of Activation Barrier Measurements for Reactions with Deactivation, Ind. Eng. Chem. Res. 56 (2017) 1360-1364.

[56] H.K. Livingston, The cross-sectional areas of molecules adsorbed on solid surfaces, J. Colloid Sci. 4 (1949) 447-458.

Chapter 3 Steam reforming kinetics of olefins and aromatics over Mn-Cr-O spinel oxides

Work presented in this chapter was submitted to the Journal of Catalysis as:

L. Yang, M.P. Bukhovko, A. Malek, L. Li, C.W. Jones, P.K. Agrawal, R.J. Davis, Steam reforming kinetics of olefins and aromatics over Mn-Cr-O spinel oxides.

Abstract

Catalytic steam reforming of propylene, benzene and toluene was investigated over Mn-Cr-O spinel oxides with different stoichiometry. The catalysts were structurally stable during reforming conditions except for Mn_3O_4, which reduced *in situ* to MnO. The Cr_2O_3 catalyst showed the highest initial rate for propylene reforming, whereas the Mn-rich $Mn_{1.5}Cr_{1.5}O_4$ spinel was the most active and stable catalyst for aromatic reforming. Reforming rates of olefins and aromatics were comparable under 0.05 bar hydrocarbon and 0.40 bar steam at 873 K. The reforming rate of olefins and aromatics was first order in hydrocarbon and slightly inhibited by H_2O, which is consistent with a Mars-van Krevelen type mechanism. Of the hydrocarbons investigated, only the rate of toluene reforming was negative first order in excess H_2. Results from diffuse reflectance infrared Fourier transform spectroscopy of adsorbed toluene on a spinel catalyst suggest that H_2 inhibits the rapid oxidation of the methyl group of toluene.

3.1 Introduction

Olefins are important building blocks for chemical and polymer syntheses. In particular, the production of ethylene has grown rapidly over recent years and is predicted to continue doing so with the increasing global demand [1,2]. Industrial ethylene production relies heavily on the steam cracking process, where a hydrocarbon feedstock is diluted with steam and heated from 773-923 K to 1023-1148 K to initiate the radical process [3,4]. As a result of expanding shale gas supplies, the feedstock for steam cracking furnaces in the United States has shifted gradually from naphtha to ethane, which produces predominantly ethylene through dehydrogenation and less heavier side products like propylene, butenes and aromatics [5,6].

Carbonaceous deposit, commonly known as coke, is an undesired side product formed during the steam cracking of hydrocarbons. The accumulation of coke leads to an increase in the pressure drop along the cracking reactor that favors bimolecular reactions to form heavier byproducts (*e.g.*, aromatics) and a higher fuel input to compensate for the increase in heat transfer resistance [7,8]. Eventually, the deposited carbon needs to be removed by combustion in oxygen-containing gases, which ceases the production periodically and thus has a negative impact on the economy of the process [9]. Coke deposition can occur through three mechanisms, namely catalytic coking, radical coking and droplet condensation coking, of which the former two mainly contribute to the coke deposition in the cracking furnace [10]. Catalytic coking can occur rapidly even at low temperatures over the metallic sites present on the surfaces of the Fe-Ni-Cr alloy commonly used to fabricate the tubular cracking reactors [11]. However, for the Fe-Ni-Cr alloy containing Mn, a dense barrier layer enriched with $MnCr_2O_4$ spinel oxides can form upon oxidative pretreatment, which physically separates the Fe and Ni on the alloy surface from the gas-phase coking precursors [12,13]. The $MnCr_2O_4$ spinel layer has been reported to effectively prevent catalytic coking during steam cracking, but radical coke continued to form since it was initiated through gas-phase radical processes and was less dependent on the composition of the reactor surface [14–16].

In efforts to relieve radical coke buildup over these state-of-the-art Mn-Cr-O spinel barrier oxide layers, the catalytic activity of these Mn-Cr-O spinel oxides is of interest for *in situ* removal of radical coke through steam gasification [17–19]. By analogy to our previous work on Ce-Zr mixed oxides [20], we have systematically investigated the steam reforming kinetics of olefins and aromatics that are common coking precursors present in the steam cracker as model reactions for steam gasification of coke over the Mn-Cr-O spinel oxides. Following our previous work on ethylene steam reforming [21], we have evaluated and compared the reforming kinetics of propylene, benzene and toluene, with the involved reactions shown below:

Steam Reforming:

$$C_3H_6 + 3H_2O \Longrightarrow 3CO + 6H_2 \qquad \Delta H_r^o = 373.9\ kJ \cdot mol^{-1} \tag{3.1}$$

$$C_6H_6 + 6H_2O \Longrightarrow 6CO + 9H_2 \qquad \Delta H_r^o = 705.2\ kJ \cdot mol^{-1} \tag{3.2}$$

$$C_7H_8 + 7H_2O \Longrightarrow 7CO + 11H_2 \qquad \Delta H_r^o = 868.7\ kJ \cdot mol^{-1} \tag{3.3}$$

Water-gas Shift:

$$CO + H_2O \Longrightarrow CO_2 + H_2 \quad \Delta H_r^o = -41.2\ kJ \cdot mol^{-1} \tag{3.4}$$

Methanation:

$$CO + 3H_2 \Longrightarrow CH_4 + H_2O \quad \Delta H_r^o = -205.9\ kJ \cdot mol^{-1} \tag{3.5}$$

Herein, we have compared the activity and stability of Mn-Cr-O spinel oxides during toluene steam reforming to the single component oxides of Mn and Cr. The reforming kinetics of propylene, benzene and toluene were also investigated over two spinel catalysts and compared to our previously reported ethylene reforming kinetics [21]. Results from rate measurements and *in situ* diffuse reflectance infrared Fourier transform spectroscopy of aromatic adsorption on the spinel oxide surface were used to develop a Mars-van Krevelen type mechanism. Finally, the turnover frequency of olefins and aromatics steam reforming over the spinel catalysts was estimated under conditions free of heat and mass transfer artifacts assuming an active site density evaluated by adsorption of H_2O [21]. Together with the proposed mechanism, these results provide new insights for potential improvements in the design of catalytically active barrier oxide layers to suppress radical coke buildup during steam cracking.

3.2 Experimental section

3.2.1 Catalyst preparation

The Mn-Cr-O spinel oxide catalysts were synthesized from a conventional sol-gel method detailed in our previous work using $Mn(NO_3)_2 \cdot 4H_2O$ (98 %, Alfa Aesar) and $Cr(NO_3)_3 \cdot 9H_2O$ (99 %, Sigma-Aldrich) as the metal precursors and citric acid (99.5 %, Sigma-Aldrich) as the gelling agent, followed by a thermal treatment at 1273 K in 100 $cm^3 \cdot min^{-1}$ air flow for 4 h [21]. The catalysts were denoted as $Mn_xCr_{3-x}O_4$ (x = 0.5, 1.0 and 1.5) depending on the starting Cr/Mn molar ratio. Single oxide sample of Mn (Mn_3O_4) and Cr (Cr_2O_3) were prepared for comparison from the same procedure using one of the nitrate precursors.

3.2.2 Catalyst characterization

Specific surface area and porosity of the catalysts were measured from N_2 physisorption at 77 K on a Micromeritics ASAP 2020 analyzer using the Brunauer-Emmett-Teller (BET) and the

Barrett-Joyner-Halenda (BJH) method of analysis, respectively. A sample of 3 g catalyst was evacuated at 473 K for 4 h prior to N_2 physisorption.

Powder X-ray diffraction (XRD) patterns of the catalysts were recorded on a PANalytical Empyrean X-ray Diffractometer equipped with a Cu Kα radiation source in the Bragg-Brentano geometry. The sample was scanned through a 2θ range of 15° to 80° at a constant rate of $5°\cdot min^{-1}$ under ambient conditions. Lattice constants from Rietveld refinement were calculated using the Material Analysis Using Diffraction (MAUD) software package [22].

The cumulative amount of carbon deposited during steam reforming was assessed by temperature-programmed oxidation of the spent catalyst using a thermogravimetric analyzer (TA Instruments SDT Q600). A sample of 30 mg was heated at a constant ramp rate of $10\ K\cdot min^{-1}$ to 973 K in a synthetic air flow of $50\ cm^3\cdot min^{-1}$.

Toluene and benzene adsorption on the $Mn_{1.5}Cr_{1.5}O_4$ spinel surface was examined by diffuse reflectance infrared Fourier transform spectroscopy (DRIFTS). Spectra were acquired on a Bruker Vertex 70 FT-IR spectrometer equipped with a liquid-nitrogen-cooled MCT detector by averaging over 100 scans at $2\ cm^{-1}$ resolution. The catalyst sample was exposed to the aromatic carried by a flow of $30\ cm^3\cdot min^{-1}$ He or excess H_2 (> 90 vol %) in He at 573 K using an *in situ* reactor cell (Harrick Praying Mantis) with KBr windows. The upstream gas was purified using an OMI purifier (Supelco) before the aromatic was introduced through a saturator. Typically, the sample was first pretreated at 773 K for 1 h and then cooled down to 573 K in a He flow. The sample was then exposed to the aromatic in a H_2-rich flow for 40 min, followed by a purge in this H_2-rich flow without the aromatic for 20 min. Subsequently, the sample was pretreated again at 773 K for 1 h and then cooled down to 573 K in a He flow. The sample was exposed to the same aromatic in a He flow for 40 min at 573 K, followed by a purge in this He flow without the aromatic for 20 min at 573 K. The DRIFTS were processed using the Kubelka-Munk theory with spectra recorded prior to exposure to the aromatic in the corresponding gas flow being applied as reflectance reference spectra.

3.2.3 Steam reforming of olefins and aromatics

The catalysts were evaluated in catalytic steam reforming of various hydrocarbons (toluene, benzene and propylene) in a temperature range of 853 K to 893 K under atmospheric total pressure. Typically, a total gas flow of 100 $cm^3 \cdot min^{-1}$ (corresponding to ~ 0.10 s residence time at 873 K) was directed to 2 g catalyst (sieved to 250-425 μm) loaded in a fixed-bed quartz reactor (10.5 mm I.D. × 12.75 mm O.D.). After removing dissolved O_2 by a N_2 purge, liquid reactants including C_7H_8 (99.8 %, Sigma-Aldrich), C_6H_6 (99.8 %, Sigma-Aldrich) and distilled deionized H_2O were introduced by syringe pumps (ISCO, 500D) to a stainless steel evaporator maintained at 403 K to ensure complete vaporization and uniform mixing with other gas components supplied from mass flow controllers (Brooks, 5850E), including C_3H_6 (99.5 %, Praxair), H_2 (99.999 %, Praxair), N_2 (99.999 %, Praxair) and Ar (99.999 %, Praxair). The reaction effluent gas was first directed to a condenser to trap unconverted aromatics (C_7H_8 or C_6H_6) and H_2O, then passed through an infrared gas analyzer (Fuji Electric ZPA) to analyze the produced CO_2, and finally sampled using an online gas chromatograph (Agilent 7890A) equipped with a CarboPlot P7 column and a thermal conductivity detector to analyze the produced H_2, CO and CH_4. The produced C_6H_6 during toluene steam reforming was analyzed by injecting the organic phase of the recovered liquid into an offline gas chromatograph (Agilent 7890A) equipped with a HP-5 column and a flame ionization detector.

The overall rate of steam reforming was evaluated at a hydrocarbon conversion less than 10 % and is reported on a carbon basis (production rate of C_1), which is defined as the total formation rate of CO, CO_2 and CH_4 normalized by the BET surface area of the catalyst:

$$r_{C_1} = \frac{F(CO) + F(CO_2) + F(CH_4)}{S_{BET}} \tag{3.6}$$

The conversion of hydrocarbon is evaluated from the produced CO, CO_2 and CH_4:

$$C_xH_y \text{ conversion } (\%) = \frac{F(CO) + F(CO_2) + F(CH_4)}{xF_0(C_xH_y)} \times 100\ \% \tag{3.7}$$

The product selectivity is defined as the molar fraction of a specific component with respect to all analyzed steam reforming products (H_2, CO, CO_2 and CH_4):

$$\text{Selectivity of X } (\%) = \frac{F(X)}{F(H_2) + F(CO) + F(CO_2) + F(CH_4)} \times 100\ \% \tag{3.8}$$

where F(X) denotes the molar flow rate of component X in the reaction effluent gas, $F_0(C_xH_y)$ denotes the molar flow rate of C_xH_y fed to the catalyst, and S_{BET} denotes the BET surface area of the catalyst assessed from N_2 physisorption.

Reproducibility of the measured steam reforming rate was within approximately 15 % relative uncertainty. Replicates of toluene steam reforming over the Mn-Cr-O spinel catalysts are shown in **Figure B1** as an example. The material balance is verified based on the stoichiometry among the steam reforming products (see **Appendix B1** of the Supplementary Material for details).

3.3 Results and discussion

3.3.1 Properties of the Mn oxide, Cr oxide and Mn-Cr-O spinel oxides

The textural properties of the oxide catalysts evaluated from N_2 physisorption are summarized in **Table 3.1**. All of the catalysts had a low BET surface area (< 10 $m^2 \cdot g^{-1}$) after the high-temperature thermal treatment. The low cumulative BJH pore volume (< 0.05 $cm^3 \cdot g^{-1}$) of the catalysts likely resulted from the voids between particle aggregates instead of intracrystalline pores [20,23]. Since the crystallites were essentially non-porous, the measured BET surface area was attributed solely to their external surface. Catalyst particles loaded into the reactor are likely composed of aggregates of these primary non-porous crystallites.

Table 3.1 Properties of the fresh Mn oxide, Cr oxide and Mn-Cr-O spinel catalysts assessed from N_2 physisorption and H_2O chemisorption

Catalyst	BET surface area S_{BET} ($m^2 \cdot g^{-1}$)	Pore volume V_p ($cm^3 \cdot g^{-1}$)[a]	Monolayer coverage of H_2O $Q_m(H_2O)$ ($\mu mol \cdot m^{-2}$)[b]
Mn_3O_4	1.0	0.003	-
$Mn_{1.5}Cr_{1.5}O_4$	2.4	0.008	2.9
$MnCr_2O_4$	5.2	0.020	4.8
$Mn_{0.5}Cr_{2.5}O_4$	4.4	0.017	5.8
Cr_2O_3	4.1	0.015	-

[a] Cumulative pore volume from BJH adsorption method.

[b] Adapted from our previous work in ref. [21]. The monolayer coverage was extrapolated from the linear physisorption region to $p(H_2O) = 0$.

The Mn oxide, Cr oxide and Mn-Cr-O spinel oxides have been extensively characterized in our prior work using X-ray diffraction, X-ray absorption spectroscopy, X-ray photoelectron spectroscopy and temperature-programmed reduction in H_2 [21]. The pure component oxide of Mn and Cr adopted the Mn_3O_4 and Cr_2O_3 phase, respectively. While excess Cr in the $Mn_{0.5}Cr_{2.5}O_4$ sample separated into Cr_2O_3, the excess Mn in the $Mn_{1.5}Cr_{1.5}O_4$ sample existed as Mn^{3+} that substituted for the Cr^{3+} in the octahedral sites of the spinel lattice without the formation of any crystalline Mn oxide phases. These octahedral Mn^{3+} sites in the $Mn_{1.5}Cr_{1.5}O_4$ sample were substantially more stable against reduction to Mn^{2+} compared to those in Mn_3O_4.

3.3.2 Steam reforming of toluene over the Mn oxide, Cr oxide and Mn-Cr-O spinel oxides

The catalytic performance of the Mn oxide, Cr oxide and Mn-Cr-O spinel catalysts was first evaluated in toluene steam reforming at 873 K, a temperature at which no background steam reforming activity was observed (*i.e.,* no detectable C_1 products). One well-known side reaction that has been reported for toluene steam reforming over metal particles is the hydrogenolysis of toluene to form benzene and methane [24–26]:

$$C_7H_8 + H_2 \rightarrow C_6H_6 + CH_4 \quad \Delta H_r = -42.4 \text{ kJ·mol}^{-1} \tag{3.9}$$

To verify that the observed rate of C_1 production was representative of toluene steam reforming, the formation rate of C_6H_6 under steam reforming conditions at 873 K was quantified over the $MnCr_2O_4$ catalyst, which was approximately 10^{-4} μmol·m^{-2}·s^{-1} and not significantly affected by the partial pressure of C_7H_8, H_2O or H_2 (**Table B1**). Since the typical rate of C_1 production observed during toluene steam reforming (at least initially) was one to two orders-of-magnitude higher, the majority of the C_1 products originated from steam reforming instead of hydrogenolysis. Thus, the steam reforming rate of the catalysts will be reported and compared on a C_1 basis.

Table 3.2 Toluene steam reforming over the Mn oxide, Cr oxide and Mn-Cr-O spinel catalysts

Catalyst	C_7H_8 conversion (%)[a]	C_1 production rate (μmol·m^{-2}·s^{-1})	Product selectivity (%)			
			CO	CO_2	CH_4	H_2
Mn_3O_4[b]	5.3	0.14	3	34	1	63
$Mn_{1.5}Cr_{1.5}O_4$	4.1	0.044	< 1	31	3	65
$MnCr_2O_4$	5.1	0.027	< 1	31	4	65
$Mn_{0.5}Cr_{2.5}O_4$[c]	5.2	0.030	< 1	31	3	65
Cr_2O_3[b]	5.5	0.035	1	27	< 1	71

[a] Conversion based on C_1 product formation. Reaction conditions: 873 K, 2 g catalyst, 100 cm^3·min^{-1} total flow, 1 % C_7H_8, 40 % H_2O, 5 % N_2, balance Ar.
[b] Initial results at t = 0.5 h on stream.
[c] Initial results averaged over t < 2 h on stream.

Although the initial conversion of toluene over the catalysts was similar (4-6 %, **Table 3.2**), only the $Mn_{1.5}Cr_{1.5}O_4$ and $MnCr_2O_4$ catalysts showed steady formation rate of C_1 products up to 7.5 h on stream whereas deactivation occurred over the single oxides and the $Mn_{0.5}Cr_{2.5}O_4$ catalyst to different extents (**Figure 3.1**). As listed in **Table 3.2**, catalysts with excess Mn (Mn_3O_4 and $Mn_{1.5}Cr_{1.5}O_4$) exhibited a higher initial reforming rate than the stoichiometric $MnCr_2O_4$ spinel and catalysts with excess Cr ($Mn_{0.5}Cr_{2.5}O_4$ and Cr_2O_3). The product distribution during toluene steam reforming was similar over all of the catalysts, favoring the production of H_2 and CO_2 as a result of the nearly equilibrated water-gas shift reaction that is concurrent with steam reforming in the

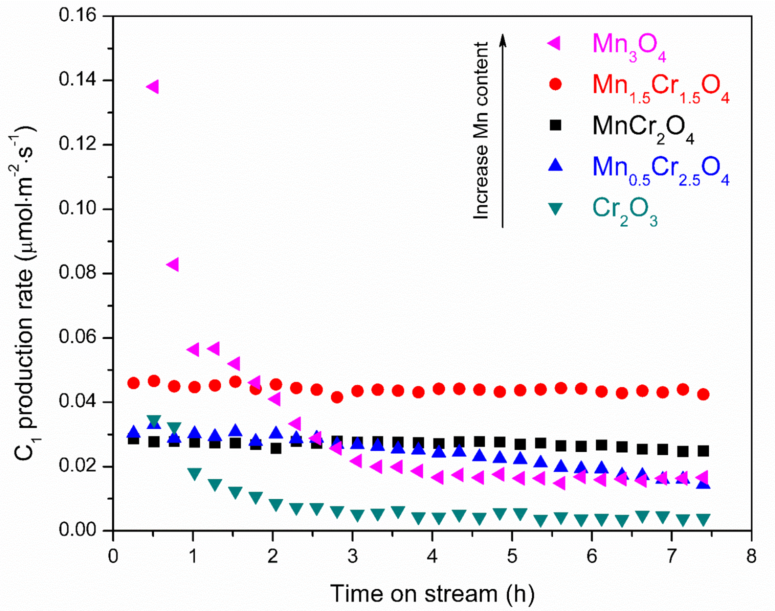

Figure 3.1 Rate of C_1 product formation during toluene steam reforming over the Mn oxide, Cr oxide and Mn-Cr-O spinel catalysts. Reaction conditions: 873 K, 2 g catalyst, 100 $cm^3 \cdot min^{-1}$ total flow, 1 % C_7H_8, 40 % H_2O, 5 % N_2, balance Ar.

presence of excess H_2O. By analogy to our previous work on ethylene steam reforming [21], the highest initial reforming rate observed over the Mn_3O_4 catalyst (0.14 $\mu mol \cdot m^{-2} \cdot s^{-1}$) was likely attributed to the highly active octahedral Mn^{3+} sites, which underwent *in situ* reduction to Mn^{2+} by C_7H_8 and (or) the produced H_2 and rapidly deactivated. As shown in **Figure 3.2a**, the XRD patterns of the spent Mn oxide catalyst revealed a phase transition from Mn_3O_4 to MnO, which is consistent with the reduction of Mn^{3+} to Mn^{2+}. Although this *in situ* reduction was found not to change the surface area of the catalyst appreciably in ethylene steam reforming [21], the Mn oxide catalyst recovered after toluene steam reforming showed an increase in the BET surface area from 1.0 $m^2 \cdot g^{-1}$ to 2.4 $m^2 \cdot g^{-1}$ which might be attributed to deposited carbon (catalyst appeared dark grey instead of green from MnO). Therefore, the deactivation of the Mn_3O_4 catalyst during toluene reforming is likely to result from both reduction of Mn^{3+} to Mn^{2+} and to carbon deposition. While no obvious phase change was detected for the spent Cr_2O_3 (**Figure 3.2a**) and spent Mn-Cr-O spinel catalysts (**Figure 3.2b**) compared to the fresh samples [21], the XRD patterns of the spent Mn-Cr-

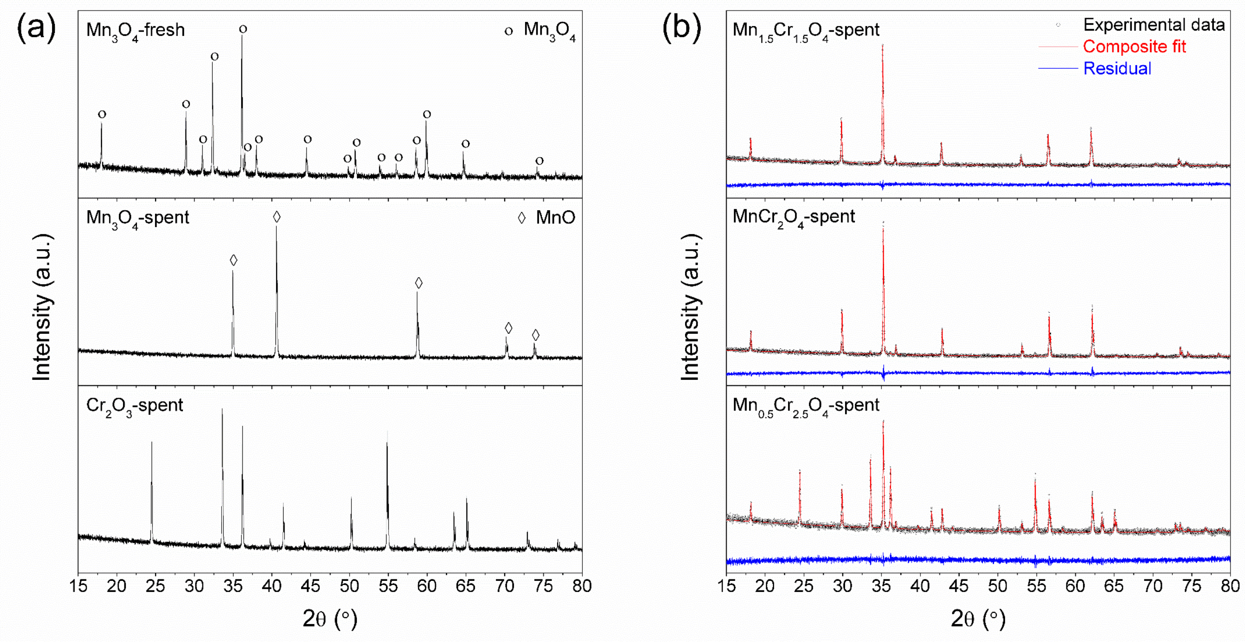

Figure 3.2 X-ray diffraction patterns of (a) the Mn oxide, Cr oxide and (b) Mn-Cr-O spinel catalysts spent in toluene steam reforming. Lattice parameters of the spent Mn-Cr-O spinel catalysts from Rietveld refinement are compared to those of the fresh catalysts in **Table B2**.

O spinel catalysts were refined to investigate any potential change in the composition of the spinel phase, which has been shown to correlate with the spinel lattice constant [27]. Both the spinel lattice constant and atomic Cr/Mn ratio refined for the spent $MnCr_2O_4$ (a = 8.439 Å, Cr/Mn = 2.1) and $Mn_{0.5}Cr_{2.5}O_4$ (a = 8.440 Å, Cr/Mn = 5.7) catalysts were comparable to the respective values from the fresh samples (**Table B2**). The spinel phase in these two samples was assigned to the stoichiometric $MnCr_2O_4$ phase according to the reported lattice constant values in a range of 8.437-8.439 Å [28–30]. The replacement of Cr^{3+} by excess Mn^{3+} in the octahedral sites led to an expansion in the lattice constant of $Mn_{1.5}Cr_{1.5}O_4$ into 8.455-8.458 Å [27,28,31], which was also consistently observed in the spent $Mn_{1.5}Cr_{1.5}O_4$ catalyst (a = 8.459 Å). This comparison suggested the highly active Mn^{3+} sites in $Mn_{1.5}Cr_{1.5}O_4$ were stabilized against reduction to Mn^{2+} and therefore were retained in the spinel lattice during steam reforming, which contrasted the rapid deactivation observed for Mn_3O_4.

Given the stability of both the $MnCr_2O_4$ spinel phase and Cr_2O_3 phase under steam reforming conditions [21], the deactivation observed over the $Mn_{0.5}Cr_{2.5}O_4$ (< 10 % decrease in surface area) and Cr_2O_3 (~ 16 % decrease in surface area) catalyst was likely attributed to coke deposition. In particular, the deactivation of $Mn_{0.5}Cr_{2.5}O_4$ likely resulted from the excess Cr_2O_3 present since the Cr_2O_3 catalyst deactivated much faster compared to the $MnCr_2O_4$ catalyst. Interestingly, the cumulative amount of coke deposited on $Mn_{0.5}Cr_{2.5}O_4$ was very low after 7.5 h on stream (typically < 0.5 wt. %, see **Figure B2** for instance) even for a fully deactivated catalyst. Nevertheless, the estimated coking rate during steam reforming was generally much lower than the initial formation rate of C_1 products and thus did not significantly contribute to the observed product distribution during steam reforming.

3.3.3 Kinetics of toluene steam reforming over the Mn-Cr-O spinel oxides

Kinetics of toluene steam reforming were investigated over the Mn-Cr-O spinel catalysts, which exhibited more stable activity than the single component oxides. As a major product from steam reforming, the effect of H_2 on toluene reforming rate was studied first. As shown in **Figure 3.3a**, the C_1 production rate from toluene steam reforming over the $Mn_{1.5}Cr_{1.5}O_4$ catalyst was significantly inhibited upon the introduction of excess H_2 whereas the production rate recovered to the original value once the excess H_2 was stopped. Such reversible inhibition of the rate by H_2 was also observed over the $MnCr_2O_4$ catalyst (not shown). The reaction order in H_2 was determined over a range of H_2 partial pressures (0.04-0.18 bar) for the Mn-Cr-O spinel catalysts as shown in **Figure 3.3b**. The toluene steam reforming rate was approximately negative first order over the spinel catalysts: $Mn_{1.5}Cr_{1.5}O_4$ (-1.0), $MnCr_2O_4$ (-1.1), and $Mn_{0.5}Cr_{2.5}O_4$ (-1.2). Intriguingly, this observation contrasted the ethylene steam reforming kinetics reported in our previous study whereby excess H_2 (> 0.10 bar) did not affect the rate of ethylene steam reforming over these same spinel catalysts [21].

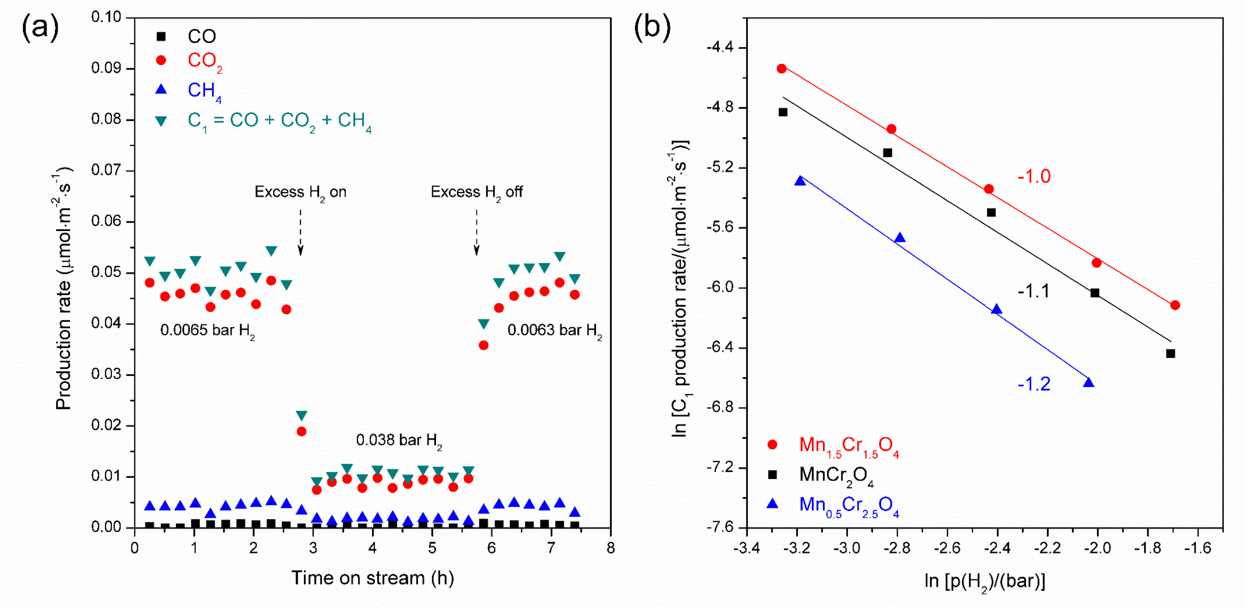

Figure 3.3 (a) Effect of H_2 partial pressure on the formation rate of C_1 products during toluene steam reforming over the $Mn_{1.5}Cr_{1.5}O_4$ catalyst and (b) fitted reaction order in H_2 for toluene steam reforming over the Mn-Cr-O spinel catalysts. Reaction conditions: 873 K, 2 g catalyst, 100 $cm^3 \cdot min^{-1}$ total flow, 1 % C_7H_8, 40 % H_2O, 4-18 % H_2, 5 % N_2, balance Ar.

Given the strong inhibition by H_2, toluene reforming kinetics with respect to other components needed to be evaluated under a relatively constant H_2 partial pressure. As shown in **Table 3.3** and **Figure B3** for runs performed in excess H_2, the conversion of toluene decreased by half when the feed flow rate was doubled from 100 $cm^3 \cdot min^{-1}$ to 200 $cm^3 \cdot min^{-1}$, without affecting the rate or selectivity to C_1 products. Therefore, toluene steam reforming was unaffected by the C_1 reforming products since the partial pressures of all C_1 products (mostly CO_2 and CH_4) were nearly halved in the high flow rate case. Moreover, the potential effects from external heat and mass transfer artifacts on the measured reforming rate were found to be insignificant when the external heat and mass transport were changed explicitly by doubling the flow rate. Further analysis (see

Appendix B2 of the Supplementary Material for details) confirmed the measured reforming rate of toluene was also unaffected by intraparticle heat and mass transfer artifacts.

Table 3.3 Formation of C_1 products at different total flow rates during toluene steam reforming over the Mn-Cr-O spinel catalysts

Catalyst	Total flow ($cm^3 \cdot min^{-1}$)	C_7H_8 conversion (%)[a]	C_1 production rate ($\mu mol \cdot m^{-2} \cdot s^{-1}$)	Carbon selectivity (%)		
				CO	CO_2	CH_4
$Mn_{1.5}Cr_{1.5}O_4$	100	0.8	0.016	3	82	15
	200	0.4	0.015	4	79	17
$MnCr_2O_4$	100	1.4	0.014	3	80	17
	200	0.7	0.014	2	76	22
$Mn_{0.5}Cr_{2.5}O_4$[b]	100	0.9	0.010	4	85	11
	200	0.4	0.010	3	85	12

[a] Conversion based on C_1 product formation. Reaction conditions: 873 K, 2 g catalyst, 2 % C_7H_8, 40 % H_2O, 4 % H_2, 5 % N_2, balance Ar.

[b] Initial results averaged over t < 4 h on stream.

The effect of C_7H_8 partial pressure on the reforming rate was investigated in 0.40 bar H_2O and 0.04 bar of H_2. As shown in **Figure 3.4a**, the initial reforming rate over the $MnCr_2O_4$ catalyst increased substantially with increasing C_7H_8 partial pressure (0.005 to 0.03 bar) while the highest partial pressure of C_7H_8 (0.03 bar) accelerated catalyst deactivation. The fitted reaction order in C_7H_8 (shown in **Figure 3.4b**) over the Mn-Cr-O spinel catalysts ranged from 0.78 to 0.91, indicating a nearly first order dependence of the reforming rate on C_7H_8 partial pressure. Comparatively, increasing the H_2O partial pressure improved the stability of the $MnCr_2O_4$ catalyst but slightly inhibited the toluene reforming rate (**Figure 3.4c**). Consequently, the fitted reaction order in H_2O (-0.26 ~ -0.38) was slightly negative over the Mn-Cr-O spinel catalysts (**Figure 3.4d**) under the tested H_2O partial pressures (0.20-0.50 bar). The first-order dependence in hydrocarbon and slight inhibition by H_2O observed in toluene steam reforming are consistent with ethylene reforming kinetics reported previously by us, where the inhibitive effect of H_2O was explained by a higher strength of H_2O adsorption on the spinel oxide surface compared to the hydrocarbon [21].

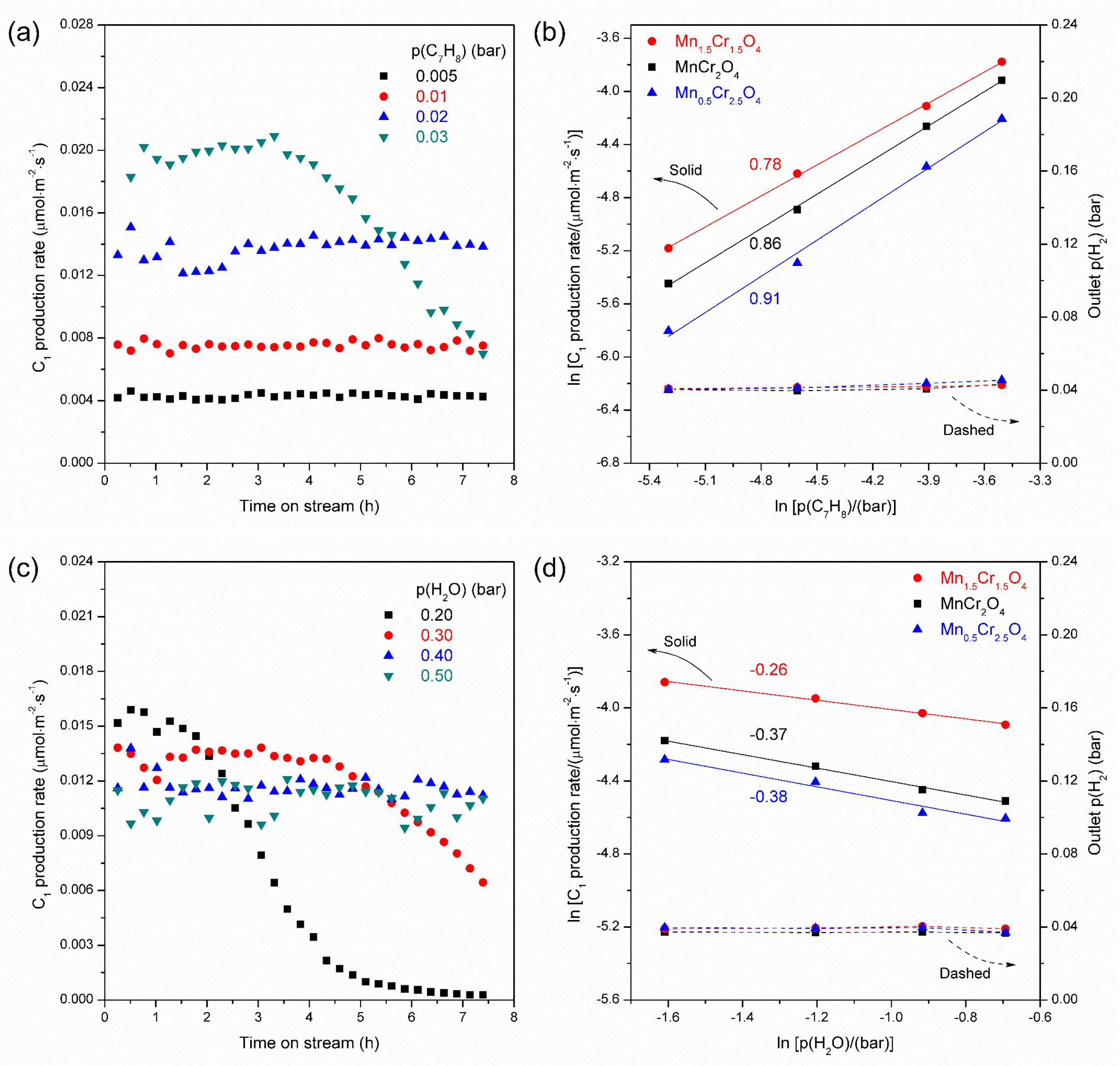

Figure 3.4 Effect of (a) C_7H_8 and (c) H_2O partial pressure on the formation rate of C_1 products during toluene steam reforming over the $MnCr_2O_4$ catalyst and fitted reaction order in (b) C_7H_8 and (d) H_2O for toluene steam reforming over the Mn-Cr-O spinel catalysts. Reaction conditions: 873 K, 2 g catalyst, 100 $cm^3 \cdot min^{-1}$ total flow, (ab) 0.5-3 % C_7H_8, 40 % H_2O, 4 % H_2, 5 % N_2, balance Ar; (cd) 2 % C_7H_8, 20-50 % H_2O, 4 % H_2, 5 % N_2, balance Ar.

Interestingly, the inhibitive effect of H_2O was less prominent (*i.e.*, less than 10 % change in toluene reforming rate when varying p(H_2O) in the same range) over all three spinel catalysts in the absence of excess H_2 (**Figure B4**). The nearly constant reforming rate resulted in similar downstream partial pressures of H_2 even if the H_2O partial pressure varied significantly. This phenomenon was likely attributed to a stronger adsorption of H_2O in excess H_2 where the spinel oxide surface was partially reduced to form more O vacancies that had been shown to bind H_2O more strongly in previous DFT studies [32–35].

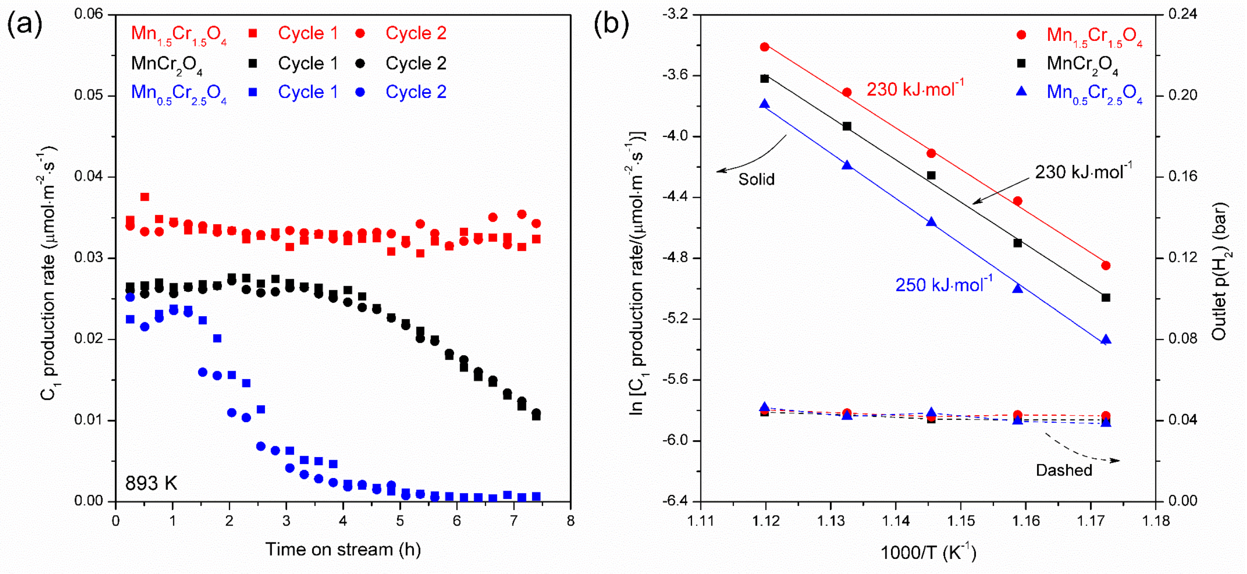

Figure 3.5 (a) Effect of catalyst re-oxidation on the formation rate of C_1 products during toluene steam reforming at 893 K and (b) fitted apparent activation energy for toluene steam reforming over the Mn-Cr-O spinel catalysts. Reaction conditions: (a) 893 K; (b) 853-893 K, 2 g catalyst, 100 cm^3·min^{-1} total flow, 2 % C_7H_8, 40 % H_2O, 4 % H_2, 5 % N_2, balance Ar. Catalyst spent after cycle 1 was re-oxidized in 100 cm^3·min^{-1} air flow at 873 K for 6 h before tested in cycle 2.

Due to rapid catalyst deactivation at elevated temperatures, the apparent activation energy of toluene steam reforming could not be assessed by changing reaction temperature continuously on stream. Fortunately, a deactivated catalyst could be easily regenerated by re-oxidation in air to remove the deposited carbon. As shown in **Figure 3.5a**, initial rate of toluene reforming over all three Mn-Cr-O spinel catalysts was regenerated via re-oxidation at 873 K even after being tested at the highest reaction temperature of 893 K where the catalyst was most prone to deactivation (see **Figure B5** for the trend over $MnCr_2O_4$). In addition, the oxidative regeneration did not affect the surface area of the catalyst appreciably (*i.e.*, less than 10 %). The results in **Figure 3.5a** also demonstrated that both the reforming rate and stability of the spinel catalyst increased with increasing Mn content. Using this reaction-regeneration strategy, the reforming rate of the Mn-Cr-O spinel catalysts was evaluated in a temperature range from 853 to 893 K, with the apparent activation energy fitted from the Arrhenius-type plot shown in **Figure 3.5b**. The apparent activation energy for toluene steam reforming over the three spinel catalysts was similar (230-250 $kJ\cdot mol^{-1}$), all of which were substantially higher than the respective values for ethylene steam reforming (130-190 $kJ\cdot mol^{-1}$) [21]. This difference in the apparent activation energy is likely associated with the strong inhibition of toluene reforming by H_2 and will be discussed in more detail in section 3.3.6.

3.3.4 Kinetics of propylene and benzene steam reforming over the $MnCr_2O_4$ and $Mn_{1.5}Cr_{1.5}O_4$ catalysts

To understand the influence of molecular features on the reforming behavior of the hydrocarbon, steam reforming kinetics of propylene and benzene were also examined. Along with our previous studies on ethylene steam reforming [21] and the aforementioned results on toluene steam reforming, these results will enable a comparison of reforming kinetics between olefins and aromatics as well as in the absence and presence of a side chain methyl group on the unsaturated carbon. Under the tested conditions, propylene steam reforming over the catalysts did not produce any detectable C_2 hydrocarbons. As listed in **Table 3.4**, despite a much higher initial reforming rate (averaged across the catalyst bed) compared to the spinel catalysts, the Cr_2O_3 catalyst deactivated continuously on stream even in the presence of excess H_2 (**Figure B6**), which was likely the result of coke deposition as we reported previously for ethylene steam reforming [21]. Even at a higher H_2O/C ratio, the Cr_2O_3 catalyst deactivated more rapidly in propylene reforming ($H_2O/C = 2.7$) than in ethylene reforming ($H_2O/C = 1.0$) [21], which was in agreement with a reported higher gas-phase coking tendency of propylene than ethylene [36]. The higher initial steam reforming rate of both ethylene [21] and propylene over Cr_2O_3 than the $MnCr_2O_4$ spinel is possibly attributed to a higher density of cationic Cr sites that have been reported to be responsible for olefin activation in olefin polymerization studies [37,38].

Table 3.4 Propylene steam reforming over the Cr oxide and Mn-Cr-O spinel catalysts

Catalyst	C_3H_6 conversion (%)[a]	C_1 production rate ($\mu mol \cdot m^{-2} \cdot s^{-1}$)	Product selectivity (%)			
			CO	CO_2	CH_4	H_2
$Mn_{1.5}Cr_{1.5}O_4$	1.5	0.037	< 1	25	6	69
$MnCr_2O_4$	3.9	0.042	< 1	26	12	61
Cr_2O_3[b]	15	0.23	1	26	25	48

[a] Conversion based on C_1 product formation. Reaction conditions: 873 K, 2 g catalyst, 100 $cm^3 \cdot min^{-1}$ total flow, 5 % C_3H_6, 40 % H_2O, 5 % N_2, balance Ar.

[b] Initial results averaged over t < 1.5 h on stream, reforming rate listed was an average across the catalyst bed estimated from global C_3H_6 conversion.

As summarized in **Figure 3.6**, propylene steam reforming kinetics were investigated over two of the spinel catalysts ($MnCr_2O_4$ and $Mn_{1.5}Cr_{1.5}O_4$). The propylene reforming rate over both catalysts, as shown in **Figure 3.6a**, was inhibited by a low pressure of H_2 (0.04 bar) whereas further increasing the H_2 partial pressure did not affect the rate significantly. The inhibition of the rate by H_2 was reversible (**Figure B7a**) and the reaction order in H_2 fitted for both the $MnCr_2O_4$ (-0.16) and $Mn_{1.5}Cr_{1.5}O_4$ (-0.12) catalysts approached zero as the H_2 partial pressure increased (**Figure B7b**). Under a controlled H_2 partial pressure of 0.18 bar, propylene steam reforming exhibited a nearly first-order dependence on C_3H_6 partial pressure (1.1 for $MnCr_2O_4$ and 0.84 for $Mn_{1.5}Cr_{1.5}O_4$, **Figure 3.6b**) and was slightly inhibited by H_2O (-0.37 for $MnCr_2O_4$ and -0.23 for $Mn_{1.5}Cr_{1.5}O_4$, **Figure 3.6c**) over both spinel catalysts. Although both catalysts remained stable during propylene steam reforming in excess H_2 at 893 K, the apparent activation energy for propylene reforming in 853-893 K (130 $kJ \cdot mol^{-1}$ for $MnCr_2O_4$ and 170 $kJ \cdot mol^{-1}$ for $Mn_{1.5}Cr_{1.5}O_4$, **Figure 3.6d**) was still measured by the reaction-regeneration strategy applied in toluene reforming to prevent any artifacts from the deposited carbon species. The re-oxidation treatment did not affect

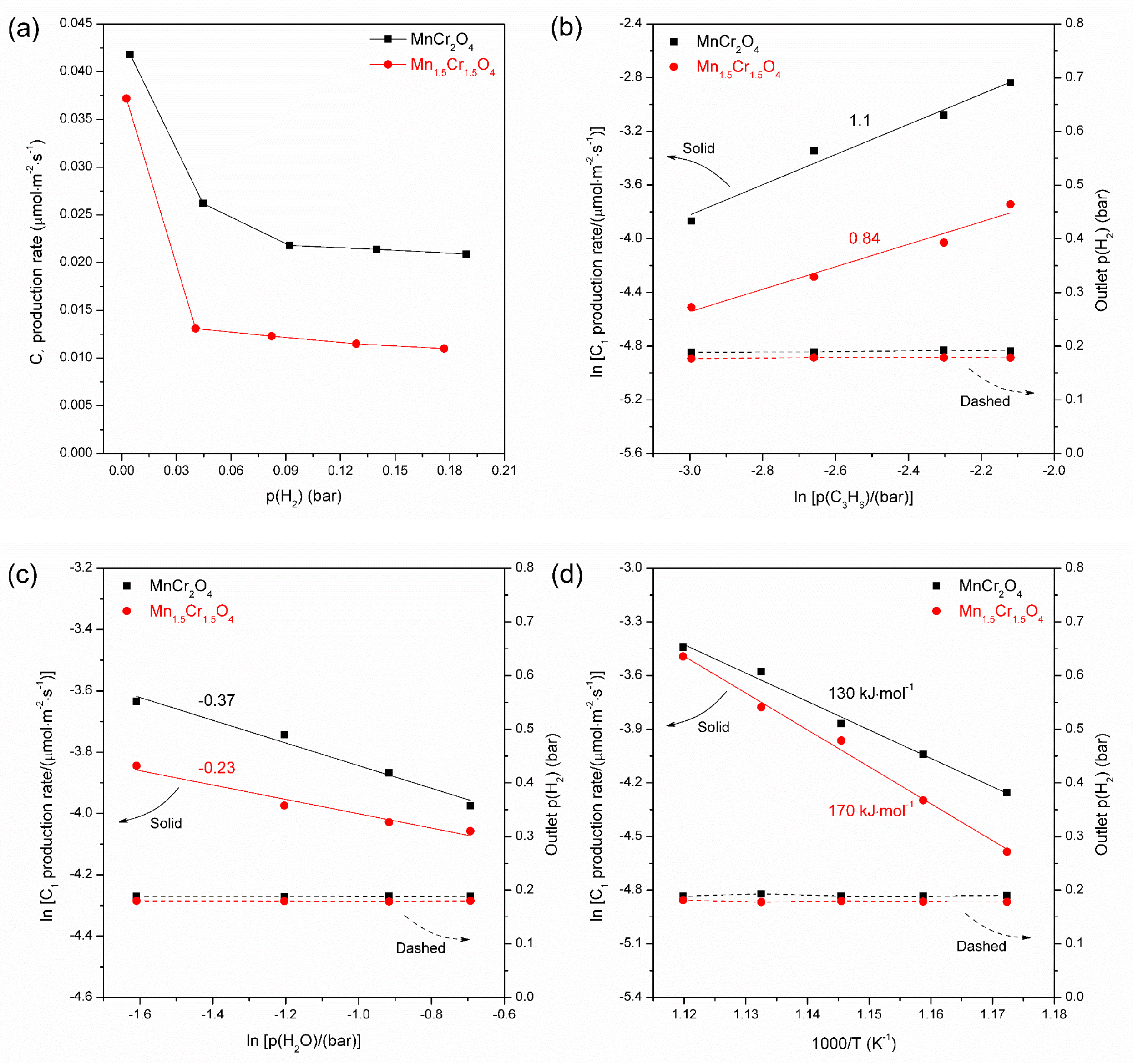

Figure 3.6 Effect of (a) H_2, (b) C_3H_6 and (c) H_2O partial pressure and (d) reaction temperature on the formation rate of C_1 products during propylene steam reforming over the Mn-Cr-O spinel catalysts. Reaction conditions: (a,b,c) 873 K; (d) 853-893 K, 2 g catalyst, 100 cm^3·min^{-1} total flow. Detailed feed composition used for propylene steam reforming is listed in **Table B3**. Catalyst was re-oxidized in 100 cm^3·min^{-1} air flow at 873 K for 6 h in between reactions.

the reforming rate over both catalysts (**Figure B8**), which suggested severe collapse of catalyst surface area did not occur under the tested temperature range. As listed in **Table 3.6**, the kinetics of propylene reforming over both $Mn_{1.5}Cr_{1.5}O_4$ and $MnCr_2O_4$, including reaction orders and apparent activation energy, were quite similar to the respective kinetics of ethylene reforming reported in our previous work [21], except that the side methyl group introduced a slightly stronger inhibition of H_2 at low partial pressure in propylene steam reforming. It is worth noting that the C_3H_6 partial pressure in the reforming results over $Mn_{1.5}Cr_{1.5}O_4$ shown in **Figure 3.6c** and **Figure 3.6d** was adjusted from 0.05 bar to 0.10 bar (see **Table B3** for details) to enhance quantification accuracy of the products by increasing the reforming rate. Thus, the relative activity of the two catalysts should not be directly compared in these two figures.

Table 3.5 Benzene steam reforming over the Cr oxide and Mn-Cr-O spinel catalysts

Catalyst	C_6H_6 conversion (%)[a]	C_1 production rate ($\mu mol \cdot m^{-2} \cdot s^{-1}$)	Product selectivity (%)			
			CO	CO_2	CH_4	H_2
$Mn_{1.5}Cr_{1.5}O_4$	0.7	0.033	< 1	30	8	62
$MnCr_2O_4$	0.7	0.014	< 1	30	7	63
Cr_2O_3	0.5	0.016	< 1	30	3	68

[a] Conversion based on C_1 product formation. Reaction conditions: 873 K, 2 g catalyst, 100 $cm^3 \cdot min^{-1}$ total flow, 5 % C_6H_6, 40 % H_2O, 5 % N_2, balance Ar.

The Cr_2O_3 catalyst and the two spinel catalysts were then tested for benzene steam reforming under similar conditions, where no hydrogenation activity to cyclohexane was detected in the presence of excess H_2. In the absence of excess H_2, the benzene reforming rate over Cr_2O_3 and $MnCr_2O_4$ was similar, both of which were significantly less active compared to $Mn_{1.5}Cr_{1.5}O_4$ (**Table 3.5**). These trends were consistent with the observations for toluene steam reforming shown in **Figure 3.1**, suggesting the Mn^{3+} sites to be more active for the activation of aromatics. However, severe deactivation over Cr_2O_3 observed in toluene steam reforming ($H_2O/C = 5.7$) did not occur in the benzene case (**Figure B9**) even under an elevated C_6H_6 partial pressure of 0.05 bar ($H_2O/C = 1.3$), which was in agreement with a lower gas-phase coking tendency of benzene compared to toluene likely due to the high stability of the aromatic C-H bond [39].

The reforming kinetics of benzene over the two spinel catalysts were evaluated to be quite similar (**Figure 3.7**). As a result, the high activity of Mn^{3+} sites for benzene steam reforming was

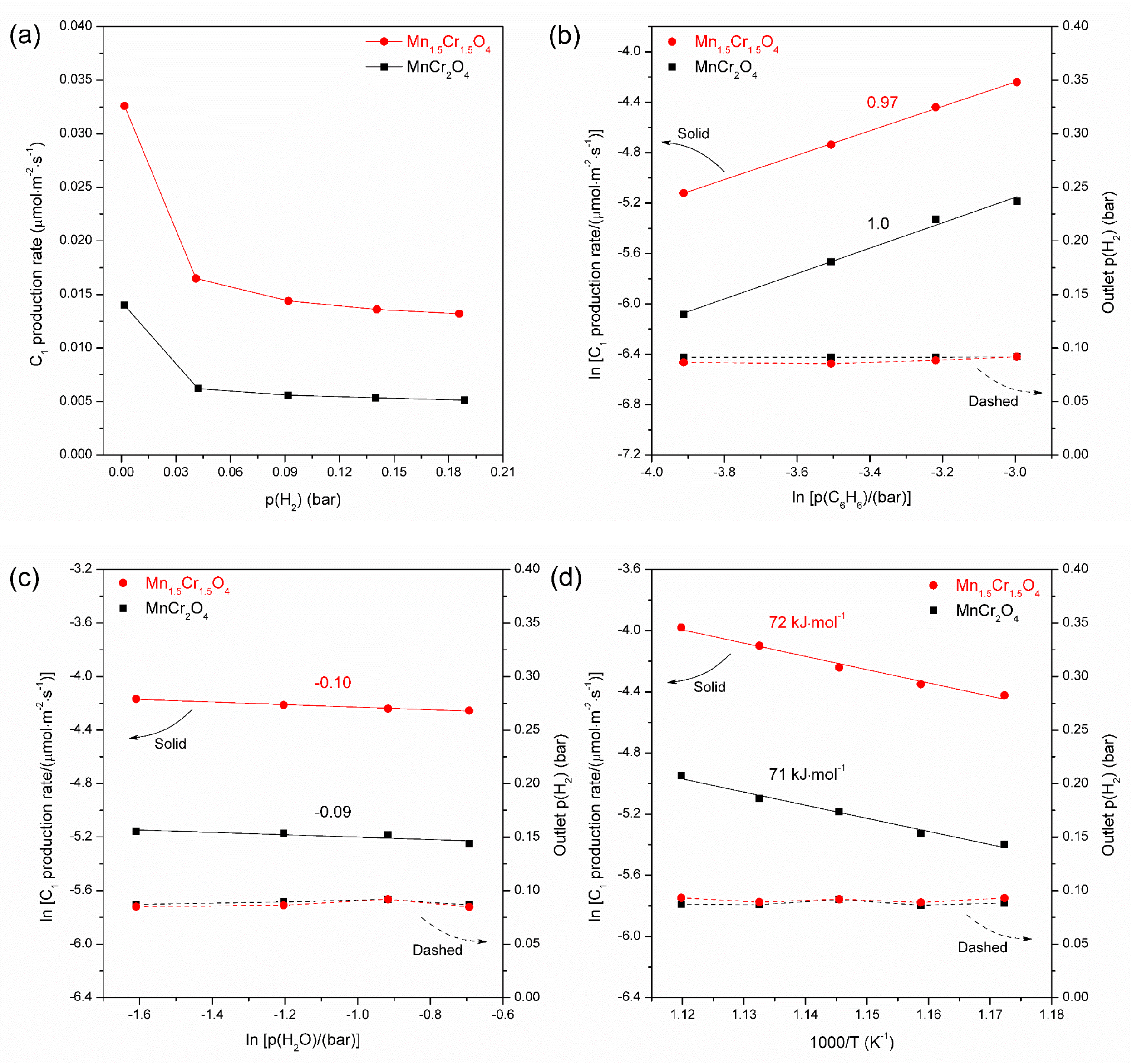

Figure 3.7 Effect of (a) H_2, (b) C_6H_6 and (c) H_2O partial pressure and (d) reaction temperature on the formation rate of C_1 products during benzene steam reforming over the Mn-Cr-O spinel catalysts. Reaction conditions: (a,b,c) 873 K; (d) 853-893 K, 2 g catalyst, 100 $cm^3 \cdot min^{-1}$ total flow. Detailed feed composition used for benzene steam reforming is listed in **Table B4**. Catalyst was re-oxidized in 100 $cm^3 \cdot min^{-1}$ air flow at 873 K for 6 h in between reactions.

clearly demonstrated by the consistently higher reforming rate of $Mn_{1.5}Cr_{1.5}O_4$ than $MnCr_2O_4$ regardless of the change in partial pressure of H_2, C_6H_6 and H_2O or reaction temperature. As shown in **Figure 3.7a**, reforming rate over both catalysts was inhibited by about 50-60 % upon the introduction of 0.04 bar excess H_2 while further increase in H_2 partial pressure only showed a minor effect on the reforming rate. Such reversible inhibition by H_2 at low partial pressure (**Figure B10a**) followed by an asymptotic H_2 order close to zero (-0.15 for $Mn_{1.5}Cr_{1.5}O_4$ and -0.13 for $MnCr_2O_4$, **Figure B10b**) observed in benzene steam reforming resembled the reforming behavior of olefins (ethylene and propylene), instead of toluene where the reforming rate was consistently negative first order in H_2. The contrast in H_2 reaction order between toluene and benzene steam reforming emphasizes the particular importance of the methyl group in the activation of aromatics compared to olefins (*i.e.*, C_3H_6 versus C_2H_4). Under a constant H_2 partial pressure of 0.09 bar, while benzene steam reforming also showed an expected first order dependence on C_6H_6 partial pressure (0.97 for $Mn_{1.5}Cr_{1.5}O_4$ and 1.0 for $MnCr_2O_4$, **Figure 3.7b**), the effect of H_2O was found to be minor with a reaction order close to zero (-0.10 for $Mn_{1.5}Cr_{1.5}O_4$ and -0.09 for $MnCr_2O_4$, **Figure 3.7c**). Applying the same reaction-regeneration strategy where catalyst re-oxidation did not affect the benzene reforming rate (**Figure B11**), the apparent activation energy for benzene reforming over both spinel catalysts (72 $kJ \cdot mol^{-1}$ for $Mn_{1.5}Cr_{1.5}O_4$ and 71 $kJ \cdot mol^{-1}$ for $MnCr_2O_4$, **Figure 3.7d**) was surprisingly lower compared to all other three hydrocarbons tested.

3.3.5 DRIFTS of adsorbed toluene and benzene

In an effort to explore the origin of the difference in reforming kinetics associated with toluene (~ -1 order in excess H_2) and benzene (~ 0 order in excess H_2), we examined the DRIFTS spectrum of the aromatics on a $Mn_{1.5}Cr_{1.5}O_4$ spinel catalyst as a function of gas treatment (He or H_2). As shown in **Figure 3.8a**, the intensity of DRIFTS bands increased by more than one order-of-magnitude when the catalyst was exposed to toluene in He compared to the exposure in H_2. The observed features in He were in good agreement with those reported for catalytic oxidation of toluene over metal oxides: The band at 1593 cm^{-1} was assigned to skeleton vibration of the aromatic ring, whereas the bands at 1540 cm^{-1} and 1405 cm^{-1} were assigned respectively to asymmetric and symmetric COO vibration of the carboxyl group [40–42]. These features were also consistent with those observed in the adsorption of benzoic acid over Mn_3O_4 [43], suggesting that even in the absence of O_2, the side methyl group of toluene could be oxidized by the spinel surface to form benzoate species, which has been proposed as an intermediate during total oxidation of toluene [44]. As the IR bands were associated with the oxidation of toluene to benzoate, the low absorbance intensity in H_2 indicated this process was substantially inhibited, which is consistent with toluene steam reforming rate being severely inhibited by excess H_2. Intriguingly, although the DRIFTS features were different in 97 % H_2 and He in the case of benzene, the band intensity did not change significantly with respect to H_2 partial pressure (**Figure 3.8b**). In 97 % H_2, the only band at 1432 cm^{-1} was likely attributed to ring vibration without any characteristics of carboxylate formation [41,42]. The bands observed in He for benzene adsorption at 1589 cm^{-1}, 1540 cm^{-1} and 1406 cm^{-1} were similar to those observed for toluene adsorption in He and may have originated from trace toluene impurity in the benzene reagent. Nevertheless, they were still assigned to ring vibration, asymmetric and symmetric COO vibration of the carboxyl group correspondingly, which were in accordance with previous reports on catalytic benzene oxidation over metal oxides [42,45,46]. The broad shoulder at 1333 cm^{-1} was speculated to contain both the contribution from olefin rocking vibration of maleate species (~ 1310 cm^{-1} [40,47]) and CH_3 stretching vibration of acetate species (~ 1360 cm^{-1} [45,46,48]), which were the proposed ring-opening products during benzene total oxidation [47]. This shoulder was not detected in the toluene adsorption experiments, suggesting the activation of toluene selectively occurred on the reactive side chain before any ring-opening process. It was worth noticing that the absorbance intensity in He for benzene adsorption was significantly lower than that for toluene adsorption (see the scale bars in **Figure 3.8**) even though we used a higher gas-phase concentration of benzene.

This observation suggests that in the absence of excess H_2, toluene was much more reactive than benzene toward oxidation, which is consistent with both the higher reactivity of the benzyl C-H bond than the aromatic C-H bond [42,49] and the higher steam reforming rate of toluene even at a lower partial pressure (**Table 3.2** and **Table 3.5**). Although distinct features from carboxylates only appeared in He for both aromatics, the sharp contrast in absorbance intensity of the bands for toluene adsorption suggests that inhibition of the side chain oxidation of toluene was likely responsible for the -1 reaction order in H_2 observed during toluene steam reforming.

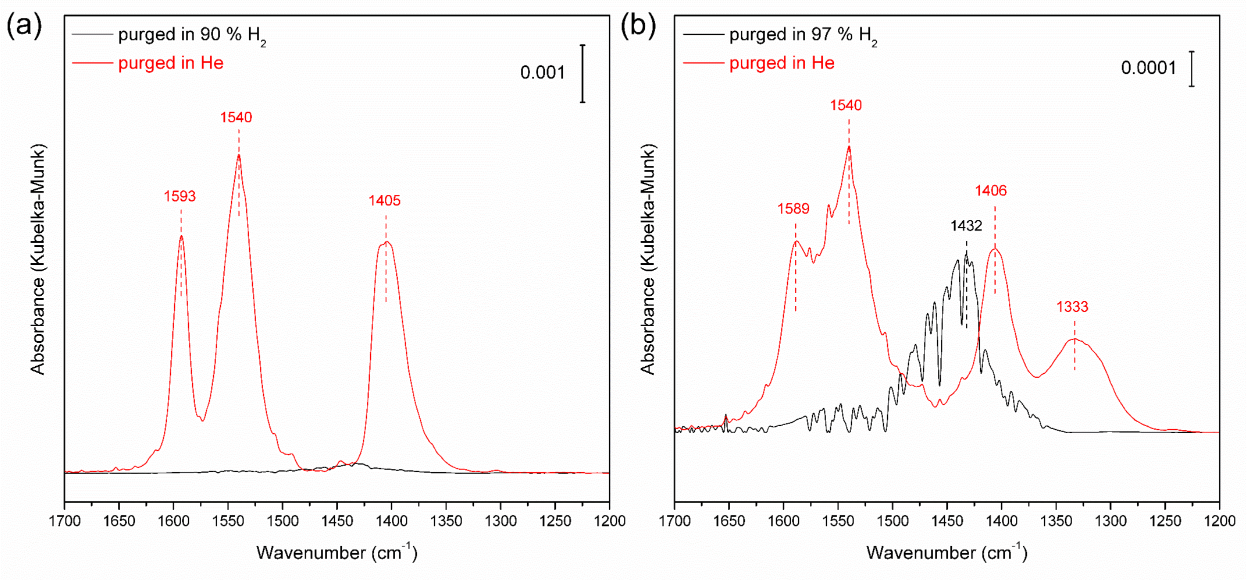

Figure 3.8 *In situ* DRIFTS spectra of aromatic adsorption over the $Mn_{1.5}Cr_{1.5}O_4$ catalyst upon sequential exposure of (a) 0.1 % C_7H_8 in 90 % H_2 followed by 0.1 % C_7H_8 in He at 573 K; (b) 0.4 % C_6H_6 in 97 % H_2 followed by 0.4 % C_6H_6 in He at 573 K.

3.3.6 Mechanistic interpretation of reaction kinetics

As summarized in **Table 3.6**, along with our previous studies on ethylene steam reforming [21], the reforming kinetics of each hydrocarbon were not significantly affected by the catalyst composition, $Mn_{1.5}Cr_{1.5}O_4$ and $MnCr_2O_4$. While the reforming rate was nearly first order in the partial pressure of hydrocarbon for all tested hydrocarbons, only toluene reforming exhibited a consistently strong inhibition by excess H_2 and an associated high apparent activation energy.

Table 3.6 Summary of steam reforming kinetics of olefins and aromatics over the Mn-Cr-O spinel catalysts

Catalyst	Hydrocarbon	Reaction order			E_{app} ($kJ \cdot mol^{-1}$)
		H_2	C_xH_y	H_2O	
$Mn_{1.5}Cr_{1.5}O_4$	C_2H_4[a]	-0.05[b]	0.93	-0.40	150
	C_3H_6	-0.12	0.84	-0.23	170
	C_6H_6	-0.15	0.97	-0.10	72
	C_7H_8	-1.0	0.78	-0.26	230
$MnCr_2O_4$	C_2H_4[a]	0.03	0.91	-0.21	130
	C_3H_6	-0.16	1.1	-0.37	130
	C_6H_6	-0.13	1.0	-0.09	71
	C_7H_8	-1.1	0.86	-0.37	230

[a] Adapted from our previous work in Ref. [21].

[b] Valid when $p(H_2)$ is at least 0.1 bar.

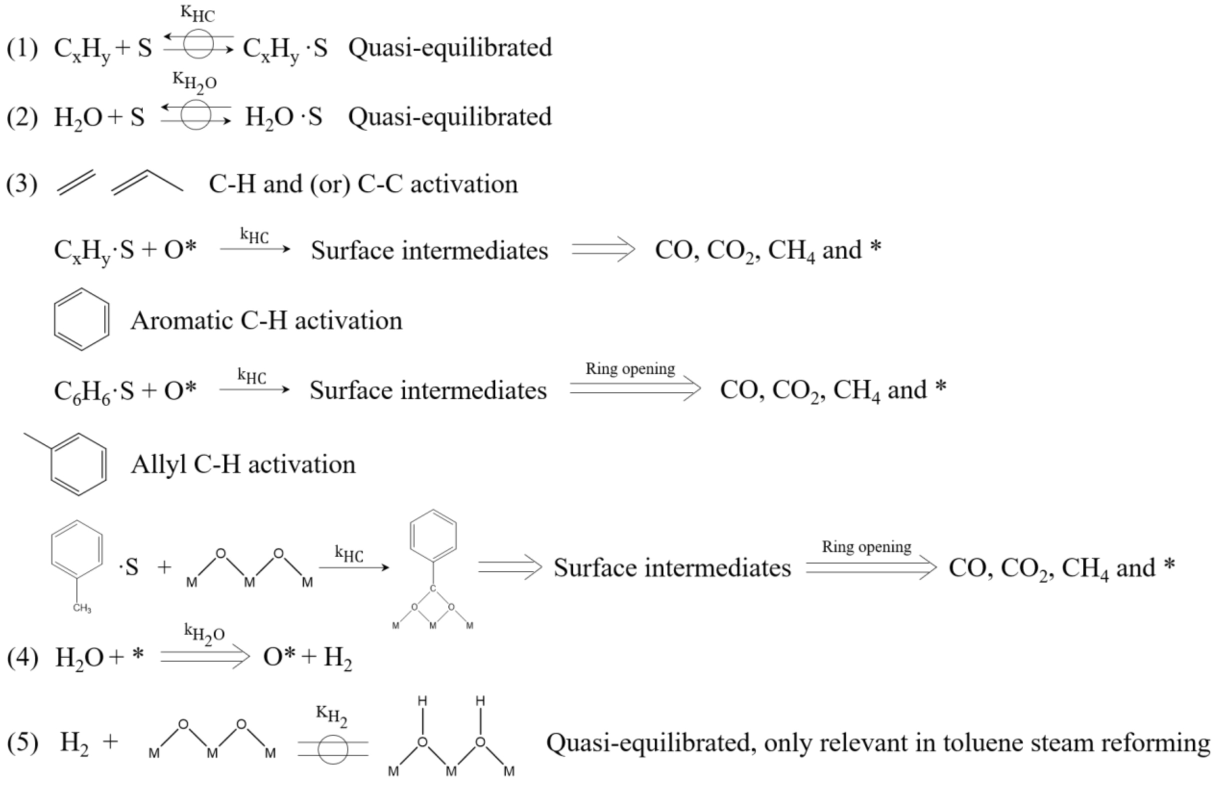

Scheme 3.1 A two-site Mars-van Krevelen mechanism proposed for olefins and aromatics steam reforming over the Mn-Cr-O spinel catalysts.

Steam reforming of benzene, on the other hand, showed the lowest apparent activation energy and was nearly unaffected by H_2O partial pressure, which was slightly inhibitive on the reforming rate of other three hydrocarbons. As proposed in our previous work [21], we have suggested a two-site Mars-van Krevelen type mechanism for hydrocarbon steam reforming over the Mn-Cr-O spinel oxides as depicted in **Scheme 3.1,** but we have expanded our mechanism to account for the inhibition of toluene reforming by H_2. In all cases it is assumed that the adsorption of the hydrocarbon (step 1) and H_2O (step 2) is competitive and quasi-equilibrated. The adsorbed hydrocarbon is oxidized by the lattice oxygen O* (step 3) from the spinel surface, where the created vacancies are regenerated by H_2O (step 4). To simplify the mathematical derivations, we hypothesize that the overall reforming rate is determined only by the initial activation of the hydrocarbon by the lattice oxygen whereas subsequent steps are kinetically irrelevant. For propylene and benzene, assuming the density of vacancies are negligible compared to the available lattice oxygen ([O*] >> [*]) under reaction conditions, the reforming rate in C_1 product formation can be described (following the derivation for ethylene reforming [21]):

$$r_3 = -\frac{d[C_xH_y]}{dt} = \frac{k_{HC}K_{C_xH_y}[C_xH_y][S]_0[*]_0}{1 + K_{C_xH_y}[C_xH_y] + K_{H_2O}[H_2O]} \sim k'_{HC}(K_{C_xH_y}[C_xH_y])^{\alpha}(K_{H_2O}[H_2O])^{\beta} \qquad (3.10)$$

Given the similarity in reforming kinetics of the two olefins, this rate expression is naturally consistent with the results on propylene steam reforming in excess H_2 where the effect of H_2 was minor. The apparent activation energy is correlated with the respective reaction order and heat of adsorption of the hydrocarbon and H_2O:

$$E_{app} = E_a + \alpha\Delta H_{ads}(C_xH_y) + \beta\Delta H_{ads}(H_2O) \qquad (3.11)$$

With $\alpha \sim 1$ for all hydrocarbons and assuming $\Delta H_{ads}(H_2O)$ remains nearly constant, eqn. (11) suggests the low apparent activation energy of benzene reforming may be attributed to a stronger adsorption of benzene than the olefins on the spinel surface (*i.e.*, more negative $\Delta H_{ads}(C_xH_y)$) and an associatively less intense inhibition of H_2O (*i.e.,* less negative β). The adsorption energy of H_2O

on metal oxides (non-defect sites) varies with coverage and surface configuration, but generally in a range of about 100-180 kJ·mol^{-1} based on DFT calculations [33,50–54]. Therefore, comparing the values of β for benzene (~ -0.1) to those of other hydrocarbons (-0.2 ~ -0.4), the low reaction order in H_2O can cause the apparent activation energy of benzene reforming to decrease by roughly 10-60 kJ·mol^{-1}. It is also worth noticing that the apparent activation energy was fitted from the reforming rate on a basis of C_1 product formation, which assumed that the interconversion between CO, CO_2 and CH_4 occurred after the decomposition of the hydrocarbon. In such a scenario, the selectivity of the C_1 products was likely determined by the thermodynamics of the water-gas shift and methanation reactions and remained nearly constant over a small temperature change (± 20 K from 873 K). We therefore expect the activation energy determined from individual C_1 reforming products to be consistent and comparable to that from the overall formation of C_1 products. However, as shown in **Figure B12** and **Figure B13**, this expectation was only validated for steam reforming of olefins whereas the activation energy fitted from CO_2 and CH_4 (selectivity of CO was no more than 6 % and thus omitted) was substantially different for the aromatics. This comparison suggests the low apparent activation energy of benzene reforming over both spinel catalysts (~ 70 kJ·mol^{-1}) results from a low sensitivity of CH_4 formation to temperature change (< 30 kJ·mol^{-1}), whereas the activation energy fitted from CO_2 (~ 110 kJ·mol^{-1}) is only slightly lower than those of olefin reforming (which can be explained by the differences in H_2O order). Based on the results from DRIFTS (**Figure 3.8b**), we speculate that this observation is potentially associated with reactions of ring-opening intermediates that directly produce CH_4 (*e.g.*, decomposition of acetic acid: $CH_3COOH \rightarrow CH_4 + CO_2$).

The reforming rate of toluene is proposed to be determined by the side chain oxidation of adsorbed toluene to benzoate intermediates, as supported by the DRIFTS results in **Figure 3.8a**.

In particular, we propose this oxidation requires an adjacent pair of lattice oxygen atoms for carboxylate formation, which can be inhibited via reduction of the spinel surface by H_2 to form OH groups (**Scheme 3.1,** step (5)). Although such reduction, also known as homolytic dissociation of H_2 over metal oxides ($H_2 + 2O^* \rightarrow 2O^*\text{-}H$), is thermodynamically favored, previous studies have shown that the initial dissociation of H_2 likely undergoes the kinetically favored heterolytic pathway ($H_2 + M\text{-}O^* \rightarrow M\text{-}H + O^*\text{-}H$) that has a lower activation energy [55,56]. Thus, the dissociation of H_2 over the spinel surface hereby during high-temperature steam reforming is proposed to be quasi-equilibrated, but not necessarily elementary. In the presence of excess H_2, assuming the vast majority of the pair oxygen sites are converted to OH groups as well as a negligible density of vacancies, the reforming rate of toluene and the associated apparent activation energy can be expressed as (see **Appendix B3** of the Supplementary Material for a detailed derivation):

$$r_3 = \frac{k_{C_7H_8}K_{C_7H_8}[C_7H_8][S]_0[*\,*]_0}{K_{H_2}[H_2](1 + K_{C_7H_8}[C_7H_8] + K_{H_2O}[H_2O])} \sim k'_{C_7H_8}(K_{C_7H_8}[C_7H_8])^{\alpha}(K_{H_2O}[H_2O])^{\beta}(K_{H_2}[H_2])^{\gamma} \tag{3.12}$$

$$E_{app} = E_a + \alpha\Delta H_{ads}(C_xH_y) + \beta\Delta H_{ads}(H_2O) + \gamma\Delta H_{diss}(H_2) \tag{3.13}$$

The experimentally-observed strong inhibition by H_2 on the toluene reforming rate ($\gamma \sim -1$) results from the homolytic dissociation of H_2 that impedes the selective activation of toluene on the side methyl group. Moreover, the dissociative adsorption energy of H_2 in a homolytic pattern (*i.e.*, -$\Delta H_{diss}(H_2)$) was reported in the range of 50-190 $kJ\cdot mol^{-1}$ over a series of metal oxide surfaces [55,57–60], which gives rise to the increase in apparent activation energy of toluene reforming compared to olefin reforming where the reaction orders in hydrocarbon and H_2O are similar (**Table 3.6**).

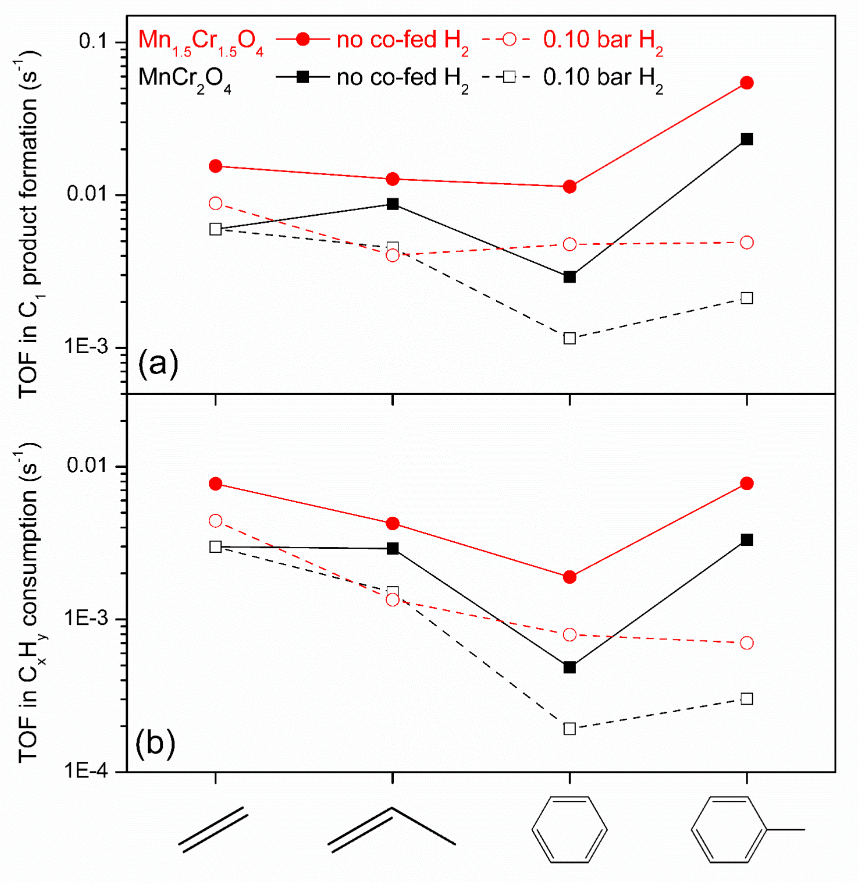

Figure 3.9 Turnover frequency of steam reforming over the Mn-Cr-O spinel catalysts estimated from H_2O adsorption capacity and calculated with respect to (a) C_1 product formation rate and (b) C_xH_y consumption rate. Reforming rates were measured or extrapolated using kinetic results to the following conditions: 873 K, 5 % C_xH_y, 40 % H_2O, 0 or 10 % H_2. Results on ethylene steam reforming and monolayer capacity of H_2O adsorption measured for the catalysts were adapted from our previous work in ref. [21].

The turnover frequency (TOF) of olefins and aromatics steam reforming over the Mn-Cr-O spinel catalysts was estimated from further normalizing the reforming rate per surface area by the active site density on the spinel oxide surface. Since the hydrocarbon is proposed to adsorb competitively with H_2O on site S (likely a metal cation site), we used H_2O as a probe molecule for measuring the site density of S, which interacts stronger with the site than the hydrocarbon as evident from the slightly negative reaction order in H_2O. The active site density estimated by extrapolating the monolayer H_2O coverage from the linear region of the isotherm above saturation coverage to zero partial pressure of H_2O [21] is listed in **Table 3.1**. Using the measured kinetics of the reforming reactions, we arbitrarily chose to compare rates at 0.05 bar hydrocarbon partial pressure and 0.40 bar H_2O partial pressure and extrapolated the reforming rate to this condition as a function of H_2 partial pressure. In the absence of excess H_2, the TOF based on C_1 product formation of different hydrocarbons was comparable (**Figure 3.9a**) while the TOF with respect to hydrocarbon consumption discriminated benzene to be less reactive than others (**Figure 3.9b**) due to the stable aromatic C-H bonds. Under a H_2 partial pressure of 0.10 bar, the reforming rate of all hydrocarbons was inhibited except for C_2H_4 reforming over $MnCr_2O_4$. Not surprisingly, the TOF of toluene reforming decreased the most compared to other hydrocarbons as a result of being negative first order in H_2. The strong inhibition by excess H_2 and an associated high apparent activation energy for toluene steam reforming mimics the behavior of steam gasification of coke reported in our previous work over the same group of compounds [17], suggesting toluene is a reasonable coke-surrogate molecule possibly due to a combination of aliphatic and aromatic features. The highest activity of the Mn-rich $Mn_{1.5}Cr_{1.5}O_4$ spinel for toluene steam reforming is consistent with the high rate of coke gasification over the same catalyst [17] as well as the inhibition of coke deposition potentially through *in situ* coke gasification identified under steam cracking conditions [18].

3.4 Conclusions

Whereas Mn-Cr-O spinel catalysts and Cr_2O_3 were structurally stable under steam reforming conditions at 873 K, Mn_3O_4 reduced *in situ* to MnO. The Cr_2O_3 catalyst showed the highest initial rate for propylene reforming but deactivated in the absence of co-fed H_2, presumably the result of coke deposition. Under similar reforming conditions, the Mn-rich $Mn_{1.5}Cr_{1.5}O_4$ spinel was both the most active and stable catalyst for aromatic (benzene and toluene) steam reforming.

Kinetics of olefin and aromatic steam reforming (first order in hydrocarbon, slightly negative order in H_2O) could be described by a two-site Mars-van Krevelen type mechanism. However, toluene steam reforming was negative first order in H_2, which contrasted the near zero reaction order in H_2 for other molecules examined in the study. *In situ* DRIFTS of toluene and benzene adsorption on the spinel surface suggests the inhibition on toluene reforming rate by H_2 was likely associated with a slower oxidation of the side methyl group of toluene in H_2. The Mn-rich $Mn_{1.5}Cr_{1.5}O_4$ spinel oxide is a promising barrier oxide layer for steam crackers because of its steam reforming activity toward aromatics likely from the excess Mn^{3+} sites.

3.5 References for Chapter 3

[1] S.M. Sadrameli, Thermal/catalytic cracking of hydrocarbons for the production of olefins: A state-of-the-art review I: Thermal cracking review, Fuel. 140 (2015) 102-115.

[2] I. Amghizar, L.A. Vandewalle, K.M. Van Geem, G.B. Marin, New Trends in Olefin Production, Engineering. 3 (2017) 171-178.

[3] H. Zimmermann, R. Walzl, Ethylene, in: Ullmann's Encyclopedia of Industrial Chemistry, Wiley-VCH Verlag GmbH & Co. KGaA, Weinheim, 2012, p. 470.

[4] L. Yang, M.P. Bukhovko, A. Malek, L. Li, C.W. Jones, P.K. Agrawal, R.J. Davis, Steam reforming of ethylene over nickel based spinel oxides, Appl. Catal. A Gen. 603 (2020) 117739.

[5] Q. Wang, X. Chen, A.N. Jha, H. Rogers, Natural gas from shale formation - The evolution , evidences and challenges of shale gas revolution in United States, Renew. Sustain. Energy Rev. 30 (2014) 1-28.

[6] P.C.A. Bruijnincx, B.M. Weckhuysen, Shale Gas Revolution: An Opportunity for the Production of Biobased Chemicals?, Angew. Chem. Int. Ed. 52 (2013) 11980-11987.

[7] C.M. Schietekat, S.A. Sarris, P.A. Reyniers, L.B. Kool, W. Peng, P. Lucas, K.M. Van Geem, G.B. Marin, Catalytic Coating for Reduced Coke Formation in Steam Cracking Reactors, Ind. Eng. Chem. Res. 54 (2015) 9525-9535.

[8] S.A. Sarris, N. Olahova, K. Verbeken, M.F. Reyniers, G.B. Marin, K.M. Van Geem, Optimization of the in Situ Pretreatment of High Temperature Ni-Cr Alloys for Ethane Steam Cracking, Ind. Eng. Chem. Res. 56 (2017) 1424-1438.

[9] S. Mahamulkar, K. Yin, M.T. Claure, R.J. Davis, L. Li, H. Shibata, A. Malek, C.W. Jones, P.K. Agrawal, Thermally stable α-alumina supported ceria for coking resistance and oxidation of radical coke generated in-situ, Fuel. 218 (2018) 357-365.

[10] S. Mahamulkar, K. Yin, P.K. Agrawal, R.J. Davis, C.W. Jones, A. Malek, H. Shibata, Formation and Oxidation/Gasification of Carbonaceous Deposits: A Review, Ind. Eng. Chem. Res. 55 (2016) 9760-9818.

[11] S. Mahamulkar, K. Yin, R.J. Davis, H. Shibata, A. Malek, C.W. Jones, P.K. Agrawal, In Situ Generation of Radical Coke and the Role of Coke-Catalyst Contact on Coke Oxidation, Ind. Eng. Chem. Res. 55 (2016) 5271-5278.

[12] A.E. Muñoz Gandarillas, K.M. Van Geem, M.F. Reyniers, G.B. Marin, Influence of the reactor material composition on coke formation during ethane steam cracking, Ind. Eng. Chem. Res. 53 (2014) 6358-6371.

[13] A.E. Muñoz Gandarillas, K.M. Van Geem, M.F. Reyniers, G.B. Marin, Coking resistance of specialized coil materials during steam cracking of sulfur-free naphtha, Ind. Eng. Chem. Res. 53 (2014) 13644-13655.

[14] B. Bao, Z. Wang, H. Xu, J. Liu, Anti-coking Effect of $MnCr_2O_4$ Spinel Coating during Light Naphtha Thermal Cracking, Energy Procedia. 105 (2017) 4808-4813.

[15] B. Bao, J. Liu, H. Xu, B. Liu, W. Zhang, Inhibitory effect of $MnCr_2O_4$ spinel coating on coke formation during light naphtha thermal cracking, RSC Adv. 6 (2016) 68934-68941.

[16] B. Bao, J. Liu, H. Xu, Z. Wang, K. Zhang, Fabrication of spinel coating on HP40 alloy and its inhibition effect on catalytic coking during thermal cracking of light naphtha, Brazilian J. Chem. Eng. 35 (2018) 721-730.

[17] M.P. Bukhovko, L. Yang, L. Li, A. Malek, R.J. Davis, P.K. Agrawal, C.W. Jones, Gasification of Radical Coke with Steam and Steam-Hydrogen Mixtures over Manganese-Chromium Oxides, Ind. Eng. Chem. Res. 59 (2020) 10813-10822.

[18] M.P. Bukhovko, L. Yang, I. Nezam, L. Li, A. Malek, R.J. Davis, P.K. Agrawal, C.W. Jones, Enhanced Coke Gasification Activity of $Mn_{1.5}Cr_{1.5}O_4$ Spinel Catalyst during Coking in Ethylene-Steam Mixture, submitted.

[19] S.H. Symoens, N. Olahova, A.E. Muñoz Gandarillas, H. Karimi, M.R. Djokic, M.F. Reyniers, G.B. Marin, K.M. Van Geem, State-of-the-art of Coke Formation during Steam Cracking: Anti-Coking Surface Technologies, Ind. Eng. Chem. Res. 57 (2018) 16117-16136.

[20] K. Yin, R.J. Davis, S. Mahamulkar, C.W. Jones, P. Agrawal, H. Shibata, A. Malek, Catalytic Oxidation of Solid Carbon and Carbon Monoxide over Cerium-Zirconium Mixed Oxides, AIChE J. 63 (2017) 725-738.

[21] L. Yang, M.P. Bukhovko, G. Brezicki, A. Malek, L. Li, C.W. Jones, P.K. Agrawal, R.J. Davis, Steam reforming of ethylene over manganese-chromium spinel oxides, J. Catal. 380 (2019) 224-235.

[22] L. Lutterotti, M. Bortolotti, G. Ischia, I. Lonardelli, H.R. Wenk, Rietveld texture analysis from diffraction images, Z. Kristallogr. Suppl. 26 (2007) 125-130.

[23] K. Yin, S. Mahamulkar, J. Xie, H. Shibata, A. Malek, L. Li, C.W. Jones, P. Agrawal, R.J. Davis, Catalytic reactions of coke with dioxygen and steam over alkaline-earth-metal-doped cerium-zirconium mixed oxides, Appl. Catal. A Gen. 535 (2017) 17-23.

[24] X. Wang, R.J. Gorte, A study of steam reforming of hydrocarbon fuels on Pd/ceria, Appl. Catal. A Gen. 224 (2002) 209-218.

[25] J. Pu, T. Toyoda, E.W. Qian, Evaluation of Reactivities of Various Compounds in Steam Reforming over RuNi/$BaOAl_2O_3$ Catalyst, Energy Fuels 32 (2018) 1804-1811.

[26] F.M. Josuinkas, C.P.B. Quitete, N.F.P. Ribeiro, M.M.V.M. Souza, Steam reforming of model gasification tar compounds over nickel catalysts prepared from hydrotalcite precursors, Fuel Process. Technol. 121 (2014) 76-82.

[27] A. Naoumidis, H.A. Schulze, W. Jungen, P. Lersch, Phase studies in the chromium-manganese-titanium oxide system at different oxygen partial pressures, J. Eur. Ceram. Soc. 7 (1991) 55-63.

[28] E. Stefan, J.T.S. Irvine, Synthesis and characterization of chromium spinels as potential electrode support materials for intermediate temperature solid oxide fuel cells, J. Mater. Sci. 46 (2011) 7191-7197.

[29] X. Liu, Z. Xiong, S.R. Shieh, Q. He, L. Deng, Y. Zhang, L. Chang, F. Wang, X. Hong, Z. Chen, Non-monotonic compositional dependence of isothermal bulk modulus of the $(Mg_{1-x}Mn_x)Cr_2O_4$ spinel solid solutions, and its origin and implication, Solid Earth Sci. 1 (2016) 89-100.

[30] F.F. Fava, I. Baraille, A. Lichanot, C. Larrieu, R. Dovesi, On the structural, electronic and magnetic properties of $MnCr_2O_4$ spinel, J. Phys. Condens. Matter 9 (1997) 10715-10724.

[31] B.L. Chamberland, J.A. Kafalas, J.B. Goodenough, Characterization of $MnCrO_3$ and $CrMnO_4$, Inorg. Chem. 16 (1977) 44-46.

[32] F. Ahmad, M.K. Agusta, R. Maezono, H.K. Dipojono, DFT + U study of H_2O adsorption and dissociation on stoichiometric and nonstoichiometric CuO(1 1 1) surfaces, J. Phys. Condens. Matter. 32 (2020) 045001.

[33] R. Ovcharenko, E. Voloshina, J. Sauer, Water adsorption and O-defect formation on Fe_2O_3(0001) surfaces, Phys. Chem. Chem. Phys. 18 (2016) 25560-25568.

[34] C. Guo, X. Liu, L. Gao, X. Ma, M. Zhao, J. Zhou, X. Kuang, W. Deng, X. Sun, Q. Wei, Oxygen defect engineering in cobalt iron oxide nanosheets for promoted overall water splitting, J. Mater. Chem. A. 7 (2019) 21704-21710.

[35] R. Schaub, P. Thostrup, N. Lopez, E. Lægsgaard, I. Stensgaard, J.K. Nørskov, F. Besenbacher, Oxygen vacancies as active sites for water dissociation on rutile TiO_2(110), Phys. Rev. Lett. 87 (2001) 266104.

[36] F.D. Kopinke, G. Zimmermann, G.C. Reyniers, G.F. Froment, Relative Rates of Coke Formation from Hydrocarbons in Steam Cracking of Naphtha. 2. Paraffins, Naphthenes, Mono-, Di-, and Cycloolefins, and Acetylenes, Ind. Eng. Chem. Res. 32 (1993) 56-61.

[37] Y.V. Kissin, A.J. Brandolini, Chemistry of olefin polymerization reactions with chromium-based catalysts, J. Polym. Sci. A Polym. Chem. 46 (2008) 5330-5347.

[38] A. Chakrabarti, M. Gierada, J. Handzlik, I.E. Wachs, Operando Molecular Spectroscopy During Ethylene Polymerization by Supported CrO_x/SiO_2 Catalysts: Active Sites, Reaction Intermediates, and Structure-Activity Relationship, Top. Catal. 59 (2016) 725-739.

[39] F.D. Kopinke, G. Zimmermann, G.C. Reyniers, G.F. Froment, Relative Rates of Coke Formation from Hydrocarbons in Steam Cracking of Naphtha. 3. Aromatic Hydrocarbons, Ind. Eng. Chem. Res. 32 (1993) 2620-2625.

[40] C. Dong, Z. Qu, Y. Qin, Q. Fu, H. Sun, X. Duan, Revealing the Highly Catalytic Performance of Spinel $CoMn_2O_4$ for Toluene Oxidation: Involvement and Replenishment of Oxygen Species Using in Situ Designed-TP Techniques, ACS Catal. 9 (2019) 6698-6710.

[41] S. Mo, Q. Zhang, J. Li, Y. Sun, Q. Ren, S. Zou, Q. Zhang, J. Lu, M. Fu, D. Mo, J. Wu, H. Huang, D. Ye, Highly efficient mesoporous MnO_2 catalysts for the total toluene oxidation: Oxygen-Vacancy defect engineering and involved intermediates using in situ DRIFTS, Appl. Catal. B Environ. 264 (2020) 118464.

[42] E. Finocchio, G. Busca, V. Lorenzelli, R.J. Willey, The activation of hydrocarbon C-H bonds over transition metal oxide catalysts: A FTIR study of hydrocarbon catalytic combustion over $MgCr_2O_4$, J. Catal. 151 (1995) 204-215.

[43] C.A. Koutstaal, V. Ponec, FT-IR study on the adsorption of benzoic acid and its derivatives on transition-metal oxides, Appl. Surf. Sci. 70-71 (1993) 206-210.

[44] J. Zhong, Y. Zeng, D. Chen, S. Mo, M. Zhang, M. Fu, J. Wu, Z. Su, P. Chen, D. Ye, Toluene oxidation over Co^{3+}-rich spinel Co_3O_4: Evaluation of chemical and by-product species identified by in situ DRIFTS combined with PTR-TOF-MS, J. Hazard. Mater. 386 (2020) 121957.

[45] X. Wang, W. Zhao, X. Wu, T. Zhang, Y. Liu, K. Zhang, Y. Xiao, L. Jiang, Total oxidation of benzene over ACo_2O_4 (A = Cu, Ni and Mn) catalysts: In situ DRIFTS account for understanding the reaction mechanism, Appl. Surf. Sci. 426 (2017) 1198-1205.

[46] X. Wang, Y. Liu, T. Zhang, Y. Luo, Z. Lan, K. Zhang, J. Zuo, L. Jiang, R. Wang, Geometrical-Site-Dependent Catalytic Activity of Ordered Mesoporous Co-Based Spinel for Benzene Oxidation: In Situ DRIFTS Study Coupled with Raman and XAFS Spectroscopy, ACS Catal. 7 (2017) 1626-1636.

[47] J. Zeng, X. Liu, J. Wang, H. Lv, T. Zhu, Catalytic oxidation of benzene over MnO_x/TiO_2 catalysts and the mechanism study, J. Mol. Catal. A Chem. 408 (2015) 221-227.

[48] X. Wang, W. Zhao, T. Zhang, Y. Zhang, L. Jiang, S. Yin, Facile fabrication of shape-controlled $Co_xMn_yO_\beta$ nanocatalysts for benzene oxidation at low temperatures, Chem. Commun. 54 (2018) 2154-2157.

[49] S.J. Blanksby, G.B. Ellison, Bond dissociation energies of organic molecules, Acc. Chem. Res. 36 (2003) 255-263.

[50] D. Costa, K. Sharkas, M.M. Islam, P. Marcus, Ab initio study of the chemical states of water on Cr_2O_3(0 0 0 1): From the isolated molecule to saturation coverage, Surf. Sci. 603 (2009) 2484-2493.

[51] L. Shi, S. Meng, S. Jungsuttiwong, S. Namuangruk, Z.H. Lu, L. Li, R. Zhang, G. Feng, S. Qing, Z. Gao, X. Yu, High coverage H_2O adsorption on $CuAl_2O_4$ surface: A DFT study, Appl. Surf. Sci. 507 (2020) 145162.

[52] J. Chen, A. Selloni, Water adsorption and oxidation at the Co_3O_4 (110) surface, J. Phys. Chem. Lett. 3 (2012) 2808-2814.

[53] X.L. Xu, J.Q. Li, DFT studies on H_2O adsorption and its effect on CO oxidation over spinel Co_3O_4 (110) surface, Surf. Sci. 605 (2011) 1962-1967.

[54] A.V. Bandura, J.D. Kubicki, J.O. Sofo, Comparisons of multilayer H_2O adsorption onto the (110) surfaces of α-TiO_2 and SnO_2 as calculated with density functional theory, J. Phys. Chem. B. 112 (2008) 11616-11624.

[55] G. Hu, Z. Wu, D. Jiang, First Principles Insight into H_2 Activation and Hydride Species on TiO_2 Surfaces, J. Phys. Chem. C. 122 (2018) 20323-20328.

[56] M. García-Melchor, N. López, Homolytic Products from Heterolytic Paths in H_2 Dissociation on Metal Oxides: The Example of CeO_2, J. Phys. Chem. C 118 (2014) 10921-10926.

[57] X. Yu, X. Zhang, S. Wang, High coverage hydrogen adsorption on the Fe_3O_4(1 1 0) surface, Appl. Surf. Sci. 353 (2015) 973-978.

[58] N. Mulakaluri, R. Pentcheva, Hydrogen adsorption and site-selective reduction of the Fe_3O_4(001) surface: Insights from first principles, J. Phys. Chem. C. 116 (2012) 16447-16453.

[59] T. Yang, X. Wen, C. Huo, Y. Li, J. Wang, H. Jiao, Structure and energetics of hydrogen adsorption on Fe_3O_4(1 1 1), J. Mol. Catal. A Chem. 302 (2009) 129-136.

[60] Y.C. Zhang, L. Pan, J. Lu, J. Song, Z. Li, X. Zhang, L. Wang, J.J. Zou, Unraveling the facet-dependent and oxygen vacancy role for ethylene hydrogenation on Co_3O_4 (110) surface: A DFT+U study, Appl. Surf. Sci. 401 (2017) 241-247.

Chapter 4 Steam reforming of ethylene over nickel based spinel oxides

Work presented in this chapter was published as:

L. Yang, M.P. Bukhovko, A. Malek, L. Li, C.W. Jones, P.K. Agrawal, R.J. Davis, Steam reforming of ethylene over nickel based spinel oxides, Appl. Catal. A Gen 603 (2020) 117739.

Abstract

Spinel oxides containing Ni cations can be present in the barrier layers of ethane steam cracker tubes. As Ni is known to catalyze steam reforming side reactions as well as coke deposition, the catalytic performance of Ni spinel catalysts was investigated. A series of NiM_2O_4 spinel catalysts (M = Al, Cr, Fe) was synthesized from a sol-gel method and thoroughly characterized. The $NiAl_2O_4$ and $NiCr_2O_4$ catalysts were active for ethylene steam reforming at 873 K without degradation of the spinel structure. The $NiFe_2O_4$ catalyst was the least stable because of partial reduction of Fe^{3+} to form Fe_3O_4, which facilitated Ni-Fe alloy particle formation and severe coking. The reforming activity and the coke deposited on the $NiAl_2O_4$ and $NiCr_2O_4$ catalyst both increased after oxidative regeneration at 873 K, suggesting a slow reduction of Ni^{2+} to Ni metal particles during steam reforming that subsequently sinter into larger NiO particles during oxidative regeneration.

4.1 Introduction

Olefins are critical raw materials in chemical synthesis and the polymer industry. Indeed, the demand for olefins has been increasing to fulfill the growing markets for rubber, plastic and other consumer goods [1]. Ethylene is the most important chemical building block among the olefins and relies heavily on the steam cracking process for industrial scale production [2]. During the steam cracking process, hydrocarbon feedstocks, including ethane, naphtha or gasoil, are diluted in steam and pyrolyzed at extremely high temperatures (1023–1273 K) to initiate the free radical process [3,4]. The steam dilution improves the selectivity toward light olefins versus the undesired heavy aromatics [5].

One major side reaction that impacts the economy of the steam cracking process is the formation of carbonaceous deposits known as coke on the inner walls of the tubular reactors [6]. Despite the inhibitive effect of the diluting steam on coke deposition, the accumulation of carbon will occur inevitably after a long period of operation, which leads to an increase in pressure drop through the reactor, extra heat input to overcome the heat resistance of carbon, and degradation of the reactor alloy due to carburization of the protective oxide layer [7]. Hence, coke removal through the gasification in an air and(or) steam flow is required periodically [8]. The decoking process requires the production to be halted for up to 48 h, which significantly affects the profitability of the steam crackers [9].

Coke formation during the steam cracking process can occur through three types of mechanisms: catalytic coking, radical coking and droplet condensation [10]. As Fe-Ni-Cr alloys are commonly used for the tubes within steam crackers, catalytic coking can occur rapidly at low temperatures due to the presence of metallic sites on these alloy surfaces [11]. One method to suppress catalytic coke formation is the creation of a barrier material [3,10], or anti-coking layer, which impedes the migration of Ni and Fe metal particles from the base alloy to the surface and therefore prevents them from being in contact with the gaseous hydrocarbons [5]. For Fe-Ni-Cr alloys containing small amounts of Mn, a protective oxide layer consisting of $MnCr_2O_4$-Cr_2O_3 spinel oxides can form upon oxidative pretreatment at high temperatures, which has been shown to be effective for catalytic coking suppression [12,13]. The incorporation of Al in Fe-Ni-Cr alloys was also shown to reduce coke formation and improve resistance to carburization [14,15]. A protective oxide layer of Al_2O_3, which surpasses the stability of Cr_2O_3 against carburization at a temperature above 1200 K [16], forms during oxidative pretreatment of the Al-containing alloy surface, which further reduces coke formation over the metallic alloy and deteriorates less over time compared to the conventional Fe-Ni-Cr alloys [17,18]. Because of the high thermodynamic stability of the spinel $NiAl_2O_4$ phase, both thermodynamic calculations [17,19] and experimental results [20] indicate $NiAl_2O_4$ spinel can form on the alloy surface after the oxidative pretreatment, with other possible Ni-based spinels $NiCr_2O_4$ and $NiFe_2O_4$ predicted to form as well. Given the potential existence of Ni-containing spinels on the alloy surface, their catalytic activity and stability in steam reforming of ethylene (a potential side reaction occurring when hydrocarbons are present with steam at high temperatures) are worthy of exploration.

Ethylene steam reforming involves the concurrence of the following reactions:

Steam Reforming:

$$C_2H_4 + 2H_2O \rightarrow 2CO + 4H_2 \quad \Delta H_r^o = 210.1\ kJ{\cdot}mol^{-1} \tag{4.1}$$

Water Gas Shift:

$$CO + H_2O \rightarrow CO_2 + H_2 \quad \Delta H_r^o = -41.2\ kJ{\cdot}mol^{-1} \tag{4.2}$$

Methanation:

$$CO + 3H_2 \rightarrow CH_4 + H_2O \quad \Delta H_r^o = -205.9\ kJ{\cdot}mol^{-1} \tag{4.3}$$

In our prior work, we examined the activity and stability of Mn-Cr-O spinel oxides with different stoichiometry in catalytic ethylene steam reforming [4]. Herein, we have extended those studies to Ni-based spinel oxides. The $NiAl_2O_4$ based catalysts were commonly studied for hydrocarbon steam reforming reactions [21,22]. Previous studies have shown that the $NiAl_2O_4$ catalysts were active for steam reforming of diesel and other hydrocarbons without reductive pretreatment [23,24] and remained stable without decomposition to NiO or reduction to Ni metal by the produced H_2 [25]. On the other hand, pre-reduction of the $NiAl_2O_4$ catalyst significantly increased its activity for methane steam reforming [26], potentially resulting from an improved ability for methane activation [27]. Although the $NiFe_2O_4$ spinel was reported to catalyze dry reforming of methane without reductive pretreatment [28], the spinel phase decomposed as a result of *in situ* reduction by the generated H_2 to form Ni-Fe alloy particles [29]. While monometallic Ni [30] and Ni-containing bimetallic catalysts (*e.g.*, Ni-W and Ni-Ru) [31] have been explored previously, ethylene steam reforming studies over the Ni-based spinel catalysts were relatively sparse. In this work, three Ni-based spinel oxides with Al, Cr or Fe were synthesized and characterized by various techniques regarding phase composition, elemental analysis and chemical properties. The samples were then evaluated in catalytic ethylene steam reforming without reductive pretreatment under the same conditions used to probe Mn-Cr-O spinel oxides to enable comparisons of reforming activity, coke deposition and Ni reducibility. It should be emphasized that the goal of the current work is not to optimize activity of Ni catalysts for ethylene steam reforming, but instead to probe the reforming activity of potential components in ethane steam crackers in an effort to guide the development of new barrier layers. In other words, reduction of Ni cations to highly active Ni metal particles is to be avoided as those particles would convert the desired product ethylene to coke or reforming products under the conditions of steam cracking.

4.2 Experimental methods

4.2.1 Catalyst preparation

The NiM_2O_4 (M = Al, Cr and Fe) spinel catalysts were prepared from a conventional sol-gel method. Typically, $Ni(NO_3)_2{\cdot}6H_2O$ (99.999 %, Sigma-Aldrich) and $M(NO_3)_3{\cdot}9H_2O$ (98 %, Sigma-Aldrich) corresponding to a 3 g NiM_2O_4 equivalence were first dissolved in 100 cm^3 distilled deionized water under vigorous stirring (10 cm^3 concentrated HNO_3 was added during the synthesis of $NiFe_2O_4$ to prevent hydrolysis of Fe^{3+}). The metal solution was then mixed with 50 cm^3 aqueous solution of citric acid (CA) (99.5 %, Sigma-Aldrich) to achieve a molar ratio of Ni^{2+}:M^{3+}:CA = 1:2:6. The resulting solution was stirred at 368 K until the formation of a viscous gel. The gel precursor was dried overnight in air at 393 K and thermally treated at 1273 K in flowing air for 4 h. The powders collected after the thermal treatment were referred to as the fresh NiM_2O_4 catalysts.

4.2.2 Catalyst characterization

Scanning Electron Microscopy (SEM) was performed on a FEI Quanta 650 FEG-SEM microscope operated at 10 kV under the secondary electron imaging mode. Elemental composition of the catalysts was further analyzed using an Oxford X-Max^N Energy Dispersive X-ray Spectroscopy (EDS) detector based on the corresponding Kα radiations of the metal elements. The sample was prepared using a conductive double-sided carbon tape to adhere the catalyst powders to the sample stage.

Specific surface areas and pore volumes of the catalysts were assessed by N_2 physisorption at 77 K on a Micromeritics ASAP 2020 analyzer using the Brunauer-Emmett-Teller (BET) and the Barrett-Joyner-Halenda (BJH) method of analysis, respectively. A sample of 2 g catalyst was outgassed at 473 K for 4 h before N_2 physisorption.

Powder X-ray diffraction (XRD) patterns of the catalysts were recorded using a PANalytical Empyrean X-ray Diffractometer equipped with a Cu Kα radiation source. The sample was scanned in a 2θ range from 15° to 80° with a scan rate of $5°\cdot min^{-1}$ at room temperature. Rietveld refinement of the diffraction patterns was performed using the Material Analysis Using Diffraction (MAUD) software package [32].

X-ray photoelectron spectroscopy (XPS) was conducted on a Phi VersaProbe III Scanning X-ray Photoelectron Spectrometer equipped with a monochromatic Al Kα radiation source (1486.7 eV) and a hemispherical energy analyzer. High resolution spectra of the catalysts were collected using an X-ray beam size of 100 μm with the pass energy and stepwise dwell time of the energy analyzer to be 55 eV and 100 ms, respectively. During the measurements of the depth profile, the sample was etched by a high-energy Ar ion beam (3 μm×3 μm) with a bias of 3 kV for 1 min in between the collection of the spectra. All scans were accompanied by a dual charge compensation using a low-energy electron flood gun and a low-energy Ar ion beam. The binding energy was calibrated to C1s (284.8 eV) from the adventitious carbon.

Temperature-programmed reduction in H_2 (H_2-TPR) of the catalysts was measured on a Micromeritics AutoChem II 2920 Analyzer equipped with a thermal conductivity detector. Typically, a sample of 300 mg catalyst was first pretreated in Ar at 773 K for 0.5 h and cooled down to 323 K. The sample was then heated in 5 vol % H_2 in flowing Ar to 1273 K at a constant ramp rate of $10\ K\cdot min^{-1}$.

Thermogravimetric analysis of the spent catalysts was carried out using a TA Instruments SDT Q600 thermogravimetric analyzer. The weight changes of a 30 mg sample were recorded while the sample was heated in synthetic air to 1073 K at a constant ramp rate of 10 K·min^{-1}.

4.2.3 Steam reforming of ethylene

The NiM_2O_4 spinel catalysts were evaluated in catalytic steam reforming of ethylene at 873 K under atmospheric total pressure. Typically, a feed gas flow of 100 cm^3·min^{-1} consisting of 25 vol % C_2H_4, 50 vol % H_2O, 5 vol % N_2 and 20 vol % Ar was introduced to 1 g catalyst (sieved to 250-425 μm) loaded in a fixed-bed quartz reactor (10.5 mm I.D. × 12.75 mm O.D.). After a N_2 purge to remove dissolved O_2, a syringe pump (ISCO, 500D) was used to supply H_2O into a stainless steel evaporator maintained at 413 K for uniform mixing with other gases upon vaporization. The effluent gas after reaction was first directed to a condenser to remove unreacted H_2O, then passed through an infrared analyzer (Fuji Electric ZPA) for the quantification of CO_2, and eventually to an online gas chromatograph (Agilent 7890A) equipped with a CarboPlot P7 column and a thermal conductivity detector for the quantification of H_2, CO, CH_4 and C_2H_4. Characteristic steam reforming activity, evaluated at an ethylene conversion below 10 %, is reported on a carbon basis (production rate of C_1), defined as the sum of the production rates of CO, CO_2 and CH_4 normalized by the BET surface area of the catalyst:

$$r_{C_1} = \frac{F(CO) + F(CO_2) + F(CH_4)}{S_{BET}} \tag{4.4}$$

The ethylene conversion is evaluated based on the produced CO, CO_2 and CH_4:

$$C_2H_4 \text{ conversion } (\%) = \frac{F(CO) + F(CO_2) + F(CH_4)}{2F_0(C_2H_4)} \times 100\ \% \tag{4.5}$$

The selectivity is defined as the mole fraction of a certain product (H_2, CO, CO_2 and CH_4) relative to all the products:

$$\text{Selectivity of X (\%)} = \frac{F(X)}{F(H_2) + F(CO) + F(CO_2) + F(CH_4)} \times 100\ \% \tag{4.6}$$

where F(X) denotes the molar flowrate of component X measured downstream of the reactor, $F_0(C_2H_4)$ denotes the molar flowrate of C_2H_4 fed to the reactor, S_{BET} denotes the dinitrogen BET surface area of the catalyst.

4.3 Results and discussion

4.3.1 Characterization of the NiM_2O_4 spinel catalysts

The textural properties of the NiM_2O_4 spinel catalysts evaluated using N_2 physisorption are summarized in **Table 4.1**. After the thermal treatment, the BET surface areas of all three NiM_2O_4 catalysts were observed to be extremely small (< 5 $m^2 \cdot g^{-1}$). Approximating a spherical morphology, the average particle diameter of $NiCr_2O_4$ calculated from the BET surface area and bulk density was 290 nm, which is in good agreement with the surface-weighted average diameter of 300 nm evaluated from the SEM image (middle micrograph in **Figure 4.1a**). This comparison suggests the minor pore volume assessed using the BJH method likely resulted from the void between the particle aggregates rather than intracrystalline pores [33]. Thus, the NiM_2O_4 catalysts are concluded to be non-porous and the BET surface areas measured are attributed exclusively to the external surface.

Table 4.1 Textural properties of the fresh NiM_2O_4 spinel catalysts from N_2 physisorption

Catalyst	BET surface area ($m^2 \cdot g^{-1}$)	Pore volume ($cm^3 \cdot g^{-1}$)[a]
$NiAl_2O_4$	1.5	0.004
$NiCr_2O_4$	3.8	0.010
$NiFe_2O_4$	0.4	0.0004

[a] BJH cumulative pore volume.

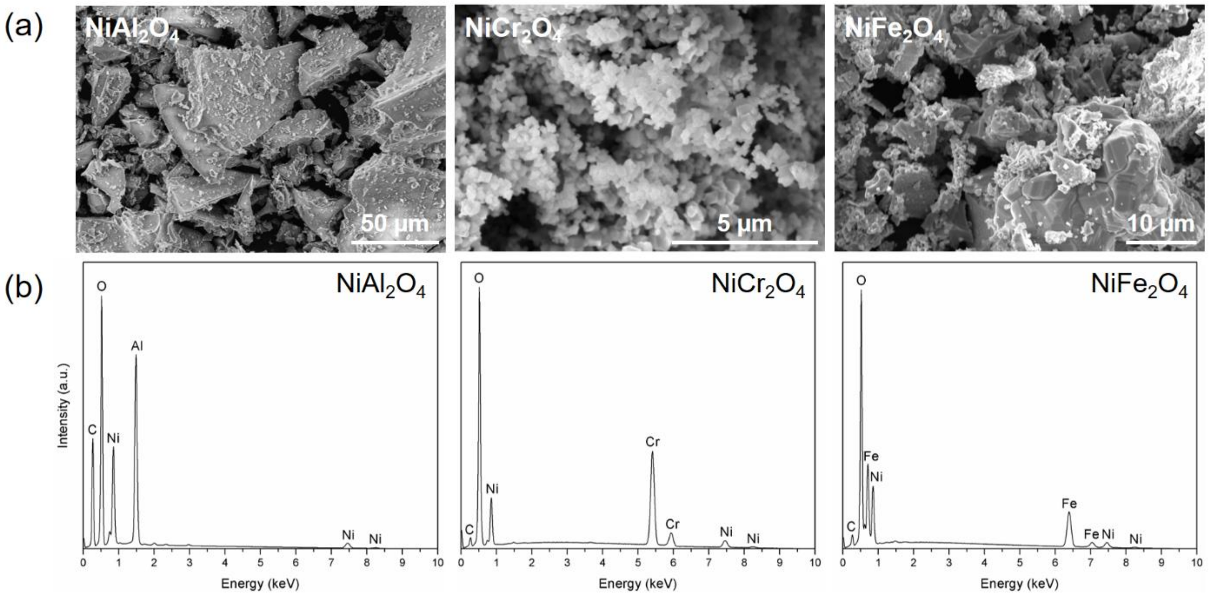

Figure 4.1 Scanning electron microscopy images (a) and energy dispersive X-ray spectra (b) of the fresh NiM_2O_4 spinel catalysts.

As shown in **Figure 4.1a**, the $NiCr_2O_4$ particles exhibited a relatively uniform morphology whereas larger agglomerates were observed in $NiAl_2O_4$ and $NiFe_2O_4$. The corresponding EDS analysis (**Figure 4.1b**) confirms the existence of Ni, the respective co-cation M and O in the catalyst particles, which is consistent with the formation of NiM_2O_4 mixed oxides. The atomic ratio of M/Ni measured for the NiM_2O_4 catalysts from EDS and XPS is compared in **Table 4.2**. Since the estimated penetration depth of the electron beam was 0.4 μm, the M/Ni ratio measured from EDS was considered to reflect the bulk composition of the catalysts. Consistent with the NiM_2O_4 stoichiometry, the EDS M/Ni ratio measured for all three catalysts was close to 2. Comparatively, the elemental composition near the surface region of the catalyst was characterized by XPS, corresponding to a depth of 30-90 Å estimated from the mean free path of the photoelectrons. The XPS M/Ni ratio evaluated for $NiAl_2O_4$ and $NiCr_2O_4$ were fairly consistent with their respective EDS results. As evident from a significantly lower Fe/Ni ratio measured from XPS (1.2) compared to that from EDS (1.7), the $NiFe_2O_4$ catalyst apparently had a non-uniform elemental distribution with an enrichment of Ni near surface. The elemental composition measured

Table 4.2 Elemental composition of the fresh NiM_2O_4 spinel catalysts measured by different techniques

Catalyst	EDS M/Ni (atomic)	XPS M/Ni (atomic)
$NiAl_2O_4$	1.9	1.6[a]
$NiCr_2O_4$	1.9	2.0
$NiFe_2O_4$	1.7	1.2

[a] Slightly underestimated due to overlapping of Al 2p with Ni 3p in XPS.

from the XPS depth profiling as a function of etching cycle is shown in **Figure C1**. Starting from second cycle, the M/Ni ratio for all three samples approached 2.0, which was consistent with the NiM_2O_4 stoichiometry and the EDS results. Although less significant compared to the $NiFe_2O_4$ sample, the XPS depth profile suggests an enrichment of Ni near the surface also occurred in $NiAl_2O_4$. The Cr/Ni ratio in $NiCr_2O_4$ was observed to be nearly constant regardless of the etching cycle.

The phase composition of the three NiM_2O_4 spinel catalysts characterized by XRD (shown in **Figure 4.2**) revealed the spinel structure in each case. The XRD pattern of the $NiAl_2O_4$ sample is consistent with previous reports [34,35], and the diffraction features of very low intensity at $2\theta = 43.3°$ and $2\theta = 62.9°$ (inserted graph) are attributed to a trace amount of NiO, which has been observed in synthetic $NiAl_2O_4$ depending on the starting stoichiometry [36] and sintering conditions [37]. The XRD pattern of the $NiCr_2O_4$ sample is also consistent with a prior report [38], without any appreciable presence of crystalline Cr_2O_3, which is a known impurity when annealed at lower temperatures [39]. The XRD pattern of the $NiFe_2O_4$ sample is in accordance with the cubic spinel structure [40]. The lattice constant of $NiFe_2O_4$ assessed from the Rietveld refinement (**Figure C2**) is 8.340 Å, which is similar to the reported range of values (8.338-8.339 Å) for $NiFe_2O_4$ [41,42] compared to those of Fe_3O_4 (8.392-8.397 Å) [43,44]. Our results indicate the diffraction features arise from a uniform $NiFe_2O_4$ spinel phase instead of a Fe_3O_4 phase, both having inverse spinel structures. The small features in the diffraction pattern of $NiCr_2O_4$ compared to a typical cubic spinel structure (*i.e.*, patterns for $NiAl_2O_4$ and $NiFe_2O_4$ in **Figure 4.2**) result from the phase transition of $NiCr_2O_4$ from cubic to tetragonal below 310 K [45] caused by the Jahn-Teller distortion of tetrahedrally coordinated Ni^{2+} [46]. The Ni^{2+} cations in $NiAl_2O_4$ [47] and $NiFe_2O_4$ [48] are octahedrally coordinated whereas the M^{3+} cations reside in both octahedral and tetrahedral sites. Consistent with their inverse spinel structures, the Jahn-Teller distortion was not observed for $NiAl_2O_4$ and $NiFe_2O_4$ at ambient temperature.

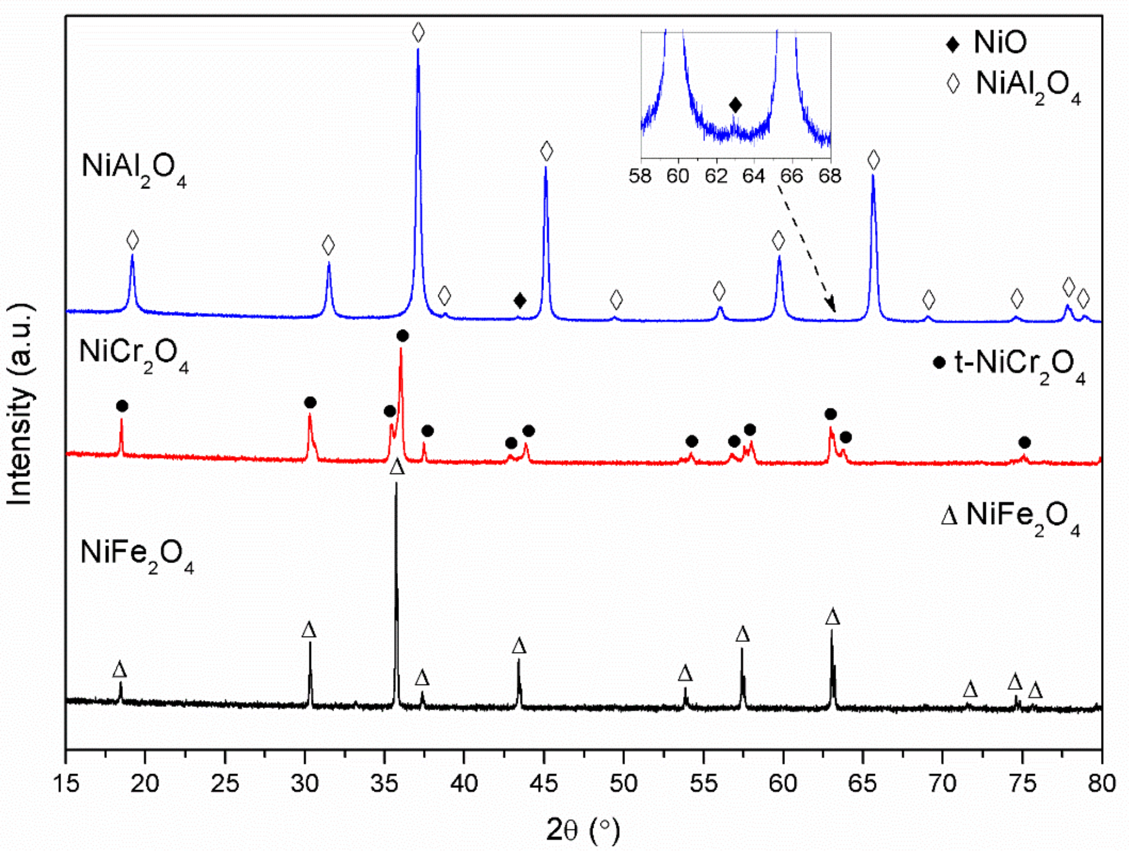

Figure 4.2 X-ray diffraction patterns of the fresh NiM_2O_4 spinel catalysts. The inset demonstrates the diffraction resulted from trace amount of NiO in the $NiAl_2O_4$ sample. The label t-$NiCr_2O_4$ refers to the tetragonal $NiCr_2O_4$ phase with $I4_1$/amd symmetry.

The speciation of Ni and the cation M on the surface of the NiM_2O_4 spinel catalysts was investigated by XPS. As shown in **Figure 4.3a**, the spectra in the Ni 2p region reveal features associated with $2p_{3/2}$ and $2p_{1/2}$, resulting from the strong spin-orbit coupling effect of Ni. For the

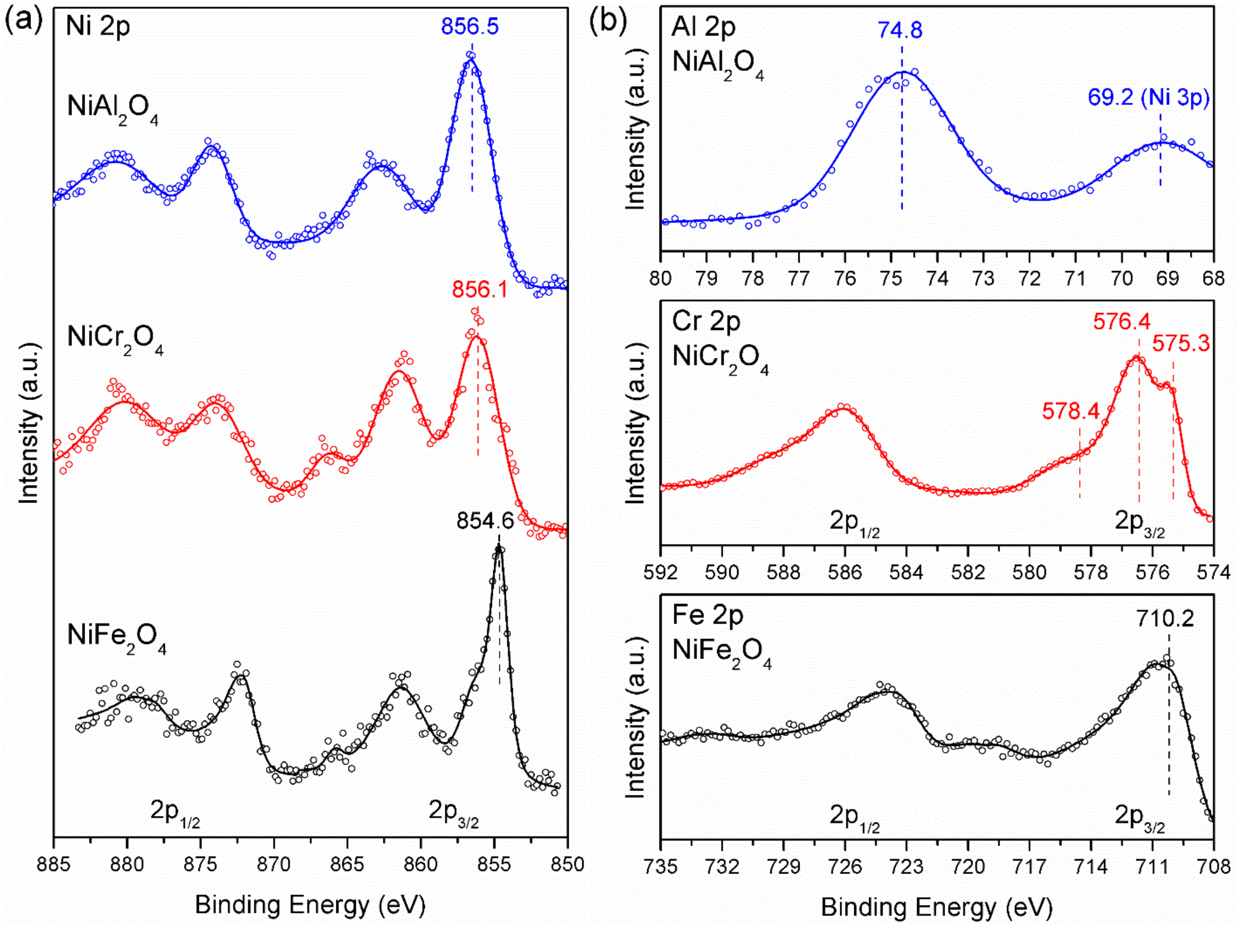

Figure 4.3 X-ray photoelectron spectra of (a) Ni 2p and (b) M 2p on the surface of the fresh NiM_2O_4 spinel catalysts.

Ni 2p spectra of all three catalysts, the Ni $2p_{3/2}$ peak is accompanied by a significant satellite feature (861-863 eV), which is consistent with the presence of Ni^{2+} instead of metallic Ni^0 [49]. The Ni $2p_{3/2}$ binding energy of the $NiAl_2O_4$ sample at 856.5 eV agrees well with a reported value of 856.0-856.8 eV [49–52]. Since the Ni $2p_{3/2}$ binding energy of NiO has been reported to be significantly lower (854.1-854.8 eV [49,50,52,53]), the Ni^{2+} in the $NiAl_2O_4$ sample is assigned to the lattice of the spinel $NiAl_2O_4$ phase instead of NiO, which is consistent with the XRD pattern and the surface elemental composition. The Ni $2p_{3/2}$ binding energy of $NiCr_2O_4$ was reported to be higher than that of $NiFe_2O_4$, within a range of 855.7-856.4 eV and 854.7-855.3 eV, respectively [52–55]. The comparison of the Ni $2p_{3/2}$ binding energy for our $NiCr_2O_4$ (856.1 eV) and $NiFe_2O_4$

(854.6 eV) is consistent with previous reports. In addition, the Ni $2p_{3/2}$ peak of $NiFe_2O_4$ is substantially skewed and has a larger intensity relative to the satellite compared to that of $NiCr_2O_4$, which has been correlated with the corresponding Ni^{2+} coordination environment. In particular, a large proportion of Ni^{2+} resides in the octahedral site in $NiFe_2O_4$ whereas Ni^{2+} predominantly resides in the tetrahedral site of $NiCr_2O_4$ [54,56]. Consistent with the tetragonal distortion from XRD discussed earlier, the tetrahedrally coordinated Ni^{2+} in $NiCr_2O_4$ exhibits a much higher binding energy than that of NiO and therefore is assigned to the Ni^{2+} in the $NiCr_2O_4$ spinel lattice. In contrast, the similarity of the Ni $2p_{3/2}$ binding energy of $NiFe_2O_4$ and NiO suggests that the appreciable enrichment of Ni on the surface of the $NiFe_2O_4$ sample (**Table 4.2**) may result from the existence of surface NiO. The Ni speciation in the $NiCr_2O_4$ sample below the surface layers was not accessible, since Ni^{2+} underwent reduction to metallic Ni^0 by the Ar ion beam during the depth profiling (**Figure C3**). Similar observations occurred for the $NiAl_2O_4$ and $NiFe_2O_4$ sample as well (not shown).

The XPS results in the 2p region of the respective co-cation M are shown in **Figure 4.3b**. The observed binding energy of Al 2p in the $NiAl_2O_4$ sample is 74.8 eV and agrees well with reported values of 74.1-75.4 eV for Al^{3+} in various Al-containing spinel compounds (MAl_2O_4) [57,58]. According to our previous work [4], the two major peaks of Cr $2p_{3/2}$ in the $NiCr_2O_4$ sample at 576.4 eV and 575.3 eV are associated with the strong multiplet split of Cr^{3+}, whereas the broad peak at 578.4 eV is attributed to the Cr^{6+} present in trace CrO_3. While being larger than the value reported for the Fe^{2+} in FeO (709.5 eV [59,60]), a Fe $2p_{3/2}$ binding energy of 710.2 eV observed for our $NiFe_2O_4$ sample is slightly smaller than the reported values of 710.6-710.7 eV for the Fe^{3+} in $NiFe_2O_4$ [56,61]. Since the weak satellite feature of the $NiFe_2O_4$ sample at 717-720 eV resembles that reported for Fe_3O_4 instead of the explicit features seen in FeO and Fe_2O_3 [59], it is likely that Fe^{3+} and Fe^{2+} both exist on the surface of the $NiFe_2O_4$ sample.

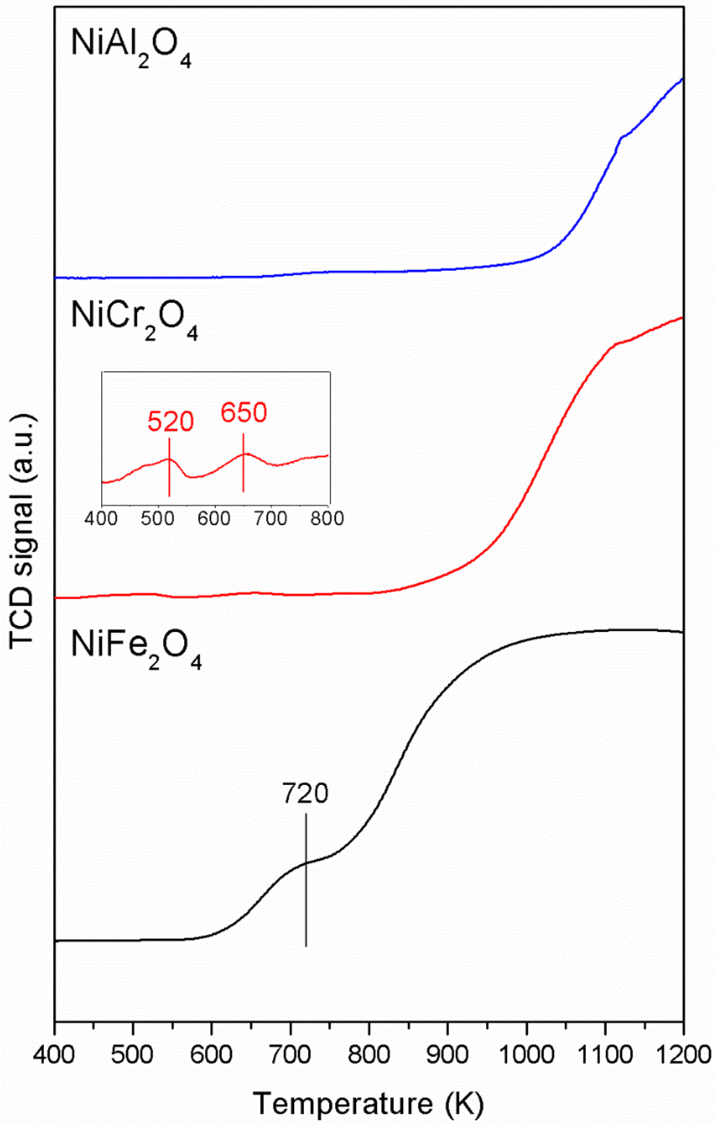

Figure 4.4 Temperature-programed reduction of the fresh NiM_2O_4 spinel catalysts in H_2. The inset demonstrates the minor H_2 uptake from the reduction of surface Cr^{6+} species.

The redox properties of the NiM_2O_4 spinel catalysts were probed by H_2-TPR. The reduction of NiO separate from the spinel structure was commonly observed at a temperature lower than 873 K , whereas the Ni^{2+} in the $NiAl_2O_4$ spinel framework was reduced at a much higher temperature over 1073 K [62–64]. As shown in **Figure 4.4**, the $NiAl_2O_4$ sample exhibited minor reduction before 900 K whereas the H_2 uptake substantially increased above 1000 K. These observations are consistent with the XRD pattern, suggesting the majority of Ni exists within the $NiAl_2O_4$ spinel phase. The $NiCr_2O_4$ sample showed a similar reduction profile, except the reduction of Ni^{2+} in $NiCr_2O_4$ started at a lower temperature of about 800 K. The doublet feature at 520 K and 650 K were attributed to the reduction of surface Cr^{6+} species, potentially stepwise from Cr^{6+} to Cr^{3+} and then to Cr^{2+} [65,66], which is in agreement with the identification of trace Cr^{6+} from XPS. Comparatively, the $NiFe_2O_4$ sample showed a significant reduction feature at 720 K, followed by rapid reduction at higher temperatures. According to previous studies [67,68], this low temperature feature was associated with the reduction of Fe^{3+} to Fe^{2+} to form Fe_3O_4, which potentially led to the degradation of the spinel structure and accelerated the reduction of Ni^{2+}. The phase composition of the three NiM_2O_4 catalysts after H_2-TPR was investigated by XRD and shown in **Figure C4a**. The diffraction features of metallic Ni were present in all three samples, indicating the reduction of Ni^{2+} to Ni^0 during the H_2-TPR. The slightly lower 2θ values of the metal diffraction features in the reduced $NiFe_2O_4$ sample were attributed to the formation of fcc Ni-Fe alloy particles [69–71]. The lattice constant of the Ni-Fe alloy particles estimated from the (111) diffraction feature (2θ = 44°) was 3.55 Å, which corresponded to a Fe content of 20-30 mol% according to previous reports [72,73]. The $NiAl_2O_4$ sample did not undergo complete reduction given the persistence of the $NiAl_2O_4$ spinel phase, whereas the spinel structure in the $NiCr_2O_4$ and $NiFe_2O_4$ sample decomposed severely as revealed by the appearance of Cr_2O_3 and Fe_3O_4 features. The spinel feature in the reduced $NiFe_2O_4$ sample was assigned to Fe_3O_4 based on a refined lattice parameter of 8.393 Å as shown in **Figure C4b**, which agrees well with the reported values of 8.392-8.397 Å for Fe_3O_4 [43,44]. Evidently, the $NiAl_2O_4$ catalyst was the most stable against reduction in H_2 among the three NiM_2O_4 spinels, but the stability did not correlate with the Ni coordination environment (*i.e.*, tetrahedral vs. octahedral) explicitly.

4.3.2 Steam reforming of ethylene over the NiM_2O_4 spinel catalysts

Table 4.3 Steam reforming of ethylene over the NiM_2O_4 spinel catalysts at 873 K

Catalyst	C_2H_4 conversion (%)[a]	C_1 production rate ($\mu mol \cdot m^{-2} \cdot s^{-1}$)	Product selectivity (%)			
			CO	CO_2	CH_4	H_2
$NiAl_2O_4$	8.8[b]	2.1[b]	6.6	22	0.4	71
$NiCr_2O_4$	2.1[c]	0.20[c]	3.1	24	8.4	65
$NiFe_2O_4$	89[d]	80[e]	10	11	2.1	77

[a] Product-based conversion. Reaction conditions: 873 K, 1 g catalyst, 100 $cm^3 \cdot min^{-1}$ total flow, 25 % C_2H_4, 50 % H_2O, 5 % N_2 and 20 % Ar.

[b] Steady state results at t > 1.5 h.

[c] Initial results at t < 1 h.

[d] Conversion determined from disappearance of C_2H_4 is > 99 % (*i.e.*, no C_2H_4 was detected downstream the catalyst).

[e] Average rate across the catalyst bed estimated from the global C_2H_4 conversion.

The catalytic performance of the NiM_2O_4 spinel catalysts was evaluated in ethylene steam reforming at 873 K, a temperature at which the background ethylene conversion was negligible [4]. The results in **Figure 4.5** show the different time profiles of the reaction over the NiM_2O_4 catalysts. The $NiAl_2O_4$ catalyst exhibited an initial ethylene conversion of 1.7 %, which gradually increased and plateaued at 8.8 % conversion after about 1.5 h on stream. A similar initial ethylene conversion of 2.1 % was observed for the $NiCr_2O_4$ catalyst, but it was followed by continuous deactivation to only 25 % of its initial activity after 7 h on stream. As denoted in **Table 4.3**, ethylene was almost entirely converted over the $NiFe_2O_4$ catalyst, with the detected C_1 products recovering 89 % of the carbon fed to the system. The initial C_1 production rate over the $NiCr_2O_4$ catalyst was 0.20 $\mu mol \cdot m^{-2} \cdot s^{-1}$, which is in the range of values (0.13-0.21 $\mu mol \cdot m^{-2} \cdot s^{-1}$) reported previously for the $Mn_xCr_{3-x}O_4$ spinel catalysts under the same conditions [4]. The steady C_1 production rate observed over the $NiAl_2O_4$ catalyst (2.1 $\mu mol \cdot m^{-2} \cdot s^{-1}$) was one order of magnitude higher (**Table 4.3**) than that over $NiCr_2O_4$. The product selectivity over the $NiAl_2O_4$ and $NiCr_2O_4$

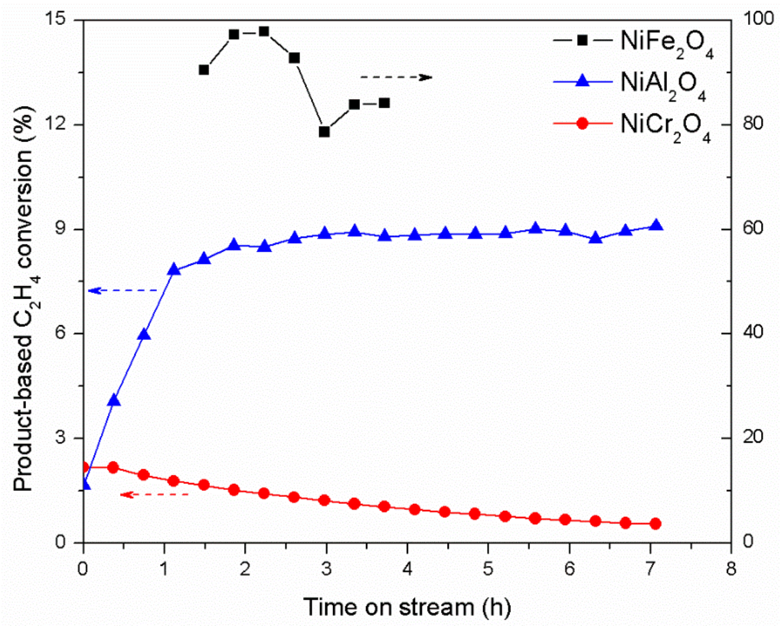

Figure 4.5 Product-based ethylene conversion in the steam reforming of ethylene over the NiM_2O_4 spinel catalysts. Reaction conditions: 873 K, 1 g catalyst, 100 $cm^3 \cdot min^{-1}$ total flow, 25 % C_2H_4, 50 % H_2O, 5 % N_2 and 20 % Ar.

catalysts favors H_2 and CO_2, which can be attributed to the nearly equilibrated water-gas shift reaction that occurred simultaneously with steam reforming. The high selectivity of H_2 relative to CO_2 for the $NiFe_2O_4$ catalyst suggests coke formation from dehydrogenation of ethylene, potentially catalyzed by the presence of Ni metal particles formed by the *in situ* reduction of the catalyst under reaction conditions. The presence of Ni metal would explain the very high rate of ethylene conversion of that sample. Unfortunately, the steam reforming rate of the $NiFe_2O_4$ catalyst was inaccessible under the tested conditions.

The spent NiM_2O_4 spinel catalysts were characterized using XRD and TGA to investigate any phase transition and coke deposition that may have occurred during ethylene steam reforming, with the results summarized in **Figure 4.6** and **Figure 4.7**, respectively. The XRD pattern of the spent $NiFe_2O_4$ indicates the spinel structure of that catalyst decomposed via reduction to Ni-Fe alloy and Fe_3O_4 during the reaction. As discussed above, the Ni-Fe alloy particles formed on the

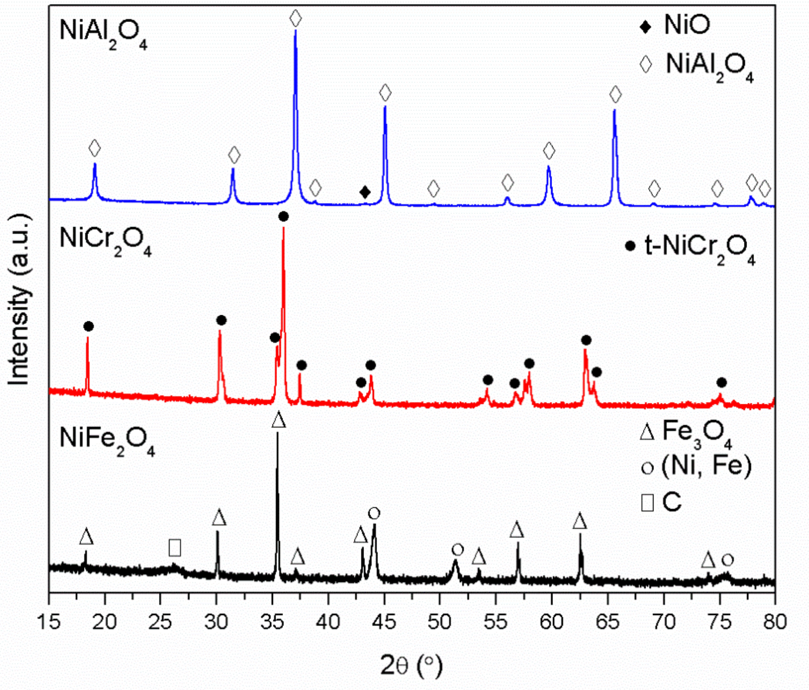

Figure 4.6 X-ray diffraction patterns of the spent NiM_2O_4 spinel catalysts after the steam reforming of ethylene at 873 K.

spent $NiFe_2O_4$ catalyst contained 20-30 mol% Fe according to a lattice constant of 3.55 Å estimated from the (111) diffraction feature [72,73], whereas the identification of the Fe_3O_4 phase is based on the comparison between a refined lattice constant of 8.398 Å (**Figure C5**) and the reported values of 8.392-8.397 Å for Fe_3O_4 [43,44]. Moreover, the broad diffraction feature at 2θ ~ 25-27° is attributed to the formation of graphitic carbon. This is also in agreement with a significant weight loss of 18.8 % due to coke removal observed during the temperature-programmed oxidation in the TGA (**Figure 4.7**). However, the weight fraction of coke deposited could be underestimated given the continuous mass gain of the spent $NiFe_2O_4$ sample starting at 500 K, which may be associated with the re-oxidation of Ni to NiO [74] and Fe_3O_4 to Fe_2O_3 [75]. The spent $NiAl_2O_4$ and $NiCr_2O_4$ catalyst did not show any appreciable changes in their XRD patterns, suggesting the Ni remained in a 2+ oxidation state in the spinel structure. While the amount of coke deposited on the $MnCr_2O_4$ spinel was negligible under identical reforming conditions [4], all spent NiM_2O_4 spinel catalysts exhibited weight loss that was indicative of coke deposition during the temperature-programmed oxidation of the TGA (**Figure 4.7**). Although the relative amount of coke deposited on the $NiCr_2O_4$ catalyst (2.0 wt %) was slightly higher than that on the $NiAl_2O_4$ catalyst (1.1 wt %), both catalysts had substantially lower coke levels than $NiFe_2O_4$, which is consistent with the absence of Ni^{2+} reduction to metal on the former two samples.

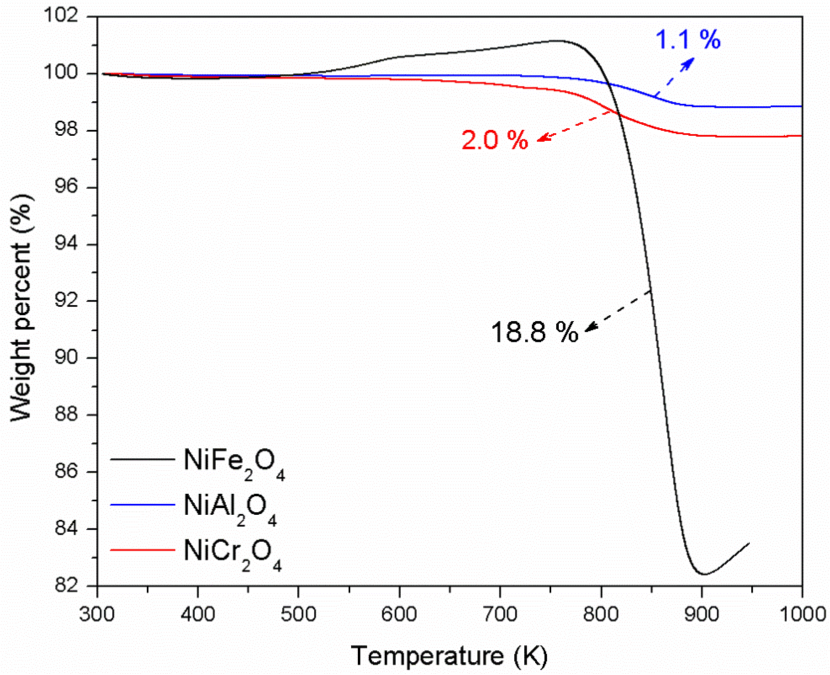

Figure 4.7 Thermogravimetric analysis in synthetic air of the spent NiM_2O_4 spinel catalysts after the steam reforming of ethylene at 873 K. The labelled percentages are the maximum weight loss of the sample below 923 K.

4.3.3 Ethylene steam reforming cycles over the $NiAl_2O_4$ and $NiCr_2O_4$ spinel catalysts

The $NiAl_2O_4$ and $NiCr_2O_4$ spinel catalysts were further evaluated in ethylene steam reforming for two cycles, separated by an oxidative treatment at 873 K. Despite their improved stability against the formation of large Ni metal particles, it is still possible that nanoparticles of Ni could be formed in small amounts that are not detectable by XRD. The re-oxidation treatment, which is sufficient to remove the deposited coke from the first cycle as evident by the TGA (**Figure**

4.7), could potentially oxidize highly dispersed Ni nanoparticles to NiO and facilitate aggregation [76]. Since larger NiO particles are more prone to reduction [62,64,77], the resulting Ni metal particles might be expected to contribute to observed reactivity in the second cycle. As shown in **Figure 4.8**, the activity of both the $NiAl_2O_4$ and $NiCr_2O_4$ catalyst in the second cycle significantly increased compared to their corresponding first cycle. During the second cycle of the $NiAl_2O_4$ sample, the gradual increase in activity that was observed in the initial stage of the first cycle did not occur. Instead, the $NiAl_2O_4$ sample exhibited a stable C_1 production rate of 2.9 $\mu mol \cdot m^{-2} \cdot s^{-1}$, which was more than twice the steady rate (> 2 h on stream) of the first cycle (1.2 $\mu mol \cdot m^{-2} \cdot s^{-1}$). The rate in the second cycle over the $NiCr_2O_4$ sample could not be determined with confidence because of the major fluctuations in the product formation. Nevertheless, the activity of the $NiCr_2O_4$ sample in the second cycle showed an increase of five times on average compared to the initial rate of the first cycle (0.22 $\mu mol \cdot m^{-2} \cdot s^{-1}$). The XRD patterns of the spent $NiAl_2O_4$ and $NiCr_2O_4$ catalyst after the second cycle (**Figure C6**) suggest that the spinel structure in both

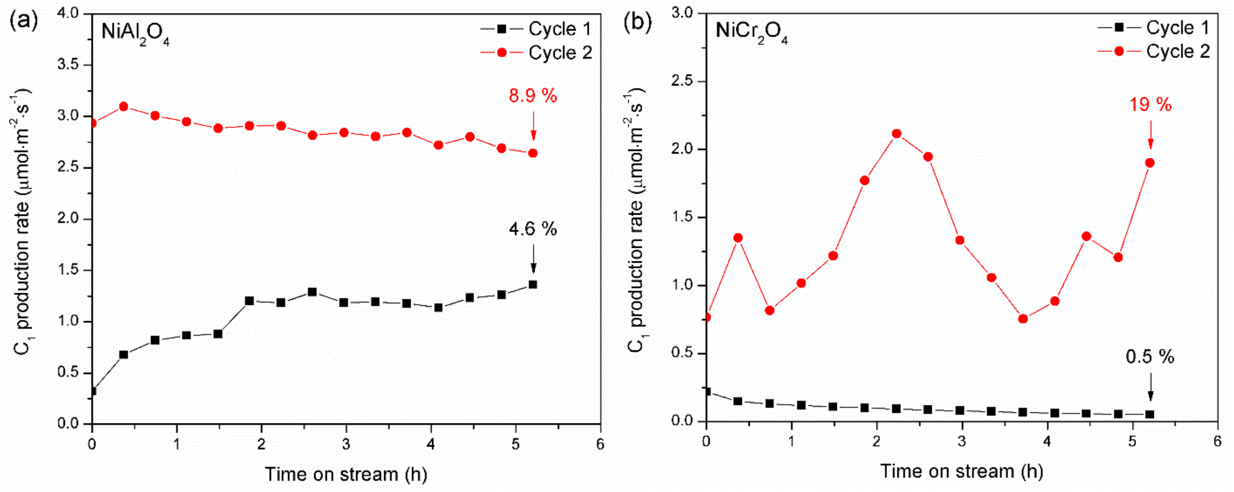

Figure 4.8 Rate of C_1 product formation during ethylene steam reforming cycles over the $NiAl_2O_4$ and $NiCr_2O_4$ spinel catalyst. The C_2H_4 conversion after 5 h on stream is indicated on the plots. Reaction conditions: 873 K, 1 g catalyst, 100 $cm^3 \cdot min^{-1}$ total flow, 25 % C_2H_4, 50 % H_2O, 5 % N_2 and 20 % Ar. The catalyst was thermally treated at 873 K in 100 $cm^3 \cdot min^{-1}$ air flow for 4 h in between the two cycles.

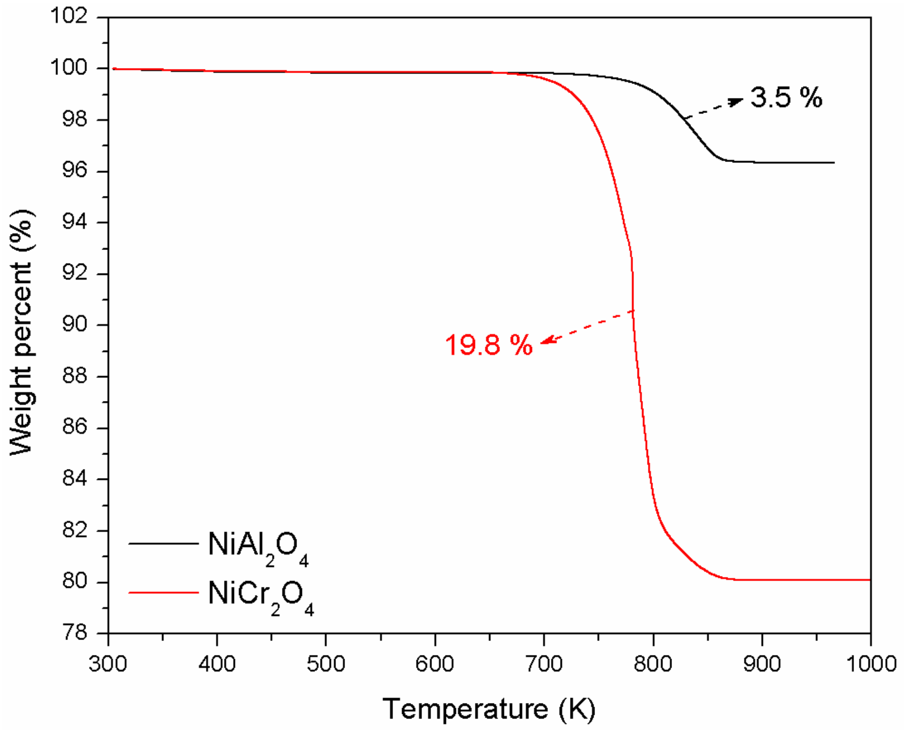

Figure 4.9 Thermogravimetric analysis in synthetic air of the spent $NiAl_2O_4$ and $NiCr_2O_4$ spinel catalysts after the 2nd cycle of ethylene steam reforming at 873 K. The labelled percentages are the maximum weight loss of the sample below 923 K.

catalysts was retained without any diffraction features corresponding to bulk Ni metal. The mass fraction of the coke deposited during the second cycle on the two catalysts was measured by TGA and compared in **Figure 4.9**. Even though the second reaction cycle (**Figure 4.8**) was slightly shorter than the previous steam reforming test (**Figure 4.5**), the amount of coke deposited on the spent $NiAl_2O_4$ and $NiCr_2O_4$ catalyst during the second cycle was 3.5 wt % and 19.8 wt % respectively (**Figure 4.9**), higher than the corresponding values measured from the previous steam reforming test (1.1 wt % and 2.0 wt %, respectively, **Figure 4.7**). Given the appreciable increase in steam reforming activity and the higher coking tendency observed in the second cycle, we speculate that a minor fraction of Ni^{2+} on the spinel surface reduced to metallic Ni^0 in the first cycle and potentially sintered into NiO particles upon oxidation. Previous studies have indicated that $NiAl_2O_4$ spinel can interact strongly with Ni metal particles and prevent further sintering of

Ni [76,78–80]. Therefore, the agglomeration of very small amounts of Ni metal formed on the $NiAl_2O_4$ catalyst may be inhibited by the stabilization of the substrate $NiAl_2O_4$ spinel phase. We expect that Ni is less stabilized by the $NiCr_2O_4$ spinel phase, leading to a larger extent of Ni agglomeration upon oxidation, which further enhances in activity and coke deposition during the second cycle.

4.4 Conclusions

The synthesized NiM_2O_4 (M = Al, Cr, Fe) catalysts adopt the spinel structure with the existence of Ni^{2+} and M^{3+} cations on the catalyst surface confirmed by the X-ray photoelectron spectroscopy. High temperature treatment with H_2 reduced Ni^{2+} to large Ni metal particles (detected by XRD) for all three NiM_2O_4 spinel catalysts, with the reduction of Fe^{3+} in $NiFe_2O_4$ facilitating Ni reduction in that sample. The $NiFe_2O_4$ catalyst was also reduced to Ni metal and Fe_3O_4 during steam reforming of ethylene at 873 K. The $NiAl_2O_4$ and $NiCr_2O_4$ catalyst were both active and significantly more stable than the $NiFe_2O_4$ catalyst in steam reforming of ethylene, with the rate over the $NiAl_2O_4$ catalyst being an order of magnitude greater than that over $NiCr_2O_4$. An oxidative regeneration treatment of $NiAl_2O_4$ and $NiCr_2O_4$ enhanced both the reforming rate and coke deposition amount, likely the result of trace Ni reducing to form metal particles on the surface. These observations suggest that periodic oxidative treatments for coke removal from Ni-containing barrier layers on steam cracker tubes might facilitate aggregation of surface Ni atoms followed by reduction to Ni metal particles in the highly reducing environment of an operating steam cracker.

4.5 References for Chapter 4

[1] S.M. Sadrameli, Thermal/catalytic cracking of hydrocarbons for the production of olefins: A state-of-the-art review I: Thermal cracking review, Fuel 140 (2015) 102-115.

[2] I. Amghizar, L.A. Vandewalle, K.M. Van Geem, G.B. Marin, New Trends in Olefin Production, Engineering. 3 (2017) 171-178.

[3] K. Yin, S. Mahamulkar, J. Xie, H. Shibata, A. Malek, L. Li, C.W. Jones, P. Agrawal, R.J. Davis, Catalytic reactions of coke with dioxygen and steam over alkaline-earth-metal-doped cerium-zirconium mixed oxides, Appl. Catal. A Gen. 535 (2017) 17-23.

[4] L. Yang, M.P. Bukhovko, G. Brezicki, A. Malek, L. Li, C.W. Jones, P.K. Agrawal, R.J. Davis, Steam reforming of ethylene over manganese-chromium spinel oxides, J. Catal. 380 (2019) 224-235.

[5] M.P. Bukhovko, L. Yang, L. Li, A. Malek, R.J. Davis, P.K. Agrawal, C.W. Jones, Gasification of radical coke with steam and steam-hydrogen mixtures over manganese-chromium oxides, Ind. Eng. Chem. Res. 59 (2020) 10813-10822.

[6] S. Mahamulkar, K. Yin, R.J. Davis, H. Shibata, A. Malek, C.W. Jones, P.K. Agrawal, In Situ Generation of Radical Coke and the Role of Coke-Catalyst Contact on Coke Oxidation, Ind. Eng. Chem. Res. 55 (2016) 5271-5278.

[7] A.E. Muñoz Gandarillas, K.M. Van Geem, M.F. Reyniers, G.B. Marin, Coking resistance of specialized coil materials during steam cracking of sulfur-free naphtha, Ind. Eng. Chem. Res. 53 (2014) 13644-13655.

[8] C.M. Schietekat, S.A. Sarris, P.A. Reyniers, L.B. Kool, W. Peng, P. Lucas, K.M. Van Geem, G.B. Marin, Catalytic Coating for Reduced Coke Formation in Steam Cracking Reactors, Ind. Eng. Chem. Res. 54 (2015) 9525-9535.

[9] S.H. Symoens, N. Olahova, A.E. Muñoz Gandarillas, H. Karimi, M.R. Djokic, M.F. Reyniers, G.B. Marin, K.M. Van Geem, State-of-the-art of Coke Formation during Steam Cracking : Anti-Coking Surface Technologies, Ind. Eng. Chem. Res. 57 (2018) 16117-16136.

[10] S. Mahamulkar, K. Yin, P.K. Agrawal, R.J. Davis, C.W. Jones, A. Malek, H. Shibata, Formation and Oxidation/Gasification of Carbonaceous Deposits: A Review, Ind. Eng. Chem. Res. 55 (2016) 9760-9818.

[11] S. Mahamulkar, K. Yin, T. Sulmonetti, H.T. Kwon, R.J. Davis, L. Li, H. Shibata, A. Malek, C.W. Jones, P.K. Agrawal, α-Alumina supported doped ceria catalysts for steam gasification and oxidation of radical coke, Chem. Eng. Res. Des. 151 (2019) 1-9.

[12] B. Bao, Z. Wang, H. Xu, J. Liu, Anti-coking Effect of $MnCr_2O_4$ Spinel Coating during Light Naphtha Thermal Cracking, Energy Procedia. 105 (2017) 4808-4813.

[13] B. Bao, J. Liu, H. Xu, B. Liu, W. Zhang, Inhibitory effect of $MnCr_2O_4$ spinel coating on coke formation during light naphtha thermal cracking, RSC Adv. 6 (2016) 68934-68941.

[14] A. Niaei, D. Salari, J. Towfighi, A. Chamandeh, R. Nabavi, Aluminized Steel and Zinc Coating for Reduction of Coke Formation in Thermal Cracking of Naphtha, Int. J. Chem. React. Eng., 6 (2008) Note S3.

[15] A. Niaei, D. Salari, N. Daneshvar, A. Chamandeh, R. Nabavi, Effect of Tube Materials and Special Coating on Coke Deposition in the Steam Cracking of Hydrocarbons, World Acad. Sci. Eng. Technol. 1 (2007) 41-43.

[16] J. Yan, Y. Gao, F. Yang, Y. Bai, Y. Liu, C. Yao, S. Hou, G. Liu, Cyclic carburizing behaviour of Al modified high Si-containing HP40 alloy, Corros. Sci. 67 (2013) 161-168.

[17] A.E. Muñoz Gandarillas, K.M. Van Geem, M.F. Reyniers, G.B. Marin, Influence of the reactor material composition on coke formation during ethane steam cracking, Ind. Eng. Chem. Res. 53 (2014) 6358-6371.

[18] S. Mahamulkar, K. Yin, M.T. Claure, R.J. Davis, L. Li, H. Shibata, A. Malek, C.W. Jones, P.K. Agrawal, Thermally stable α-alumina supported ceria for coking resistance and oxidation of radical coke generated in-situ, Fuel 218 (2018) 357-365.

[19] S.A. Sarris, N. Olahova, K. Verbeken, M.F. Reyniers, G.B. Marin, K.M. Van Geem, Optimization of the in Situ Pretreatment of High Temperature Ni-Cr Alloys for Ethane Steam Cracking, Ind. Eng. Chem. Res. 56 (2017) 1424-1438.

[20] A. Shaaban, Influence of $NiAl_2O_4$ spinel formation on the oxidation behavior of the Ni50Al alloy at 1273 K in air, Surf. Coat. Technol. 379 (2019) 125023.

[21] C. Jiménez-González, M. Gil-Calvo, B. de Rivas, J.R. González-Velasco, J.I. Gutiérrez-Ortiz, R. López-Fonseca, Oxidative Steam Reforming and Steam Reforming of Methane, Isooctane, and N-Tetradecane over an Alumina Supported Spinel-Derived Nickel Catalyst, Ind. Eng. Chem. Res. 55 (2016) 3920-3929.

[22] I. Sebai, A. Boulahaouache, M. Trari, N. Salhi, Preparation and characterization of 5%Ni/γ-Al_2O_3 catalysts by complexation with NH_3 derivatives active in methane steam reforming, Int. J. Hydrogen Energy. 44 (2019) 9949-9958.

[23] I.E. Achouri, N. Abatzoglou, N. Braidy, S. Bastien, New insights on the role of YSZ in a $NiAl_2O_4/Al_2O_3$-YSZ catalyst, Appl. Catal. A Gen. 497 (2015) 42-50.

[24] C. Fauteux-Lefebvre, N. Abatzoglou, J. Blanchard, F. Gitzhofer, Steam reforming of liquid hydrocarbons over a nickel-alumina spinel catalyst, J. Power Sources. 195 (2010) 3275-3283.

[25] C. Fauteux-Lefebvre, N. Abatzoglou, N. Braidy, I.E. Achouri, Diesel steam reforming with a nickel-alumina spinel catalyst for solid oxide fuel cell application, J. Power Sources. 196 (2011) 7673-7680.

[26] J.L. Rogers, M.C. Mangarella, A.D. D'Amico, J.R. Gallagher, M.R. Dutzer, E. Stavitski, J.T. Miller, C. Sievers, Differences in the Nature of Active Sites for Methane Dry Reforming and Methane Steam Reforming over Nickel Aluminate Catalysts, ACS Catal. 6 (2016) 5873-5886.

[27] B.C. Enger, R. Lødeng, J. Walmsley, A. Holmen, Inactive aluminate spinels as precursors for design of CPO and reforming catalysts, Appl. Catal. A Gen. 383 (2010) 119-127.

[28] M. Chamoumi, N. Abatzoglou, J. Blanchard, M.C. Iliuta, F. Larachi, Dry reforming of methane with a new catalyst derived from a negative value mining residue spinellized with nickel, Catal. Today. 291 (2017) 86-98.

[29] M. Chamoumi, N. Abatzoglou, $NiFe_2O_4$ production from α-Fe_2O_3 via improved solid state reaction: Application as catalyst in CH_4 dry reforming, Can. J. Chem. Eng. 94 (2016) 1801-1808.

[30] J.N. Kuhn, Z. Zhao, A. Senefeld-Naber, L.G. Felix, R.B. Slimane, C.W. Choi, U.S. Ozkan, Ni-olivine catalysts prepared by thermal impregnation: Structure, steam reforming activity, and stability,Appl. Catal. A Gen. 341 (2008) 43-49.

[31] M. Rangan, M.M. Yung, J.W. Medlin, NiW and NiRu bimetallic catalysts for ethylene steam reforming: Alternative mechanisms for sulfur resistance, Catal. Letters. 142 (2012) 718-727.

[32] L. Lutterotti, M. Bortolotti, G. Ischia, I. Lonardelli, H.R. Wenk, Rietveld texture analysis from diffraction images, Z. Kristallogr. Suppl. 26 (2007) 125-130.

[33] K. Yin, R.J. Davis, S. Mahamulkar, C.W. Jones, P. Agrawal, H. Shibata, A. Malek, Catalytic Oxidation of Solid Carbon and Carbon Monoxide over Cerium-Zirconium Mixed Oxides, AIChE J. 63 (2017) 725-738.

[34] R.D. Peelamedu, R. Roy, D.K. Agrawal, Microwave-induced reaction sintering of $NiAl_2O_4$, Mater. Lett. 55 (2002) 234-240.

[35] N. Salhi, A. Boulahouache, C. Petit, A. Kiennemann, C. Rabia, Steam reforming of methane to syngas over $NiAl_2O_4$ spinel catalysts, Int. J. Hydrogen Energy 36 (2011) 11433-11439.

[36] E. Leal, L.S. Neiva, J.P.L.M.L. Sousa, F. Argolo, H.M.C. Andrade, A.C.F.M. Costa, L. Gama, Evaluation of Glycine Excess over $NiAl_2O_4$ Catalysts Prepared by Combustion Reaction for Steam Methane Reforming, Mater. Sci. Forum 660-661 (2010) 916-921.

[37] Y.S. Han, J.B. Li, X.S. Ning, X.Z. Yang, B. Chi, Study on NiO excess in preparing $NiAl_2O_4$, Mater. Sci. Eng. A369 (2004) 241-244.

[38] X. Xu, J. Gao, W. Hong, Ni-based chromite spinel for high-performance supercapacitors, RSC Advances 6 (2016) 29646-29653.

[39] M. Ştefănescu, M. Barbu, P. Barvinschi, O. Ştefănescu, The obtaining of $NiCr_2O_4$ nanoparticles by unconventional synthesis methods, J. Therm. Anal. Calorim. 111 (2013) 1121-1127.

[40] P. Sivakumar, R. Ramesh, A. Ramanand, S. Ponnusamy, C. Muthamizhchelvan, Synthesis, studies and growth mechanism of ferromagnetic $NiFe_2O_4$ nanosheet, Appl. Surf. Sci. 258 (2012) 6648-6652.

[41] S.E. Ziemniak, L.M. Anovitz, R.A. Castelli, W.D. Porter, Magnetic contribution to heat capacity and entropy of nickel ferrite ($NiFe_2O_4$), J. Phys. Chem. Solids 68 (2007) 10-21.

[42] T.M. Naidu, P.V.L. Narayana, Synthesis and Characterization of Fe-TiO_2 and $NiFe_2O_4$ Nanoparticles and Its Thermal Properties, J. Nanosci. Tech. 5 (2019) 769-772.

[43] Y.B. Khollam, S.R. Dhage, H.S. Potdar, S.B. Deshpande, P.P. Bakare, S.D. Kulkarni, S.K. Date, Microwave hydrothermal preparation of submicron-sized spherical magnetite (Fe_3O_4) powders, Mater. Lett. 56 (2002) 571-577.

[44] S. Tiwari, R. Prakash, R.J. Choudhary, D.M. Phase, Oriented growth of Fe_3O_4 thin film on crystalline and amorphous substrates by pulsed laser deposition, J. Phys. D Appl. Phys. 40 (2007) 4943-4947.

[45] M. Ptak, M. Maczka, A. Gągor, A. Pikul, L. Macalik, J. Hanuza, Temperature-dependent XRD, IR, magnetic, SEM and TEM studies of Jahn-Teller distorted $NiCr_2O_4$ powders, J. Solid State Chem. 201 (2013) 270-279.

[46] R.J. Arnott, A. Wold, D.B. Rogers, Electron ordering transitions in several chromium spinel systems, J. Phys. Chem. Solids 25 (1964) 161-166.

[47] H. Furuhashi, M. Inagaki, S. Naka, Determination of cation distribution in spinels by X-ray diffraction method, J. inorg, nucl. Chem 35 (1973) 3009-3014.

[48] Z.Ž. Lazarević, Č. Jovalekić, D. Sekulić, M. Slankamenac, M. Romčević, A. Milutinović, N.Ž. Romčević, Characterization of Nanostructured Spinel $NiFe_2O_4$ Obtained by Soft Mechanochemical Synthesis, Sci. Sinter. 44 (2012) 331-339.

[49] R.B. Shalvoy, B.H. Davis, P.J. Reucroft, Studies of the Metal-Support Interaction in Coprecipitated Nickel on Alumina Methanation Catalysts Using X-Ray Photoelectron Spectroscopy (XPS), Surf. Interface Anal. 2 (1980) 11-16.

[50] C. Jiménez-González, Z. Boukha, B. de Rivas, J.R. González-Velasco, J.I. Gutiérrez-Ortiz, R. López-Fonseca, Behavior of Coprecipitated $NiAl_2O_4/Al_2O_3$ Catalysts for Low-Temperature Methane Steam Reforming, Energy Fuels 28 (2014) 7109-7121.

[51] L. Zhang, X. Wang, C. Chen, X. Zou, X. Shang, W. Ding, X. Lu, Investigation of mesoporous $NiAl_2O_4/MO_x$ (M = La, Ce, Ca, Mg)-γ-Al_2O_3 nanocomposites for dry reforming of methane, RSC Adv. 7 (2017) 33143-33154.

[52] M. Lenglet, F. Hochu, J. Dürr, M.H. Tuilier, Investigation of the chemical bonding in $3d^8$ nickel(II) charge transfer insulators (NiO, oxidic spinels) from ligand-field spectroscopy, Ni 2p XPS and X-ray absorption spectroscopy, Solid State Commun. 104 (1997) 793-798.

[53] G.C. Allen, S.J. Harris, J.A. Jutson, A study of a number of mixed transition metal oxide spinels using X-ray photoelectron spectroscopy, Appl. Surf. Sci. 37 (1989) 111-134.

[54] M. Lenglet, A. D'Huysser, C.K. Jørgensen, Optical Spectra, X-ray Photoelectron Spectra and XANES of Divalent Nickel in Mixed Spinels $NiFe_{2-x}Cr_xO_4$, Inorg. Chim. Acta 133 (1987) 61-65.

[55] L. Marchetti, F. Miserque, S. Perrin, M. Pijolat, XPS study of Ni-base alloys oxide films formed in primary conditions of pressurized water reactor, Surf. Interface Anal. 47 (2015) 632-642.

[56] R.S. Yadav, I. Kuřitka, J. Vilcakova, J. Havlica, J. Masilko, L. Kalina, J. Tkacz, V. Enev, M. Hajdúchová, Structural, magnetic, dielectric, and electrical properties of $NiFe_2O_4$ spinel ferrite nanoparticles prepared by honey-mediated sol-gel combustion, J. Phys. Chem. Solids 107 (2017) 150-161.

[57] M. Han, Z. Wang, Y. Xu, R. Wu, S. Jiao, Y. Chen, S. Feng, Physical properties of $MgAl_2O_4$, $CoAl_2O_4$, $NiAl_2O_4$, $CuAl_2O_4$, and $ZnAl_2O_4$ spinels synthesized by a solution combustion method, Mater. Chem. Phys. 215 (2018) 251-258.

[58] R. Benrabaa, A. Barama, H. Boukhlouf, J. Guerrero-Caballero, A. Rubbens, E. Bordes-Richard, A. Löfberg, R. Vannier, Physico-chemical properties and syngas production via dry reforming of methane over $NiAl_2O_4$ catalyst, Int. J. Hydrog. Energy 42 (2017) 12989-12996.

[59] T. Yamashita, P. Hayes, Analysis of XPS spectra of Fe^{2+} and Fe^{3+} ions in oxide materials, Appl. Surf. Sci. 254 (2008) 2441-2449.

[60] A.P. Grosvenor, B.A. Kobe, M.C. Biesinger, N.S. McIntyre, Investigation of multiplet splitting of Fe 2p XPS spectra and bonding in iron compounds, Surf. Interface Anal. 36 (2004) 1564-1574.

[61] J. Li, Y. Lin, X. Liu, Q. Zhang, H. Miao, T. Zhang, B. Wen, The study of transition on $NiFe_2O_4$ nanoparticles prepared by co-precipitation/calcination, Phase Transit. 84 (2011) 49-57.

[62] Z. Boukha, C. Jiménez-González, B. de Rivas, J.R. González-Velasco, J.I. Gutiérrez-Ortiz, R. López-Fonseca, Synthesis, characterisation and performance evaluation of spinel-derived Ni/Al_2O_3 catalysts for various methane reforming reactions, Appl. Catal. B Environ. 158-159 (2014) 190-201.

[63] L. Blas, P. Dutournié, S. Dorge, L. Josien, D. Kehrli, A. Lambert, Thermal stability study of $NiAl_2O_4$ binders for Chemical Looping Combustion application, Fuel. 182 (2016) 50-56.

[64] N. Sahli, C. Petit, A.C. Roger, A. Kiennemann, S. Libs, M.M. Bettahar, Ni catalysts from $NiAl_2O_4$ spinel for CO_2 reforming of methane, Catal. Today 113 (2006) 187-193.

[65] Y. Ramesh, P. Thirumala Bai, B. Hari Babu, N. Lingaiah, K.S. Rama Rao, P.S. Sai Prasad, Oxidative dehydrogenation of ethane to ethylene on $Cr_2O_3/Al_2O_3-ZrO_2$ catalysts: the influence of oxidizing agent on ethylene selectivity, Appl. Petrochem. Res. 4 (2014) 247-252.

[66] B.M. Weckhuysen, R.A. Schoonheydt, J.-M. Jehng, I.E. Wachs, S.J. Cho, R. Ryoo, S. Kijistra, E. Poels, Combined DRS-RS-EXAFS-XANES-TPR study of supported chromium catalysts, J. Chem. Soc. Faraday Trans. 91 (1995) 3245-3253.

[67] T.P. Braga, B.M.C. Sales, A.N. Pinheiro, W.T. Herrera, E. Baggio-Saitovitch, A. Valentini, Catalytic properties of cobalt and nickel ferrites dispersed in mesoporous silicon oxide for ethylbenzene dehydrogenation with CO_2, Catal. Sci. Technol. 1 (2011) 1383-1392.

[68] Y. Huang, S. Wang, A. Tsai, S. Kameoka, Catalysts prepared from copper-nickel ferrites for the steam reforming of methanol, J. Power Sources 281 (2015) 138-145.

[69] C.W. Su, E.L. Wang, Y.B. Zhang, F.J. He, $Ni_{1-x}Fe_x$ ($0.1 < x < 0.75$) alloy foils prepared from a fluorborate bath using electrochemical deposition, J. Alloys Compd. 474 (2009) 190-194.

[70] W.S. Chang, Y. Wei, J.M. Guo, F.J. He, Thermal Stability of Ni-Fe Alloy Foils Continuously Electrodeposited in a Fluorborate Bath, Open J. Met. 2 (2012) 18-23.

[71] K.S. Dijith, R. Aiswarya, M. Praveen, S. Pillai, K.P. Surendran, Polyol derived Ni and NiFe alloys for effective shielding of electromagnetic interference, Mater. Chem. Front. 2 (2018) 1829-1841.

[72] S.D. Leith, S. Ramli, D.T. Schwartz, Characterization of Ni_xFe_{1-x} ($0.10 < x < 0.95$) Electrodeposition from a Family of Sulfamate-Chloride Electrolytes, J. Electrochem. Soc. 146 (1999) 1431-1435.

[73] H. Li, F. Ebrahimi, Synthesis and characterization of electrodeposited nanocrystalline nickel-iron alloys, Mater. Sci. Eng. A347 (2003) 93-101.

[74] Y. Unutulmazsoy, R. Merkle, D. Fischer, J. Mannhart, The oxidation kinetics of thin nickel films between 250 and 500 °C, J. Maier, Phys. Chem. Chem. Phys. 19 (2017) 9045-9052.

[75] Z. Li, C. Chanéac, G. Berger, S. Delaunay, A. Graff, G. Lefèvre, Mechanism and kinetics of magnetite oxidation under hydrothermal conditions, RSC Adv. 9 (2019) 33633-33642.

[76] J. Du, J. Gao, F. Gu, J. Zhuang, B. Lu, L. Jia, G. Xu, Q. Liu, F. Su, A strategy to regenerate coked and sintered Ni/Al_2O_3 catalyst for methanation reaction, Int. J. Hydrogen Energy 43 (2018) 20661-20670.

[77] Z. Boukha, C. Jiménez-González, M. Gil-calvo, B. de Rivas, J.R. González-Velasco, J.I. Gutiérrez-Ortiz, R. López-Fonseca, MgO/$NiAl_2O_4$ as a new formulation of reforming catalysts: Tuning the surface properties for the enhanced partial oxidation of methane, Appl. Catal. B Environ. 199 (2016) 372-383.

[78] P.H. Bolt, F.H.P.M. Habraken, J.W. Geus, On the Role of a $NiAl_2O_4$ Intermediate Layer in the Sintering Behavior of Ni/α-Al_2O_3, J. Catal. 151 (1995) 300-306.

[79] L. Zhou, L. Li, N. Wei, J. Li, J. Basset, Effect of $NiAl_2O_4$ Formation on Ni/Al_2O_3 Stability during Dry Reforming of Methane, ChemCatChem 7 (2015) 2508-2516.

[80] N. Ichikuni, D. Murata, S. Shimazu, T. Uematsu, Promoting effect of $NiAl_2O_4$ for supported Ni particles on sprayed Ni/Al_2O_3 catalysts, Catal. Lett. 69 (2000) 33-36.

Chapter 5 Influence of Co on ethylene steam reforming over Co-Cr-O spinel catalysts

Work presented in this chapter was published as:

L. Yang, M.P. Bukhovko, A. Malek, L. Li, C.W. Jones, P.K. Agrawal, R.J. Davis, Influence of Co on ethylene steam reforming over Co-Cr-O spinel catalysts, Catal. Lett. (2020).

Abstract

Two Co-Cr-O spinel catalysts with different stoichiometry were synthesized and characterized by X-ray diffraction, X-ray photoelectron spectroscopy, N_2 physisorption and temperature-programmed reduction in H_2. Excess Co in $Co_{1.5}Cr_{1.5}O_4$ existed as Co^{3+} that substituted for Cr^{3+} in the octahedral sites of the spinel lattice. High temperature treatment of the spinel catalysts in H_2 resulted in stepwise reduction of Co^{3+} to Co^{2+} and eventually to Co metal. Both the $CoCr_2O_4$ and $Co_{1.5}Cr_{1.5}O_4$ catalyst were active and structurally stable in ethylene steam reforming under differential reaction conditions at 873 K, with the areal reforming rate over $Co_{1.5}Cr_{1.5}O_4$ being one order-of-magnitude greater than that over $CoCr_2O_4$. The steady state reforming rate after oxidation was comparable to that over the fresh catalyst for both $CoCr_2O_4$ and $Co_{1.5}Cr_{1.5}O_4$, indicating the stability of the spinel structure against reduction under steam reforming conditions.

5.1 Introduction

Transition metal oxides have been widely studied as potential candidates for catalyzing oxidation of hazardous components from industries and automobile exhausts in light of their high stability and low cost [1,2]. Among those, the remarkable performance of Cr_2O_3 was identified in the oxidation of various compounds, including CO [3], CH_4 [4] and heavier hydrocarbons [5]. The application of Cr_2O_3 catalysts remains limited due to concerns about gradually forming Cr^{6+} species (*e.g.*, CrO_3) that are significantly more volatile and poisonous [6]. Thus Cr-containing spinel catalysts have been explored given the improved stability of Cr^{3+} in the spinel lattice [7,8]. In particular, the $CoCr_2O_4$ spinel catalyst exhibited promising performance in the catalytic oxidation of hydrocarbons [8,9].

Despite extensive studies on the $CoCr_2O_4$ spinel in catalytic oxidation, the activity and stability of the $CoCr_2O_4$ spinel under reductive environments was rarely explored. Moreover, the reactivity of Co^{3+} , which was suggested to play an important role in the oxidation of CO [10] and hydrocarbons [11] over Co_3O_4, is not favored in stoichiometric $CoCr_2O_4$ where Co predominantly exists as Co^{2+}. In our previous studies, the activity and stability of $MnCr_2O_4$ [12] and $NiCr_2O_4$ [13] were evaluated in ethylene steam reforming, where ethylene was oxidized to carbon oxides accompanied by H_2 production. Specifically, the following reactions occurred simultaneously:

Steam Reforming:

$$C_2H_4 + 2H_2O \rightarrow 2CO + 4H_2 \quad \Delta H_r^o = 210.1\ kJ\cdot mol^{-1} \tag{5.1}$$

Water Gas Shift:

$$CO + H_2O \rightarrow CO_2 + H_2 \quad \Delta H_r^o = -41.2\ kJ\cdot mol^{-1} \tag{5.2}$$

Methanation:

$$CO + 3H_2 \rightarrow CH_4 + H_2O \quad \Delta H_r^o = -205.9\ kJ\cdot mol^{-1} \tag{5.3}$$

Herein, we have extended our ethylene steam reforming studies to the Co-Cr-O spinel system. Two spinel catalysts, $CoCr_2O_4$ and $Co_{1.5}Cr_{1.5}O_4$, were synthesized and thoroughly characterized. The reforming rate over the catalysts and stability against reduction to Co metal was evaluated in catalytic steam reforming of ethylene under the same conditions to investigate the influence of excess Co^{3+} in the spinel as well as to compare performance to $MnCr_2O_4$ and $NiCr_2O_4$ spinel catalysts.

5.2 Experimental methods

5.2.1 Catalyst synthesis

The two Co-Cr-O spinel catalysts were synthesized from a conventional sol-gel method. Specifically, $Co(NO_3)_2 \cdot 6H_2O$ (98 %, Sigma-Aldrich) and $Cr(NO_3)_3 \cdot 9H_2O$ (98 %, Sigma-Aldrich) of the desired molar ratio (Cr/Co = 2.0 for $CoCr_2O_4$ and Cr/Co = 1.0 for $Co_{1.5}Cr_{1.5}O_4$) were dissolved in 100 cm^3 distilled deionized water with a total metal concentration of 0.4 M at ambient temperature. A 50 cm^3 aqueous solution containing 1.6 M citric acid (99.5 %, Sigma-Aldrich) was then added under vigorous stirring. The mixed solution was stirred at 368 K until the formation of a viscous gel. The gel precursor was transferred to an oven and dried overnight at 393 K in air. The dried gel was then pulverized and thermally treated in 100 $cm^3 \cdot min^{-1}$ air flow at 1273 K for 4 h based on the conditions reported for Co-Cr-O spinel formation [14]. The pretreatment conditions were identical to those in our previous studies on ethylene steam reforming over $MnCr_2O_4$ [12] and $NiCr_2O_4$ [13]. The resulting powders were denoted as fresh $CoCr_2O_4$ and fresh $Co_{1.5}Cr_{1.5}O_4$ catalyst depending on the starting stoichiometry.

5.2.2 Catalyst characterization

Physisorption of N_2 at 77 K was conducted on a Micromeritics ASAP 2020 analyzer with a sample of 2 g catalyst for the measurement of specific surface area and porosity, using the Brunauer-Emmett-Teller (BET) and the Barrett-Joyner-Halenda (BJH) method of analysis, respectively. The sample was evacuated at 473 K for 4 h prior to N_2 physisorption.

Powder X-ray diffraction (XRD) patterns of the catalysts were recorded on a PANalytical Empyrean X-ray Diffractometer equipped with a Cu Kα radiation source in Bragg-Brentano geometry. The sample was scanned at a constant rate of $5°\cdot min^{-1}$ within a 2θ range from 15° to 80° under ambient conditions. The collected XRD patterns were refined using the Material Analysis Using Diffraction (MAUD) software package [15].

Temperature-programmed reduction in H_2 (H_2-TPR) of the catalysts was measured on a Micromeritics AutoChem II 2920 Analyzer. A sample of 300 mg catalyst was first pretreated in 20 $cm^3\cdot min^{-1}$ Ar flow at 773 K for 0.5 h and cooled down to 323 K in the Ar flow. Upon the introduction of 20 $cm^3\cdot min^{-1}$ flow of 5 vol % H_2 in Ar, the sample was heated to 1273 K at a constant ramp rate of 10 $K\cdot min^{-1}$ with the consumption of H_2 monitored by a thermal conductivity detector (TCD).

X-ray photoelectron spectroscopy (XPS) was performed on a Phi VersaProbe III Scanning X-ray Photoelectron Spectrometer. The sample was excited by an incident X-ray of 100 μm beam size and 25 W power output from a monochromatic Al Kα radiation source (1486.7 eV). Kinetic energy of the photoelectrons was analyzed by a hemispherical energy analyzer under a passing energy of 55 eV and a stepwise dwell time of 100 ms to ensure high energy resolution. The XPS depth profiles were acquired by etching the sample surface with a high-energy Ar ion beam (3 kV bias, 3 μm×3 μm beam size) during the intervals between the collections. The sample was etched while rotating horizontally for 30 s in each cycle. A dual charge compensation using a low-energy electron flood gun and a low-energy Ar ion beam was applied in all scans. The reported binding energy was calibrated with respect to C1s (284.8 eV) from the adventitious carbon on the surface.

Thermogravimetric analysis (TGA) of the spent catalysts was carried out using a TA Instruments SDT Q600 thermogravimetric analyzer. The weight change of the sample was recorded during a temperature-programmed oxidation procedure, in which 30 mg catalyst was heated to 973 K from ambient temperature at a constant ramp rate of 10 K·min^{-1} in 40 cm^{3}·min^{-1} synthetic air (20 vol % O_2 in He) flow.

5.2.3 Ethylene steam reforming

The two Co-Cr-O spinel catalysts were evaluated in catalytic steam reforming of ethylene at 873 K under atmospheric total pressure. A typical feed flow of 100 cm^{3}·min^{-1} containing 25 vol % C_2H_4, 50 vol % H_2O, 5 vol % N_2 and 20 vol % Ar was directed to 1 g catalyst loaded in a vertical, down-flow, fixed-bed quartz reactor (10.5 mm I.D. × 12.75 mm O.D.). The catalyst was sieved to 250-425 μm for $CoCr_2O_4$ and 70-180 μm for $Co_{1.5}Cr_{1.5}O_4$ prior to reaction. Although two different particle sizes were utilized in this study because of difficulty forming compressed pellets, reforming rates measured on both samples were not influenced by intraparticle mass transfer artifacts as confirmed by the Weisz-Prater criterion [16]. Liquid water with dissolved O_2 removed by a N_2 purge was introduced by a syringe pump (ISCO, 500D) into a steel evaporator maintained at 413 K, where steam was generated and mixed with other gas components supplied from mass flow controllers (Brooks, 5850E). Upon removal of unreacted H_2O in the effluent gas through condensation, the produced CO_2 was measured by an infrared gas analyzer (Fuji Electric ZPA) and the produced H_2, CO and CH_4 were measured by a gas chromatograph (Agilent 7890A) equipped with a CarboPlot P7 column and a TCD. To properly compare the intrinsic activity of the catalysts, reaction rates were normalized by the exposed surface area instead of catalyst mass. Assessed under an ethylene conversion below 10 %, the characteristic rate of steam reforming is defined on the basis of overall C_1 product formation (CO, CO_2 and CH_4) normalized by the BET surface area:

$$r_{C_1} = \frac{F(CO) + F(CO_2) + F(CH_4)}{S_{BET}} \tag{5.4}$$

The product-based ethylene conversion is evaluated assuming 100 % carbon recovery from the C_1 products:

$$C_2H_4 \text{ conversion } (\%) = \frac{F(CO) + F(CO_2) + F(CH_4)}{2F_0(C_2H_4)} \times 100\ \% \tag{5.5}$$

The product selectivity is defined as the mole fraction of a certain component with respect to all quantified steam reforming products (H_2, CO, CO_2 and CH_4):

$$\text{Selectivity of X } (\%) = \frac{F(X)}{F(H_2) + F(CO) + F(CO_2) + F(CH_4)} \times 100\ \% \tag{5.6}$$

where F(X) denotes the molar flowrate of component X measured downstream of the reactor, $F_0(C_2H_4)$ denotes the molar flowrate of C_2H_4 in the feed gas and S_{BET} denotes the BET surface area of the catalyst from N_2 physisorption. Given the identical reaction conditions and similar ethylene conversion levels to our previous work [12], the ethylene reforming rates reported in the present study were not affected by mass and heat transfer artifacts.

5.3 Results and discussion

5.3.1 Characterization of the $CoCr_2O_4$ and $Co_{1.5}Cr_{1.5}O_4$ catalyst

The textural properties of the catalysts assessed from N_2 physisorption are summarized in **Table 5.1**. The BET surface area of both $CoCr_2O_4$ and $Co_{1.5}Cr_{1.5}O_4$ catalysts was very low (*i.e.*, less than 10 $m^2 \cdot g^{-1}$) as a result of the high temperature treatment. Similar to the case of $MnCr_2O_4$ and $Mn_{1.5}Cr_{1.5}O_4$ [12], the introduction of excess Co caused a substantial decrease in the BET surface area of $Co_{1.5}Cr_{1.5}O_4$ (0.58 $m^2 \cdot g^{-1}$) compared to the stoichiometric $CoCr_2O_4$ (5.4 $m^2 \cdot g^{-1}$). The low cumulative pore volume calculated from the BJH method suggested both catalysts were essentially non-porous. The estimated pore diameter (70-140 Å) was likely representative of the voids between the particle aggregates [17]. Therefore, the measured BET surface area of the catalysts was attributed solely to external surface area.

Table 5.1 Textural properties of the fresh $CoCr_2O_4$ and $Co_{1.5}Cr_{1.5}O_4$ catalysts assessed from N_2 physisorption

Catalyst	BET surface area ($m^2 \cdot g^{-1}$)	Pore volume ($cm^3 \cdot g^{-1}$)^a
$CoCr_2O_4$	5.4	0.019
$Co_{1.5}Cr_{1.5}O_4$	0.58	0.0011

^{a} BJH cumulative pore volume.

The phase composition of the catalysts was characterized by XRD. As shown in **Figure 5.1**, the $CoCr_2O_4$ sample exhibited the typical diffraction patterns corresponding to a cubic spinel structure without detectable crystalline Cr_2O_3 impurities that appeared when Cr was in excess [18]. By analogy to our previously reported Mn-rich $Mn_{1.5}Cr_{1.5}O_4$ spinel [12], the diffraction features observed for the $Co_{1.5}Cr_{1.5}O_4$ sample are attributed to a Co-rich spinel phase according to prior reports [19–22], in which the octahedrally coordinated Cr^{3+} cations are partially substituted by the Co^{3+} cations as a result of the introduction of excess Co. The lattice parameter of the spinel phase in $CoCr_2O_4$ (8.332 Å) and $Co_{1.5}Cr_{1.5}O_4$ (8.270 Å) was acquired from Rietveld refinement, which is in agreement with the respective range of values of 8.327-8.333 Å for $CoCr_2O_4$ and 8.267-8.273 Å for $Co_{1.5}Cr_{1.5}O_4$ from prior reports [19–21], while both being significantly larger than the range of values of 8.082-8.083 Å reported for the Co_3O_4 spinel phase [19–21]. The significant decrease in the lattice constant of $Co_{1.5}Cr_{1.5}O_4$ with respect to the stoichiometric $CoCr_2O_4$ spinel is consistent with the distortion resulting from the replacement of Cr^{3+} by smaller Co^{3+} [21]. The occupancy from Rietveld refinement for both tetrahedrally and octahedrally coordinated cations was unity for the two Co-Cr-O spinel catalysts.

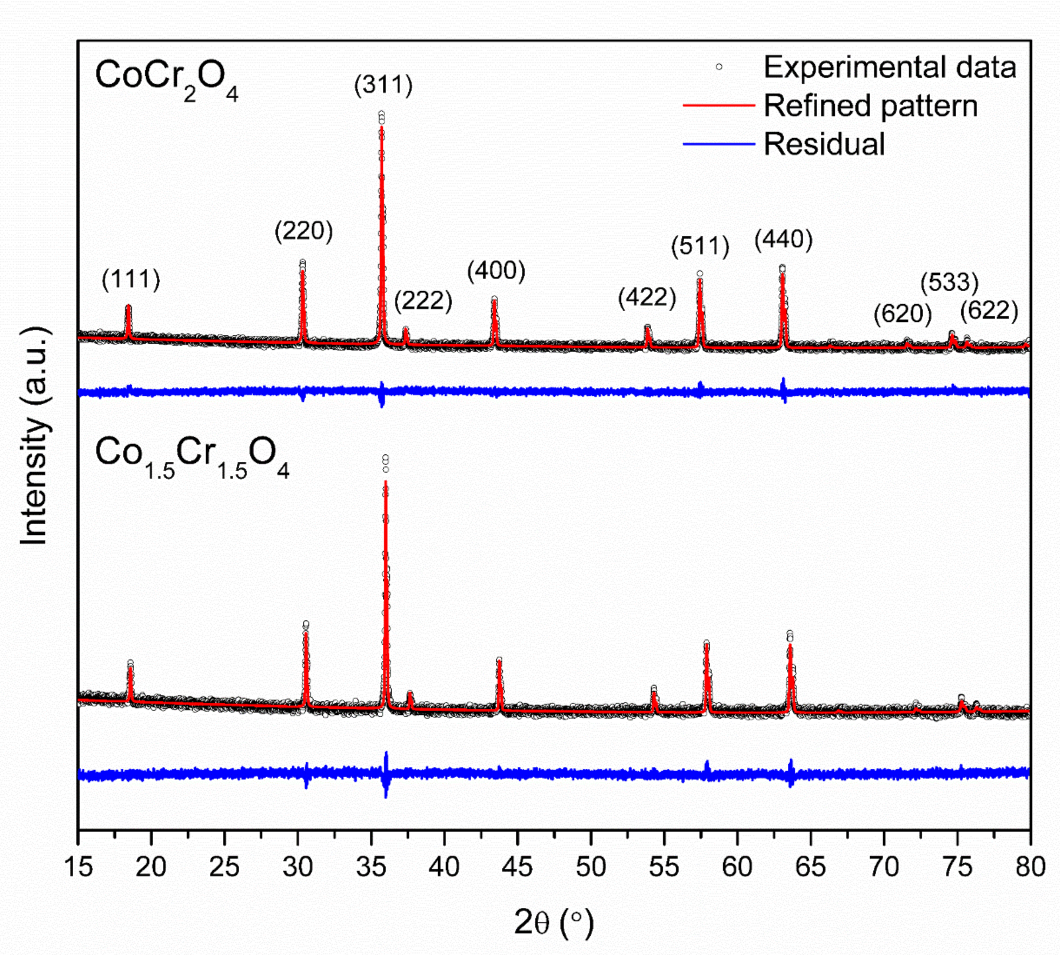

Figure 5.1 Rietveld refinement of the XRD patterns of the fresh $CoCr_2O_4$ and $Co_{1.5}Cr_{1.5}O_4$ catalysts. The refined lattice parameter for $CoCr_2O_4$ and $Co_{1.5}Cr_{1.5}O_4$ is 8.332 Å and 8.270 Å, respectively.

The redox properties of the catalysts were probed by H_2-TPR with the reduction profiles shown in **Figure 5.2a**. The results indicated the Co cations in the Co-Cr-O spinels were substantially more stable against reduction compared to Co_3O_4, which underwent complete reduction to Co metal at much lower temperatures (*i.e.*, below 823 K) [23,24]. The very small H_2 consumption below 450 K observed for both samples (**Figure 5.2a**, inset) was attributed to the reduction of surface Cr^{6+} species that occurred over various Cr-based spinel oxides [25]. The reduction feature initiated at about 900 K in the profile of $CoCr_2O_4$ was assigned to the reduction of tetrahedrally coordinated Co^{2+} in the spinel lattice to Co^0 metal [26]. Consistent with this assignment, the formation of a trace amount of Co metal particles was detected in the XRD pattern of the $CoCr_2O_4$ sample after reduction in H_2 (**Figure 5.2b**). However, due to a low reduction degree of Co^{2+} (3.3 %), the small amount of Cr_2O_3 formed was dispersed and not detectable by XRD. Comparatively, the $Co_{1.5}Cr_{1.5}O_4$ sample exhibited a reduction feature at 960 K followed by a rapid increase in H_2 uptake above 1100 K, which was assigned to the stepwise reduction of Co^{3+} to Co^{2+} and Co^{2+} to Co^0, respectively [27]. Unfortunately, the overall reduction degree of Co (6.5 %) could not be separated into individual reduction events as multiple processes occurred simultaneously. While the appearance of CoO diffraction feature was in accordance with the reduction of Co^{3+} to Co^{2+}, the diffraction feature corresponding to Co metal was not observed in the reduced $Co_{1.5}Cr_{1.5}O_4$ sample (**Figure 5.2b**). We speculate that the CoO formed upon reduction of Co^{3+} in the octahedral sites interacts strongly with the Cr-containing spinel lattice and therefore impedes continuous reduction of the spinel to Co metal by retarding the outward diffusion of Co^{2+} and Co^{3+} cations [24,28,29]. Moreover, very small Co metal particles exposed to air during collection of the XRD patterns will likely oxidize surface Co metal.

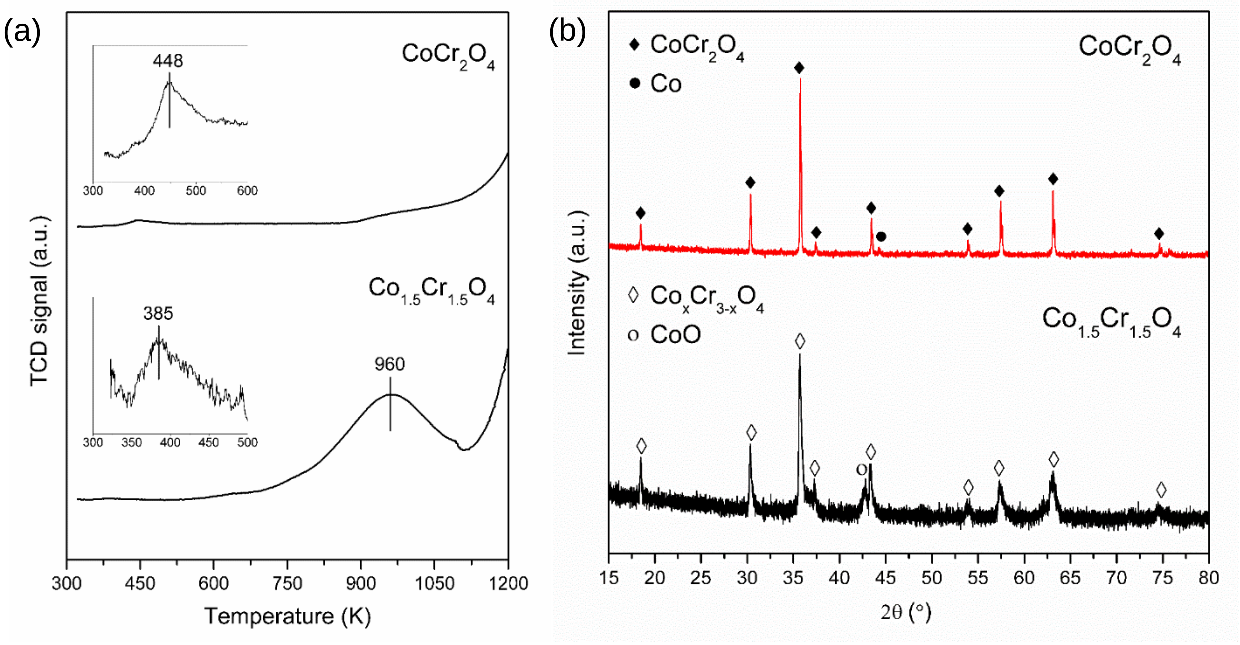

Figure 5.2 (a) Temperature-programed reduction of the fresh $CoCr_2O_4$ and $Co_{1.5}Cr_{1.5}O_4$ catalysts in H_2. A minor H_2 consumption peak at low T from the reduction of surface Cr^{6+} species is shown in the inset. (b) X-ray diffraction patterns of the $CoCr_2O_4$ and $Co_{1.5}Cr_{1.5}O_4$ catalysts after H_2-TPR to 1273 K. The remaining spinel structure in the reduced $Co_{1.5}Cr_{1.5}O_4$ was labelled as $Co_xCr_{3-x}O_4$ since the stoichiometry changed as a result of CoO formation.

The chemical speciation of Co and Cr on the catalyst surface was investigated by XPS. Results from previous reports have shown that the 2p binding energy of Co^{2+} and Co^{3+} did not correlate explicitly with the oxidation state, so discrimination between Co^{2+} and Co^{3+} from the 2p binding energy can be ambiguous [24,30,31]. As shown in **Figure 5.3a**, the spectra of Co $2p_{3/2}$ were deconvoluted into two peaks including the major $2p_{3/2}$ energy state and a satellite feature from Co^{2+} and Co^{3+} [32,33] according to the report from Xie *et al.* [34]. The Co $2p_{3/2}$ binding energy of the $CoCr_2O_4$ sample (780.9 eV) was slightly higher than that of the $Co_{1.5}Cr_{1.5}O_4$ sample (780.4 eV). The predominant presence of Co^{2+} on the surface of $CoCr_2O_4$ was confirmed by the intense satellite feature at 786.4 eV [34,35], whereas the weak satellite feature at 784.6 eV in $Co_{1.5}Cr_{1.5}O_4$ was consistent with those seen in Co_3O_4 and Co-excess Co-Cr-O spinels, suggesting the presence of Co^{3+} on the surface of that sample [24,36]. The Cr $2p_{3/2}$ spectra were deconvoluted

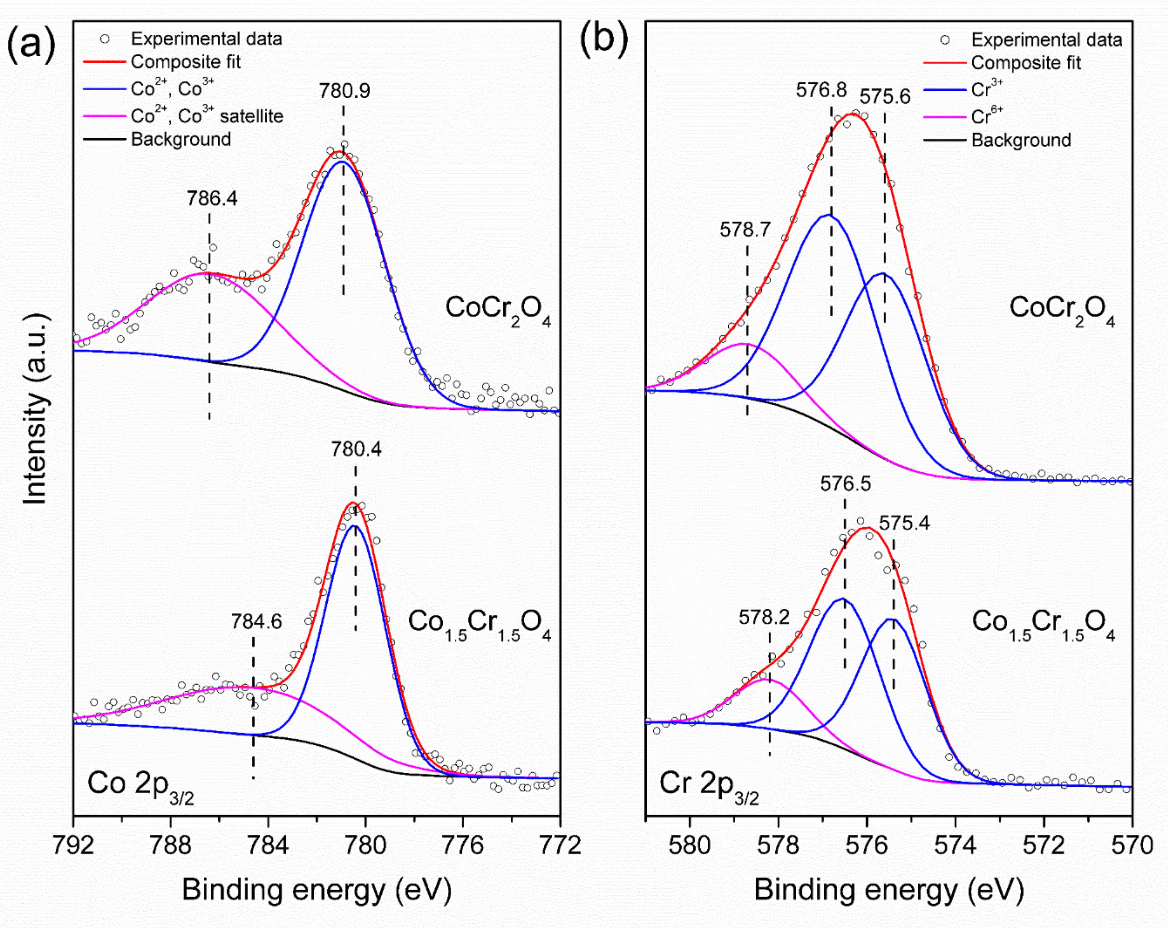

Figure 5.3 X-ray photoelectron spectra at (a) Co $2p_{3/2}$ and (b) Cr $2p_{3/2}$ region on the surface of the fresh $CoCr_2O_4$ and $Co_{1.5}Cr_{1.5}O_4$ catalysts.

into three peaks as described by Keturakis *et al.* [37] with one peak at *ca.* 578.9 eV assigned to Cr^{6+} and two peaks at *ca.* 576.6 and 575.6 eV assigned to Cr^{3+} to account for the multiplet splitting of Cr^{3+} [38]. As shown in **Figure 5.3b**, the broad peak with the highest binding energy of 578.7 eV in $CoCr_2O_4$ and 578.2 eV in $Co_{1.5}Cr_{1.5}O_4$ suggested the presence of Cr^{6+} species on the surface of both samples, which was supported by the weak low temperature reduction features observed in H_2-TPR (**Figure 5.2a**). The two peaks of lower binding energies in the $CoCr_2O_4$ (576.8 and 575.6 eV) and $Co_{1.5}Cr_{1.5}O_4$ (576.5 and 575.4 eV) samples were associated with Cr^{3+} cations likely residing in the spinel lattice. The fraction of Cr^{6+} with respect to total surface Cr (Cr^{3+} and Cr^{6+})

estimated from the peak areas was 12 % for $CoCr_2O_4$ and 15 % for $Co_{1.5}Cr_{1.5}O_4$, respectively, indicating Cr^{3+} to be the predominant form of existence for surface Cr in both samples.

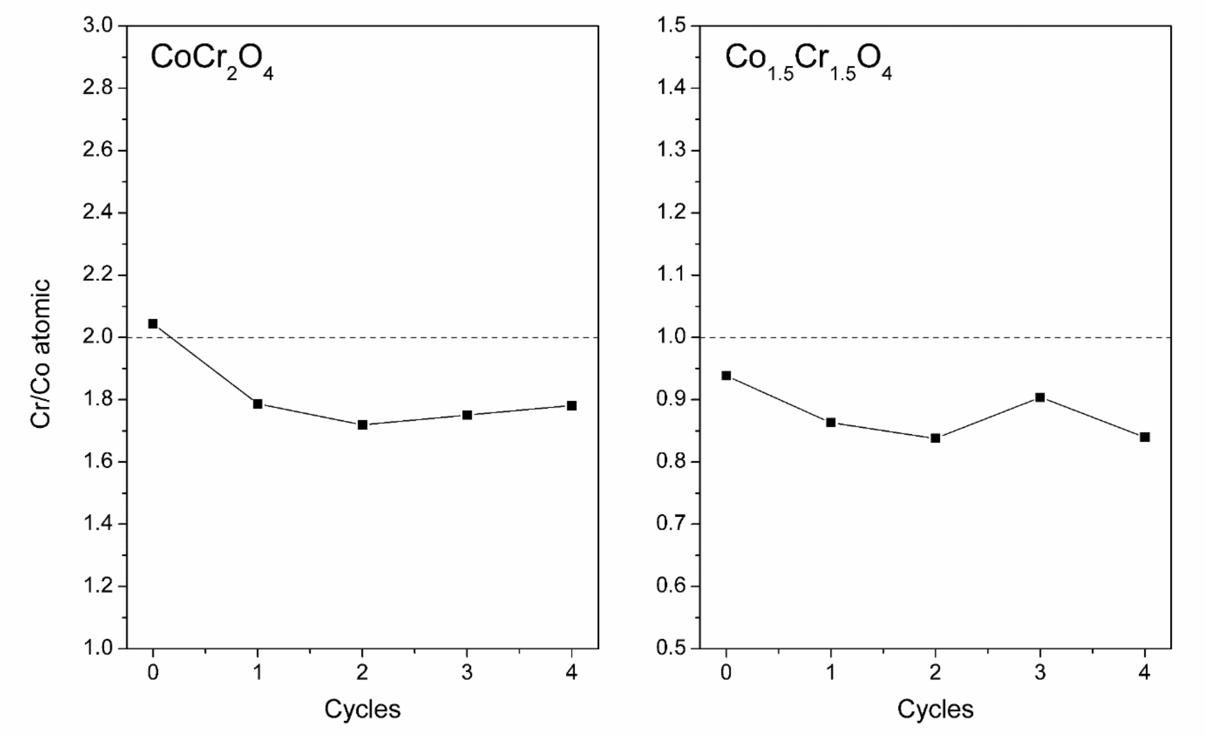

Figure 5.4 Profiles of atomic Cr/Co ratio in the fresh $CoCr_2O_4$ and $Co_{1.5}Cr_{1.5}O_4$ catalysts measured by XPS. Cycle 0: as prepared; Cycle 1-4: etched with Ar ion beam prior to the measurement.

The elemental composition of the catalysts was analyzed by XPS depth profiling using Ar ion beam etching. As shown in **Figure 5.4**, the Cr/Co ratio measured on the surface of the $CoCr_2O_4$ sample was 2.0, which was slightly higher than the range of values from 1.7 to 1.8 observed in the later four cycles with pre-sputtering before each measurement. The Cr/Co ratios measured for the $Co_{1.5}Cr_{1.5}O_4$ sample appeared in a narrow range of 0.8 to 0.9 regardless of the measuring depth. Despite a minor enrichment of Cr possibly on the surface of $CoCr_2O_4$, the depth profiles indicated a fairly uniform elemental distribution for both samples that was consistent with the desired stoichiometry. The spectra associated with the Co $2p_{3/2}$ and Cr $2p_{3/2}$ regions of the $Co_{1.5}Cr_{1.5}O_4$ sample during depth profiling are shown in **Figure 5.5**. The chemical state of Co in the bulk spinel was unfortunately inaccessible from the current depth profiling since Co cations were rapidly reduced to Co^0 metal upon exposure to the Ar ion beam, as evident by the development of the peak at 778.2 eV corresponding to metallic Co. The chemical state of Cr did not change appreciably with the probing depth except the decline of the broad Cr^{6+} feature at 578.2 eV starting from the first cycle. A similar trend was observed in the XPS spectra during depth profiling of $CoCr_2O_4$ (not shown).

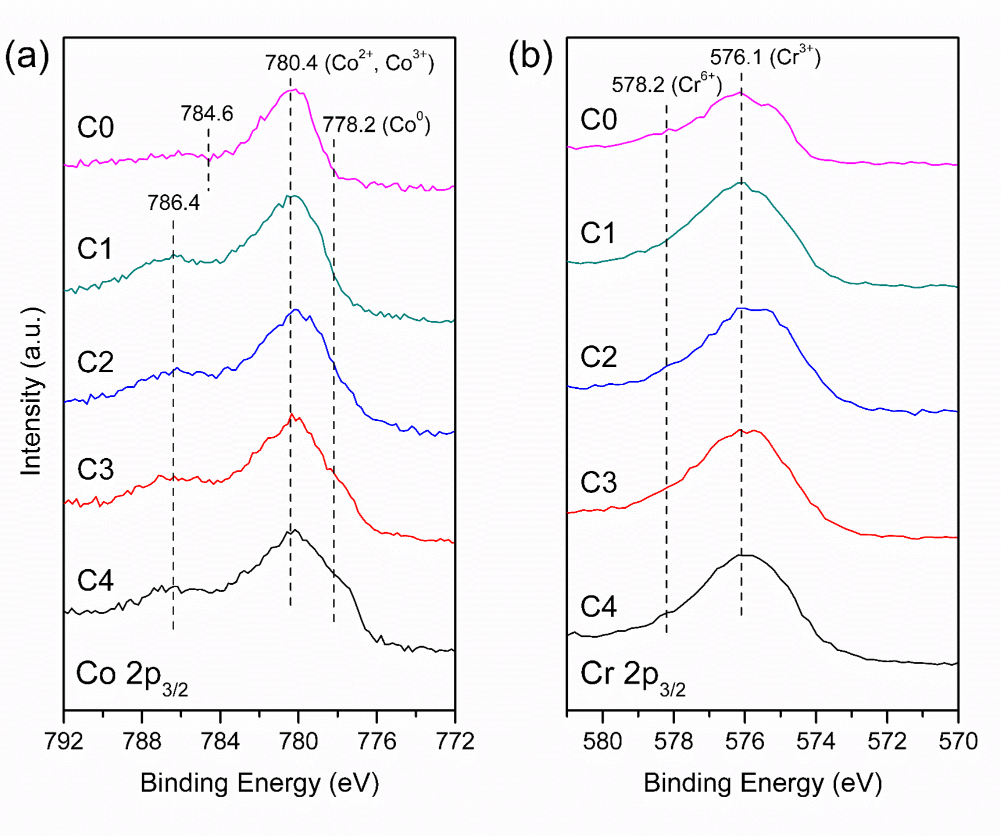

Figure 5.5 X-ray photoelectron spectra during depth profiling at (a) Co $2p_{3/2}$ and (b) Cr $2p_{3/2}$ region of the fresh $Co_{1.5}Cr_{1.5}O_4$ catalyst. Cycle 0: as prepared; Cycles 1-4: etched with Ar ion beam prior to the measurement.

5.3.2 Rate and stability of the $CoCr_2O_4$ and $Co_{1.5}Cr_{1.5}O_4$ catalyst in ethylene steam reforming

The catalytic performance of the $CoCr_2O_4$ and $Co_{1.5}Cr_{1.5}O_4$ catalysts was evaluated in ethylene steam reforming at 873 K, a temperature at which the background ethylene conversion was negligible [12]. Since Cr_2O_3 was found to be nearly inactive for ethylene steam reforming

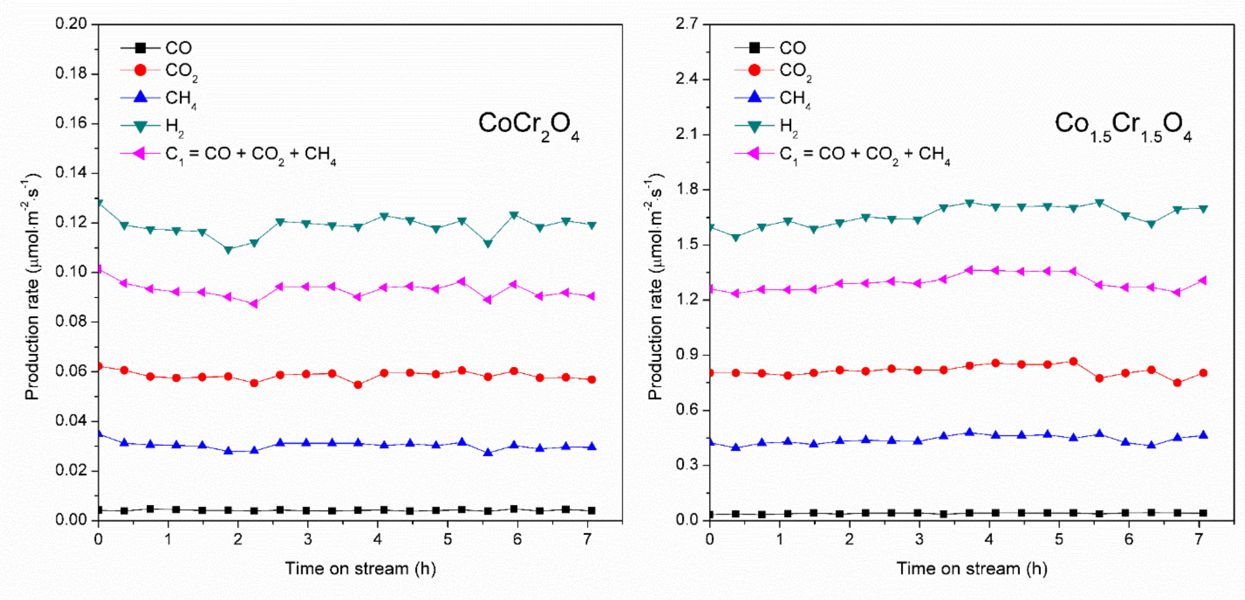

Figure 5.6 Product formation rate during ethylene steam reforming over the fresh $CoCr_2O_4$ and $Co_{1.5}Cr_{1.5}O_4$ catalysts. Reaction conditions: 873 K, 1 g catalyst, 100 cm^{3}·min^{-1} total flow, 25 % C_2H_4, 50 % H_2O, 5 % N_2 and 20 % Ar.

under identical reaction conditions [12], the observed reforming activity for the Co-Cr-O spinel oxides was attributed to the Co sites. As shown in **Figure 5.6**, a steady rate of formation for H_2 and C_1 molecules (CO, CO_2 and CH_4) was observed over both catalysts after introduction of the reactants. Both catalysts exhibited stable steam reforming activity without appreciable deactivation up to 7 h on stream, suggesting severe coke formation did not occur. As listed in **Table 5.2**, the product-based ethylene conversion over the $Co_{1.5}Cr_{1.5}O_4$ catalyst (2.0 %) was slightly higher than that over the $CoCr_2O_4$ catalyst (1.3 %) for an equivalent mass loading of

Table 5.2 Rate and product distribution of ethylene steam reforming over the fresh $CoCr_2O_4$ and $Co_{1.5}Cr_{1.5}O_4$ catalysts

Catalyst	C_2H_4 conversion (%)[a]	C_1 production rate (μmol·m^{-2}·s^{-1})	Product selectivity (%)			
			CO	CO_2	CH_4	H_2
$CoCr_2O_4$	1.3	0.093	2	28	14	56
$Co_{1.5}Cr_{1.5}O_4$	2.0	1.3	1	28	15	56

[a] Product-based conversion. Reaction conditions: 873 K, 1 g catalyst, 100 cm^{3}·min^{-1} total flow, 25 % C_2H_4, 50 % H_2O, 5 % N_2 and 20 % Ar.

catalyst in the reactor. The product distribution favoring H_2 and CO_2 was observed for both catalysts, which was attributed to the nearly equilibrated water-gas shift reaction that occurred simultaneously with ethylene steam reforming. The steady state rate of C_1 formation over $CoCr_2O_4$ (0.093 $\mu mol\cdot m^{-2}\cdot s^{-1}$) was comparable to the steady state rate over $MnCr_2O_4$ (0.13 $\mu mol\cdot m^{-2}\cdot s^{-1}$) [12] and the initial rate over $NiCr_2O_4$ (0.20 $\mu mol\cdot m^{-2}\cdot s^{-1}$) [13] under identical conditions (see **Table 5.3**). Along with the results from H_2-TPR (**Figure 5.2a**), this comparison suggested the steam reforming activity was likely from the stable Co-Cr-O spinel surfaces without severe decomposition of the spinel structure to form Co metal particles. Interestingly, the steady state rate of C_1 formation over $Co_{1.5}Cr_{1.5}O_4$ (1.3 $\mu mol\cdot m^{-2}\cdot s^{-1}$) was an order-of-magnitude greater compared to $CoCr_2O_4$ (0.093 $\mu mol\cdot m^{-2}\cdot s^{-1}$), which potentially resulted from Co^{3+} on the surface that was proposed as the active site for the oxidation of hydrocarbons [39,40]. The structure and oxidation state of Co in the octahedral Co sites during steam reforming conditions remain undetermined.

Table 5.3 Comparison of ethylene steam reforming rates over the MCr_2O_4 spinel catalysts

Catalyst	C_2H_4 conversion (%)^a	C_1 production rate ($\mu mol\cdot m^{-2}\cdot s^{-1}$)	Source
$CoCr_2O_4$	1.3	0.093	This work
$MnCr_2O_4$	1.8	0.13	Ref. [12]
$NiCr_2O_4$	2.1^b	0.20^b	Ref. [13]

[a] Product-based conversion. Reaction conditions: 873 K, 1 g catalyst, 100 $cm^3\cdot min^{-1}$ total flow, 25 % C_2H_4, 50 % H_2O, 5 % N_2 and 20 % Ar.

[b] Initial results at t < 1 h.

The spent $CoCr_2O_4$ and $Co_{1.5}Cr_{1.5}O_4$ catalysts were re-oxidized and then evaluated in ethylene steam reforming for a second cycle to examine whether slow reduction of Co cations to Co^0 metal occurred during the first cycle. As shown in **Figure 5.7**, the rate of C_1 formation over the re-oxidized $CoCr_2O_4$ (0.086 $\mu mol\cdot m^{-2}\cdot s^{-1}$, second cycle) was stable and nearly identical to that

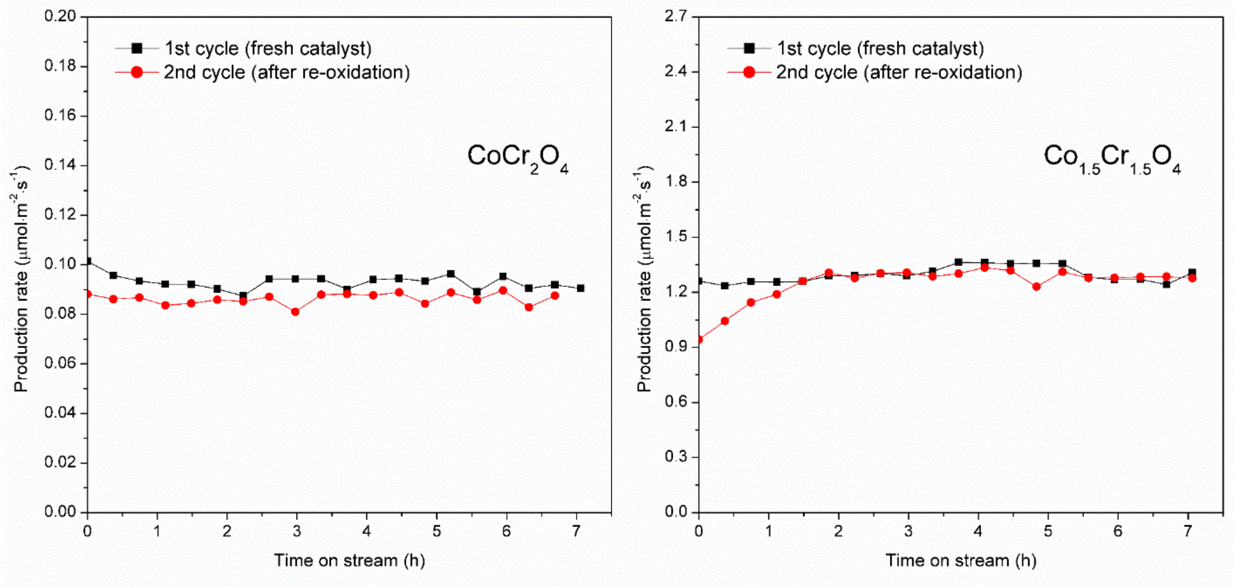

Figure 5.7 Comparison of C_1 formation rate during ethylene steam reforming over the fresh and re-oxidized $CoCr_2O_4$ and $Co_{1.5}Cr_{1.5}O_4$ catalysts. Reaction conditions: 873 K, 1 g catalyst, 100 $cm^3 \cdot min^{-1}$ total flow, 25 % C_2H_4, 50 % H_2O, 5 % N_2 and 20 % Ar. The catalysts were re-oxidized at 873 K for 4 h under 100 $cm^3 \cdot min^{-1}$ air flow in between the two cycles.

of the fresh catalyst (0.093 $\mu mol \cdot m^{-2} \cdot s^{-1}$, first cycle). This comparison suggests the reduction of Co^{2+} in the $CoCr_2O_4$ spinel lattice to Co^0 metal was negligible under reaction conditions and did not contribute to the observed reforming activity. These results contrast the behavior of $NiCr_2O_4$ where the reforming rate increased substantially in the second cycle as a result of the formation of NiO agglomerates upon re-oxidation [13]. Interestingly, the re-oxidized $Co_{1.5}Cr_{1.5}O_4$ exhibited an induction period for about 1.5 h before reaching steady state during the second cycle, over which the C_1 formation rate gradually increased from 0.94 $\mu mol \cdot m^{-2} \cdot s^{-1}$ and plateaued at a rate of 1.3 $\mu mol \cdot m^{-2} \cdot s^{-1}$ that was comparable with the first cycle. Although the reason for the induction period was unclear, the consistency in the steady state rate between the two cycles nevertheless indicated the stability of the $Co_{1.5}Cr_{1.5}O_4$ catalyst against the formation of Co metal particles. We speculate this phenomenon was related to the interconversion between Co^{3+} and Co^{2+}. In particular, the Co^{3+} on the surface was potentially reduced to Co^{2+} during steam reforming based on the H_2-TPR results

(**Figure 5.2a**), forming a CoO-like layer with octahedrally coordinated Co^{2+}. These octahedral Co^{2+} sites might be partially converted to the less reactive tetrahedral Co^{2+} sites when oxidized to Co_3O_4 during the re-oxidation [36,39], whereas this process was perhaps reversible when the catalyst was exposed to the reductive environment during the second cycle of steam reforming.

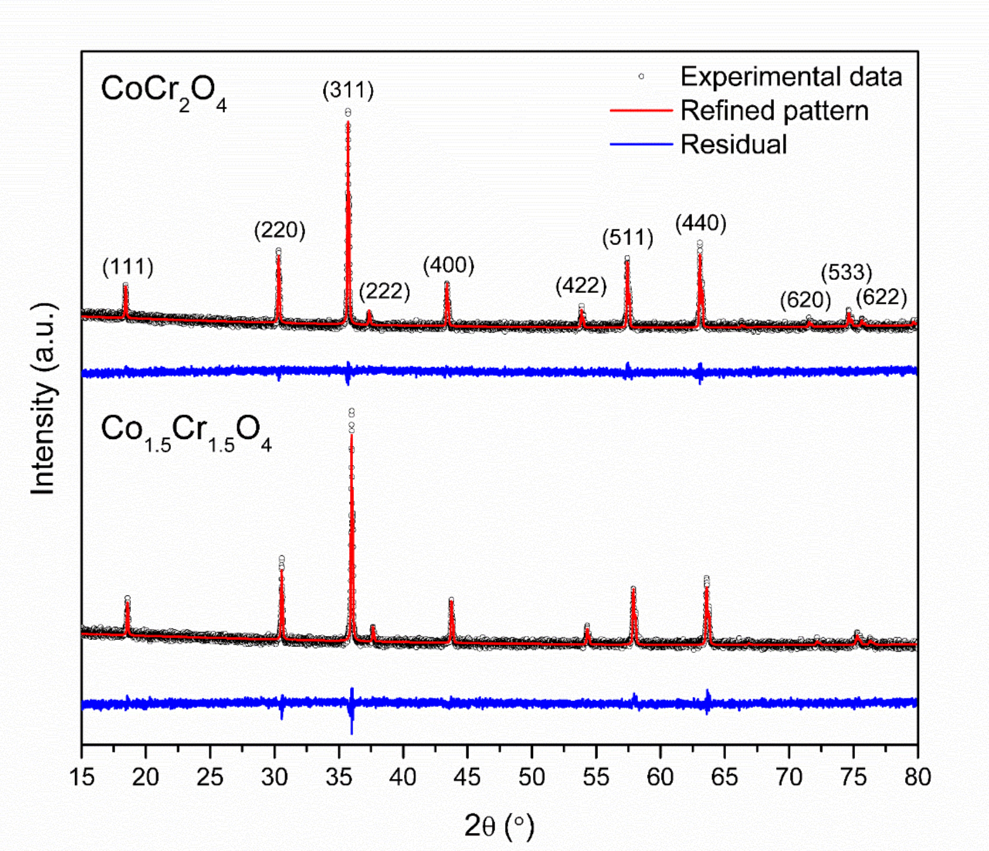

Figure 5.8 Rietveld refinement of the XRD patterns of the $CoCr_2O_4$ and $Co_{1.5}Cr_{1.5}O_4$ catalysts after two ethylene steam reforming cycles. The refined lattice parameter for $CoCr_2O_4$ and $Co_{1.5}Cr_{1.5}O_4$ is 8.332 Å and 8.270 Å, respectively.

The stability of the spinel structure in both catalysts was also evident from the XRD patterns after the second steam reforming cycle. As shown in **Figure 5.8**, diffraction features corresponding to CoO or metallic Co resulting from the decomposition of the spinel structure were not detected in either of the two catalysts. The refined lattice parameter for the $CoCr_2O_4$ (8.332 Å) and $Co_{1.5}Cr_{1.5}O_4$ (8.270 Å) spent catalysts after the second cycle remained identical to the respective value of the fresh catalyst, suggesting most of the excess Co^{3+} cations in $Co_{1.5}Cr_{1.5}O_4$ were retained in the lattice under reaction conditions. The occupancy for both tetrahedrally and octahedrally coordinated cations in the two catalysts remained unity. As expected from the steady reforming rate observed over both catalysts (after 1.5 h on stream), the amount of coke deposited during the second reforming cycle measured by temperature-programmed oxidation (**Figure 5.9**) was negligible over either $CoCr_2O_4$ or $Co_{1.5}Cr_{1.5}O_4$ (*i.e.*, less than 0.5 wt %).

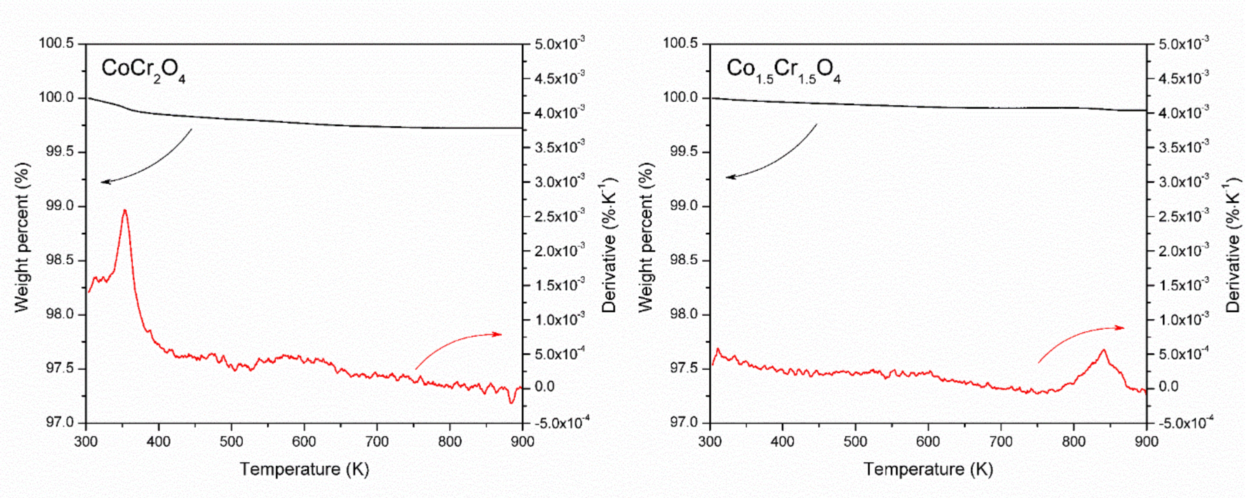

Figure 5.9 Thermogravimetric analysis profiles during temperature-programmed oxidation of the $CoCr_2O_4$ and $Co_{1.5}Cr_{1.5}O_4$ catalysts in synthetic air after two ethylene steam reforming cycles.

5.4 Conclusions

The synthesized $CoCr_2O_4$ and $Co_{1.5}Cr_{1.5}O_4$ catalysts both adopted a cubic spinel structure. The excess Co in $Co_{1.5}Cr_{1.5}O_4$ was attributed to octahedrally coordinated Co^{3+} that partially substituted for Cr^{3+} in the stoichiometric $CoCr_2O_4$ spinel lattice, resulting in a significant decrease in lattice constant. High temperature treatment in H_2 reduced the Co^{2+} in the $CoCr_2O_4$ spinel lattice to Co metal particles, whereas the reduction of Co^{3+} to Co^{2+} in $Co_{1.5}Cr_{1.5}O_4$ occurred at lower temperatures. Both the $CoCr_2O_4$ and $Co_{1.5}Cr_{1.5}O_4$ catalyst were active and structurally stable for ethylene steam reforming at 873 K. The areal reforming rate over $Co_{1.5}Cr_{1.5}O_4$ was one order-of-magnitude greater than that over $CoCr_2O_4$, which was potentially related to the presence of Co^{3+}

on the catalyst surface as evident by X-ray photoelectron spectroscopy. The steady state rate of ethylene steam reforming over both catalysts after re-oxidation was comparable to the respective rate from the fresh catalysts, suggesting an outstanding stability of the Co-Cr-O spinel structure against reduction to Co metal under steam reforming conditions.

5.5 References for Chapter 5

[1] J. Zeng, X. Liu, J. Wang, H. Lv, T. Zhu, Catalytic oxidation of benzene over MnO_x/TiO_2 catalysts and the mechanism study, J. Mol. Catal. A Chem. 408 (2015) 221-227.

[2] L.F. Liotta, H. Wu, G. Pantaleo, A.M. Venezia, Co_3O_4 nanocrystals and Co_3O_4-MO_x binary oxides for CO, CH_4 and VOC oxidation at low temperatures: A review, Catal. Sci. Technol. 3 (2013) 3085-3102.

[3] A.A. Ali, M. Madkour, F. Al Sagheer, M.I. Zaki, A.A. Nazeer, Low-temperature catalytic CO oxidation over non-noble, efficient chromia in reduced graphene oxide and graphene oxide nanocomposites, Catalysts. 10 (2020) 105.

[4] S. Ordóñez, J.R. Paredes, F.V. Díez, Sulphur poisoning of transition metal oxides used as catalysts for methane combustion, Appl. Catal. A Gen. 341 (2008) 174-180.

[5] J.B. Wang, M.S. Chou, Kinetics of catalytic oxidation of benzene, n-hexane, and emission gas from a refinery oil/water separator over a chromium oxide catalyst, J. Air Waste Manag. Assoc. 50 (2000) 227-233.

[6] B. Guo, I.M. Kennedy, The speciation and morphology of chromium oxide nanoparticles in a diffusion flame, Aerosol Sci. Technol. 38 (2004) 424-436.

[7] D. Fino, N. Russo, G. Saracco, V. Specchia, Catalytic removal of NO_x and diesel soot over nanostructured spinel-type oxides, J. Catal. 242 (2006) 38-47.

[8] D. Fino, N. Russo, G. Saracco, V. Specchia, CNG engines exhaust gas treatment via Pd-Spinel-type-oxide catalysts, Catal. Today. 117 (2006) 559-563.

[9] D.C. Kim, S.K. Ihm, Application of spinel-type cobalt chromite as a novel catalyst for combustion of chlorinated organic pollutants, Environ. Sci. Technol. 35 (2001) 222-226.

[10] H.F. Wang, R. Kavanagh, Y.L. Guo, Y. Guo, G. Lu, P. Hu, Origin of extraordinarily high catalytic activity of Co_3O_4 and its morphological chemistry for CO oxidation at low temperature, J. Catal. 296 (2012) 110-119.

[11] X. Ma, X. Yu, X. Yang, M. Lin, M. Ge, Hydrothermal Synthesis of a Novel Double-Sided Nanobrush Co_3O_4 Catalyst and Its Catalytic Performance for Benzene Oxidation, ChemCatChem. 11 (2019) 1214-1221.

[12] L. Yang, M.P. Bukhovko, G. Brezicki, A. Malek, L. Li, C.W. Jones, P.K. Agrawal, R.J. Davis, Steam reforming of ethylene over manganese-chromium spinel oxides, J. Catal. 380 (2019) 224-235.

[13] L. Yang, M.P. Bukhovko, A. Malek, L. Li, C.W. Jones, P.K. Agrawal, R.J. Davis, Steam reforming of ethylene over nickel based spinel oxides, Appl. Catal. A Gen. 603 (2020) 117739.

[14] J. Östby, M. Chen, Thermodynamic assessment of the CoO_x-$CrO_{1.5}$ system, 485 (2009) 427-434.

[15] L. Lutterotti, M. Bortolotti, G. Ischia, I. Lonardelli, H.R. Wenk, Rietveld texture analysis from diffraction images, Z. Kristallogr. Suppl. 26 (2007) 125-130.

[16] M.E. Davis, R.J. Davis, Fundamentals of Chemical Reaction Engineering, McGraw-Hill Higher Education, 2003.

[17] K. Yin, S. Mahamulkar, J. Xie, H. Shibata, A. Malek, L. Li, C.W. Jones, P. Agrawal, R.J. Davis, Catalytic reactions of coke with dioxygen and steam over alkaline-earth-metal-doped cerium-zirconium mixed oxides, Appl. Catal. A Gen. 535 (2017) 17-23.

[18] B.Y. Kim, J.W. Yoon, K. Lim, S.H. Park, J.W. Yoon, J.H. Lee, Hollow spheres of $CoCr_2O_4$-Cr_2O_3 mixed oxides with nanoscale heterojunctions for exclusive detection of indoor xylene, J. Mater. Chem. C. 6 (2018) 10767-10774.

[19] A.N. Hansson, S. Linderoth, M. Mogensen, M.A.J. Somers, X-ray diffraction investigation of phase stability in the Co-Cr-O and the Fe-Co-Cr-O systems in air at 1323 K, J. Alloys Compd. 402 (2005) 194-200.

[20] H.S.C. O'Neill, The influence of next nearest neighbours on cation radii in spinels: the example of the Co_3O_4-$CoCr_2O_4$ solid solution, Mineral. Mag. 67 (2003) 547-554.

[21] W.M. Liao, P.P. Zhao, B.H. Cen, A.P. Jia, J.Q. Lu, M.F. Luo, Co-Cr-O mixed oxides for low-temperature total oxidation of propane: Structural effects, kinetics, and spectroscopic investigation, Chinese J. Catal. 41 (2020) 442-453.

[22] P. Bracconi, L. Berthod, L.C. Dufour, Ann. Chim. Fr. 4 (1979) 331-338.

[23] J. Zhong, Y. Zeng, D. Chen, S. Mo, M. Zhang, M. Fu, J. Wu, Z. Su, P. Chen, D. Ye, Toluene oxidation over Co^{3+}-rich spinel Co_3O_4: Evaluation of chemical and by-product species identified by in situ DRIFTS combined with PTR-TOF-MS, J. Hazard. Mater. 386 (2020) 121957.

[24] J. Chen, X. Zhang, H. Arandiyan, Y. Peng, H. Chang, J. Li, Low temperature complete combustion of methane over cobalt chromium oxides catalysts, Catal. Today. 201 (2013) 12-18.

[25] J. Wang, G. Yang, L. Cheng, E.W. Shin, Y. Men, Three-dimensionally ordered macroporous spinel-type MCr_2O_4 (M = Co, Ni, Zn, Mn) catalysts with highly enhanced catalytic performance for soot combustion, Catal. Sci. Technol. 5 (2015) 4594-4601.

[26] S.A. Hosseini, M.C. Alvarez-Galvan, J.L.G. Fierro, A. Niaei, D. Salari, MCr_2O_4 (M=Co, Cu, and Zn) nanospinels for 2-propanol combustion: Correlation of structural properties with catalytic performance and stability, Ceram. Int. 39 (2013) 9253-9261.

[27] Y. Wang, P. Yang, G. Liu, L. Xu, M. Jia, W. Zhang, D. Jiang, Stability and deactivation of spinel-type cobalt chromite catalysts for ortho-selective alkylation of phenol with methanol, Catal. Commun. 9 (2008) 2044-2047.

[28] P. Bracconi, L.C. Dufour, Hydrogen reduction of cobalt-chromium spinel oxides. I. Stoichiometric cobalt chromite, J. Phys. Chem. 79 (1975) 2395-2400.

[29] P. Bracconi, L.C. Dufour, Hydrogen reduction of cobalt-chromium spinel oxides. II. $CoCr_2O_4$-Co_3O_4 solid solutions, J. Phys. Chem. 79 (1975) 2400-2405.

[30] M.C. Biesinger, B.P. Payne, A.P. Grosvenor, L.W.M. Lau, A.R. Gerson, R.S.C. Smart, Resolving surface chemical states in XPS analysis of first row transition metals, oxides and hydroxides: Cr, Mn, Fe, Co and Ni, Appl. Surf. Sci. 257 (2011) 2717-2730.

[31] S. Mo, S. Li, J. Li, Y. Deng, S. Peng, J. Chen, Y. Chen, Rich surface Co(III) ions-enhanced Co nanocatalyst benzene/toluene oxidation performance derived from $Co^{II}Co^{III}$ layered double hydroxide, Nanoscale. 8 (2016) 15763-15773.

[32] C. Huck-Iriart, L. Soler, A. Casanovas, C. Marini, J. Prat, J. Llorca, C. Escudero, Unraveling the Chemical State of Cobalt in Co-Based Catalysts during Ethanol Steam Reforming: An in Situ Study by Near Ambient Pressure XPS and XANES, ACS Catal. 8 (2018) 9625-9636.

[33] C.A.F. Vaz, D. Prabhakaran, E.I. Altman, V.E. Henrich, Experimental study of the interfacial cobalt oxide in Co_3O_4/ α-Al_2O_3 (0001) epitaxial films, Phys. Rev. B 80 (2009) 155457.

[34] J. Xie, J.D. Kammert, N. Kaylor, J.W. Zheng, E. Choi, H.N. Pham, X. Sang, E. Stavitski, K. Attenkofer, R.R. Unocic, A.K. Datye, R.J. Davis, Atomically Dispersed Co and Cu on N-Doped Carbon for Reactions Involving C-H Activation, ACS Catal. 8 (2018) 3875-3884.

[35] Y. Wang, A.P. Jia, M.F. Luo, J.Q. Lu, Highly active spinel type $CoCr_2O_4$ catalysts for dichloromethane oxidation, Appl. Catal. B Environ. 165 (2015) 477-486.

[36] Y. Tang, L. Ma, J. Dou, C.M. Andolina, Y. Li, H. Ma, S.D. House, X. Zhang, J. Yang, F. Tao, Transition of surface phase of cobalt oxide during CO oxidation, Phys. Chem. Chem. Phys. 20 (2018) 6440-6449.

[37] C.J. Keturakis, M. Zhu, E.K. Gibson, M. Daturi, F. Tao, A.I. Frenkel, I.E. Wachs, Dynamics of CrO_3-Fe_2O_3 Catalysts during the High-Temperature Water-Gas Shift Reaction: Molecular Structures and Reactivity, ACS Catal. 6 (2016) 4786-4798.

[38] E. Ünveren, E. Kemnitz, S. Hutton, A. Lippitz, W.E.S. Unger, Analysis of highly resolved x-ray photoelectron Cr 2p spectra obtained with a Cr_2O_3 powder sample prepared with adhesive tape, Surf. Interface Anal. 36 (2004) 92-95.

[39] X. Wang, Y. Liu, T. Zhang, Y. Luo, Z. Lan, K. Zhang, J. Zuo, L. Jiang, R. Wang, Geometrical-Site-Dependent Catalytic Activity of Ordered Mesoporous Co-Based Spinel for Benzene Oxidation: In Situ DRIFTS Study Coupled with Raman and XAFS Spectroscopy, ACS Catal. 7 (2017) 1626-1636.

[40] C.Y. Ma, Z. Mu, J.J. Li, Y.G. Jin, J. Cheng, G.Q. Lu, Z.P. Hao, S.Z. Qiao, Mesoporous Co_3O_4 and Au/Co_3O_4 catalysts for low-temperature oxidation of trace ethylene, J. Am. Chem. Soc. 132 (2010) 2608-2613.

Chapter 6 Conclusions and future directions

6.1 Concluding remarks

Synthetic powder catalyst samples ($Mn_xCr_{3-x}O_4$) based on the conventional $MnCr_2O_4/Cr_2O_3$ barrier layers catalyze olefins and aromatics steam reforming. While the excess Cr in $Mn_{0.5}Cr_{2.5}O_4$ exists separately as Cr_2O_3, the excess Mn in $Mn_{1.5}Cr_{1.5}O_4$ exists as Mn^{3+} that substitutes for the Cr^{3+} in the octahedral sites of the spinel lattice instead of forming crystalline Mn oxides. A single oxide of Mn (Mn_3O_4) showed the highest reforming rate for both ethylene and toluene but rapidly deactivated due to reduction to MnO at 873 K whereas the spinel catalysts and Cr_2O_3 remained structurally stable under identical reforming conditions. The Cr_2O_3 catalyst exhibited a much higher initial reforming rate for olefins than the spinel catalysts followed by a rapid deactivation likely resulting from coke deposition. On the other hand, the $Mn_{1.5}Cr_{1.5}O_4$ catalyst was the most active and stable catalyst for aromatic steam reforming likely attributed to the presence of Mn^{3+} sites, while rates of aromatic reforming over $MnCr_2O_4$ and Cr_2O_3 were similar.

The steam reforming rates of olefins and aromatics were comparable over the Mn-Cr-O spinel catalysts. The reforming rates of olefins and aromatics all showed a first-order dependence on the respective hydrocarbon and were slightly inhibited by H_2O, which is consistent with a Mars-van Krevelen type mechanism. While the reaction orders in excess H_2 were nearly zero for olefins and benzene reforming, the toluene reforming rate was negative first order in excess H_2, which is likely associated with a slower oxidation of the side methyl group of toluene in H_2 as evident from *in situ* DRIFTS of toluene adsorption on the spinel surface. The inhibition by H_2 and a high apparent activation energy observed for toluene steam reforming is consistent with the steam gasification kinetics of coke studied over the same materials [1], suggesting toluene to be a reasonable model compound for coke. The higher toluene reforming rate over the Mn-rich $Mn_{1.5}Cr_{1.5}O_4$ spinel catalyst is also consistent with its higher rate for *ex situ* steam gasification of coke [1] and an improved anti-coking performance under steam cracking conditions potentially through *in situ* steam gasification of coke and coke precursors [2], which makes the Mn-rich $Mn_{1.5}Cr_{1.5}O_4$ spinel a promising candidate for catalytic barrier oxide layers.

Synthetic powder catalysts of Ni-based spinel oxides (NiM_2O_4) that are analogous to those present in the barrier oxide layers of the Al-enhanced cracking reactor tubes are active for ethylene steam reforming. Consistent with the results from H_2-TPR, reduction of Ni^{2+} to Ni-Fe alloy for $NiFe_2O_4$ was facilitated by the reduction of Fe^{3+} and resulted in severe coke deposition during steam reforming. Although the spinel structure in $NiAl_2O_4$ and $NiCr_2O_4$ was stable during ethylene steam reforming at 873 K, the ethylene reforming rate and the amount of deposited coke on both catalysts increased substantially in the second reforming cycle after an oxidation treatment following the first cycle. These observations suggest that periodic oxidative treatments for coke removal may accelerate the agglomeration of small Ni metal particles formed via reduction of Ni spinel oxides during steam cracking conditions into larger NiO particles, which easily reduce to Ni metal particles that catalyze coke deposition. Thus, the Ni-based spinel oxides are inappropriate for anti-coking barrier oxide layers even though they are catalytically active for steam reforming.

The activity and stability of Co-Cr-O spinel oxides ($Co_xCr_{3-x}O_4$) were explored in ethylene steam reforming. Excess Co in $Co_{1.5}Cr_{1.5}O_4$ is attributed to Co^{3+} in the octahedral sites of the spinel lattice that partially substitute Cr^{3+}. The Co^{3+} sites in $Co_{1.5}Cr_{1.5}O_4$ were reduced to Co^{2+} when heated in H_2 whereas reduction of Co^{2+} to Co metal occurred at much higher temperatures for $CoCr_2O_4$. Both $CoCr_2O_4$ and $Co_{1.5}Cr_{1.5}O_4$ were structurally stable during ethylene steam reforming at 873 K, with the order of magnitude higher reforming rate over $Co_{1.5}Cr_{1.5}O_4$ being potentially attributed to the Co^{3+} sites. Interestingly, the reforming rate over $CoCr_2O_4$ was comparable to that over $MnCr_2O_4$ and $NiCr_2O_4$ without a strong dependence on the identity of the tetrahedral cations in the spinel structure. The $CoCr_2O_4$ and $Co_{1.5}Cr_{1.5}O_4$ catalysts both showed similar reforming activity after re-oxidation, suggesting good stability of Co-Cr-O spinel oxides against reduction to Co metal particles.

To summarize, this dissertation has investigated the steam reforming rate of olefins and aromatics over various types of spinel oxides. While the reforming rate is comparable for MCr_2O_4 spinel oxides (where M = Mn, Ni, Co), $MnCr_2O_4$ is the most stable against reduction to metal particles and therefore suitable for the barrier oxide layers of steam cracking reactors. The introduction of excess Mn *(i.e.*, $Mn_{1.5}Cr_{1.5}O_4$) increases the rate for aromatics steam reforming but the Mn^{3+} sites can be prone to reduction when in great excess (*i.e.*, Mn_3O_4). Thus, the development of catalytic barrier oxide layers from the Mn-Cr-O spinel oxides likely requires a proper balance between activity and stability. Slow reduction of Ni-containing spinel oxides to Ni metal particles prevents them as effective barrier oxide layers due to potential catalytic coking. As a result, catalytic barrier oxide layers for Al-enhanced alloy reactors need further research on the active components, potentially forming other Al-based spinel oxides.

6.2 Future directions

Although the excess octahedral Mn^{3+} sites were proposed to be responsible for the higher rate of aromatics steam reforming over $Mn_{1.5}Cr_{1.5}O_4$, the presence of these Mn^{3+} sites was only confirmed by *ex situ* characterizations using diffraction and spectroscopy before and (or) after reaction. The oxidation state of Mn under steam reforming conditions with excess H_2 is of interest for understanding the higher rate of aromatics steam reforming over $Mn_{1.5}Cr_{1.5}O_4$. Results in this dissertation have shown that $Mn_{1.5}Cr_{1.5}O_4$ remained stable after steam reforming without bulk reduction to form MnO, therefore interconversion between Mn^{3+} and Mn^{2+} likely occurs near the catalyst surface, which can be probed by *in situ* XPS [3]. Based on the characteristic satellite features from Mn^{2+}, *in situ* XPS may identify potential changes in Mn speciation as a function of H_2 partial pressure under steam reforming conditions.

The TOF of steam reforming over the Mn-Cr-O spinel oxides was estimated using an active site density of monolayer H_2O adsorption capacity. This adsorption capacity of H_2O was determined *ex situ* for each catalyst, which assumed that the active site density did not depend on the hydrocarbon. Transient kinetic analysis (TKA) could be used to investigate the intrinsic active site density during steam reforming by switching the hydrocarbon reactant [4]. Since olefins and aromatics may interact with the spinel surface differently given their unique molecular structures, TKA provides a more trustworthy measurement of the site density for calculating and comparing the steam reforming TOF of different hydrocarbons.

In addition to $NiAl_2O_4$, $MnAl_2O_4$ is also predicted to form on the surface of the Al-containing alloy by thermodynamic calculations [5], possibly through solid spinel solutions [6]. Unlike $NiAl_2O_4$, $MnAl_2O_4$ is stable against reduction to metal particles based on thermodynamic calculations [7]. The $MnAl_2O_4$ spinel can be synthesized under reducing environments at extremely high temperatures [8,9] and was reported to catalyze soot oxidation [10]. By analogy to the Mn-Cr-O spinel oxides investigated in this dissertation, the kinetic studies on olefins and aromatics steam reforming can be potentially extended to the Mn-Al-O spinel oxides with different stoichiometry for developing catalytically active components in the Al_2O_3 barrier oxide layers.

6.3 References for Chapter 6

[1] M.P. Bukhovko, L. Yang, L. Li, A. Malek, R.J. Davis, P.K. Agrawal, C.W. Jones,

Gasification of Radical Coke with Steam and Steam-Hydrogen Mixtures over Manganese-Chromium Oxides, Ind. Eng. Chem. Res. 59 (2020) 10813-10822.

[2] M.P. Bukhovko, L. Yang, I. Nezam, L. Li, A. Malek, R.J. Davis, P.K. Agrawal, C.W. Jones, Enhanced Coke Gasification Activity of $Mn_{1.5}Cr_{1.5}O_4$ Spinel Catalyst during Coking in Ethylene-Steam Mixture, submitted.

[3] O.A. Bulavchenko, Z.S. Vinokurov, T.N. Afonasenko, P.G. Tsyrul'nikov, S.V. Tsybulya, A.A. Saraev, V.V. Kaichev, Reduction of mixed Mn-Zr oxides: In situ XPS and XRD studies, Dalt. Trans. 44 (2015) 15499-15507.

[4] J.D. Kammert, J. Xie, I.J. Godfrey, R.R. Unocic, E. Stavitski, K. Attenkofer, G. Sankar, R.J. Davis, Reduction of Propionic Acid over a Pd-Promoted ReO_x/SiO_2 Catalyst Probed by X-ray Absorption Spectroscopy and Transient Kinetic Analysis, ACS Sustain. Chem. Eng. 6 (2018) 12353-12366.

[5] A.E. Muñoz Gandarillas, K.M. Van Geem, M.F. Reyniers, G.B. Marin, Influence of the reactor material composition on coke formation during ethane steam cracking, Ind. Eng. Chem. Res. 53 (2014) 6358-6371.

[6] M. Timuçin, A. Muan, Activity-Composition Relations in $NiAl_2O_4$-$MnAl_2O_4$ Solid Solutions and Stabilities of $NiAl_2O_4$ and $MnAl_2O_4$ at 1300° and 1400°C, J. Am. Ceram. Soc. 75 (1992) 1399-1406.

[7] S. Chatterjee, Critical Evaluation and Thermodynamic Modeling of Phase Equilibria in the Fe-Ca-Mg-Mn-Al-Si-O System (Master's thesis), 2013.

[8] R.C.S. Navarro, R.R. de Avillez, T.F. Goes, A.M.S. Gomes, Low temperature thermal and volumetric behavior of $MnAl_2O_4$ spinel, J. Mater. Res. Technol. 9 (2020) 4194-4205.

[9] A.P. Grosvenor, E.M. Bellhouse, A. Korinek, M. Bugnet, J.R. McDermid, XPS and EELS characterization of Mn_2SiO_4 , $MnSiO_3$ and $MnAl_2O_4$, Appl. Surf. Sci. 379 (2016) 242-248.

[10] Q. Li, M. Meng, H. Xian, N. Tsubaki, X. Li, Y. Xie, T. Hu, J. Zhang, Hydrotalcite-derived $Mn_xMg_{3-x}AlO$ catalysts used for soot combustion, NO_x storage and simultaneous soot-NO_x removal, Environ. Sci. Technol. 44 (2010) 4747-4752.

Appendix A Supplementary material for Chapter 2

Supplementary figures (A1-A9) and tables (A1-A2)

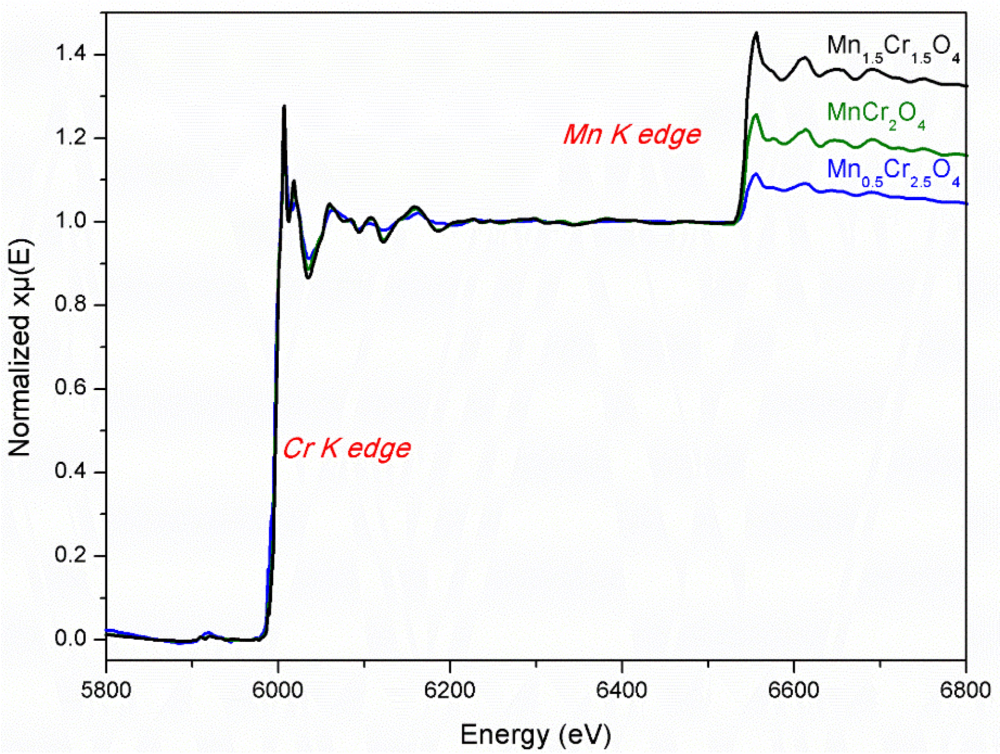

Figure A1 Cr K edge and Mn K edge X-ray absorption spectra of the fresh Mn-Cr-O spinel catalysts normalized by the Cr K edge absorption.

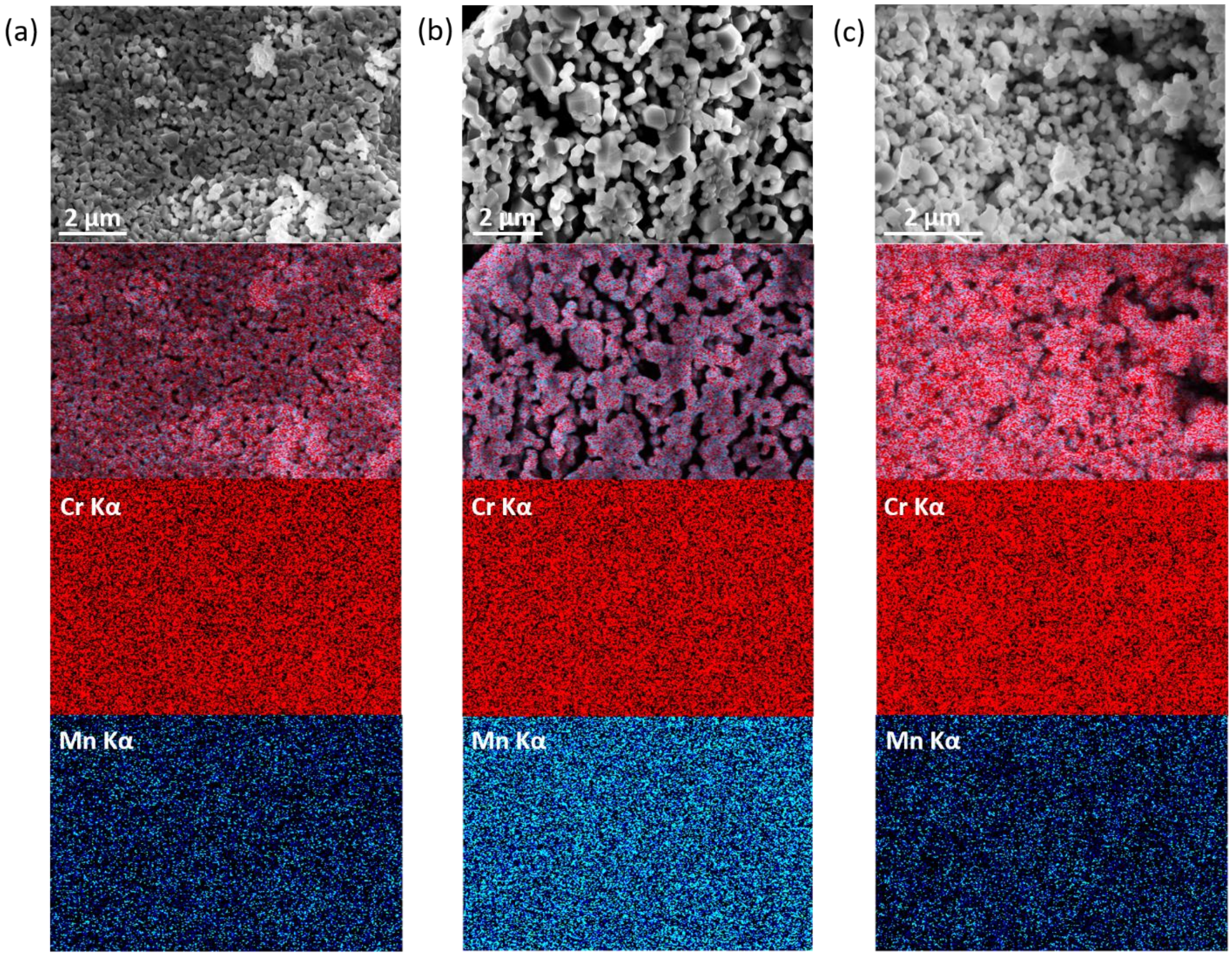

Figure A2 EDS elemental mappings of Cr and Mn in the fresh (a) $MnCr_2O_4$, (b) $Mn_{1.5}Cr_{1.5}O_4$ and (c) $Mn_{0.5}Cr_{2.5}O_4$ catalyst.

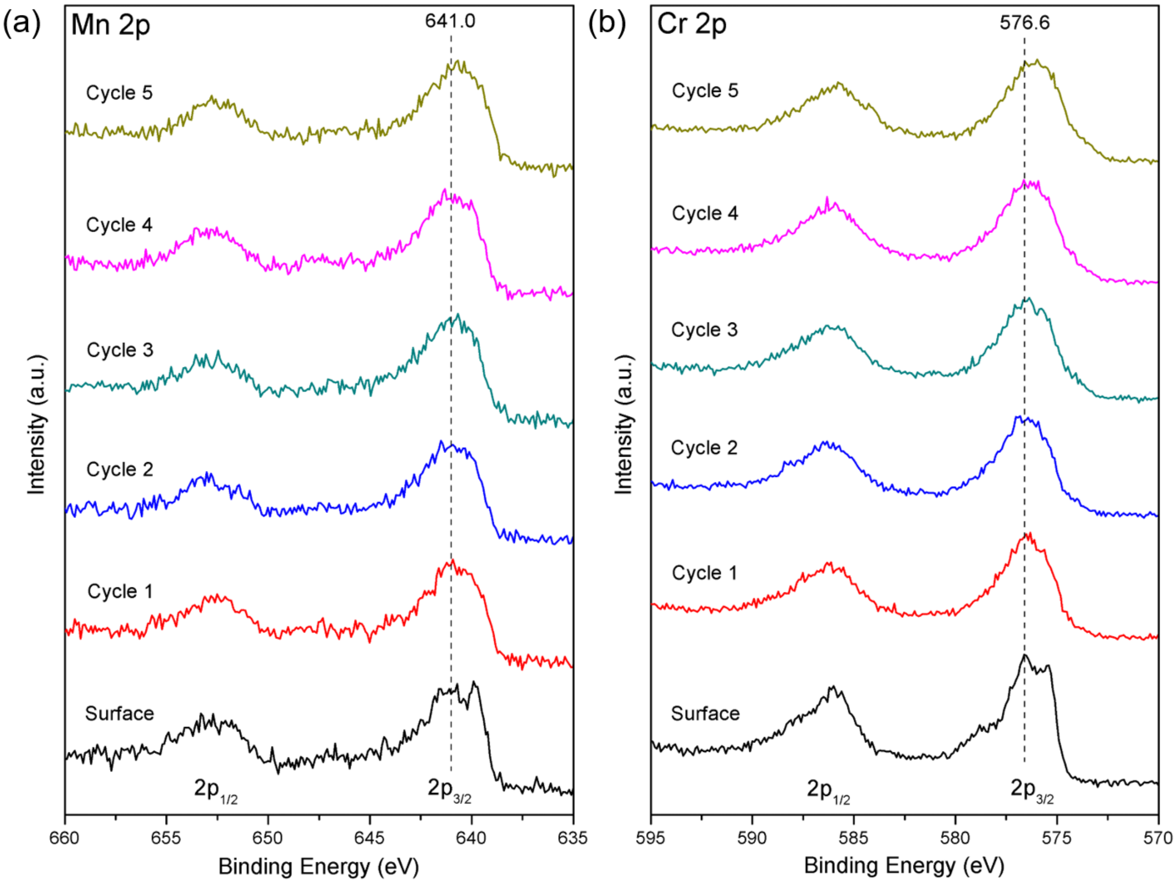

Figure A3 (a) Mn 2p and (b) Cr 2p X-ray photoelectron spectra during the depth profiling of the $MnCr_2O_4$ catalyst.

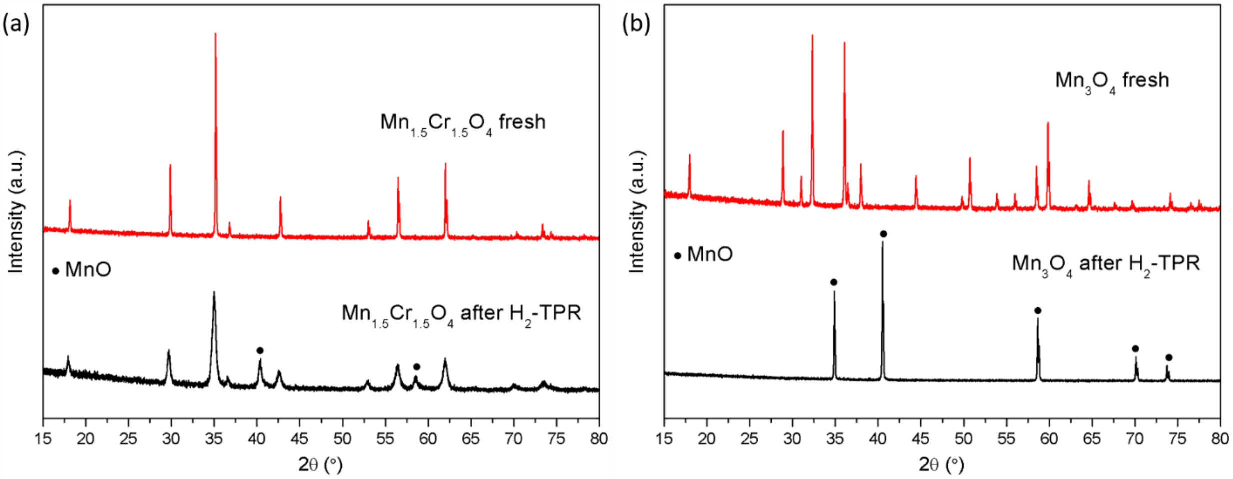

Figure A4 X-ray diffraction patterns of the fresh catalyst and after H_2-TPR of (a) $Mn_{1.5}Cr_{1.5}O_4$ and (b) Mn_3O_4.

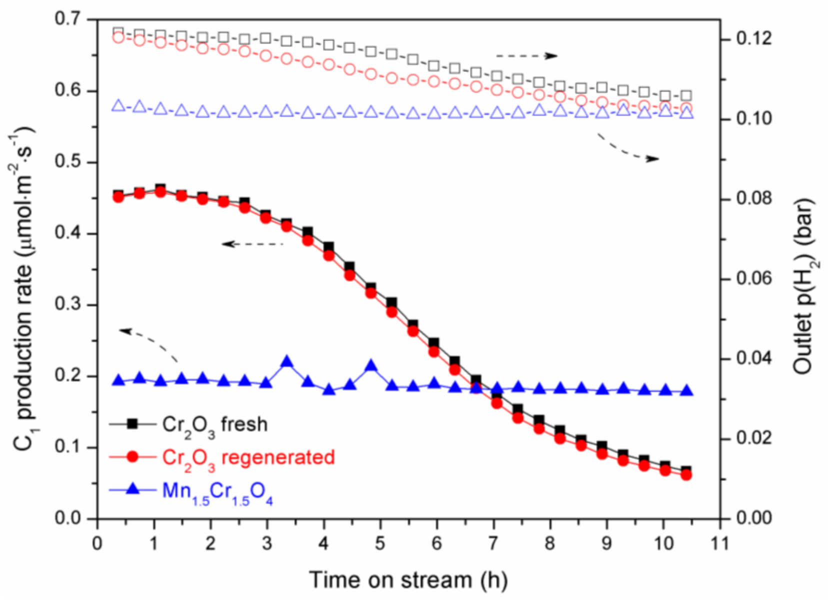

Figure A5 Rate of C_1 product formation during ethylene steam reforming over the Cr_2O_3 and $Mn_{1.5}Cr_{1.5}O_4$ catalyst. Reaction conditions: 873 K, 1 g catalyst, 100 cm^3·min^{-1} total flow, 25 % C_2H_4, 20 % H_2O, 5 % N_2, 10 % H_2 and 40 % Ar. Deactivated Cr_2O_3 catalyst was regenerated by oxidation at 873 K for 2 h in 100 cm^3·min^{-1} air flow.

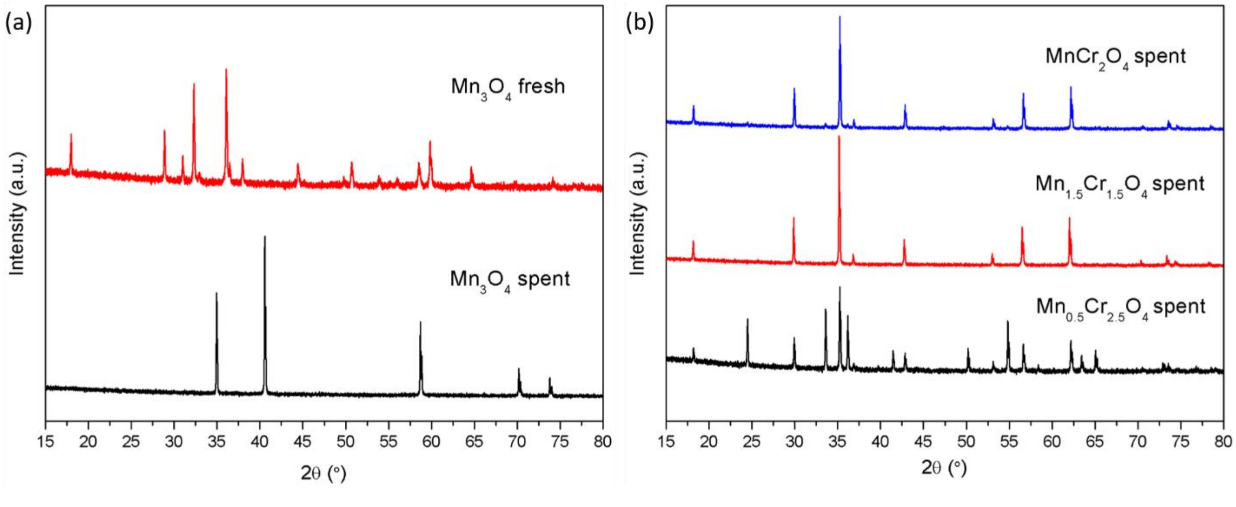

Figure A6 X-ray diffraction patterns of (a) the fresh and spent Mn_3O_4 catalyst and (b) the spent Mn-Cr-O spinel catalysts. Reaction conditions: 873 K, 1 g catalyst (2 g for Mn_3O_4), 100 cm^3·min^{-1} total flow, 25 % C_2H_4, 50 % H_2O, 5 % N_2 and 20 % Ar.

Table A1 The BET surface area of the fresh and spent Mn-Cr-O spinel catalysts

Catalyst	Fresh BET surface area ($m^2 \cdot g^{-1}$)	Spent BET surface area ($m^2 \cdot g^{-1}$)
$MnCr_2O_4$	5.3	4.6
$Mn_{1.5}Cr_{1.5}O_4$	2.6	2.6
$Mn_{0.5}Cr_{2.5}O_4$	4.5	4.4

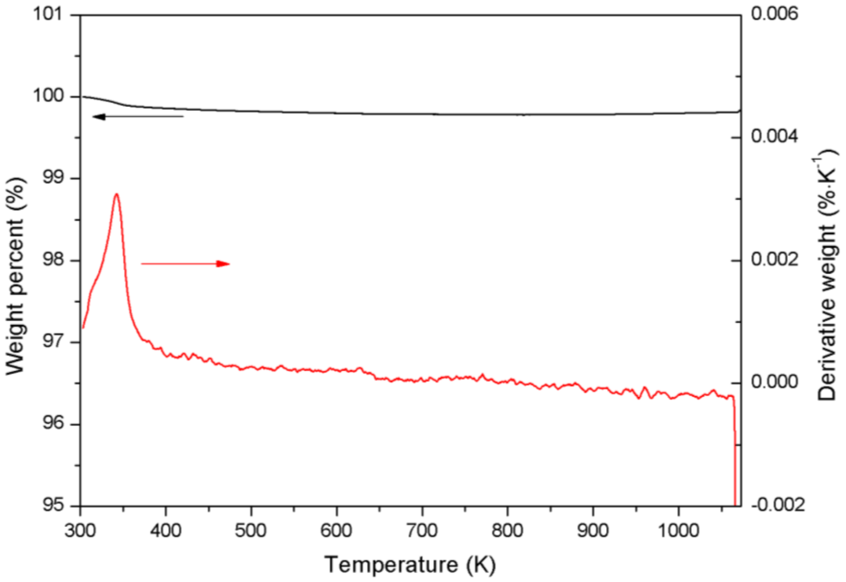

Figure A7 Thermogravimetric analysis (TGA) of the spent $MnCr_2O_4$ catalyst. Reaction conditions: 873 K, 1 g catalyst, 100 $cm^3 \cdot min^{-1}$ total flow, 25 % C_2H_4, 50 % H_2O, 5 % N_2 and 20 % Ar. TGA procedure: 30 mg catalyst was heated in a 50 $cm^3 \cdot min^{-1}$ synthetic air (20 vol % O_2 in He) flow to 1073 K at a constant ramp rate of 10 $K \cdot min^{-1}$.

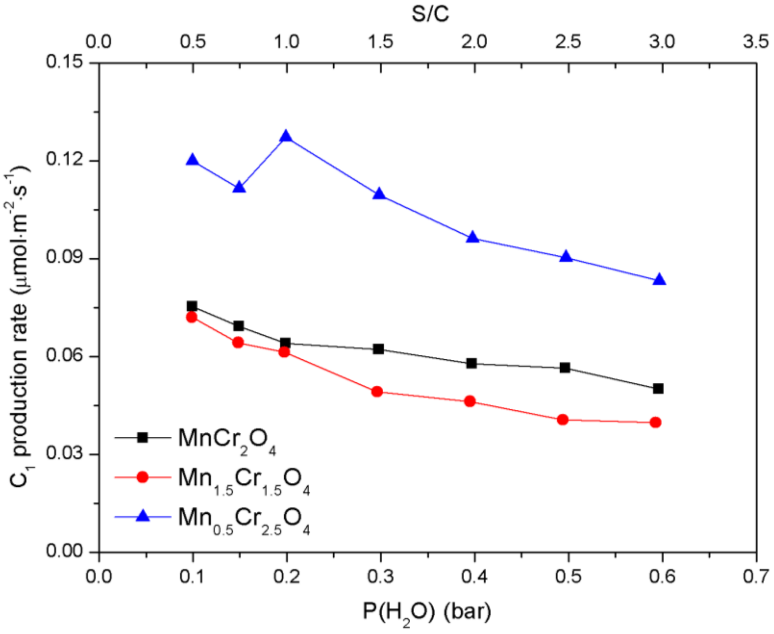

Figure A8 Effect of H_2O partial pressure on the C_1 production rate in the steam reforming of ethylene over the Mn-Cr-O spinel catalysts ranging from 0.1 bar to 0.6 bar. Reaction conditions: 873 K, 1 g catalyst, 100 $cm^3 \cdot min^{-1}$ total flow, 10 % C_2H_4, 10-60 % H_2O, 5 % N_2, balance Ar (20 % H_2 for $Mn_{1.5}Cr_{1.5}O_4$).

Table A2 Consumptions of H_2 during H_2-TPR and measurements of the oxygen storage capacity of the fresh Mn-Cr-O spinel catalysts

Catalyst	H_2 consumption ($\mu mol\ H_2 \cdot m^{-2}$)[a]	Oxygen storage capacity ($\mu mol\ O \cdot m^{-2}$)[b]
$MnCr_2O_4$	6.3	9.1
$Mn_{1.5}Cr_{1.5}O_4$	25	28
$Mn_{0.5}Cr_{2.5}O_4$	16	12

[a] Measured during H_2-TPR up to 873 K, reporting in terms of H_2 molecule

[b] Measured by O_2 pulse chemisorption at 873 K, reporting in terms of O atom

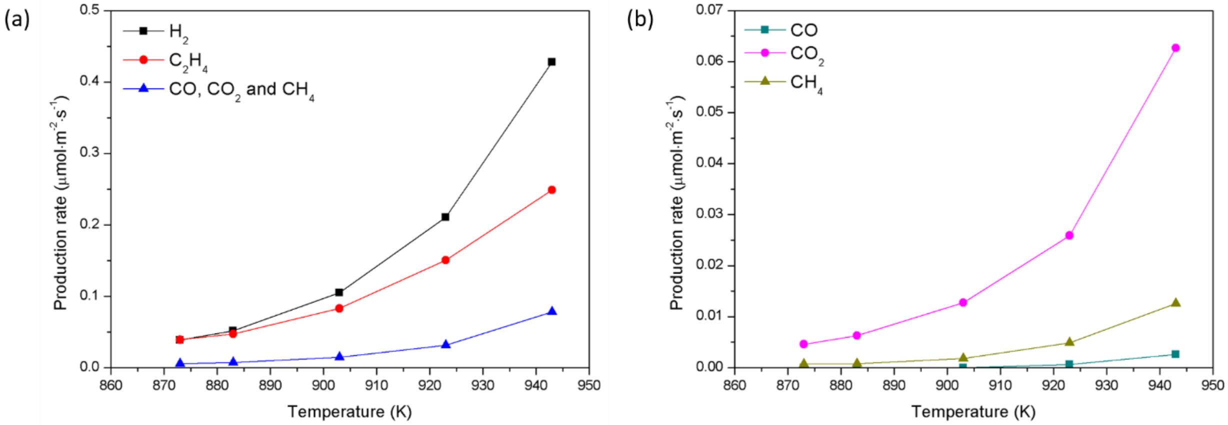

Figure A9 (a) Production rate of H_2, C_2H_4 and C_1 and (b) individual production rate of CO, CO_2 and CH_4 in ethane dehydrogenation over $Mn_{0.5}Cr_{2.5}O_4$. Reaction conditions: 873-943 K, 1 g catalyst, 100 $cm^3 \cdot min^{-1}$ total flow, 25 % C_2H_6, 50 % H_2O, 5 % N_2 and 20 % Ar.

Appendix A1 Material balance for ethylene steam reforming

Since the C_2H_4 conversion was only 1-2 % under the reaction conditions, evaluating the conversion based on the change in molar flowrate of C_2H_4 from upstream to downstream of the reactor (reactant based conversion) was inconsistent because of the inaccuracies of standard TCD detection during gas chromatography, leading to an overall carbon balance of 100-300 %. Therefore, to assess the material balance reliably on a carbon basis was not feasible. Alternatively, we utilized the H_2 balance among the steam reforming products to validate our material balance. Using the results of ethylene steam reforming over the $MnCr_2O_4$ catalyst at 873 K as an example, the material balance on a hydrogen basis can be evaluated. Since all C_1 products, including CO, CO_2 and CH_4, originate from C_2H_4, the following overall stoichiometry shall apply:

$$C_2H_4 + 2H_2O \rightarrow 2CO + 4H_2$$

$$C_2H_4 + 4H_2O \rightarrow 2CO_2 + 6H_2$$

$$C_2H_4 + 2H_2 \rightarrow 2CH_4$$

Assuming a negligible formation of coke, which was evident from the TGA results shown in **Figure A7**, the production rate of H_2 can be predicted by the production rate of CO, CO_2 and CH_4 in the following way:

$$F_{predicted}(H_2) = 2F(CO) + 3F(CO_2) - F(CH_4)$$

As shown in **Figure A10**, the predicted H_2 production rate is generally 10-20 % higher than that was measured experimentally. Regardless, the comparison still suggests a reasonably consistent material balance for the measurement of the products observed in ethylene steam reforming.

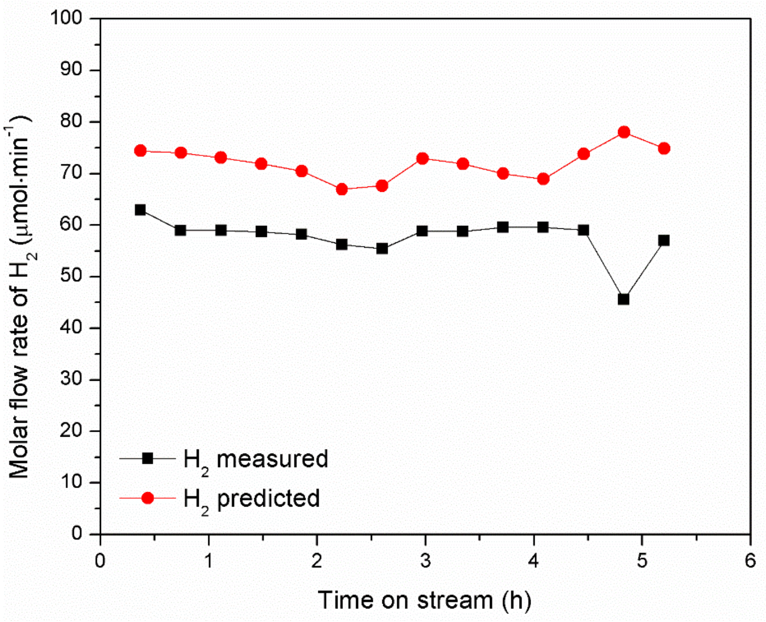

Figure A10 The measured and predicted production rate of H_2 during ethylene steam reforming over $MnCr_2O_4$.

Appendix A2 Evaluation of the potential effect of heat and mass transfer on the measured ethylene steam reforming rates

The following experiments were conducted to explore potential influences of external heat and mass transport limitations. As shown in the attached table, the C_1 production rate was unaffected by changing the flow rate by a factor of 2. These results suggest that artifacts from external transport effects on kinetics are not significant under the conditions of study.

Table A3 Influence of Flow Rate on Ethylene Steam Reforming over $MnCr_2O_4$

Catalyst	Catalyst loading (mg)	Total flow rate (STP $cm^3 \cdot min^{-1}$)	C_2H_4 conversion[a] (%)	C_1 production rate ($\mu mol \cdot m^{-2} \cdot s^{-1}$)
$MnCr_2O_4$	1017	100	1.8	0.13
	1002	100	1.9	0.14
	700	200	0.62	0.13

Reaction condition: 873 K, 25 % C_2H_4, 50 % H_2O, 5 % N_2 and 20 % Ar

[a] Product based conversion

The Weisz-Prater criterion was used to assess the potential effect of intraparticle mass transfer artifacts on the reported ethylene steam reforming rates over the stoichiometric spinel catalyst. The Weisz-Prater criterion for an irreversible, isothermal, first-order reaction in a spherical catalyst pellet is given as [1]:

$$\frac{r_{obs}\left(R_p\right)^2}{D_{TA}^e C_{AS}} < 1$$

where the observed reaction rate per unit volume $r_{obs} \sim 0.49\, mol \cdot m^{-3} \cdot s^{-1}$, the radius of the catalyst particle $R_p \sim 2 \times 10^{-4}\, m$, the effective transition diffusivity $D_{TA}^e \sim 1.2 \times 10^{-7}\, m^2 \cdot s^{-1}$, and the concentration of ethylene at the external surface $C_{AS} \sim 3.4\, mol \cdot m^{-3}$.

With the above parameters, we obtain:

$$\frac{r_{obs}(R_p)^2}{D_{TA}^e C_{AS}} = 0.048 \ll 1$$

Therefore, according to the Weisz-Prater criterion, the measured steam reforming rates are not limited by intraparticle diffusion through the pore-like voids between the particle aggregates.

The Anderson criterion was used to confirm the observed steam reforming rate over stoichiometric spinel was unaffected by intraparticle temperature gradients (within 5 %) [1]:

$$\frac{|\Delta H_r| r_{obs}(R_p)^2}{\lambda^e T_S} < 0.75 \frac{R_g T_S}{E_a}$$

where the enthalpy change of ethylene steam reforming, which is concurrent with the Water Gas Shift reaction, ($C_2H_4 + 4H_2O \rightarrow 2CO_2 + 6H_2$) $\Delta H_r \sim 1.28 \times 10^5\, J \cdot mol^{-1}$, the observed reaction rate per unit volume $r_{obs} \sim 0.49\, mol \cdot m^{-3} \cdot s^{-1}$, the radius of the catalyst particle $R_p \sim 2 \times 10^{-4}\, m$, the estimated effective thermal conductivity of the catalyst particle $\lambda^e \sim 8.4\, J \cdot s^{-1} \cdot m^{-1} \cdot K^{-1}$, the surface temperature of the catalyst particle $T_S \sim 873\, K$, the ideal gas constant $R_g \sim 8.314\, J \cdot mol^{-1} \cdot K^{-1}$ and the activation energy of the reaction (from Table 5) $E_a \sim 1.30 \times 10^5\, J \cdot mol^{-1}$.

With the above parameters, we obtain:

$$\frac{|\Delta H_r| r_{obs}(R_p)^2}{\lambda^e T_S} = 3.4 \times 10^{-7} \ll 0.042 = 0.75 \frac{R_g T_S}{E_a}$$

Thus, according to the Anderson criterion, the measured steam reforming rates are unaffected by intraphase heat transfer artifacts.

Appendix A3 Derivation of the rate expression assuming a two-site Mars-van Krevelen mechanism

The proposed two-site Mars-van Krevelen mechanism involves the following steps:

(1) $C_2H_4 + S \overset{K_{C_2H_4}}{\rightleftarrows} C_2H_4 \cdot S$ (Quasi-equilibrated)

(2) $H_2O + S \overset{K_{H_2O}}{\rightleftarrows} H_2O \cdot S$ (Quasi-equilibrated)

(3) $C_2H_4 \cdot S + O^* \xrightarrow{k_3}$ Surface intermediates

(4) $H_2O + * \xrightarrow{k_4} O^* + H_2$

The site S is proposed to represent the metal sites (Mn^{2+}, Mn^{3+} or Cr^{3+}) on the catalyst surface, on which C_2H_4 and H_2O adsorb competitively. Assuming the adsorption of C_2H_4 and H_2O to be quasi-equilibrated, we obtain:

$$[C_2H_4 \cdot S] = K_{C_2H_4}[C_2H_4][S] \tag{5}$$

$$[H_2O \cdot S] = K_{H_2O}[H_2O][S] \tag{6}$$

The site conservation of S gives:

$$[S]_0 = [S] + [C_2H_4 \cdot S] + [H_2O \cdot S] \tag{7}$$

Using Eqn. (5), (6) and (7) we obtain:

$$[C_2H_4 \cdot S] = \frac{K_{C_2H_4}[C_2H_4][S]_0}{1 + K_{C_2H_4}[C_2H_4] + K_{H_2O}[H_2O]} \tag{8}$$

The site $*$ is proposed to represent the lattice oxygen vacancy on the catalyst surface. Based on the Mars-van Krevelen mechanism, the lattice oxygen atoms oxidize the adsorbed C_2H_4 and are regenerated by the dissociation of H_2O. We assume here that the oxidation rate of C_2H_4 (r_3) is governed by reaction with the surface oxygen according to Eqn. (9):

$$r_3 = k_3[C_2H_4 \cdot S][O^*] \tag{9}$$

The rate of H_2O reduction (r_4) to regenerate the lattice oxygen sites is written as:

$$r_4 = k_4[H_2O][*] \tag{10}$$

The redox stoichiometry and the site conservation of $*$ are written as:

$$r_4 = 2r_3 \tag{11}$$

$$[*]_0 = [*] + [O^*] \tag{12}$$

Using Eqn. (9), (10), (11) and (12) we obtain:

$$[O^*] = \frac{\frac{k_4[H_2O]}{2k_3[C_2H_4 \cdot S]}[*]_0}{1 + \frac{k_4[H_2O]}{2k_3[C_2H_4 \cdot S]}} \tag{13}$$

With Eqn. (9), the reforming rate in terms of C_2H_4 consumption is:

$$r_3 = -\frac{d[C_2H_4]}{dt} = k_3[C_2H_4 \cdot S][O^*] = \frac{\frac{k_4[H_2O]}{2}[*]_0}{1 + \frac{k_4[H_2O]}{2k_3[C_2H_4 \cdot S]}} \tag{14}$$

The two terms in the denominator reflect the relative amount of lattice oxygen atoms compared to lattice vacancies. If we assume the amount of vacancies is negligible under reaction conditions:

$$\frac{k_4[H_2O]}{2k_3[C_2H_4 \cdot S]} = \frac{[O^*]}{[*]} \gg 1 \tag{15}$$

$$r_3 = k_3[C_2H_4 \cdot S][*]_0 = \frac{k_3 K_{C_2H_4}[C_2H_4][S]_0[*]_0}{1 + K_{C_2H_4}[C_2H_4] + K_{H_2O}[H_2O]} \tag{16}$$

The reforming rate in terms of C_1 product formation is therefore:

$$r_{C_1} = 2r_3 = \frac{2k_3 K_{C_2H_4}[C_2H_4][S]_0[*]_0}{1 + K_{C_2H_4}[C_2H_4] + K_{H_2O}[H_2O]} \tag{17}$$

References for Appendix A

[1] M.E. Davis, R.J. Davis, Fundamentals of Chemical Reaction Engineering, McGraw-Hill Higher Education, 2002, p. 228.

Appendix B Supplementary material for Chapter 3

Supplementary figures (B1-B14), tables (B1-B4) and scheme (B1)

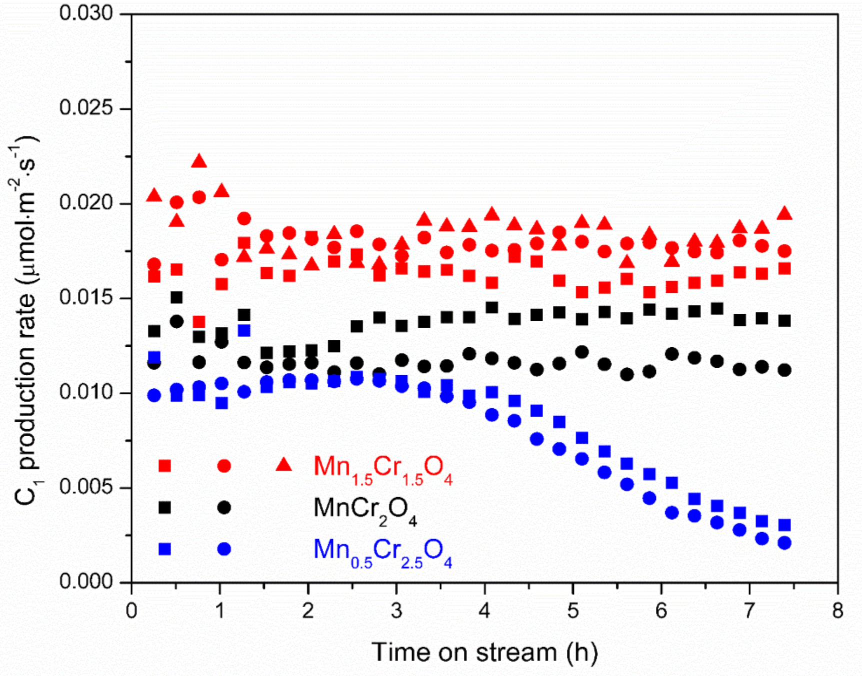

Figure B1. Replicates of rate in C_1 product formation during toluene steam reforming over the Mn-Cr-O spinel catalysts. Reaction conditions: 873 K, 2 g catalyst, 100 cm^3·min^{-1} total flow, 2 % C_7H_8, 40 % H_2O, 4 % H_2, 5 % N_2, balance Ar.

Table B1. Steady state rate of benzene production during toluene steam reforming at different C_7H_8, H_2O and H_2 partial pressures at 873 K

Catalyst[a]	$p(C_7H_8)$ (bar)	$p(H_2O)$ (bar)	$p(H_2)$ (bar)[b]	C_6H_6 production rate (10^{-4} μmol·m^{-2}·s^{-1})
SiO_2	0.25	0.50	n.d.	n.d.
	0.25	0.50	0.095[c]	n.d.
$MnCr_2O_4$	0.20	0.40	0.0040	6.9
	0.25	0.40	0.0040	8.5
	0.30	0.40	0.0044	7.6
	0.40	0.40	0.0044	8.9
	0.25	0.50	0.0048	4.3
	0.25	0.50	0.087[c]	3.4

[a] Catalyst loading (1 g for SiO_2 and 2 g for $MnCr_2O_4$) was adjusted to give similar volumetric space velocity.

[b] Quantified downstream the catalyst bed by gas chromatography.

[c] Excess H_2 was introduced in the feed.

Table B2. Results from Rietveld refinement of the XRD patterns of the Mn-Cr-O spinel catalysts spent in toluene steam reforming

Catalyst	Lattice Constant *a* ($Mn_xCr_{3-x}O_4$) (Å)		Atomic Cr/Mn	
	Fresh[a]	Spent	Fresh[a]	Spent
$Mn_{1.5}Cr_{1.5}O_4$	8.460	8.459	1 (fixed)	1 (fixed)
$MnCr_2O_4$ [b]	8.438	8.439	2.1	2.1
$Mn_{0.5}Cr_{2.5}O_4$ [b]	8.437	8.440	6.0	5.7

[a] Listed values for the fresh catalysts were from our previous work [1].

[b] The Cr/Mn ratio was calculated assuming a combination of $MnCr_2O_4$ phase (PDF 00-054-0876) and Cr_2O_3 phase (PDF 00-038-1479).

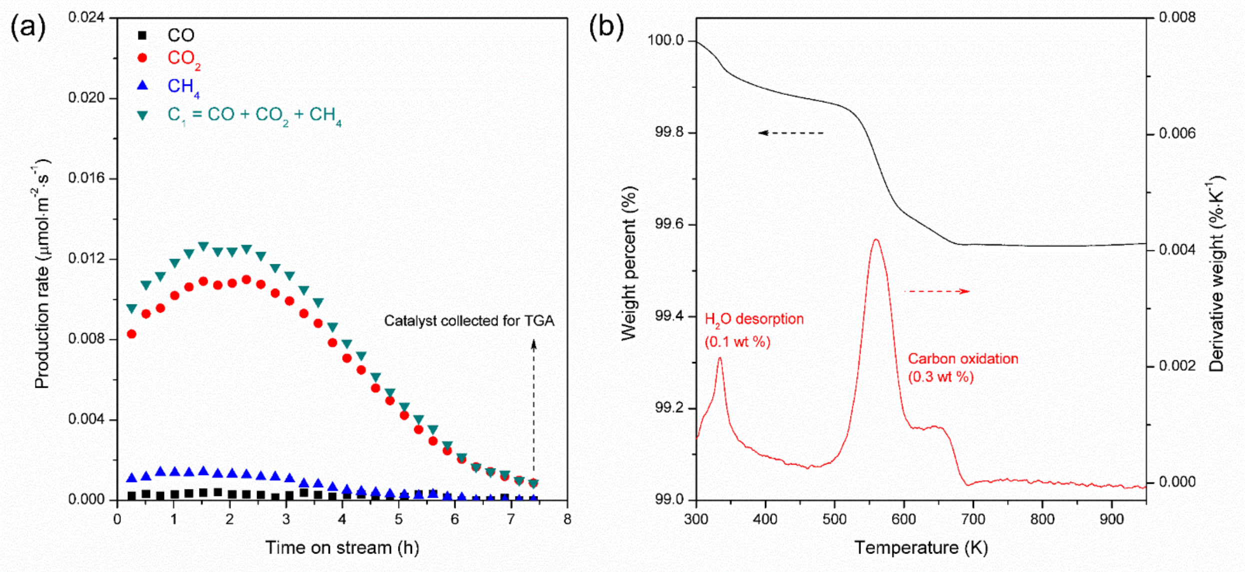

Figure B2. (a) Deactivation profile of C_1 product formation during toluene steam reforming over the $Mn_{0.5}Cr_{2.5}O_4$ catalyst and (b) thermogravimetric analysis of the spent catalyst sample in temperature-programmed oxidation. Reaction conditions: 873 K, 2 g catalyst, 100 cm^3·min^{-1} total flow, 2 % C_7H_8, 40 % H_2O, 4 % H_2, 5 % N_2, balance Ar. Integrated weight loss resulting from H_2O desorption and carbon oxidation was labelled on the plot. The estimated rate of carbon deposition from the weight loss (1.1 μmol·min^{-1}) was small relative to the initial formation rate of C_1 products (6.1 μmol·min^{-1}) averaged over the first 3.5 h onstream before rapid deactivation.

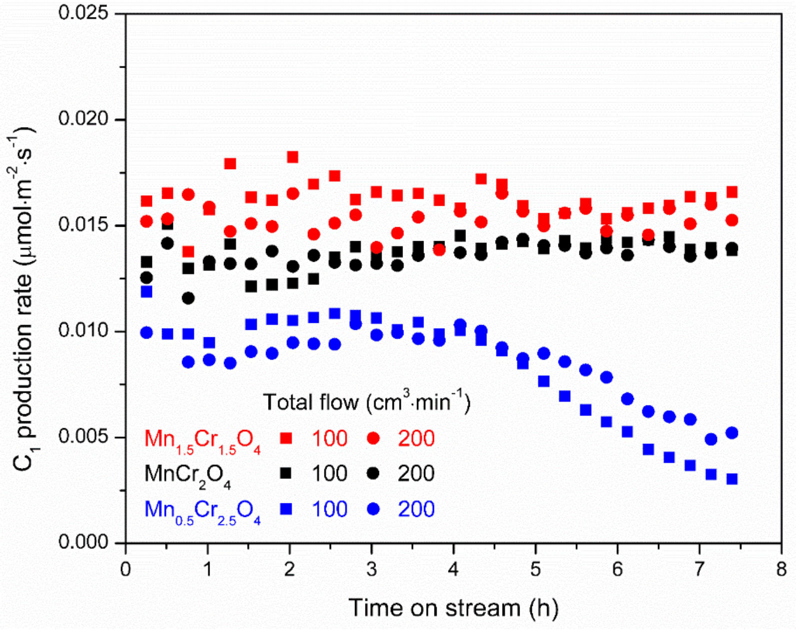

Figure B3. Effect of total flow rate on the formation rate of C_1 products during toluene steam reforming over the Mn-Cr-O spinel catalysts. Reaction conditions: 873 K, 2 g catalyst, 100 or 200 $cm^3 \cdot min^{-1}$ total flow, 2 % C_7H_8, 40 % H_2O, 4 % H_2, 5 % N_2, balance Ar.

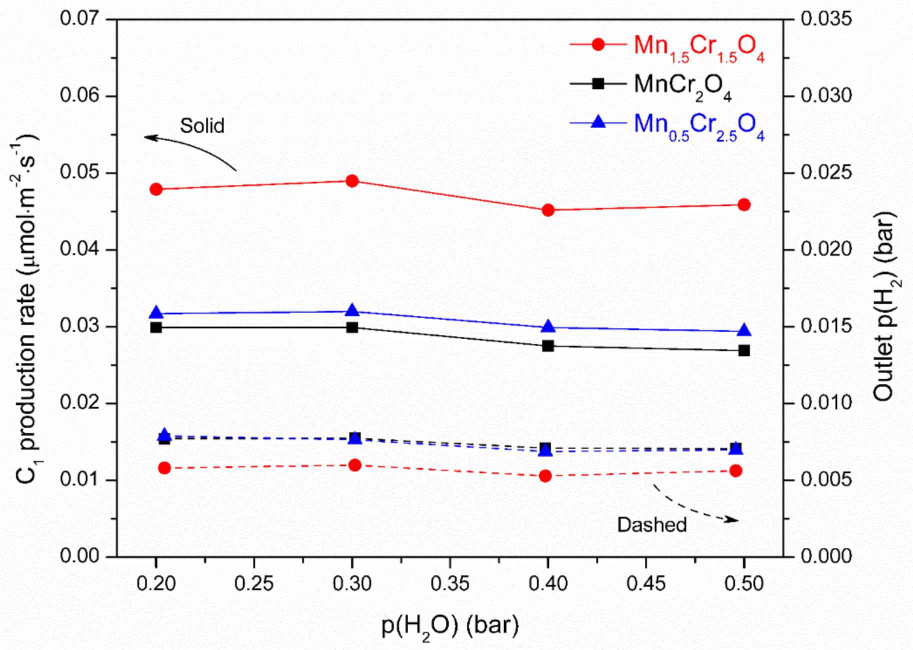

Figure B4. Effect of H_2O partial pressure on the formation rate of C_1 products during toluene steam reforming over the Mn-Cr-O spinel catalysts without introducing excess H_2. Reaction conditions: 873 K, 2 g catalyst, 100 $cm^3 \cdot min^{-1}$ total flow, 1 % C_7H_8, 20-50 % H_2O, 5 % N_2, balance Ar.

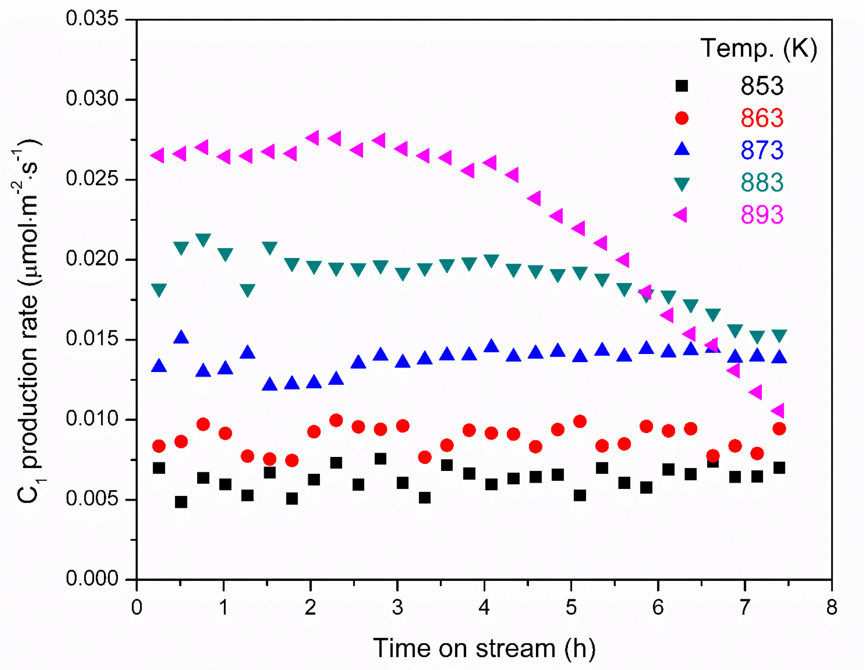

Figure B5. Effect of reaction temperature on the formation rate of C_1 products during toluene steam reforming over the $MnCr_2O_4$ catalyst. Reaction conditions: 853-893 K, 2 g catalyst, 100 $cm^3 \cdot min^{-1}$ total flow, 2 % C_7H_8, 40 % H_2O, 4 % H_2, 5 % N_2, balance Ar.

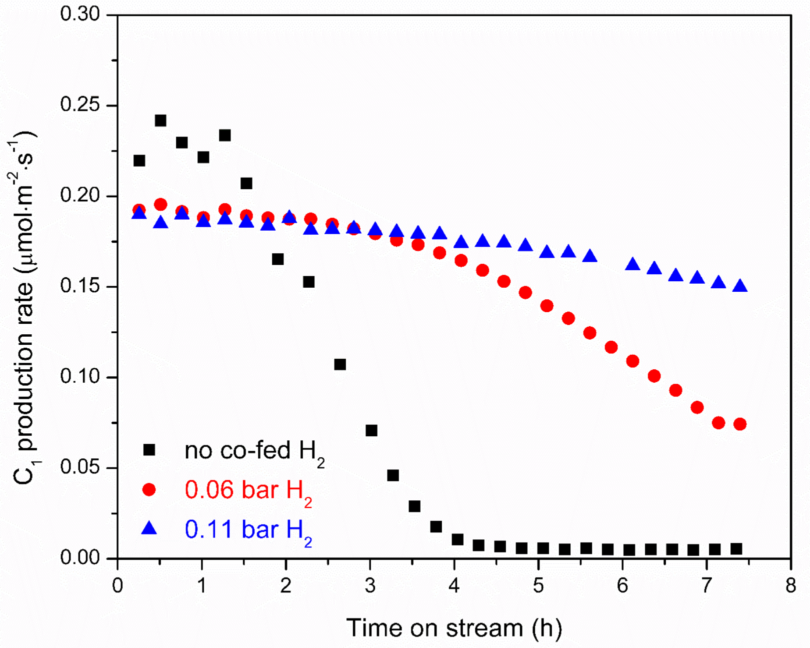

Figure B6. Effect of H_2 partial pressure on the formation rate of C_1 products during propylene steam reforming over the Cr_2O_3 catalyst. Reaction conditions: 873 K, 2 g catalyst, 100 $cm^3 \cdot min^{-1}$ total flow, 5 % C_3H_6, 40 % H_2O, 0-11 % H_2, 5 % N_2, balance Ar.

Table B3. Reaction conditions for steam reforming kinetics of propylene shown in **Figure 6**[a]

Variable	Conditions			
	T (K)	C_3H_6 (%)	H_2O (%)	H_2 (%)
p(H_2) (**Figure 6a**)	873	5	40	0-18
p(C_3H_6) (**Figure 6b**)	873	5-12	40	18
p(H_2O) (**Figure 6c**)[b]	873	5 or 10	20-50	18
Temp. (**Figure 6d**)[b]	853-893	5 or 10	40	18

[a] All tested at 2 g catalyst, 100 $cm^3 \cdot min^{-1}$ total flow. Other than those specified in the table, the gas feed always contained 5 % N_2 and was balanced by Ar. Catalyst was re-oxidized in 100 $cm^3 \cdot min^{-1}$ air flow at 873 K for 6 h in between reactions.

[b] Reactions were conducted at 5 % C_3H_6 over $MnCr_2O_4$ and 10 % C_3H_6 over $Mn_{1.5}Cr_{1.5}O_4$.

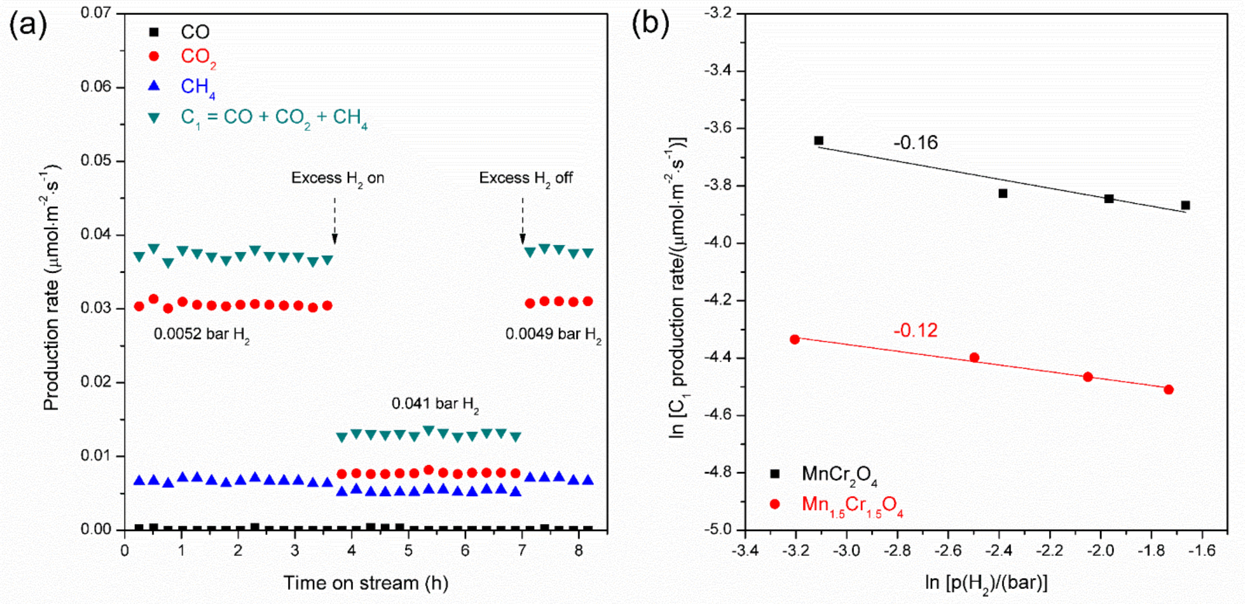

Figure B7. (a) Effect of H_2 partial pressure on the formation rate of C_1 products during propylene steam reforming over the $Mn_{1.5}Cr_{1.5}O_4$ catalyst and (b) fitted reaction order in H_2 for propylene steam reforming over the Mn-Cr-O spinel catalysts. Reaction conditions: 873 K, 2 g catalyst, 100 $cm^3 \cdot min^{-1}$ total flow, 5 % C_3H_6, 40 % H_2O, 4-18 % H_2, 5 % N_2, balance Ar.

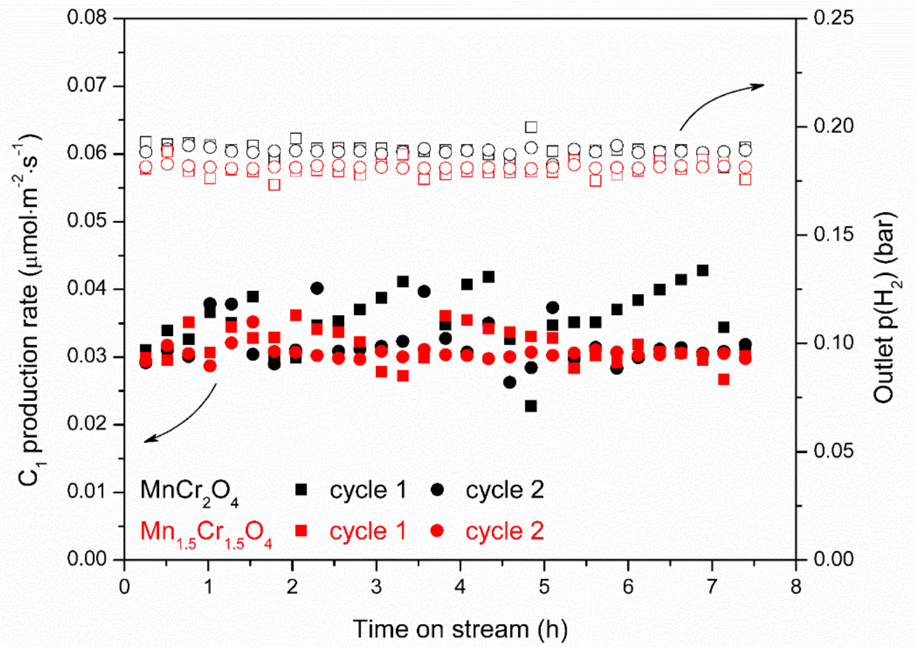

Figure B8. Effect of catalyst re-oxidation on the formation rate of C_1 products during propylene steam reforming. Reaction conditions: 893 K, 2 g catalyst, 100 cm^3·min^{-1} total flow, 5 % C_3H_6 (10 % for $Mn_{1.5}Cr_{1.5}O_4$), 40 % H_2O, 18 % H_2, 5 % N_2, balance Ar. Catalyst spent after cycle 1 was re-oxidized in 100 cm^3·min^{-1} air flow at 873 K for 6 h before tested in cycle 2.

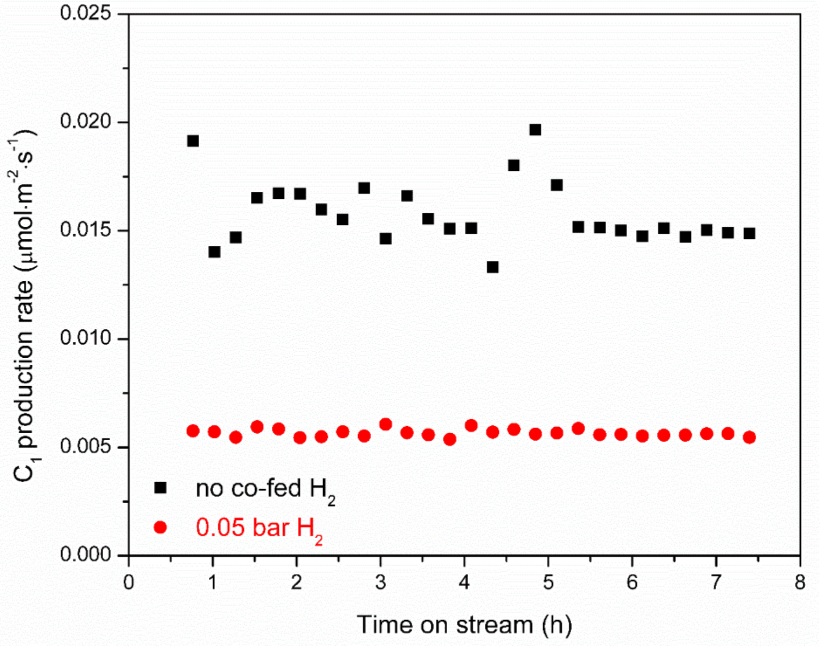

Figure B9. Effect of H_2 partial pressure on the formation rate of C_1 products during benzene steam reforming over the Cr_2O_3 catalyst. Reaction conditions: 873 K, 2 g catalyst, 100 cm^3·min^{-1} total flow, 5 % C_6H_6, 40 % H_2O, 0-5 % H_2, 5 % N_2, balance Ar.

Table B4. Reaction conditions for steam reforming kinetics of benzene shown in **Figure 7**[a]

Variable	Conditions			
	T (K)	C_6H_6 (%)	H_2O (%)	H_2 (%)
p(H_2) (**Figure 7a**)	873	5	40	0-19
p(C_6H_6) (**Figure 7b**)	873	2-5	40	9
p(H_2O) (**Figure 7c**)	873	5	20-50	9
Temp. (**Figure 7d**)	853-893	5	40	9

[a] All tested at 2 g catalyst, 100 $cm^3 \cdot min^{-1}$ total flow. Other than those specified in the table, the gas feed always contained 5 % N_2 and was balanced by Ar. Catalyst was re-oxidized in 100 $cm^3 \cdot min^{-1}$ air flow at 873 K for 6 h in between reactions.

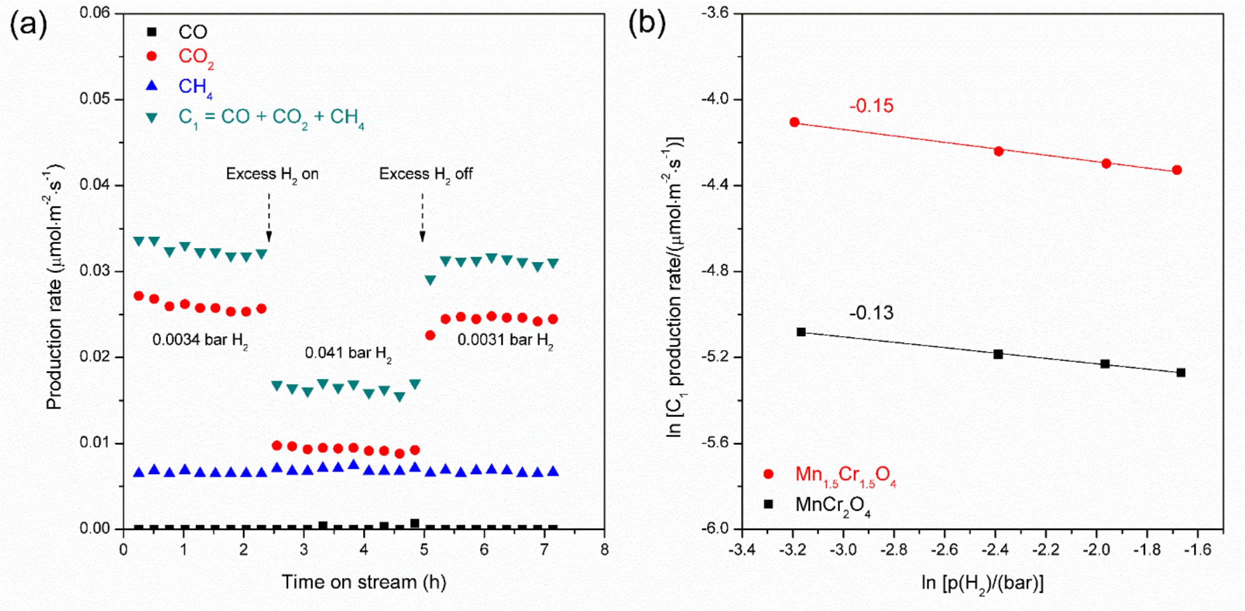

Figure B10. (a) Effect of H_2 partial pressure on the formation rate of C_1 products during benzene steam reforming over the $Mn_{1.5}Cr_{1.5}O_4$ catalyst and (b) fitted reaction order in H_2 for benzene steam reforming over the Mn-Cr-O spinel catalysts. Reaction conditions: 873 K, 2 g catalyst, 100 $cm^3 \cdot min^{-1}$ total flow, 5 % C_6H_6, 40 % H_2O, 4-19 % H_2, 5 % N_2, balance Ar.

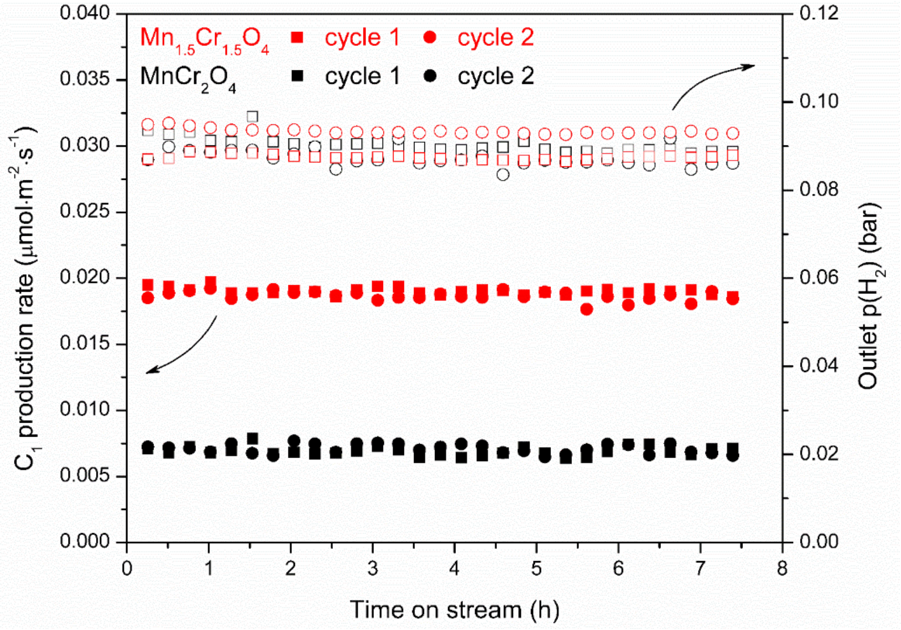

Figure B11. Effect of catalyst re-oxidation on the formation rate of C_1 products during benzene steam reforming. Reaction conditions: 893 K, 2 g catalyst, 100 $cm^3\cdot min^{-1}$ total flow, 5 % C_6H_6, 40 % H_2O, 9 % H_2, 5 % N_2, balance Ar. Catalyst spent after cycle 1 was re-oxidized in 100 $cm^3\cdot min^{-1}$ air flow at 873 K for 6 h before tested in cycle 2.

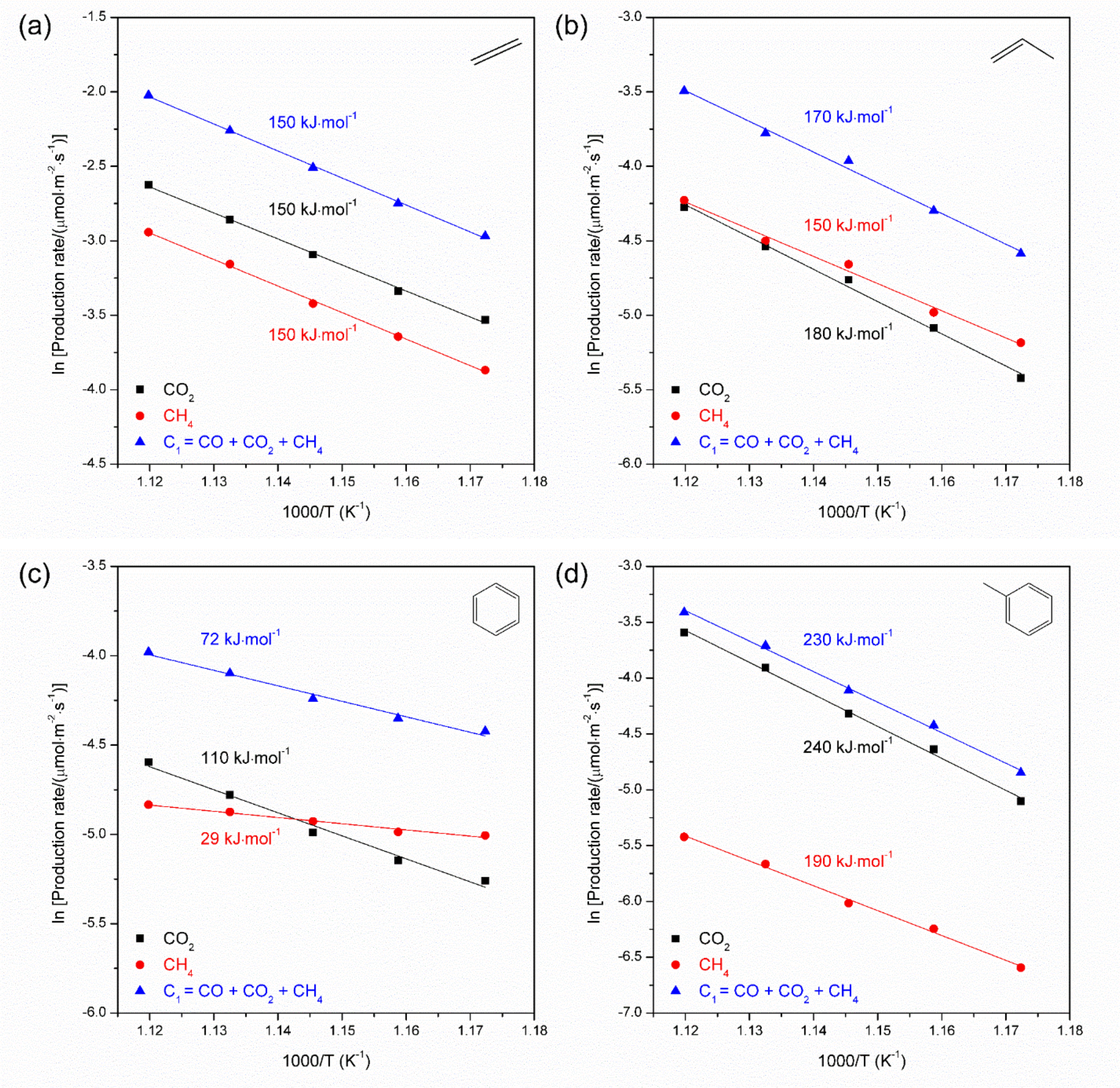

Figure B12. Apparent activation energy for steam reforming of (a) C_2H_4 (data adapted from ref. [1]); (b) C_3H_6; (c) C_6H_6 and (d) C_7H_8 with respect to CO_2 formation, CH_4 formation and overall formation of C_1 products over the $Mn_{1.5}Cr_{1.5}O_4$ catalyst within 853-893 K.

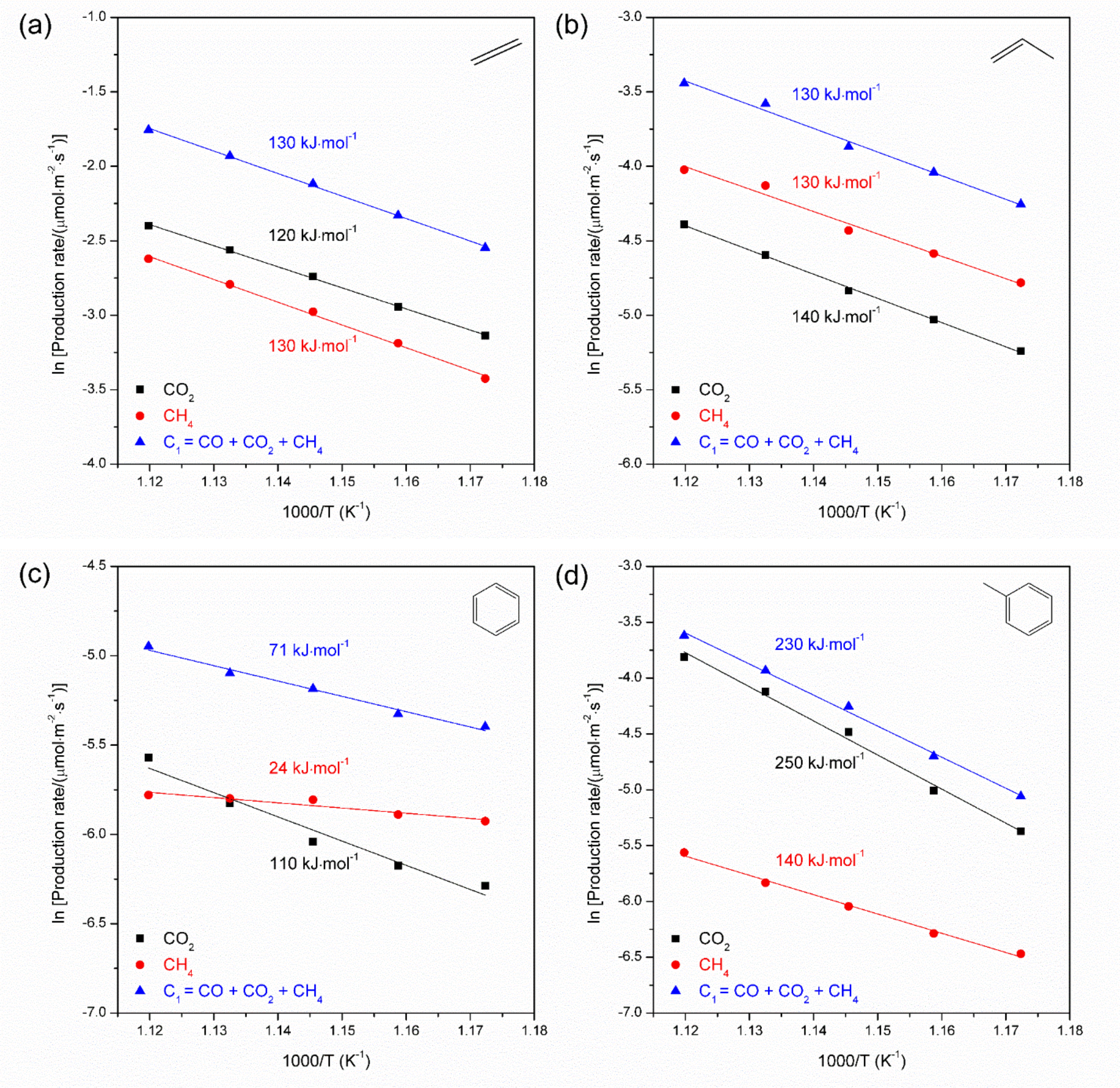

Figure B13. Apparent activation energy for steam reforming of (a) C_2H_4 (data adapted from ref. [1]); (b) C_3H_6; (c) C_6H_6 and (d) C_7H_8 with respect to CO_2 formation, CH_4 formation and overall formation of C_1 products over the $MnCr_2O_4$ catalyst within 853-893 K.

Appendix B1 Material balance for toluene steam reforming

Due to the low flow rate of liquid toluene fed in the reaction, it is not feasible to evaluate the material balance confidently on a carbon basis from the unreacted toluene recovered in the condenser. Instead, we validated our material balance according to the hydrogen balance among the C_1 steam reforming products. Since all C_1 products, including CO, CO_2 and CH_4, derive from C_7H_8, the following overall stoichiometry shall apply:

$C_7H_8 + 7H_2O \rightarrow 7CO + 11H_2$

$C_7H_8 + 14H_2O \rightarrow 7CO_2 + 18H_2$

$C_7H_8 + 10H_2 \rightarrow 7CH_4$

Assuming the rate of coke formation was negligible compared to that of steam reforming under reaction conditions, the production rate of H_2 can be predicted by correlating with the production rate of CO, CO_2 and CH_4 through the following equation:

$$F_{pred}(H_2) = \frac{11}{7}F(CO) + \frac{18}{7}F(CO_2) - \frac{10}{7}F(CH_4)$$

For instance, the comparison of the measured and predicted H_2 production rate in toluene steam reforming over the $MnCr_2O_4$ catalyst at 873 K was shown in **Figure B14**. The predicted molar flow rate of H_2 was in general 10-20 % higher than the experimentally measured value. Nevertheless, this comparison still indicates a reasonably consistent material balance for the measurements of the steam reforming products.

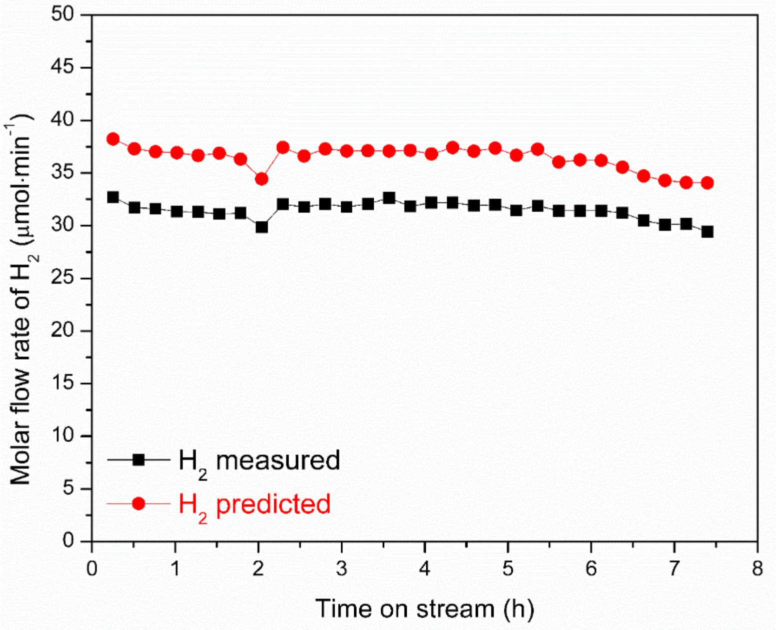

Figure B14. The measured and predicted H_2 production rate in toluene steam reforming over the $MnCr_2O_4$ catalyst. Reaction conditions: 873 K, 2 g catalyst, 100 $cm^3 \cdot min^{-1}$ total flow, 1 % C_7H_8, 40 % H_2O, 5 % N_2, balance Ar.

Appendix B2 Evaluation of the potential effect of intraparticle heat and mass transfer on the measured toluene steam reforming rates

The Anderson criterion was applied to validate the observed toluene steam reforming rate over the $MnCr_2O_4$ catalyst at 873 K was unaffected by intraparticle temperature gradients (within 5 % difference) [2]:

$$\frac{|\Delta H_r| r_{obs} (R_p)^2}{\lambda^e T_S} < 0.75 \frac{R_g T_S}{E_a}$$

where the incorporated enthalpy change of toluene steam reforming concurrent with the Water Gas Shift reaction ($C_7H_8 + 14H_2O \rightarrow 7CO_2 + 18H_2$) $\Delta H_r = 5.8\times10^5\ J\cdot mol^{-1}$, the observed reaction rate of toluene per unit volume $r_{obs} \sim 0.032\ mol\cdot m^{-3}\cdot s^{-1}$, the radius of the catalyst pellet $R_p \sim 2\times10^{-4}\ m$, the estimated effective thermal conductivity of the catalyst particle $\lambda^e \sim 7.6\ J\cdot s^{-1}\cdot m^{-1}\cdot K^{-1}$, the surface temperature of the catalyst particle $T_S \sim 873$ K, the ideal gas constant $R_g \sim 8.314\ J\cdot mol^{-1}\cdot K^{-1}$ and the activation energy of the reaction $E_a \sim 2.3\times10^5\ J\cdot mol^{-1}$.

With the above parameters, we obtain:

$$\frac{|\Delta H_r| r_{obs} (R_p)^2}{\lambda^e T_S} = 1.1\times10^{-7} \ll 0.024 = 0.75 \frac{R_g T_S}{E_a}$$

Therefore, according to the Anderson criterion, the observed toluene steam reforming rates are unaffected by intraparticle heat transfer artifacts.

The Weisz-Prater criterion was utilized to evaluate the potential effect of intraparticle mass transfer artifacts on the reported toluene steam reforming rate over the $MnCr_2O_4$ catalyst at 873 K. For an irreversible, isothermal and first-order reaction in a spherical catalyst pellet, the Weisz-Prater criterion is written as [2]:

$$\frac{r_{obs}\left(R_p\right)^2}{D_{TA}^{e}C_{AS}} \ll 1$$

where the observed reaction rate of toluene per unit volume $r_{obs} \sim 0.032$ mol·m^{-3}·s^{-1}, the radius of the catalyst pellet $R_p \sim 2\times10^{-4}$ m, the estimated effective transition diffusivity of toluene $D_{TA}^{e} \sim 1.4\times10^{-7}$ m^2·s^{-1} [3], and the concentration of toluene at the external surface $C_{AS} \sim 0.14$ mol·m^{-3}.

With the above parameters, we obtain:

$$\frac{r_{obs}\left(R_p\right)^2}{D_{TA}^{e}C_{AS}} = 0.065 \ll 1$$

Thus, according to the Weisz-Prater criterion, the reported steam reforming rates are not limited by intraparticle diffusion through the pore-like voids between the particle aggregates.

Appendix B3 Derivation of the rate expression for toluene steam reforming assuming a two-site Mars-van Krevelen mechanism

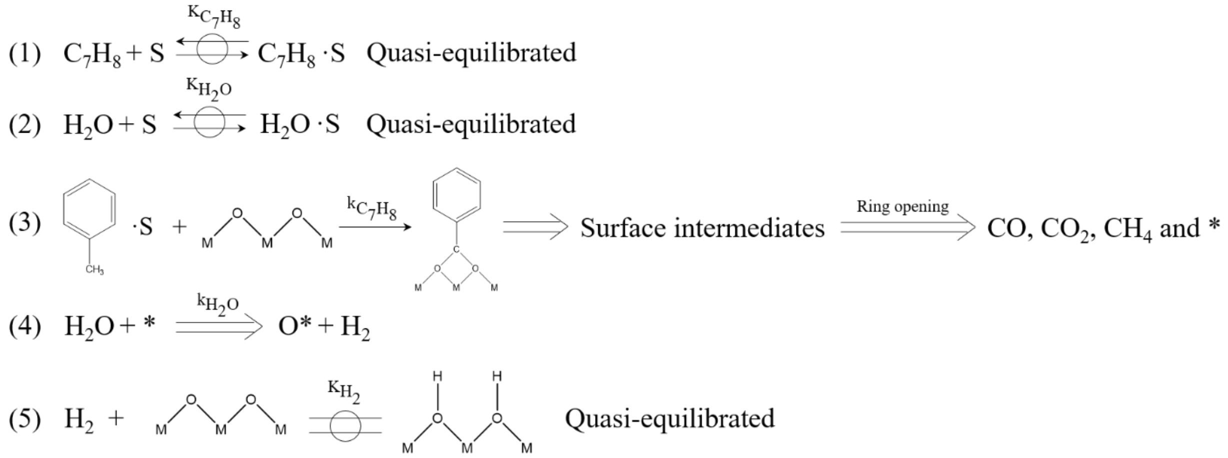

Scheme B1. A two-site Mars-van Krevelen mechanism proposed for toluene steam reforming over the Mn-Cr-O spinel catalysts.

As shown in **Scheme B1**, the adsorption of C_7H_8 (step 1) and H_2O (step 2) is proposed to be competitive over the site S, which likely represents cationic metal sites of Mn^{2+}, Mn^{3+} or Cr^{3+}. Assuming these two steps to be both quasi-equilibrated, we obtain:

$$[C_7H_8 \cdot S] = K_{C_7H_8}[C_7H_8][S] \tag{6}$$

$$[H_2O \cdot S] = K_{H_2O}[H_2O][S] \tag{7}$$

The site conservation of S is written as:

$$[S]_0 = [S] + [C_7H_8 \cdot S] + [H_2O \cdot S] \tag{8}$$

With Eqn. (6), (7) and (8), we obtain the coverage of C_7H_8:

$$[C_7H_8 \cdot S] = \frac{K_{C_7H_8}[C_7H_8][S]_0}{1 + K_{C_7H_8}[C_7H_8] + K_{H_2O}[H_2O]} \tag{9}$$

Steam reforming of toluene is proposed to undergo a sequence of intermediates and eventually to form C_1 products (step 3), with the generated lattice oxygen vacancies refilled by H_2O (step 4).

For mathematical simplicity, it is assumed that only the initial oxidation of toluene to benzoate is kinetically relevant. In this context, the reforming rate of toluene can be expressed as:

$$r_3 = k_{C_7H_8}[C_7H_8{\cdot}S][O^*\ O^*] \tag{10}$$

The inhibition of H_2 in negative first order is proposed to be associated with the homolytic dissociation of H_2 (step 5) over the spinel oxide surface that inhibits the oxidation of toluene on the side chain into benzoate evidenced by the DRIFTS results. Assuming the dissociation of H_2 to be quasi-equilibrated, we acquire:

$$[O^*H\ O^*H] = K_{H_2}[H_2][O^*\ O^*] \tag{11}$$

Although homolytic dissociation of H_2 generally produces a pair of OH groups (O*H O*H), non-paired OH group (O*H O*) can still exist due to the high mobility of H atoms. The overall site conservation of the paired lattice oxygen site is written as:

$$[*\ *]_0 = [O^*H\ O^*H] + [O^*H\ O^*] + [O^*\ O^*] + [O^*H\ *] + [O^*\ *] + [*\ *] \tag{12}$$

where [O*H *], [O* *] and [* *] represent sites containing vacancies as a result of steam reforming. We assume the density of vacancies to be negligible compared to lattice oxygen atoms under reaction conditions ($[O^*H\ *] + [O^*\ *] + [*\ *] \ll [O^*H\ O^*H] + [O^*H\ O^*] + [O^*\ O^*]$). The site conservation in Eqn. (12) can be approximated as:

$$[*\ *]_0 \approx [O^*H\ O^*H] + [O^*H\ O^*] + [O^*\ O^*] \tag{13}$$

In the presence of excess H_2, it is further assumed that the first term representing the coverage of paired OH groups dominates the right side of Eqn. (13):

$$[*\ *]_0 \approx [O^*H\ O^*H] \tag{14}$$

Using Eqn. (11) and (14) to solve for [O* O*]:

$$[O^*\ O^*] = \frac{[O^*H\ O^*H]}{K_{H_2}[H_2]} \approx \frac{[^*\ ^*]_0}{K_{H_2}[H_2]} \tag{15}$$

Rate expression of toluene steam reforming is obtained by plugging Eqn. (9) and (15) into (10):

$$r_3 = k_{C_7H_8}[C_7H_8{\cdot}S][O^*\ O^*] \approx \frac{k_{C_7H_8}K_{C_7H_8}[C_7H_8][S]_0[^*\ ^*]_0}{K_{H_2}[H_2](1 + K_{C_7H_8}[C_7H_8] + K_{H_2O}[H_2O])} \tag{16}$$

The rate expression in Eqn. (16) is consistent with the reaction kinetics observed experimentally for toluene steam reforming. With the rate of hydrodealkylation to benzene to be minor compared to that of steam reforming, the formation rate of C_1 products is obtained as:

$$r_{C_1} = 7r_3 = \frac{7k_{C_7H_8}K_{C_7H_8}[C_7H_8][S]_0[^*\ ^*]_0}{K_{H_2}[H_2](1 + K_{C_7H_8}[C_7H_8] + K_{H_2O}[H_2O])} \tag{17}$$

References for Appendix B

[1] L. Yang, M.P. Bukhovko, G. Brezicki, A. Malek, L. Li, C.W. Jones, P.K. Agrawal, R.J. Davis, J. Catal. 380 (2019) 224-235.

[2] M.E. Davis, R.J. Davis, Fundamentals of Chemical Reaction Engineering, McGraw-Hill Higher Education, 2002, p. 228.

[3] H.Y. Erbil, Y. Avci, Langmuir 18 (2002) 5113-5119.

Appendix C Supplementary material for Chapter 4

Supplementary figures (C1-C6)

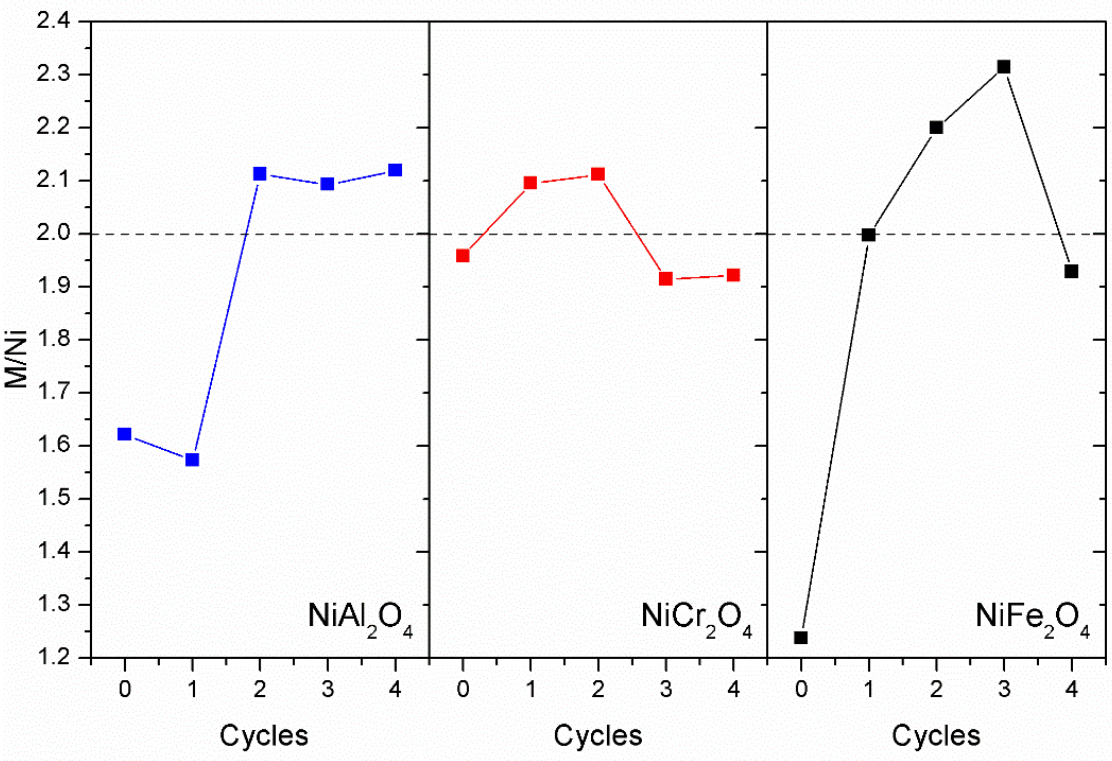

Figure C1 Elemental composition of the fresh NiM_2O_4 spinel catalysts measured from XPS depth profiling. Cycle 0: measured without any treatment; Cycle 1-4: etched with 3 kV Ar ion beam for 1 min before measurement.

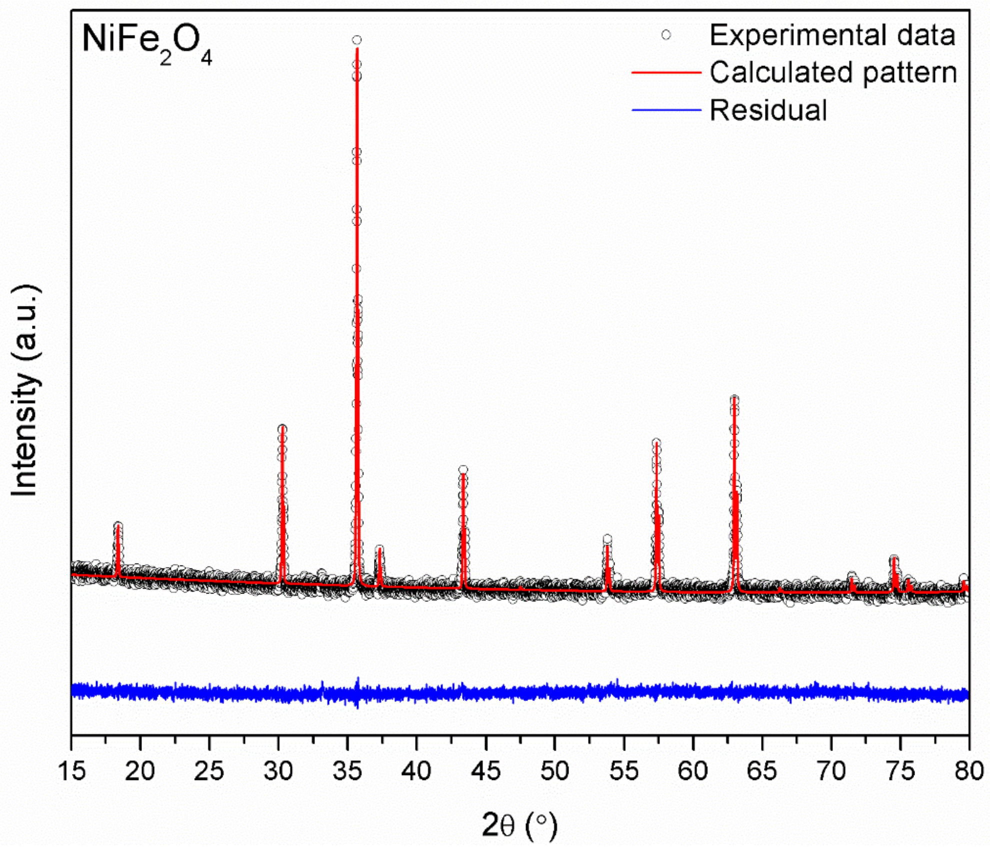

Figure C2 Rietveld refinement of the XRD pattern of the fresh NiFe$_2$O$_4$ sample. The lattice constant *a* from the refinement is 8.340 Å.

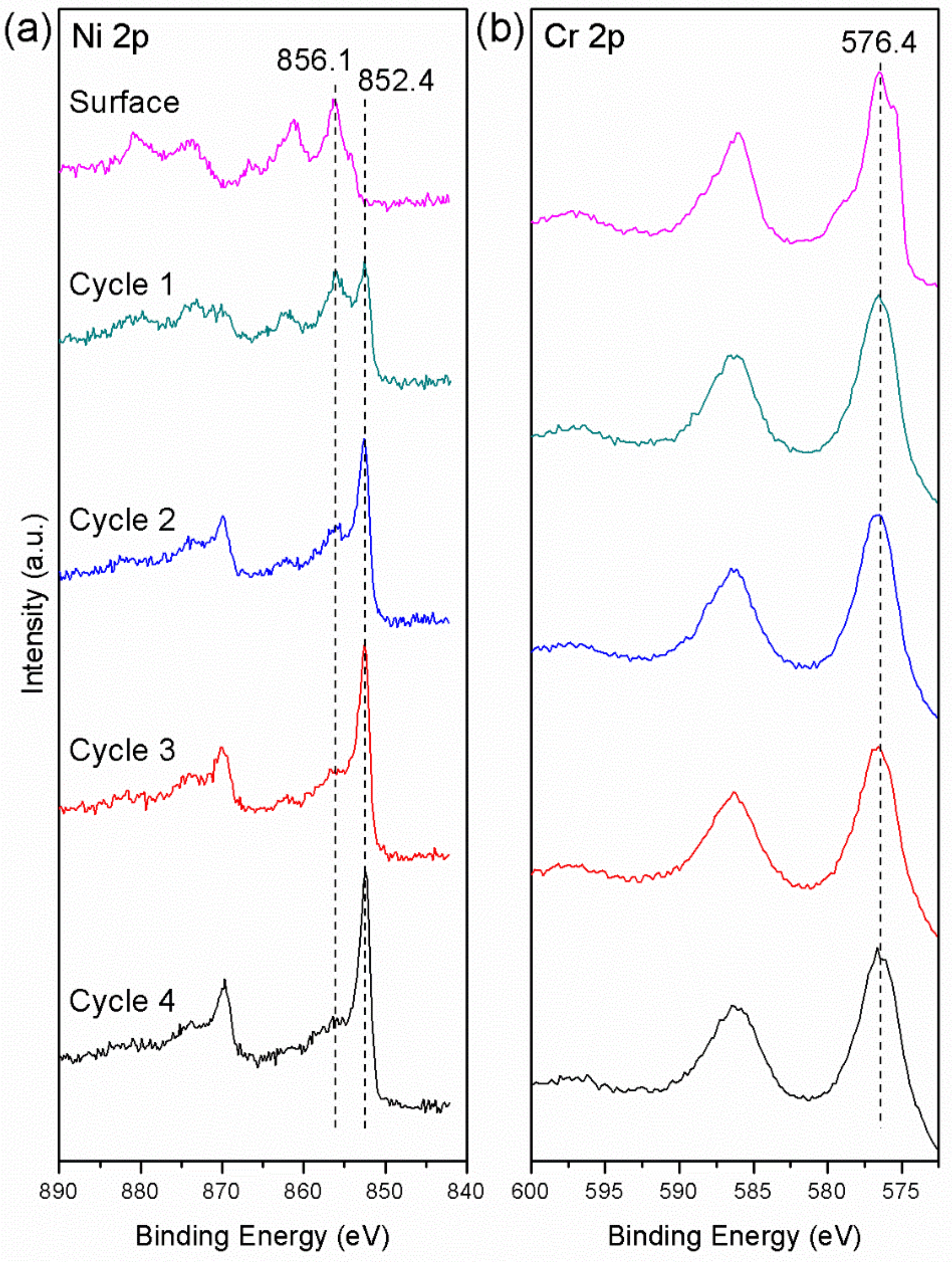

Figure C3 X-ray photoelectron spectra of (a) Ni 2p and (b) Cr 2p of the $NiCr_2O_4$ sample during XPS depth profiling. Surface: measured without any treatment; Cycle 1-4: etched with 3 kV Ar ion beam for 1 min before measurement.

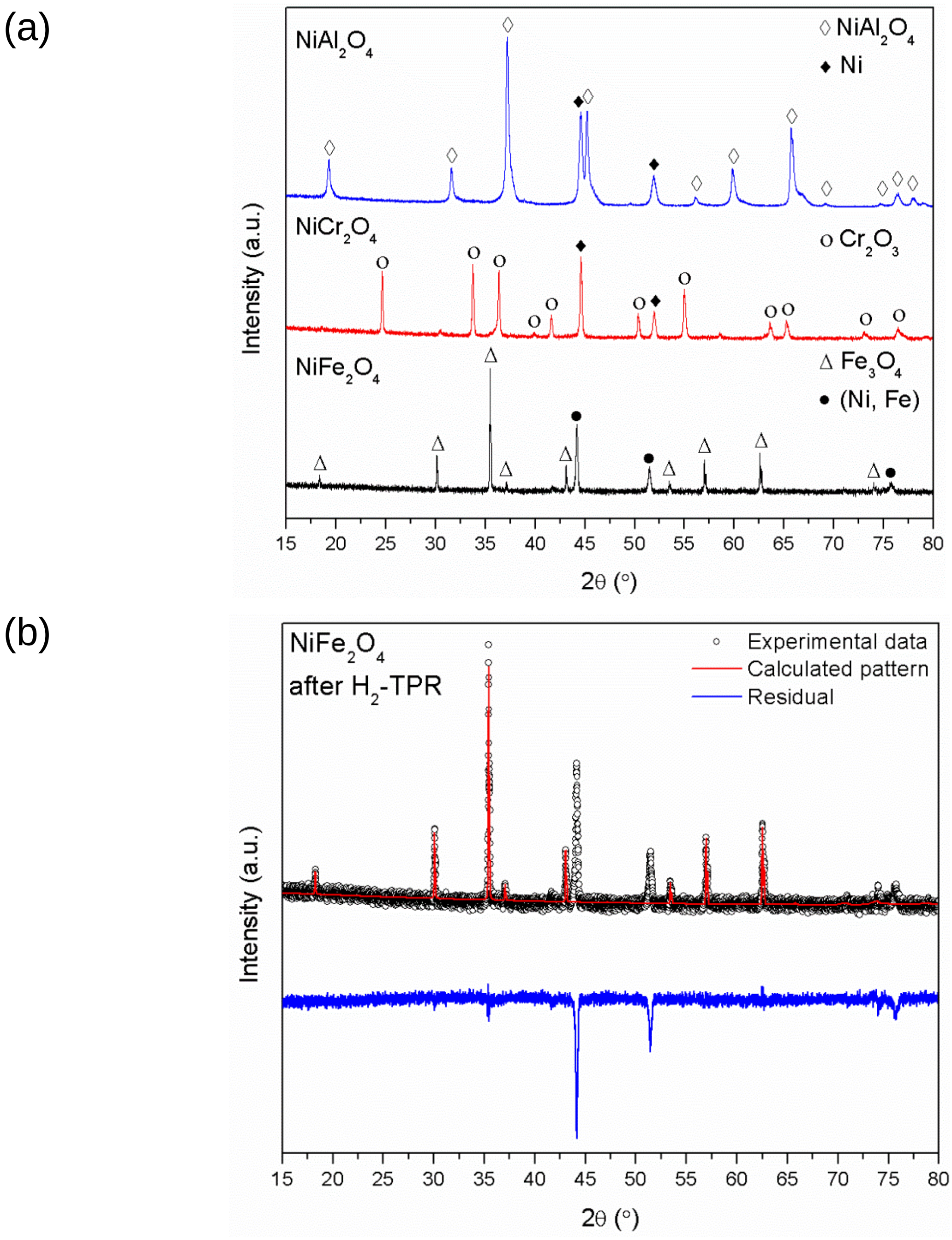

Figure C4 (a) X-ray diffraction patterns of the NiM_2O_4 spinel catalysts after being reduced during the H_2-TPR to 1273 K. (b) Rietveld refinement of the XRD pattern of the reduced $NiFe_2O_4$ catalyst after the H_2-TPR. The spinel phase is assigned to Fe_3O_4 based on a refined lattice constant *a* of 8.393 Å. The major negative peaks in the residual are attributed to Ni-Fe alloy particles, which were not included in this specific refinement.

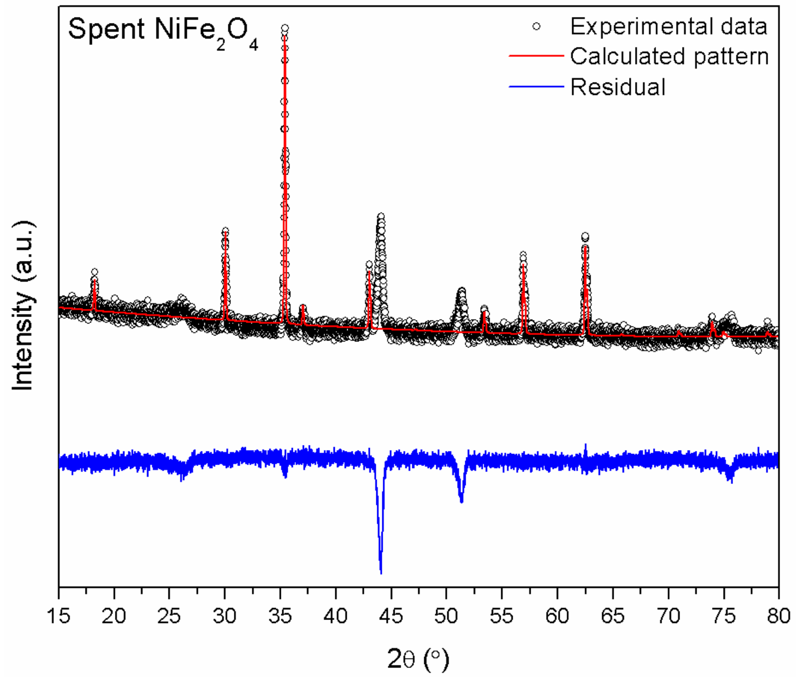

Figure C5 Rietveld refinement of the XRD pattern of the spent $NiFe_2O_4$ catalyst after the steam reforming of ethylene at 873 K. The spinel phase is assigned to Fe_3O_4 based on a refined lattice constant *a* of 8.398 Å. The major negative peaks in the residual are attributed to Ni-Fe alloy particles, which were not included in this specific refinement.

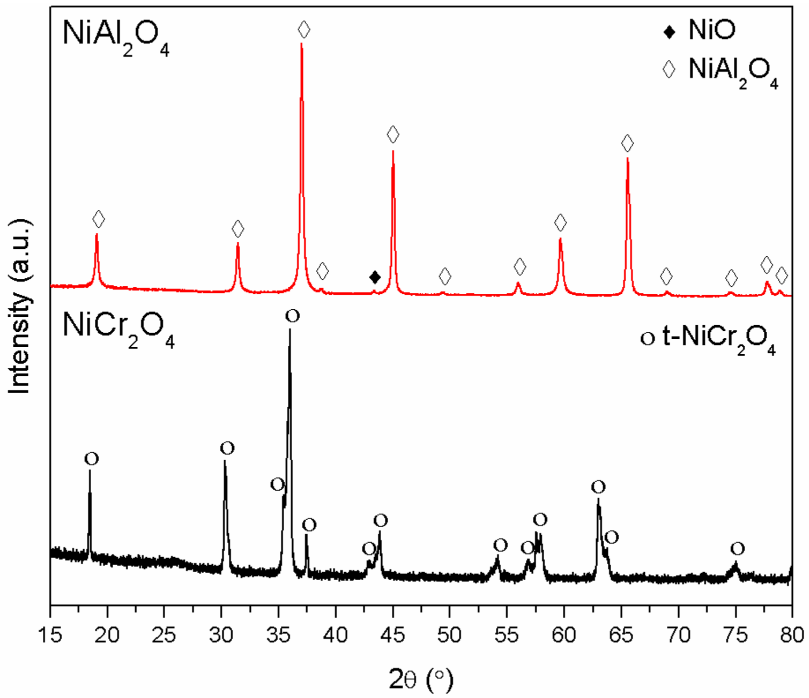

Figure C6 X-ray diffraction patterns of the spent $NiAl_2O_4$ and $NiCr_2O_4$ spinel catalyst after the 2nd cycle of ethylene steam reforming at 873 K.

Appendix C1 Mass balance for ethylene steam reforming

Since the C_2H_4 conversion over the $NiAl_2O_4$ and $NiCr_2O_4$ catalyst was below 10 % under the evaluated conditions, assessing the conversion based on the change in molar flowrate of C_2H_4 from upstream to downstream of the reactor (reactant based conversion) caused inconsistency in carbon balance (*i.e.*, > 300 %) as a result of the general inaccuracies in C_2H_4 quantification from TCD. Therefore, the material balance on a carbon basis could not be reliably validated. Alternatively, we utilized the H_2 balance across the steam reforming products to verify our material balance. Since all C_1 products, including CO, CO_2 and CH_4, originate from C_2H_4, the following overall stoichiometry shall apply:

$$C_2H_4 + 2H_2O \rightarrow 2CO + 4H_2$$

$$C_2H_4 + 4H_2O \rightarrow 2CO_2 + 6H_2$$

$$C_2H_4 + 2H_2 \rightarrow 2CH_4$$

Coke deposition on the $NiAl_2O_4$ and $NiCr_2O_4$ catalysts during steam reforming was no more than 2 wt % (**Figure 4.7**), which corresponded to 1.7 mmol carbon. Comparing to the total carbon formed as C_1 products from C_2H_4 steam reforming (> 11 mmol carbon), the effect of coke deposition on the production rate of H_2 ($C_2H_4 \rightarrow 2C + 2H_2$) was small. Therefore, the production rate of H_2 can be approximated by the production rate of CO, CO_2 and CH_4 as following:

$$F_{predicted}(H_2) = 2F(CO) + 3F(CO_2) - F(CH_4)$$

As shown in **Figure C7**, the calculated H_2 production rates from the above equation are slightly higher than the experimental values over both catalysts. Nevertheless, the comparison indicates a reasonably consistent mass balance from a perspective of product measurement.

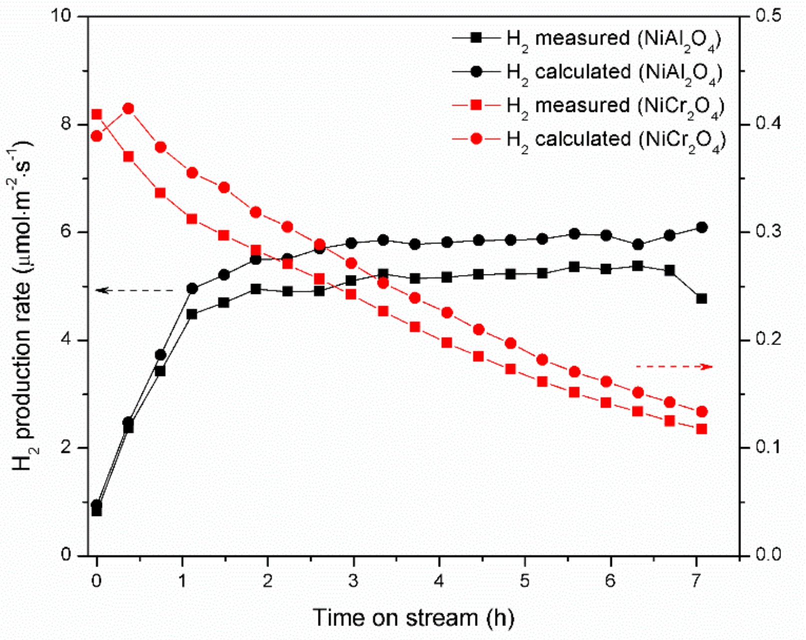

Figure C7 Comparison between the measured and calculated H_2 production rates during ethylene steam reforming over the $NiAl_2O_4$ and $NiCr_2O_4$ catalysts. Data correspond to those shown in **Table 4.3** and **Figure 4.5**. Reaction conditions: 873 K, 1 g catalyst, 100 cm^3·min^{-1} total flow, 25 % C_2H_4, 50 % H_2O, 5 % N_2 and 20 % Ar.

Appendix C2 Reproducibility of the ethylene steam reforming rate

The C_1 production rates during ethylene steam reforming replicates over the $NiAl_2O_4$ and $NiCr_2O_4$ catalysts are shown in **Figure C8**. The trends for the C_1 production rate changing with time on stream were generally reproducible for both catalysts, in which the rate over the $NiAl_2O_4$ catalyst gradually increased and plateaued whereas the $NiCr_2O_4$ catalyst deactivated with time. The initial C_1 production rate over the $NiCr_2O_4$ catalyst (0.22 ± 0.02 $\mu mol \cdot m^{-2} \cdot s^{-1}$) was consistent between four replicates, suggesting the reliability of the reforming product quantification. The C_1 production rate after about 5 h over $NiAl_2O_4$ (1.4 ± 0.6 $\mu mol \cdot m^{-2} \cdot s^{-1}$) is somewhat less reproducible than that over $NiCr_2O_4$, but was still considerably higher during all three replicates. The reforming rate variability over the $NiAl_2O_4$ catalyst was likely attributed to the presence and transformation of trace amounts of NiO that is not uniformly distributed in that sample of catalyst.

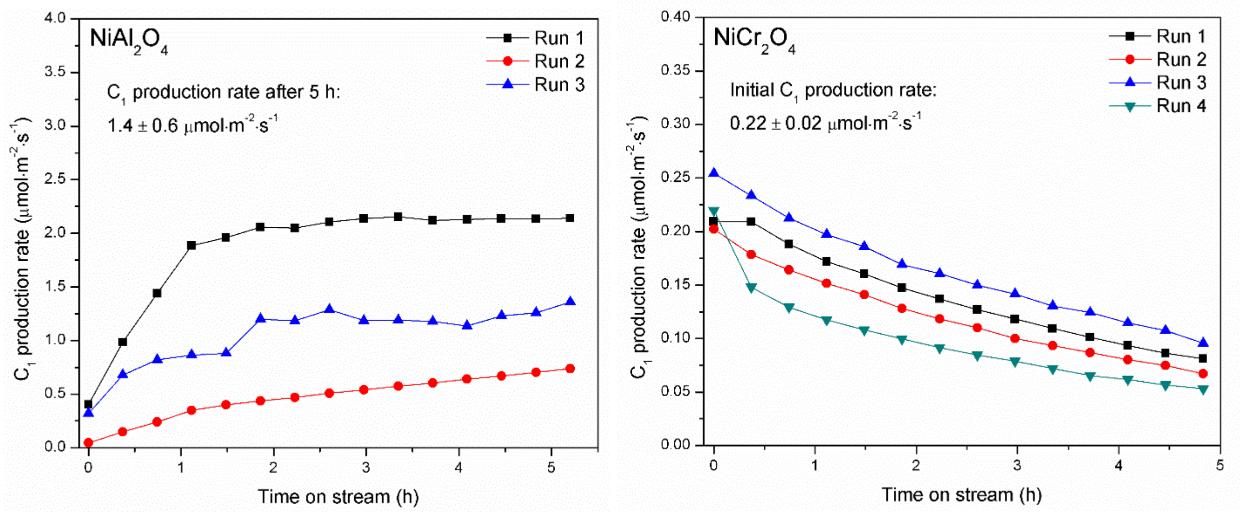

Figure C8 Rate of C_1 formation during the replicates of ethylene steam reforming tests over the $NiAl_2O_4$ (Run 1: as reported in **Table 4.3** and **Figure 4.5**, Run 3: first cycle as reported in **Figure 4.8**) and $NiCr_2O_4$ (Run 1: as reported in **Table 4.3** and **Figure 4.5**, Run 4: first cycle as reported in **Figure 4.8**) catalysts. Reaction conditions: 873 K, 1 g catalyst, 100 $cm^3 \cdot min^{-1}$ total flow, 25 % C_2H_4, 50 % H_2O, 5 % N_2 and 20 % Ar.